Ionic and Dipolar Dynamics in Glassy Electrolytes

Dissertation

zur Erlangung des akademischen Grades

Dr. rer. nat.

eingereicht an der

Mathematisch-Naturwissenschaftlich-Technischen Fakultät

der Universität Augsburg

von

Daniel Reuter

Augsburg, Mai 2020

Universität Augsburg
Institut für Physik

1. Gutachter: Prof. Dr. Alois Loidl
2. Gutachter: Prof. Dr. Dirk Volkmer

Tag der mündlichen Prüfung: 10. September 2020

Contents

List of Abbreviations

AON	2-adamantanon
ADA	adamantane
AN	adiponitrile
ac	alternating current
BE	blocking electrode
ChCl	choline chloride
CC	Cole-Cole
CD	Cole-Davidson
CNA	cyano-adamantane
HEX	cyclohexanol
OCT	cyclooctanol
DES	deep eutectic solvent
DSC	differential scanning calorimetry
dc	direct current
DRC	distributed RC
EP	electrode polarization
EG	ethylene glycol
fcc	face-centered cubic
GN	glutaronitrile
HN	Havrilia-Negami
HBD	hydrogen bond donor
IL	ionic liquid
KWW	Kohlrausch-Williams-Watts
MN	malononitrile
NADES	natural deep eutectic solvent
OC	ordered crystal
ODIC	orientationally disordered crystal
PN	pimelonitrile
PC	plastic crystal
RF	radio frequency
RBM	Random Barrier Model
RT	room temperature
sc	simple cubic
SN	succinonitrile
UDR	universal dielectric response
VFT	Vogel-Fulcher-Tammann

1 Introduction

Some may say, 2019 was the year the world woke up to climate change. Harsh wildfires burned around the globe and the arctic melting accelerated, but truly unprecedented was the number of world-wide climate protests and the formation of an international multigenerational climate consciousness. Rationally speaking, setting aside nuclear power, the eventual transformation from the fossil-fuel to a renewable-energy-based economy is unavoidable and, on the long run, only sustainable and environmentally friendly supply chains can provide humanity with goods it needs.

If we want to retain our standards of living, such transformation to an overall sustainable economy will require not only a change of consumer behavior but also a massive technological advancement. For example, nowadays much hope focuses on the lithium-ion battery (see Nobel Prize in chemistry 2019), which enabled the tremendous success of portable electronics and is still the first choice in modern electric vehicles. Still battery technology has significantly fallen behind modern demands and the battery is a prime example of a pressing technological challenge, which is mainly limited by the performance and properties of the currently available materials [1].

Hence, a major strategy for the improvement of modern technology is the development and optimization of new high-performance materials. In the case of the battery, much research focus lies on the electrolyte. The task of the electrolyte to transport ions between the electrodes might seem trivial at first, but still much potential is seen in the development of new and better electrolytes [2]. However, necessary for such a development is a sound understanding of the underlying physical processes as gained from fundamental research. Especially relevant for an electrolyte, both solid and liquid, are the ion transport mechanism and its dependence on the surrounding matrix. That is exactly what the present work aims at.

This work is a dielectric and mechanical investigation of the interaction and interdependencies of ionic and dipolar dynamics in highly ionically conducting amorphous materials with mobile dipolar molecules. The two chosen material classes possess these properties, but importantly are also up to-date-candidates for wide-spread technical applications with potential for enhanced performance and improved environmental friendliness.

On the one hand, the deep eutectic solvents (DESs) are a soaring material class for green chemistry [3]. Essentially, DESs are mixtures of two or more components, which display a significant melting-point depression in eutectic composition, so that the mixture is liquid at room temperature (RT). Importantly, the DESs reveal physical properties comparable to the popular ionic liquids (ILs) and are regarded as a potential green alternative to them [4].

ILs are salts with melting points below 100 °C and, thus, are solvent free electrolytes with generally low volatility, high electrochemical stability and low vapor pressure [5]. The physical properties of the ILs can further be fine tuned by the various possible cation-anion combinations. For DESs, the melting-point depression enables the use of otherwise solid compounds, which tremendously expands the number of usable materials. So the DES further increase the number of available liquid electrolytes and, thus, have various potential applications [4, 6, 7], even as electrolytes in lithium-ion batteries [8, 9].

Most DESs and the ones investigated in this work are mixtures of a salt with a molecular compound in composition of around 1:1 or 1:2. In the mixture, the salt dissolves and the ions move freely through the viscous medium. The liquid DESs, thus, possess both ions and molecules in large numbers and the ion transfer is presumably strongly influenced by the presence and the dynamics of the molecules.

On the other hand, molecular plastic crystal (PC) electrolytes are solids. In molecular PCs the centers of mass of the molecules form a crystalline lattice, but they are dynamically disordered with respect to their orientational degrees of freedom [10]. Small amounts of ions dissolved in the PC seem to benefit greatly from the reorientational motions of the molecules and display significant mobility within the PC lattice [11]. Thus, molecular PC electrolytes are amorphous solids with unusually high ionic conductivity, a highly sought after innovation for so-called all-solid batteries. In such all-solid batteries no potentially dangerous, flammable liquid electrolytes are used and without the need to package the liquid electrolyte the weight of the battery can be significantly reduced [12].

Similar to the DESs, the molecular PC electrolytes possess dynamically reorienting molecules and translationally moving ions. Here, however, the centers of mass of the molecules remain in fixed positions and the ions move through a dynamically varying but non-viscous surrounding. Therefore, molecular PC electrolytes also serve as a model system for ionic diffusion in a amorphous medium with translational symmetry, much like normal PCs are considered model systems for dipolar relaxation processes [10].

So far no complete experimental characterization of these materials and no comprehensive understanding of the physical mechanisms dominating the ionic charge transport in these systems are available. Most studies on DESs only provide viscosity and direct-current (dc) conductivity values in a small temperature range around RT (see, e.g., [13–15]). The only other dielectric investigation of DESs in a broad temperature and frequency range completely neglected the molecular reorientational dynamics in the evaluation of the data [16]. For the PC electrolytes comprehensive literature exists for the ionic PCs [17–19], but for molecular PC electrolytes only the succinonitrile based systems [20–22] are so far investigated with special focus on the reorientational dynamics of the molecules.

Also from a fundamental research point of view, for dielectric spectroscopy both material classes present the peculiar case of the simultaneous emergence of a dipolar relaxation and a high conductivity contribution. The individual analysis of the two contributions in the same dielectric spectrum is a controversial topic, as can be seen by the prominent example of the ILs [23]. Here, the analysis of the coexistence of the two contributions in the two material classes may shed new light on the interpretation of dielectric spectra of materials with both translationally moving ions and reorienting dipolar molecules.

Hence, the present work aims to provide a systematic investigation of the ionic conductivity of amorphous materials with dynamically reorienting dipolar molecules and to help better understanding the coexistence of dipolar relaxations and ionic conductivity contributions in dielectric spectroscopy. Based on an improved understanding of the interdependencies of ionic and molecular dynamics, strategies for the enhancement of the ionic conductivity in these materials will be proposed.

2 New Classes of Ionic Conductors

As motivated in the introduction, the two chosen material classes for this work, molecular PC electrolytes and DESs, are examples of solid and liquid ionic conductors, respectively. Both are up-to-date candidates for wide-spread technical application, but still lack complete experimental characterization. Additionally, they both possess mobile ions and dynamic molecules. This makes them interesting model systems for the investigation of the simultaneous emergence of both high ionic conductivity and dipolar relaxations in the dielectric spectrum.

2.1 Deep Eutectic Solvents

The history of the DESs begins with the rising research interest in ILs. ILs are salts that are liquid at RT. Starting in the early 1990s [24], ILs attracted widespread interest [25] due to their extraordinary physical properties and various possible applications such as, e.g., chemical solvents [26, 27] or electrolytes in energy-storage systems [28, 29]. However, high prices and toxicity [30–32] of the ILs led to the development of an alternative class of chemical solvents in the early 2000s [13, 14, 33], namely the DESs.

Shortly after their discovery, a considerable hype built up around the DESs. Since then, the number of publications on this subject increased exponentially [34]. Some highly cited review articles emphasize their various possible applications [4, 6, 7] and some even predict them to become the "solvents of the 21st century" [3, 35]. The large number of possible applications includes, e.g., synthesis and material preparation of metal-organic-frameworks [36–38], polymers [39, 40] and porous carbons [41], electrodeposition of metals [42–45] and also the replacement of commonly used electrolytes in lithium-ion batteries [8, 9].

Generally defined as an eutectic mixture of a Lewis or Brønsted acid and a base [4], some more narrow definitions include that their components should be cheap, renewable and biodegradable [6]. Additionally, the subcategory "natural DESs" (NADESs) was defined as DESs consisting of materials from natural sources [3, 46], which highlights their potential in green chemistry.

Prime examples of DESs are mixtures of hydroxyethyltrimethylammonium (choline) chloride (ChCl) with various hydrogen bond donors (HBDs) such as urea, carboxylic acids and polyols. These mixtures are classified as type III DESs [4] and in the present work only such DESs were investigated.

The core principle of DESs is the melting point reduction of a binary mixture in eutectic composition. In the following chapters, firstly this melting point depression will be introduced based on the typical binary phase-diagram and, afterwards, the existing literature on ionic conductivity of and dielectric spectroscopy on DESs will be reviewed.

2.1.1 Eutectic Mixtures

A phase diagram, in general, summarizes the distinct thermodynamic phases of a system in dependence of conditions like, e.g., the temperature, the pressure or the composition. The phase diagram is typically constructed for thermodynamic equilibrium, i.e., at any point in the diagram, the system is

given infinitely time to find its thermodynamic equilibrium. For binary mixtures the phase-transition temperatures typically strongly depends on the composition of the mixture and often a standard pattern is found (see figure 2.1).

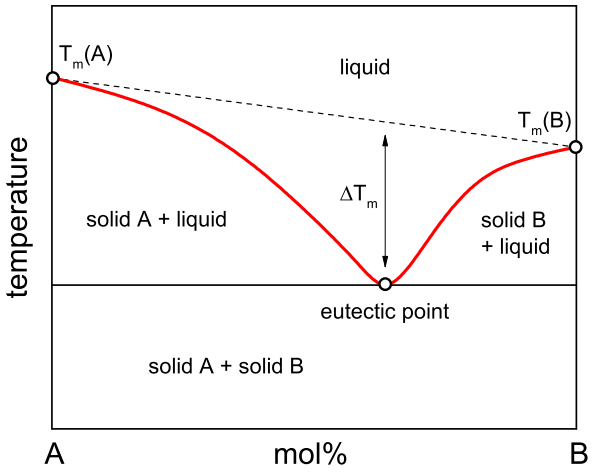

Figure 2.1: Schematic phase diagram of a two-component system with an eutectic point [4]. The red solid line shows the concentration-dependent melting temperature of the system and the black dashed line visualizes the linear interpolation of the melting temperatures of the pure components (denoted with T_m). ΔT_m represents the freezing-point depression at the eutectic composition.

The pure compounds (A and B) reveal a direct transition from the liquid to the solid phase at their respective melting temperatures T_m. Any mixture of the two components, however, has a melting point that is lower compared to the linear interpolation of the melting temperatures of the pure components and, at a certain composition, an overall minimum can be found. At this composition the system is refereed to as eutectic mixture and, in the binary phase-diagram, the composition and its melting temperature define the eutectic point (figure 2.1, black circle). Uniquely at the eutectic point the liquid directly transitions into a solid solution of solid A and solid B, while for any other mixing ratio, at the melting temperature, only one component crystallizes and a suspension is formed.

One of the most studied DESs is the liquid called "reline" [7], the 2:1 molare mixture of urea and ChCl [13]. Figure 2.2 shows reline and its two pure components urea and ChCl. Urea ($T_\mathrm{m} \approx 407\,\mathrm{K}$) and ChCl ($T_\mathrm{m} \approx 576\,\mathrm{K}$) both have melting points well above room temperature, however, in their eutectic mixture composition they form a liquid. Typcially for a DES, both components are cheap, non-toxic and biodegradable [6].

Physically, within the mixture, the halide anion (Cl^-) complexes with the hydrogen bond donor urea [13]. These interactions are energetically preferable compared to the lattice energy of the pure components [47]. Thus the freezing temperature of the liquid is drastically reduced. This mechanism takes place in all DESs consisting of chloride anions and HBD molecules, and only such DESs were investigated in the present work.

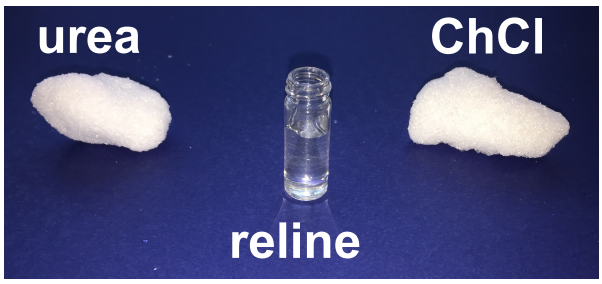

Figure 2.2: Picture of reline and its pure constituents at RT. Urea (left) and ChChl (right) are both white crystalline solids, in the mixture 2:1 they form a colorless liquid named reline.

2.1.2 Ionic Conductivity of Deep Eutectic Solvents

An important measure for the applicability of chemical solvents and electrolytes is the ionic conductivity. For example, the low conductivity of ILs compared to conventional electrolytes is considered as a major drawback for their application in energy-storage systems [48, 49]. Consequently, many studies on DESs include measurements of ionic conductivity (e.g., [13–15] and references within [6]). It was found that, due to their relative high viscosity, conductivities of DESs at RT are typically in the range of 0.1 to $1\,\mathrm{mS\,cm^{-1}}$. Still those studies only focused on small temperature ranges around RT and the direct-current (dc) conductivity alone. Further information on the ionic conductivity can be obtained from measuring its temperature dependence in a broad temperature range and from measuring the alternating-current (ac) conductivity with dielectric spectroscopy.

For the ILs, a large number of dielectric investigations in broad temperature and frequency range is already available (e.g., [23, 50–52]). Actually, excluding publications directly resulting from the present work [53, 54], to the best of the author's knowledge, so far only one study by Tripathy *et al.* [16] has reported dielectric measurements in a broad temperature and frequency range on DESs. Other dielectric spectroscopy based publications focused on rather limited frequency and temperature ranges [55, 56], a non-ionic DES [57], simulations [58] or a deep eutectic mixture with relatively high ionicity [59].

Despite sharing many similarities in their physical properties, the important difference between ILs and DESs (type III) is that ILs are entirely composed of ionic species while DESs represent a fluid mixture of molecules and ions (see figure 2.3). This is especially important for dielectric spectroscopy, as this measurement technique simultaneously detects translational motion of ions and reorientational motion of dipolar molecules. Those molecular dynamics in the liquid state of the DESs were arguably neglected in the study by Tripathy *et al.* [16], who chose a solely conductivity related interpretation of the dielectric spectra.

Similar to dielectric spectroscopy, many publications report viscosity data of DESs (e.g., [14, 46, 60, 61]), however, only in a rather limited temperature range and only for the steady-state flow viscosity η_0. Generally, it is agreed upon that the viscosity of DESs, representing the overall flow dynamics of its constituents, controls the ionic diffusivity [4, 14, 15]. However, detailed studies, including data in a wide temperature range down to the glass transition, are not available.

Altogether, experimental data from dielectric spectroscopy on DESs are rare. Especially, a comprehensive study combining dielectric and mechanical spectroscopy data in a broad temperature and frequency range is absent so far. The present work aims to fill this gap and to provide information on the relations of ionic translation motion, molecular dynamics and overall viscosity in DESs.

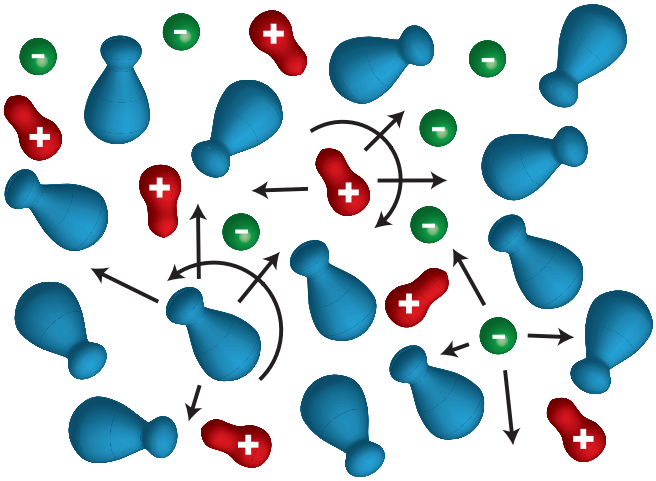

Figure 2.3: Schematic drawing of the constituents of a typical ChCl based DES [54]. Blue dumbbells represent the neutral molecules. The ChCl is dissolved into Ch^+ (red dumbbells) and Cl^- (green spheres). Black arrows indicate the possible dynamics.

2.2 Plastic Crystalline Electrolytes

In the 1930s of the past century, Timmermans [62] found a mesophase, a state between solid and liquid matter, for "some peculiar compounds, of usually relatively simple constitution" [63]. This phase was, at first glance, characterized by a relatively high entropy change of its solid-solid transition and a relatively low entropy change upon melting into the liquid ($\Delta S \leq 20\,\mathrm{J\,mol^{-1}\,K^{-1}}$). Additionally, those crystals were highly plastic, even demonstrating flow at an observable rate, which earned these materials the name plastic crystals (PCs) [64]. Another important property of PCs is that they reveal dynamic orientational disorder of their molecules sitting on fixed crystal lattice positions, the reason why they are also referred to as orientationally disordered crystals (ODICs) [10, 64, 65]. A physical explanation for the observed phenomenology relies on the rather globular shape of the molecules forming most known PCs, which provides little steric hindrance for reorientational motion.

While in the following centuries the research on PCs only focused on the fundamental physical aspects of this mesophase, in the 1980s some PCs were found to exhibit considerable ionic conductivity [66–69], which later led to their recognition as potential solid electrolytes [17, 70].

The material class of PC electrolytes can be divided into two subgroups: Ionic PC (e.g., [17–19, 70–73]) and molecular PC electrolytes (e.g., [11, 20–22, 74–76]). The former are entirely composed of ionic species, effectively representing an IL in the PC phase. The latter consist of neutral molecules with relatively small amounts of ions admixed to enable significant ionic conductivity. In the present work only molecular PC electrolytes were investigated.

Obviously, the plastic crystalline state is a rather exotic state of matter and will, therefore, be in detail introduced in the following chapter. Afterwards, the existing literature on ionic conductivity of PC electrolytes will be reviewed.

2.2.1 The Plastic Crystalline Phase

The plastic crystalline state of matter may be best introduced by giving a schematic overview on the typical solidifications a liquid can undergo upon cooling (see figure 2.4).

Any liquid (figure 2.4, orange phase) is able to flow, because of the long range translational diffusion

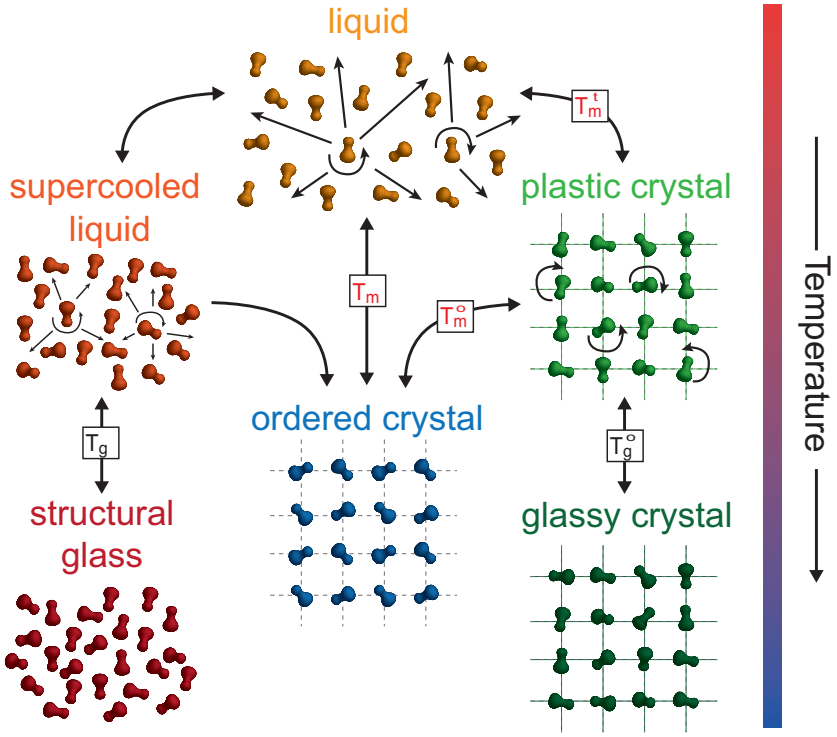

Figure 2.4: Schematic structure comparison of the liquid (orange), supercooled liquid (red), glassy (dark red), ordered crystalline (blue), plastic crystalline (green), glassy crystalline (dark green) state of matter [10]. Asymmetric bodies represent dipolar molecules and small black arrows imply their possible dynamics. Transitions are labeled with their respective transition temperatures.

of its molecules. Additionally, in the liquid phase, the molecules are able to rotate. Upon decreasing the temperature, the liquid may either transfer into an ordered crystal (OC) (figure 2.4, blue phase) at its melting temperature T_m or enter the metastable supercooled liquid phase (figure 2.4, red phase). Structurally, the supercooled liquid is identical with the normal liquid, but is characterized by the gradual slowing down of its molecular dynamics. A more detailed discussion of the supercooled liquid and of the glass transition will follow in chapter 3.1.

At any temperature below T_m, the liquid is able to crystallize into the OC. However, this is a statistical process and, under specific circumstances (e.g., fast cooling), can be totally avoided. In this case, the liquid forms a structural glass (figure 2.4, dark red phase) via a glass transition at T_g (= glass transition temperature). The structural glass is an amorphous material, where molecular diffusion processes are slowed down to an extent that they exceed the typical observation time frame (usually defined as 100 s). In contrast to the OC, the glassy state is translationally as well as orientationally disordered.

The plastic crystalline state (figure 2.4, green phase) represents an intermediate state between liquid and OC. Here, the molecules are arranged on a regular crystal lattice, however, they retain reorientational degrees of freedom, as indicated by black arrows in figure 2.4. The transition temperature is named T_m^t for translational melting temperature, because at this transition only a melting of the translational degrees of freedom of the molecules is taking place.

Upon further cooling, a PC can undergo two transitions. Either a second crystallization occurs, where the reorientational degrees of freedom order via a first order phase transition, resulting in a OC, or crystallization is suppressed sufficiently and the orientational disorder of the PC freezes via a

glass-transition like process into a glassy crystal (figure 2.4, dark green phase). Here, the transition temperatures refer to the melting (T_m^o) or glassy freezing (T_g^o) of the orientational degrees of freedom. Not every PC phase reveals full angle rotation around all three axis, but for many materials subsequent low-temperature phases with restricted reorientation were found [10].

The reorientational motion of the molecules within the PC lattice, however, cannot account for the high plasticity found for many of these compounds. Indeed the rotational disorder is enabled by the weak interaction of the molecules. Additionally, these weak interactions benefit the migration of lattice defects and vacancies as well as set up crystalline plane slips [17, 77], which altogether leads to the observed high plasticity.

From a basic research point of view, PCs are interesting model systems to study liquid-like molecular dynamics in an environment of translational symmetry. However, nowadays they gained considerable recognition for potential technical application as solid ionic conductors [17, 70] or in solid-state refrigeration technology [78].

2.2.2 Ionic Conductivity of Plastic Crystalline Electrolytes

Despite having attracted considerable research interest in the past decades, as for now, there is no widely accepted theory to explain the ionic conductivity of PCs. Many possible explanation attempts were made, but generally only focusing on certain compounds or on one of the two subgroups (ionic and molecular). Especially for the ionic conductivity in molecular PC systems (the focus of the present work), excluding publications that directly resulted from the present work, experimental data covering many different materials are not available. Thus, to review the current state of research, findings from both subgroups have to be taken into consideration.

Early works on the ionic PC Li_2SO_4 and related compounds assumed a direct coupling of the translational ionic motion to the rotator motion of the anion and coined the terms "paddle wheel" and "revolving door" for this mechanism [66–69]. The authors agreed that the ionic translation hopping process benefits from the spherical delocation of the anions.

Later, for the organic ionic PCs, a further subgroup of the ionic PCs, a number of different mechanisms were discussed (e.g., [18, 19, 71, 79, 80]), all focusing more or less on the peculiar properties of the PC lattice. To name a few, Pas *et al.* [79] identifed a direct correlation of the mean defect volume to the ionic conductivity and Abu-Lebdeh *et al.* [71] proposed interconnected channels produced from long dislocated defects as efficient pathways for the ions.

For molecular PC electrolytes, the pioneering work by Long *et al.* [74] initiated the interest in the PC succinonitrile [SN; $C_2H_4(CN)_2$]. Here, admixed with the salt LiTFSI ($LiC_2F_6NO_4S_2$) a conductivity of $0.34\,\mathrm{mS\,cm^{-1}}$ at RT was found for a 5 mol% mixture. They proposed an explanation in which the introduction of additional impurities by the salt enhances the diffusivity of the PC [74]. Following these studies, SN gained recognition as a "universal matrix for solid-state ionic conductors" [11] and many groups studied the effects of the admixture of various salts [11, 81], relative molecular compounds [20–22] and polymers [82, 83].

Interesting insights into the mechanism of ionic conductivity in molecular PCs was later gained by Geirhos *et al.* [20], who observed a drastic, up to three decades of magnitude conductivity enhancement of SN with 1 mol% $LiPF_6$ when mixed with glutaronitrile [GN; $C_3H_6(CN)_2$]. Additionally, they demonstrated that the reorientational molecular dynamics and the ionic translational motion gets gradually better coupled with increasing GN amount in the mixture. The simultaneous emergence of conductivity enhancement and increased coupling of ionic and molecular dynamics was then interpreted as an example of the revolving door mechanism in a molecular PC.

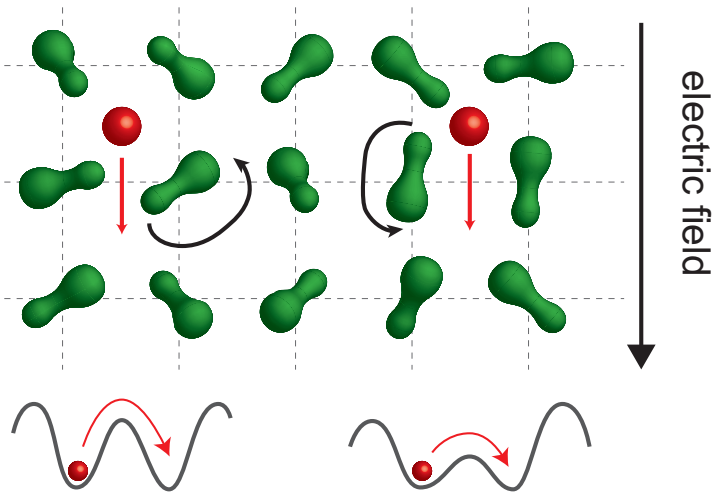

Figure 2.5: Simplified visualization of the revolving door mechanism in a molecular PC electrolyte with neutral molecules on the lattice sites and ions on interstitial sites. Red arrows symbolize ionic translation motion, black arrow the molecular reorientation. The lower part represents the experienced energy landscape of the ions during translational diffusion through the PC lattice, which is determined by the orientation of the molecules.

In this interpretation (cf. figure 2.5), the neutral molecules occupy the lattice sites and ions are located on interstitial sites or in vacancies. The reorientational motion of the molecules determines the energy landscape the ions are experiencing during their translational diffusion. This effect naturally gets improved the more asymmetric or elongated the molecules are, because in this way reorientation of the molecules opens up more vacant volume for the ions.

Compared to SN, GN possesses one additional CH_3 group making it significantly bulkier and more stretched. Thus, the integration of the bigger GN molecules might enhance a possible revolving door mechanism in the SN-GN PC.

Altogether consensus exists that the dynamic disorder in PC electrolytes generates a high entropy medium which benefits ionic translational motion [17, 19, 69, 84]. The exact mechanisms, however, seem to vary strongly between different compounds. Especially for the molecular PCs, experimental data on a wider range of different PCs is needed. As motivated in the introduction, the present work aims to systematically probe molecular PCs with very different molecular shape for their ability to enable ionic translational motion and, thereby, to provide valuable information on mechanism of ionic conductivity in molecular PCs.

3 Theoretical Basics

DESs and molecular PC electrolytes both reveal dynamic molecular disorder and ionic conductivity. Dielectric spectroscopy is an ideal tool to study these materials as it enables the detection of both the molecular as well as the ionic dynamics, simultaneously. In the case of liquid ionic conductors, rheology measurements nicely complement dielectric data as they are sensitive to the overall viscous response of the sample, which includes all types of dynamics in the system.

As long as a first-order transition into a fully ordered crystal is avoided, during cooling the investigated materials exhibit glassy freezing of their dynamics, i.e., they form a glassy state via a glass transition.

The following chapters will establish the theoretical background necessary for the evaluation, analysis and interpretation of the experimental results of the present work. In particular, the general phenomenology of glassy freezing and the theoretical basics of dielectric and mechanical spectroscopy will be introduced.

3.1 Glassy Freezing

"Glassy freezing" may be defined as the progressive slowing down and eventual freezing of any dynamic disorder via a glass transition, most prominently present in glass-forming liquids [85]. This chapter follows standard textbook knowledge comparable to ref. [86, 87] and will only focus on molecular and ionic systems as only such will be investigated in the present work.

Any pair of neutral molecules experiences repulsive and attracting forces from each other depending on the distance r between them. Repulsive forces are generated by the interaction of the electron orbitals and rapidly decrease with increasing distance between the molecules. Attracting forces are mainly Van-der-Waals, H-bonds and dipole-dipole interactions. Together those forces define a potential well with a minimum at a certain distance r_m. The effective binding energy resulting from the potential defines in which state of matter a material exists at a certain temperature and pressure. A simple example of such a potential is known as the Lennard-Jones potential [88].

Besides plasma, the three states of matter are gas, liquid and solid. If the kinetic energy of the particles greatly exceeds the binding energy, a gas is formed and the particles move freely only interacting via collisions. In a solid material the kinetic energy is much lower than the binding energy, so the particles get trapped in fixed positions without the ability to move translationally but can only vibrate. Finally, if kinetic energy and binding energy are of the same order of magnitude, particles are under strong influence of their nearest neighbors but translational jumps become possible. The result is a viscous medium: the liquid state.

Many systems can reversibly undergo transitions between the different states of matter. The liquid-gas transition is a first-order phase transition, characterized by an energy absorption during evaporation (liquid to gas) respectively energy release during condensation (gas to liquid). For the liquid-solid transition, however, there are two different routes.

One is the evaporation/condensation counterpart. When cooled below its melting temperature T_m,

nucleation occurs in a liquid. Molecular clusters are built, because the kinetic energy of the molecules is sufficiently decreased, and if such clusters exceed a critical size, they act as crystallization nuclei and crystal growth is enabled. The liquid crystallizes into a fully ordered crystal accompanied by a sharp change of physical properties like, e.g., the enthalpy and the volume (see figure 3.1, red line). Due to this two-step process and the statistical nature of the nucleation, liquids can be supercooled below T_m. During heating, however, the molecules can only escape the crystal lattice when the thermal energy is sufficient to overcome the binding energy and melting always sets in at T_m.

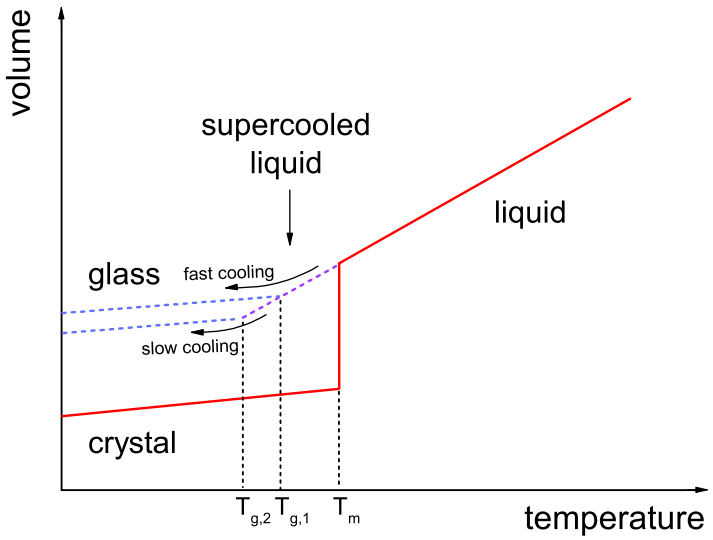

Figure 3.1: Schematic temperature dependence of the volume of a material at the transition into an ordered crystal or a glass. The solid red line depicts the idealised behavior of linear temperature dependence in the liquid state, followed by a sharp decrease at the transition into an ordered crystal. The supercooled liquid region is a straight expansion of the liquid state towards lower temperatures (dashed violet line). At the transition into the glass (blue dashed line) the temperature dependence shows a kink revealing a reduced steepness in the glassy state. Cooling-rate dependence of the glass transition is visualized by the upper and lower curve in the glass state, obtained with a faster respectively slower cooing rate. On basis of [86, 89].

The temperature ranges of ideal nucleation and ideal crystal growth are usually separated, favoring nucleation at lower and crystal growth at higher temperatures. If no sufficient nucleation occurs below the melting temperature, a liquid remains in a metastable equilibrium. Upon further cooling the molecular dynamics slow down, the volume shrinks and the viscosity increases, until eventually the molecules become trapped in fixed positions with random translational and orientational arrangement. This is called the glass transition and it is characterized by a change of the temperature dependence of physical properties as the enthalpy and the volume at the glass transition temperature T_g (see figure 3.1, transition from violet to blue line) [86]. Hence, a glass is a solid material without lattice symmetry.

The general 'rule of thumb' predicts $T_g \approx \frac{2}{3} T_m$ [89] and is found to be valid for many different systems. This rule, however, neglects a basic principle of the glass transition: its cooling rate dependence. Vividly speaking [86], a cooling rate $q = dT/dt$ can be regarded as a sequence of cooling steps ΔT with isothermal holds of length Δt in between the steps. Thermodynamic equilibrium is maintained as long as the molecular relaxation time τ, the time the molecules need to rearrange into a new equilib-

rium position after a temperature step, is shorter than Δt. τ is a temperature dependent property of a liquid, strongly increasing with decreasing temperature due the slower fluctuations of the molecules at lower temperatures. As soon as τ exceeds Δt, the relaxation is incomplete and the systems falls out of thermodynamic equilibrium, i.e., the glass transition occurs. The faster the cooling rate, the shorter becomes Δt and the earlier (at higher temperatures) the glass transition takes place. This is visualized in figure 3.1 by two different glass-transition temperatures obtained with different cooling rates.

Hence, the glass transition is not a first order transition nor is it any kind of classical phase transition. It is a kinetically driven event at which the time of molecular rearrangement exceeds the experimental timescale. Thus, a glass is a frozen liquid on the timescale of a human observer [90]. Therefore, T_g has to be defined with respect to the experimental setup. Since typically applied cooling rates in experiments are $0.1 - 100\,\mathrm{K/min}$ and the cooling-rate dependence of the glass transition is relatively weak, only varying by a few Kelvin per order of magnitude cooling rate, the glass-transition temperature of a material narrows down on a short temperature interval. While it varies from system to system, at T_g, usually relaxation times $\tau(T_\mathrm{g}) = 10 - 10^4\,\mathrm{s}$ and viscosities $\eta(T_\mathrm{g}) \approx 10^{12}\,\mathrm{Pa\,s}$ are measured [90]. For the present work, the common values [89] of $\tau(T_\mathrm{g}) = 100\,\mathrm{s}$ and $\eta(T_\mathrm{g}) = 10^{12}\,\mathrm{Pa\,s}$, when cooled with a cooling rate of the order of $10\,\mathrm{K/min}$, are used.

Another important aspect of glassy freezing are the molecular dynamics when approaching the glass transition. The so-called structural relaxation time τ of a system is a measure that includes all different kinds of molecular dynamics, such as rotation and translation of its constituents, and represents the timescale of these dynamics. It is the primary relaxation feature of the system and is, therefore, often called the α-relaxation [85, 91]. Closely related is the viscosity, the resistance of a liquid to flow. In a prefect system all different molecular dynamics are coupled, which means they have the same temperature dependence of the activation energy. All together they define the viscosity of a liquid. In the following, important equations to describe the temperature dependence of the structural relaxation time of a liquid when approaching the glass transition will be introduced. All of these equations can be written for the viscosity in straight analogy.

The natural assumption is that in a liquid the structural relaxation is a thermally activated process. At any point in time, the system sits in a potential well, defined by the arrangement of its consituents. After any kind of rearrangement, the system as a whole has to overcome an energy barrier E to relax to thermodynamic equilibrium. The probability to do so, is determined by the thermal energy of the molecules. Mathematically this can be described by the Arrhenius equation [92]:

$$\tau = \tau_0 \, \mathrm{e}^{\frac{E}{k_\mathrm{B} T}} . \tag{3.1}$$

The structural relaxation time τ is a function of its high-temperature limiting relaxation time τ_0 and exponentially depends on the energy barrier E divided by the thermal energy $k_\mathrm{B} T$. $\nu_0 = 1/(2\pi\tau_0)$ is called the attempt frequency and is thought of as the rate at which the systems tries to overcome the energy barrier, usually a microscopic excitation in the THz range. Due to $\mathrm{e}^{\frac{E}{k_\mathrm{B} T}}$ the structural relaxation time is strongly temperature dependent.

Over a broad temperature range, however, it was found that most liquids do not obey the simple Arrhenius equation. In fact, the energy barrier E seems to be temperature dependent and increases when approaching T_g. To account for this deviation, various authors proposed a simple phenomenological modification of the Arrhenius equation, which is nowadays known as the Vogel-Fulcher-Tammann (VFT) equation [93–95]:

$$\tau = \tau_0 \, \mathrm{e}^{\frac{B}{T - T_\mathrm{VF}}} . \tag{3.2}$$

The introduction of a temperature T_{VF}, a temperature below T_g at which the relaxation time diverges, led to much better fits to the experimental data.

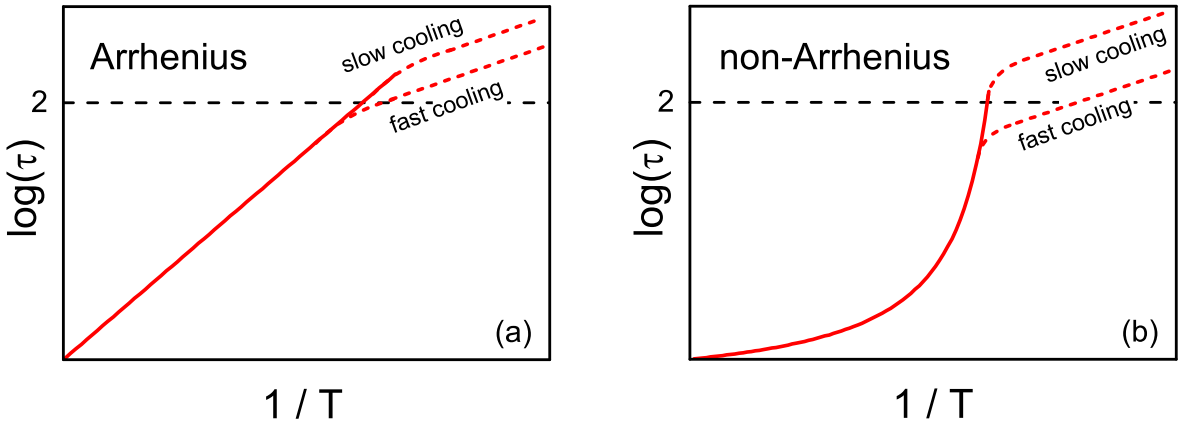

Figure 3.2: (a) Simulation of the Arrhenius equation for the structural relaxation time. At the glass transition, E changes resulting in a weaker temperature dependence below the transition (dashed lines). Indicated is the cooling rate dependence of the glass transition with the upper and lower dashed line. $\log(\tau) = 2$ marks the typical relaxation time at T_g with conventional cooling rates (chosen definition here $10\,\mathrm{K\,min^{-1}}$). (b) Simulation of the VFT equation. Notations are the same as for (a).

Originally a purely phenomenological parameter, the physical meaning of T_{VF} is debatable. For example, theories like the Adam–Gibbs entropy model [96] predict a phase transition at $T = T_{VF}$, however, some experiments do not hint at a divergence of the relaxation time at $T = T_{VF}$ [97]. Furthermore, frequently deviations from the VFT equation are found [98–101]. So there were many alternative equations proposed (see ref. [102] and references therein), some without a divergence of τ (e.g., [103]), but so far none has achieved widespread acceptance.

Besides the criticism, an important feature of the VFT equation is that it enables a quantitative measure of the deviation from Arrhenius behavior, known as the strong-fragile classification of liquids [104, 105]. Liquids more or less obeying the Arrhenius law are called strong, while liquids clearly diverging from the law are called fragile. For this purpose the VFT equation was rewritten including the so-called strenght parameter D with $B = DT_{VF}$ [104]:

$$\tau = \tau_0 \, \mathrm{e}^{\frac{DT_{VF}}{T - T_{VF}}} \tag{3.3}$$

In this form, the strength parameter D is indirectly proportional to the deviation from Arrhenius behavior. Visually the strong-fragile classification can be presented in the Angell plot [105]. Here, scaling the inverse temperature with the individual T_g of each system enables a comparison of different systems in one plot; the more a system deviates from the straight line, the more fragile it is.

Another way to quantify the deviation from Arrhenius behavior is the so called steepness index [106] or simply called the "fragility" [107]. It refers to the actual steepness of the temperature dependent relaxation time at T_g:

$$m = \left. \frac{d \log\langle\tau\rangle}{d\,(T_g/T)} \right|_{T=T_g} . \tag{3.4}$$

This quantity is directly proportional to the deviation from Arrhenius behavior. Assuming that universally for all different liquids, there is a minimum relaxation time of 10^{-14} s and maximum relaxation time of 100 s, one obtains a simple relation between m and D [108]:

$$m = 16 + 590/D. \tag{3.5}$$

In summary, the molecular dynamics and the viscosity of a liquid typically reveal a non-Arrhenius temperature dependence, thus, the energy barrier for structural relaxation and viscous flow can be assumed to increase with decreasing temperature. The VFT equation represents a phenomenological fit to the experimental data and offers a quantitative measure for the deviation from Arrhenius behavior, the so-called fragility of a liquid. Approaching the glass-transition temperature, the liquid falls out of thermodynamic equilibrium as soon as the structural relaxation time exceeds the experimental timescale set by the applied cooling rate. At the glass transition the molecules get trapped in fixed positions and the temperature dependence of its physical properties changes. The liquid and the glass state are inherently connected as a glass can be regarded as a frozen liquid on the timescale of an human observer.

3.2 Dielectric Response of Matter

Dielectric spectroscopy is one of the most commonly applied measurement techniques for the investigation of glass-forming materials. By applying an alternating electric field to a sample and measuring its response in form of a complex dielectric quantity like, e.g., the permittivity, this technique is able to detected, besides other effects, the rotational dynamics of dipolar molecules in a liquid. Given the broad frequency range from about 10^{-6} to 10^{9} Hz, rotational molecular dynamics can be studied over many decades, from the glass transition deep into the liquid state. Since the technique is only sensitive to rotational motions of dipolar molecules, hence giving a rotational relaxation time, it only measures some aspect of the overall structural relaxation introduced in chapter 3.1. In a ideal system and found for many real liquids, rotational and structural relaxation time are coupled [91]. Besides that, dielectric spectroscopy is sensible to ionic translational motions inside the sample and, thus, perfectly suitable to study ionic conductors. In the following, the theoretical basics of the dielectric response of matter will be introduced.

3.2.1 Basic Definitions

The interaction of matter with an external electric field is a wide and complex field of physics. For the sake of simplicity, the following introduction will be reduced to the case of an isotropic dielectric medium, i.e., an external electric field induces a polarization of the medium pointing in the opposite direction, and the linear regime, where the proportionality of external field and induced polarization is constant. All studied materials in the present work are isotropic and all measurements were done in the linear regime. Comparable introductions can be found in many textbooks (e.g., [109–111]).

In general, the polarization P of a medium is a function of the external field E and its electric susceptibility χ:

$$P = \varepsilon_0 \chi E, \tag{3.6}$$

where $\varepsilon_0 = 8.854 \times 10^{-12} \frac{\mathrm{As}}{\mathrm{Vm}}$ is the permittivity of free space. Hence, χ is a measure for the ability of an external field to polarize a medium. Closely related is the relative permittivity ε_r:

$$\chi = \varepsilon_\mathrm{r} - 1. \tag{3.7}$$

The displacement field D is the sum of the external field and the opposing field resulting from the polarization P of the medium:

$$D = \varepsilon_0 E + P = \varepsilon_0(1-\chi)E = \varepsilon_0\varepsilon_r E. \tag{3.8}$$

Hence, the charge displacement in a medium can be described by the relative dielectric permittivity ε_r. In the case of a static field and isotropic materials ε_r is a skalar and is often called dielectric constant.

To study dynamic processes in a medium, however, the application of an harmonic time-varying external field in the form of:

$$E(t) = E_0 e^{i\omega t} \tag{3.9}$$

is helpful, where E_0 is the amplitude of the field and $\omega = 2\pi\nu$ is the angular frequency. Due to the non-instantaneous nature of the dynamic processes in a medium, a shift between the time dependence of the dielectric displacement $D(t)$ and the applied field $E(t)$ emerges. The quasi-static relation introduced in equation 3.8 is no longer viable and the permittivity can be described as a complex quantity usually given in dependence of the applied frequency ν with $\omega = 2\pi\nu$:

$$\varepsilon^*(\omega) = \varepsilon'(\omega) - i\varepsilon''(\omega). \tag{3.10}$$

At a given frequency, $\varepsilon'(\omega)$ and $\varepsilon''(\omega)$ are proportional to the energy stored and energy dissipated in a medium, respectively. They are commonly called dielectric constant (ε') and dielectric loss (ε''). Over the whole frequency range of dielectric spectroscopy, the dielectric response of a system is typically a composition of the different contributions from various macro- and microscopic processes (see chapter 3.2.2). Together $\varepsilon'(\omega)$ and $\varepsilon''(\omega)$ contain the full information of the dielectric response of a system.

Besides the complex permittivity, there are three other commonly used dielectric quantities: the complex conductivity $\sigma^*(\omega)$, the complex resistivity $\rho^*(\omega)$ and the complex dielectric modulus $M^*(\omega)$. Notably, each of those quantities contains the full information of the dielectric response of a medium and, starting from any of them, all the others can be calculated (see figure 3.3). Nonetheless, in literature all four forms of representation can be found, because they highlight different contributions to the dielectric response. Historically, different dielectric 'schools' have developed, each typcially favoring one of the possible representations (see ref. [112] for an historical overview).

All together, the dielectric response of a dynamic system is measured with an alternating external electric field. The output of the measurement is a complex quantity and its representation is chosen in a way to highlight the individual contributions.

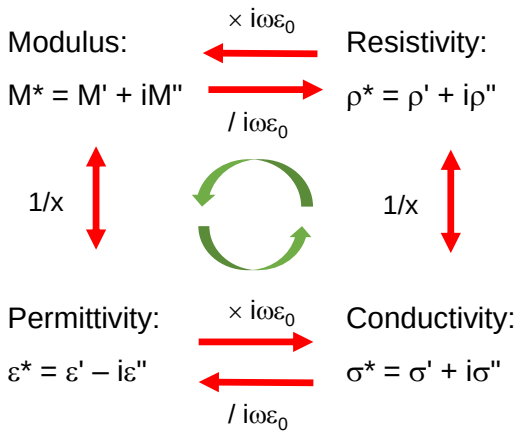

Figure 3.3: Correlation of the different dielectric quantities [113]. The relations between the different quantities are noted, e.g., $M^* = 1/\varepsilon^*$ and $\varepsilon^* \times i\omega\varepsilon_0 = \sigma^*$.

3.2.2 Polarization Mechanisms

The dielectric response of a medium is a combination of different macro- and microscopic processes. Typically each of these processes emerges on a different timescale and, hence, can be separately identified in the dielectric spectrum. In time dependence, each polarization mechanism adds a charaterisic polarization P_0 to the overall polarization as long as a static electric field is applied. After the removal of the external field, each polarization decays with its characteristic relaxation time τ. In frequency dependence, these processes arise as either relaxation or resonance features. In this chapter the main polarization mechanisms are introduced (comparable to [110]).

Much like the investigated materials in this work, the following will focus on polarization mechanism occurring in materials with dipolar molecules and mobile ions set up in a parallel plate capacitor for dielectric measurements.

Interfacial polarization, which leads to a so-called Maxwell-Wagner relaxation, is an induced polarization of the sample due to spatial heterogeneities of the sample's conductivity. It serves as collective name for a wide range of different mechanisms. In particular, the Maxwell-Wagner(-Sillars) [114–116] model was originally derived for dielectric particles in an ionic solution. The ionic motion, induced by an external field, is interrupted by the presence of these particles and accumulations of ions at the interfaces of the particles and the solution arise. The resulting spatial separation of charges leads to a macroscopic polarization. More often encountered in experiments are electrode polarization (EP) effects. Here, the high ionic conductivity of a sample leads to accumulation of ions at the capacitor plates (figure 3.4 'interfacial') at long timescales or low frequencies, effectively building insulating layers at the capacitor-sample interface [117]. In the frequency domain, interfacial polarizations show up as sigmoidally decreasing contribution to ε' (see figure 3.5). While there are many types of interfacial polarizations, only the electrode polarization plays a significant role in the present work. Such polarization is of extrinsic nature and is defined by the capacitor set up, thus providing only limited information on the microscopic processes of a system. The modeling of such contributions will be introduced in chapter 3.2.6.

Orientational polarization emerges in any medium with mobile permanent dipoles, e.g., dipolar molecules in a liquid. The application of an external field results in a partial alignment of the dipolar

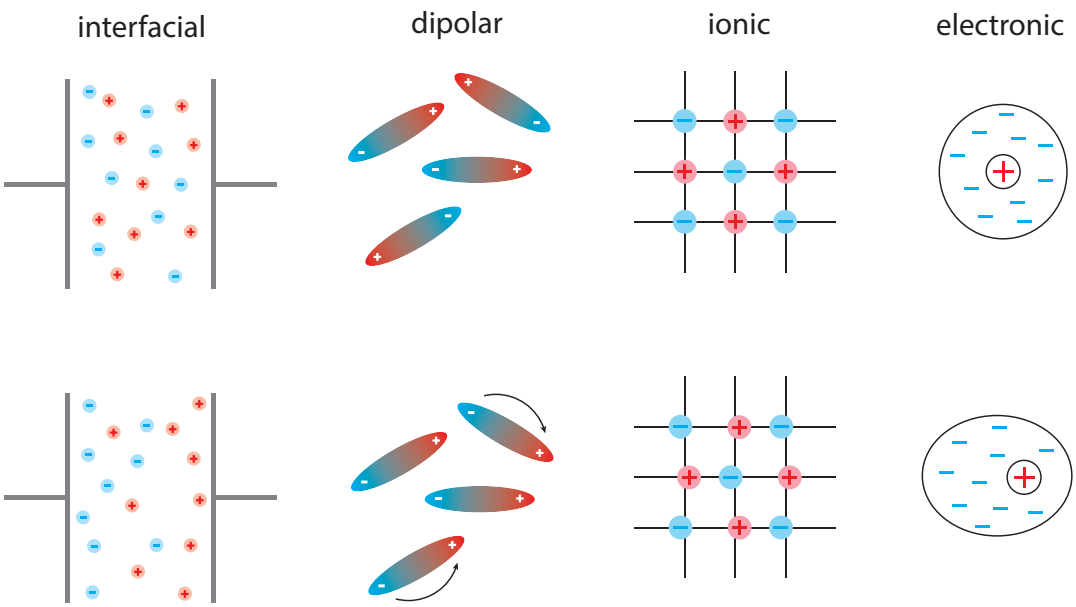

Figure 3.4: Visualization of the different polarization mechanisms in matter without external (upper row) and with external field (lower row). They are ordered from left to right by the typical timescale (long to short) of the polarization decay after the removal of the external field. On basis of [110].

moments with the field direction (figure 3.4 'dipolar'). In reality, the dipoles do not get aligned but rather their thermal fluctuation obtains a preferred direction. This mechanism is often referred to as dielectric relaxation and exhibits an sigmoidal decrease in ε' and a peak in ε'' in the dielectric spectrum. Here, the low frequency value of maximum induced polarization is called static permittivity ε_s and the high frequency limiting value, containing all faster polarization processes, is called ε_∞ (see figure 3.5). The orientational polarization is key to analyze and quantify the dipolar dynamics in a system, a major focus of the present work (see chapter 3.2.3).

Ionic and **electronic polarization** make up for the polarization at frequencies well above the typical timescale of orientational polarization and are often summarized in the value of ε_∞. The ionic polarization, not to be confused with the ionic conductivity, results from ions sitting on a crystalline lattice. Under the influence of an external field, the ions are displaced in direction of the field. The electronic polarization is due to deformation of the electronic shells of the atoms. Both are visualized in figure 3.4 under 'ionic' and 'electronic' caption. These effects are collectively named displacement polarizations and exhibit resonance features in ε' (see figure 3.5). Since they only contribute well above 10^9 Hz and, thus, are not part of the classical dielectric range but rather the THz, the infrared and the optical range, they are out of scope of the present work.

Another important contribution to the dielectric spectrum arises from dc and ac conductivity. Dc conductivity in ionically conducting systems is caused by long-ranged translationally diffusion of ions. It does not directly add to the sample's polarization but only indirectly through interfacial polarization effects. Nonetheless, it emerges prominently in the dielectric loss. The ac conductivity, however, is of more complex nature and typically applied models include a polarization effect in ε' (see chapter 3.2.4 'ac conductivity'). In ionically conducting systems, as investigated in the present work, high dc conductivity is a hallmark for potential commercial application and the ac conductivity provides important information on the physical nature of ionic translational motion [112]. A profound introduction will be

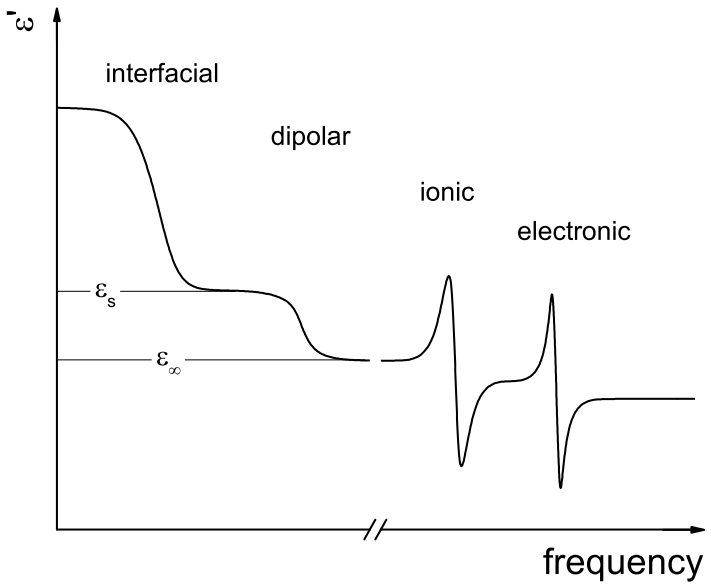

Figure 3.5: Idealized frequency dependence of ε' due to different polarization mechanisms [118]. The interfacial and dipolar relaxation processes reveal sigmoidal decrease. The ionic and electronic polarization are resonances and show derivated lorentzian shape. Included are notations of the upper ε_s and lower ε_∞ plateau of the dipolar relaxation (details in chapter 3.2.3).

given in chapter 3.2.4.

To summarize, the dielectric response of a medium, as measured by dielectric spectroscopy, is a composition of different microscopic processes. Each of them emerging on a different timescale, their contributions typically overlap and/or directly influence each other in the dielectric spectrum. Only with a thorough analysis of the spectrum utilizing the mathematical framework, the relevant information can be extracted (see chapter 3.2.6).

3.2.3 Dipolar Relaxation

A major field for application of dielectric spectroscopy is the detection of the orientational polarization, which shows up as a relaxation in the frequency dependence. The typical dipolar (often simply called dielectric) relaxation arises from full-angle reorientational dynamics of dipolar molecules. In glass-forming liquids, it is usually named the α-relaxation due to its presumable equivalence with the structural α-relaxation. Most intuitively introduced in the time domain, dielectric spectroscopy utilizes frequency dependent measurements to observe the relaxation. The following chapter will introduce the transition from time to frequency domain, the typical signature of a dielectric relaxation in the dielectric spectrum and its most common modeling functions. Similar summaries can be found in [109–111].

The transition from time to frequency domain for the dielectric relaxation function is done via a one-sided Laplace transformation [119]. Starting in the time domain, an external electric field induces a polarization $P_{\mathrm{or}}(0)$ due to orientational polarization in the sample. After switching off the field at $t = 0$, the polarization $P_{\mathrm{or}}(t)$ does not vanish instantaneously but decays with a characteristic relaxation time τ:

$$P_{\mathrm{or}}(t) = P_{\mathrm{or}}(0)\mathrm{e}^{-\frac{t}{\tau}} \tag{3.11}$$

The exponential decay is called the step-response function of the orientational polarization. For the

pulse-response function $f_{\mathrm{P}}^{\mathrm{or}}$, which accounts for any arbitrary input signal, one obtains:

$$f_{\mathrm{P}}^{\mathrm{or}} = \frac{1}{\tau} \mathrm{e}^{-\frac{t}{\tau}} \tag{3.12}$$

The classical Debye relaxation function [120] for the complex permittivity $\varepsilon^*(\omega)$ can now be derived via

$$\varepsilon^*(\omega) = \varepsilon_\infty + (\varepsilon_\mathrm{s} - \varepsilon_\infty)\mathscr{L}_{i\omega}(f_{\mathrm{P}}^{\mathrm{or}}) = \varepsilon_\infty + \frac{\Delta\varepsilon}{1 + i\omega\tau}, \tag{3.13}$$

where ε_s symbolizes the maximum induced orientational polarization at low frequencies, ε_∞ summarizes the contributions from displacement polarizations and $\Delta\varepsilon = \varepsilon_\mathrm{s} - \varepsilon_\infty$ is called the relaxation strength. $\omega = 2\pi\nu$ is the angular frequency of the external electric field. For the real $\varepsilon'(\omega)$ and the imaginary $\varepsilon''(\omega)$ part follows:

$$\varepsilon'(\omega) = \varepsilon_\infty + \frac{\Delta\varepsilon}{1 + \omega^2\tau^2} \tag{3.14}$$

and

$$\varepsilon''(\omega) = \frac{\Delta\varepsilon\omega\tau}{1 + \omega^2\tau^2}. \tag{3.15}$$

With $\varepsilon'(\omega)$ being a sigmoidally decreasing function of the frequency and $\varepsilon''(\omega)$ a peak function, together they define the typical signature of a dielectric relaxation process. Since the relaxation time τ is temperature dependent, especially in the case of dipolar liquids, in the dielectric spectrum the step-like decrease in $\varepsilon'(\omega)$ and the peak in $\varepsilon''(\omega)$ shift continuously from lower to higher frequencies with increasing temperature (see figure 3.6).

The Debye relaxation relaxation function makes the assumption that all dipoles in the system relax with the same relaxation time. In reality, however, very often the measured loss peaks are symmetrically or asymmetrically broadened and the relaxation step is smeared out. This phenomena can be ascribed to a non-exponential decrease of the polarization in time domain. Two microscopic models were purposed to describe the physical reason for the non-exponential decay: The homogeneous scenario assumes that the relaxation process of all dipoles is of non-exponential nature; and the heterogeneous scenario considers a distribution of relaxation times, which results in an overall non-exponential decay (visualization in [121]). The heterogeneous scenario explains the distribution of relaxation times in disordered systems with the varying local environment of each relaxing dipole. Nowadays, the heterogeneous scenario seems to be widely accepted, with many experimental results such as from dielectric hole-burning [122], non-linear dielectric spectroscopy [123] and nuclear magnetic resonance [124] supporting the idea.

Mathematically the non-exponetial decay can be accounted for by the Kohlrausch-Williams-Watts (KWW) formula [125], which introduces a stretched-exponential behavior in the time domain:

$$P_{\mathrm{or}}(t) = P_{\mathrm{or}}(0)\exp\left[-(t/\tau)^{\beta_{\mathrm{KWW}}}\right], \tag{3.16}$$

where $0 < \beta_{\mathrm{KWW}} \leq 1$ is called the stretching exponent. Alternatively in the frequency domain, the Havrilia-Negami (HN) function [126] is an empirical extension of the Debye formula to produce the broadened step and peak in the permittivity:

$$\varepsilon^*(\omega) = \varepsilon_\infty + \frac{\Delta\varepsilon}{\left[1 + (i\omega\tau_{\mathrm{HN}})^{1-\alpha}\right]^\beta}, \tag{3.17}$$

with $0 \leq \alpha < 1$ and $0 < \beta \leq 1$ called the width parameters.

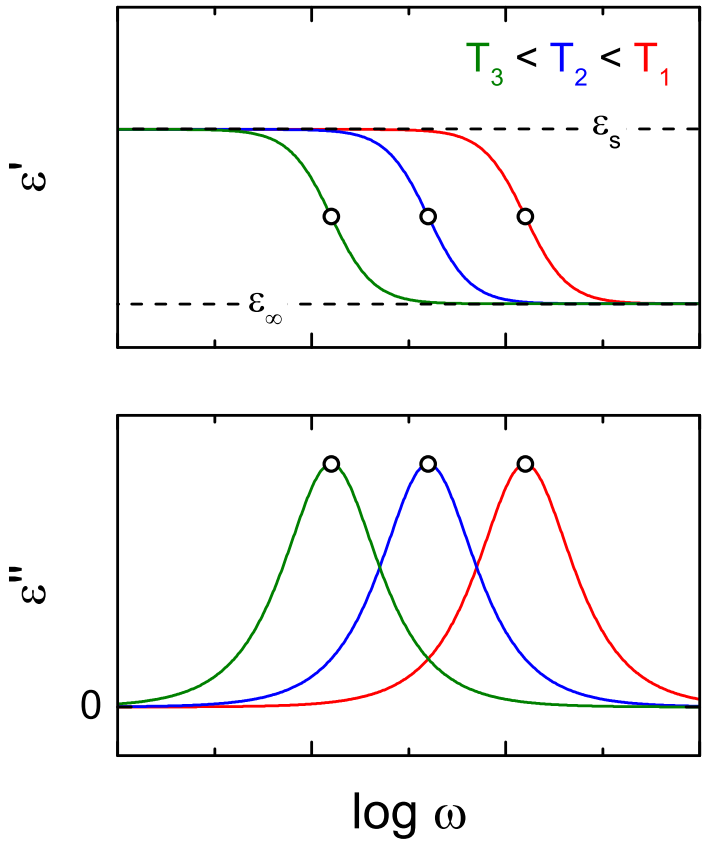

Figure 3.6: Simulated real and imaginary part of the Debye relaxation function for three different temperatures. The lowest temperature reveals the highest relaxation time and shows up at the lowest frequencies. Black circles mark $\nu_{\text{relax}} = 1/(2\pi\tau)$.

There are two special cases of the HN function, the Cole-Cole (CC) ($\beta = 1$) [127]

$$\varepsilon^*(\omega) = \varepsilon_\infty + \frac{\Delta\varepsilon}{[1+(i\omega\tau_{\text{CC}})^{1-\alpha}]}, \tag{3.18}$$

and the Cole-Davidson (CD) function ($\alpha = 0$) [128]

$$\varepsilon^*(\omega) = \varepsilon_\infty + \frac{\Delta\varepsilon}{[1+(i\omega\tau_{\text{CD}})]^{\beta}}. \tag{3.19}$$

The CC function yields a symmetrically broadened peak in ε'' and the CD function an asymmetrically broadened peak (see figure 3.7).

In a system with distributed relaxation times, the definition of an average relaxation time $\langle\tau\rangle = 1/(2\pi\nu_{\text{peak}})$ via the frequency position of the peak maximum ν_{peak} makes sense. In the symmetrical cases of the Deybe and the CC function, $\langle\tau\rangle$ is equal to the relaxation time τ and τ_{CC}, respectively. For the CD function, $\langle\tau\rangle$ can be estimated by $\beta\tau_{\text{CD}}$ [129, 130]. The asymmetrical case of the HN function reveals a more complex relation [131, 132]:

$$\frac{1}{2\pi\nu_{\text{peak}}} = \tau_{\text{HN}}\left[\frac{\sin\left(\frac{\pi(1-\alpha)\beta}{2(1+\beta)}\right)}{\sin\left(\frac{\pi(1-\alpha)}{2(1+\beta)}\right)}\right]^{1/(1-\alpha)}. \tag{3.20}$$

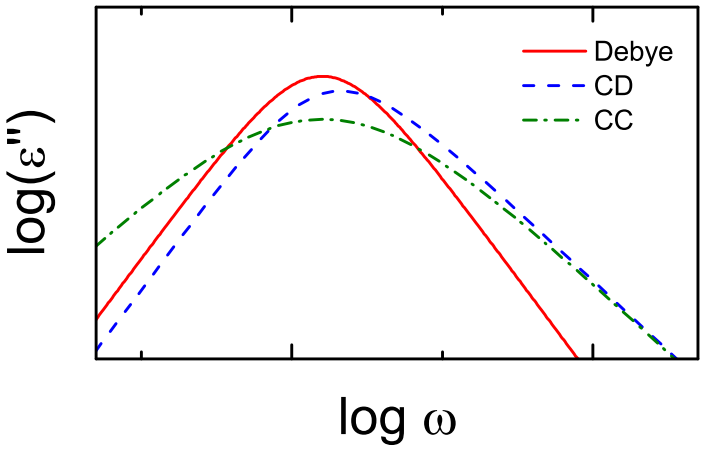

Figure 3.7: Dielectric loss simulated for the Debye, the CC ($\alpha = 0.3$) and the CD ($\beta = 0.7$) case. Parameters $\Delta\varepsilon$ and τ were held constant.

As already mentioned, the orientational polarization arises from reorientational molecular dynamics, which are one aspect of the overall structural dynamics of a viscous liquid. Like the structural relaxation time, the reorientational relaxation time is called the α-relaxation, since it is the primary relaxation feature emerging in the dielectric spectrum of dipolar liquids [85, 91].

Almost any glass-forming liquid, however, reveals the appearance of secondary, faster relaxation processes, typically named in the order of their appearance β, γ, etc., or of an excess contribution on the high-frequency flank of the alpha relaxation, named excess wing. Such contributions eventually dominate the dielectric spectrum below T_g, when the α-relaxation has shifted to frequencies well below the lower frequency limit of the measurement devices.

In literature, nomenclature and interpretation of such secondary processes, however, is rather inconsistent and under ongoing debate. Generally, faster relaxation processes due to intramolecular dynamics are expected for polymers and complexly structured molecules. However, in their pioneering work Johari and Goldstein [133] demonstrated the emergence of a β-relaxation in glass-forming liquids consisting of rigid molecules. Thus, the so-called Johari-Goldstein β_{JG}-relaxation is widely believed to be an inherent feature of glass-forming liquids [134]. Discussed physical explanations of the β_{JG}-relaxation are "islands of mobility" [133, 134] or "local small-angle reorientation of all molecules" [135, 136]. Nonetheless, distinguishing a genuine β_{JG} from other β-relaxations requires significant experimental effort [137]. Additionally, it was shown that the excess wing can be attributed to a broadened β-relaxation superimposed by the α-relaxation [138–140], though other interpretations exist as well [141, 142]. For the interpretation of the experimental results of the present work, secondary relaxations only play a minor role but are included in the modeling of the dielectric data to obtain comprehensive and reliable fit results.

Notably, often one of the special cases of the HN function is enough to describe the experimentally measured relaxation features sufficiently and it was found, that in many cases the α-relaxation can be described with a CD function [91] and secondary β-relaxations reveal symmetric broadening according to the CC function [138–140].

Altogether, reorientational dynamics of dipolar molecules in disordered systems lead to the so-called α-relaxation in the dielectric spectrum, in particular, emerging as a sigmoidal decrease in ε' and a peak in ε''. Typically, experimental data are models with empirical modifications of the Debye-relaxation

function, from which the average relaxation time $\langle\tau\rangle$ is obtained. Most commonly, the α-relaxation in dipolar liquids is described with a CD function and β-relaxations with a CC function.

3.2.4 Ionic Conductivity

Unlike electrical conduction in metals, semiconductors or superconductors, ion transfer in liquids and disordered solids is so far poorly understood and no broadly accepted model is available [143]. The fundamental difference between the two is that ions are much heavier than electrons and, therefore, quantum mechanics usually play a negligible role, especially at ambient temperatures. Ion motion in liquids or disordered solids is essentially mass transport of particles through the bulk of the phase. During this motion, work is done against the frictional forces of the medium and as ions carry charge, dissipation is detected in the dielectric response. Although being random in its nature, the ion diffusion process obtains a directional component when an external electric field E is applied to the medium.

Following standard theoretical basics [109, 143–145], the driving force F acting on a charge carrier with charge q is $F = qE$. Such force results in an average drift velocity v_d and the mobility μ_q of the charge carrier is defined as $\mu_\mathrm{q} = v_\mathrm{d}/E$. As the general current density is $j = qnv_\mathrm{d}$ with n being the charge-carrier number density and the conductivity $\sigma = j/E$, one obtains:

$$\sigma = qn\mu_\mathrm{q}. \tag{3.21}$$

This definition applies to long-ranged translational motion of ions in a medium and this conductivity is called dc conductivity σ_dc in the following. The macroscopic σ_dc of a medium is consequently a function of unit charges per ion, the ion density (number of ions per unit volume) and the complexly composed ion mobility, which depends on many different parameters such as matrix material, ion species and temperature. However, when investigating the physical nature of the ion motion, valuable insights can be found when studying the conductivity as a function of frequency of an external electric field. Most ionic conductors display a frequency independent σ_dc-plateau at low frequencies and a marked increase of the conductivity at higher frequencies, called the ac conductivity.

DC Conductivity Long-ranged translational motion of ions is usually regarded as a diffusion process. In liquids, the diffusion of all constituent ions and molecules causes the viscous flow of the medium and usually rotational and translational diffusion of all constituents is coupled. In solids materials, however, the ion diffusion arises in a rigid matrix. Still, their signature in the dielectric spectrum and their general temperature dependence is similar.

In **liquids**, diffusion can be described by the frictional forces acting on a particle moving through a viscous fluid. For non-charged particles, the mobility μ is given by Stokes' law [146] in relation to the viscosity η:

$$\mu = \frac{1}{6\pi\eta r}, \tag{3.22}$$

including the particles radius r. μ of non-charged particles is in units of $\frac{\mathrm{m}}{\mathrm{Ns}}$. On this basis, Einstein [147] and Sutherland [148] independently derived the so called Stokes-Einstein equation

$$D_\mathrm{trans} = \frac{k_\mathrm{B}T}{6\pi\eta r}, \tag{3.23}$$

which introduces the diffusion coefficient for translational motion D_trans in dependence of the thermal energy $k_\mathrm{B}T$ and the viscosity. Since rotational and translational motion in a liquid are usually coupled,

the Debye-Stokes-Einstein equation [149–151] takes the volume of the particle into account and gives the diffusion coefficient for rotational motion

$$D_{\mathrm{rot}} = \frac{k_{\mathrm{B}}T}{8\pi\eta r^3}. \tag{3.24}$$

The so called Nernst-Einstein equation describes in a similar manner the ion diffusion coefficient D_{ion}. A common form of the equation [152]

$$\Lambda_{\mathrm{m}} = D_{\mathrm{ion}}\frac{z_{\mathrm{i}}F^2}{RT} \tag{3.25}$$

uses the equivalent conductivity $\Lambda_{\mathrm{m}} = \sigma_{\mathrm{dc}}/c$, with c being the molar ion concentration, z_{i} being the valency of the ion and F being the Faraday constant. The relations [145, 153] to σ_{dc}

$$D_{\mathrm{ion}} = \frac{\sigma_{\mathrm{dc}}k_{\mathrm{B}}T}{q^2 n} \tag{3.26}$$

and the ion mobility μ_{ion} in units $\frac{\mathrm{m}^2}{\mathrm{Vs}}$ follow

$$D_{\mathrm{ion}} = \frac{\mu_{\mathrm{ion}}k_{\mathrm{B}}T}{q} = \frac{k_{\mathrm{B}}T}{6\pi\eta r}. \tag{3.27}$$

Effectively, all diffusion coefficients are indirect proportional to the viscosity. In literature, however, also exceptions from the presented laws can be found, e.g., the breakdown of the direct proportionality of D_{trans} and D_{rot} in fragile glass-forming liquids when approaching T_{g} [154–157].

From equations 3.26 and 3.27, it follows that σ_{dc} is, ideally, also indirectly proportional to η. In fact, this relation is also known as Walden rule [158]. More precisely the Walden rule applies to highly diluted electrolyte solutions and states that the product of limiting molar conductivity $\Lambda^0_{\mathrm{m}} = \sigma_{\mathrm{dc}}/n$ and the pure solvents viscosity is constant [152, 159, 160]:

$$\Lambda^0_m\eta = \text{constant}. \tag{3.28}$$

Still, empirically it was found that many different systems obey the Walden rule. This is usually done by checking for the conductivity-viscosity relationship with the help of the Walden plot, $\log(\Lambda_{\mathrm{m}})$ vs $\log(\eta^{-1})$, where systems obeying the Walden rule fall on a straight line with steepness 1.

On this basis, Angell and coworkers [152, 159, 162] developed a scheme to classify different ionically conducting liquids and polymers. At first the "ideal Walden line" is constructed by choosing 1 molar aqueous KCl solution at room temperature as reference, because this system is assumed to be fully dissociated and to have ions of equal mobility [152]. The "ideal Walden line" with steepness 1 runs through the reference point and origin of the Walden plot, when viscosity is presented in units Poise P ($= 0.1\mathrm{Pa\,s}$). The classification into the three categories follows the position of a system in the Walden plot with respect to the "ideal" Walden line [161–163] (see figure 3.8): ideal (ion-interaction free) close to the line; subionic (associated or ion-pair building) below the line; superionic (decoupled ion mobility) above the line. Thus, for an ideal liquid system, ion mobility is controlled purely by the viscosity and the system falls on the ideal Walden line. However, effects like solvation and ion-pair building [159] drag a system below the ideal line and mechanisms like the polymer effect [159] or Grotthuss conduction [161] may push a system above the ideal line.

Excluding interfacial polarizations, long-ranged translational diffusion of ions does not induce a polarization in the sample and acts like a simple ohmic resistor in dielectric measurements. Hence, the

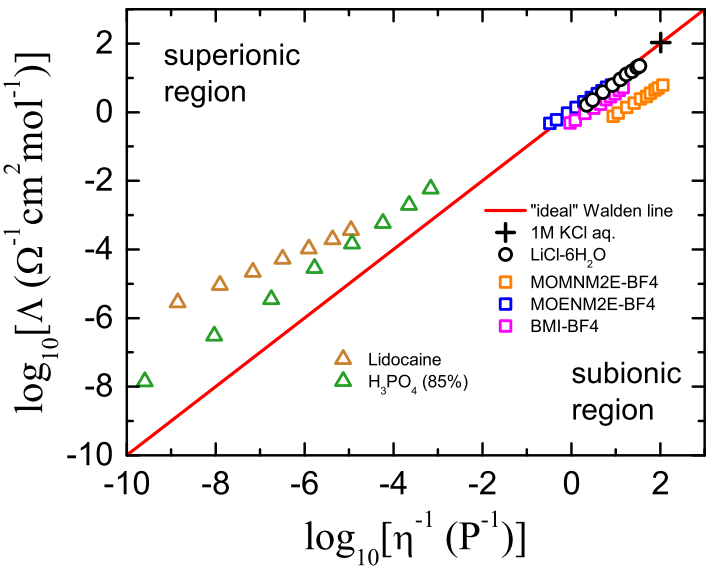

Figure 3.8: Walden plot for selected systems from literature. Straight solid line represents the "ideal" Walden line, well above and well below the line the superionic region and the subionic region are located, respectively. RT 1 molar KCl solution serves as reference point (black cross) [152]. Data from literature were selected from a variety of different systems: protic ionic conductors in the superionic region [161] (triangles), ionic liquids near the ideal line and below [152] (squares), aqueous LiCl solution very close to the ideal line [162] (circles). Abbreviations in the legend are explained in the references.

dc conductivity produces a frequency independent conductivity value in σ', a $1/\nu$ behavior in ε'' due to $\sigma'(\nu) = 2\pi\nu\varepsilon_0\varepsilon''(\nu)$ and no direct contributions in ε'.

As motivated above, the ionic conductivity in liquids is generally controlled by the viscosity and, accordingly, for its temperature dependence equations 3.1 and 3.3 found for the structural relaxation and the viscosity of liquids can be rewritten for the dc conductivity:

$$\sigma_{\mathrm{dc}} = \sigma_0 \, \mathrm{e}^{\frac{-E}{k_\mathrm{B}T}}. \tag{3.29}$$

and

$$\sigma_{\mathrm{dc}} = \sigma_0 \, \mathrm{e}^{\frac{-DT_{\mathrm{VF}}}{T-T_{\mathrm{VF}}}}. \tag{3.30}$$

Much like for the viscosity, the dc conductivity of many real liquids does not follow a simple Arrhenius law but reveals a VFT behavior in a broad temperature range (e.g., [52, 162]).

In **solid** ionic conductors, ionic translational motion is also a diffusion process, however, not controlled by the viscosity, which is absent in solids, but here the ion mobility μ_{ion} is a material specific parameter strongly depending on the composition of the solid. For disordered solids (the focus of the present work), generally a hopping mechanism is assumed where mobile ions perform jumps between energetic minima in the disordered energy landscape [143]. The presence of very high energy barriers serves as "bottleneck" for the ion motion and defines the dc conductivity of the material [164]. Hence, the σ_{dc} of disordered solid ionic conductors, similarly to ionically conducting liquids, produces a frequency independent conductivity values in σ'.

Further, the "bottleneck" energy barrier can be transferred to the Arrhenius equation to describe the temperature dependence of σ_{dc} (see equation 3.29). Still many disordered solid ionic conductors reveal

non-Arrhenius behavior in a broad temperature range [165]. Thus, the temperature dependence and the spectral shape of σ_{dc} are very similar to liquid ionic conductors.

AC Conductivity Characteristic for disordered solids and liquids is a frequency dependence of the conductivity. Usually the non-dispersive dc conductivity dominates the low-frequency side of the spectrum (excluding extrinsic effects) and after a characteristic frequency ν_p a distinct conductivity increase sets in, named ac conductivity. This pattern found particular research interest in disordered solid ionic conductors, where it is believed to reflect an inherent property of the translational motion of the ions [112, 143, 166, 167]. For liquid ionic conductors, the situation is rather complex as most of them contain dipolar molecules, which may cause an ac conductivity due to relaxation processes. However, the prominent example of ILs, liquids containing only ionic constituents, demonstrates the ongoing discussion on the correct interpretation of ac conductivity in liquid electrolytes [23].

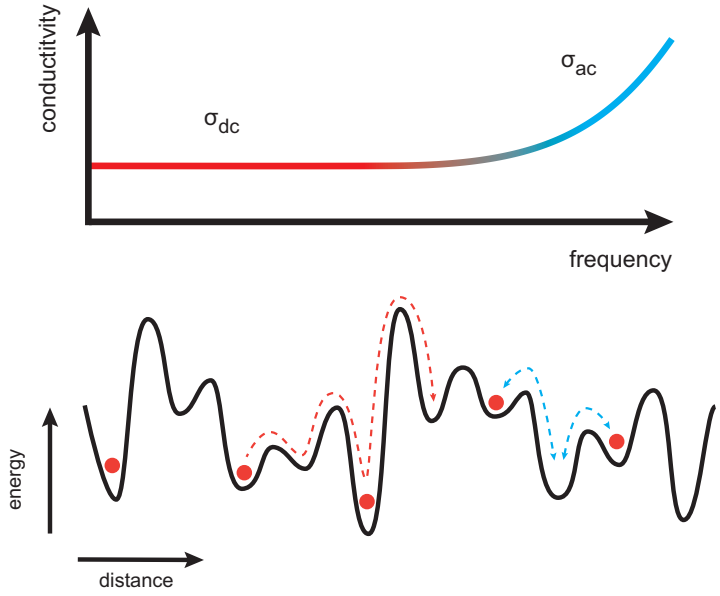

Figure 3.9: Commonly observed frequency dependence of the conductivity (log-log representation) in disorderd solids and liquids (upper picture) and corresponding illustration of the simplified picture of ion jumps in a complex energy landscape [143] (lower picture). Upper picture: Color gradient of the conductivity is adjusted to highlight the onset of ac-conductivity contribution. Lower picture: Red cicles represent ions sitting in potential wells. Red dashed line shows long-ranged translational motion over a multitude of energy barriers including very high, "bottleneck" barriers, as detected by low frequencies. Blue dashed lines represent short-ranged jumps over small barriers, as detected by high frequencies.

The commonly applied models for ionic conductivity in disordered solids rely on ion hopping mechanisms (e.g., [112, 166, 168, 169]). Here, the ion transport mechanism is described as a thermally activated hopping of the localized ion across energy barriers in a potential landscape. In disordered solids the ions move through a complex, irregular energy landscape with a distribution of well depths and barrier heights (see Figure 3.9) [143].

In a simplified picture [112, 143, 164]: The application of a low frequency alternating external field probes ion motion on long timescales, i.e., long travel distances. Here, high energy barriers become unavoidable and serve as bottlenecks for the ion motion. The result is the frequency independent σ_{dc}.

Applying high frequencies, however, detects ion motions on short timescales and short travel distances. Here, the ions preferably jump over small energy barriers with increased jumping probability and, thus, an increased conductivity is measured. Hence, in ionically conducting disordered solids a dispersion of σ' can be explained solely by the irregularity of the energy landscape the ions are traveling through.

Although, hopping models were originally derived for disordered solids, already Dyre in 1988 [112] acknowledged that highly viscous liquids display a similar frequency dependence of the conductivity and hopping models found application especially in ILs [51, 170] but also in one case in DESs [16].

Altogether, so far no widely accepted model for the ionic conductivity exists. Due to findings of dispersive contributions in the dielectric spectrum of ionic conductors lacking any permanent dipoles (e.g., [171]), one cannot exclude a general ionic ac-conductivity contribution appearing in any ionically conducting system. The materials investigated in the present work represent the case of simultaneous presence of ionic and dipolar dynamics and, thus, ionic ac conductivity has to always be considered in the interpretation of the dielectric spectra. Hence, two models to describe the frequency dependence of ionic ac conductivity will be presented in the following.

Universal Dielectric Response Measured by the citation number, the "universal" dielectric response (UDR) by Jonscher [166] is probably the most frequently applied function to model ac conductivity in solid ionic conductors. Rather than a comprehensive theory, Jonscher in 1977 offered a phenomenological description of the universal pattern found for the dielectric response of many different ionic conductors and proposed justifications for his approach by considering many-body interactions. The UDR [166] essentially predicts $\sigma' \propto \omega^{\mathrm{s}}$ to be a universality and combined with σ_{dc} one obtains

$$\sigma'(\omega) = \sigma_{\mathrm{dc}} + \sigma_0 \omega^s \tag{3.31}$$

$$\sigma''(\omega) = \tan\left(\frac{\pi s}{2}\right) \sigma_0 \omega^s \tag{3.32}$$

where σ_0 is a temperature independent parameter and $0 < s < 1$.

Further, the characteristic crossover from frequency-independent dc conductivity to strongly increasing ac conductivity is often associated with the hopping rate of the ions [172, 173] and an alternative version [143, 172, 173] of equation 3.31 emphasizes the crossover frequency ω_{p} marking the onset of ac conductivity:

$$\sigma'(\omega) = \sigma_{\mathrm{dc}} \left[1 + \left(\frac{\omega}{\omega_{\mathrm{p}}}\right)^s\right] \tag{3.33}$$

where $\omega_{\mathrm{p}} = (\frac{\sigma_{\mathrm{dc}}}{\sigma_0})^{\frac{1}{s}}$ is often called the hopping rate of the ions.

Figure 3.10 presents a simulation of the UDR for three different temperatures. For each temperature step a shift of σ_{dc} and ω_{p} of one order of magnitude was assumed and ε_∞ was introduced into equation 3.32. The parameters s and σ_0 where held constant. ε' and σ' were chosen as representatives as they together combine the full information on the conductivity dispersion and the induced polarization caused by ionic translational motion.

In ε', a constant decrease $\propto \omega^{1-\mathrm{s}}$ is found, which eventually merges with the value of ε_∞ at high frequencies. For σ', the UDR produces the characteristic crossover from σ_{dc} at low frequencies to an increase $\propto \omega^s$ at high frequencies.

Although a power law behavior of the ac conductivity is indeed found in most systems, a closer look at the rarely presented ε' of purely ionically conducting systems reveals fundamental deviations from the UDR. For the molten salt $3KNO_3 - 2Ca(NO_3)_2$, both references [174] and [171] (inset figure

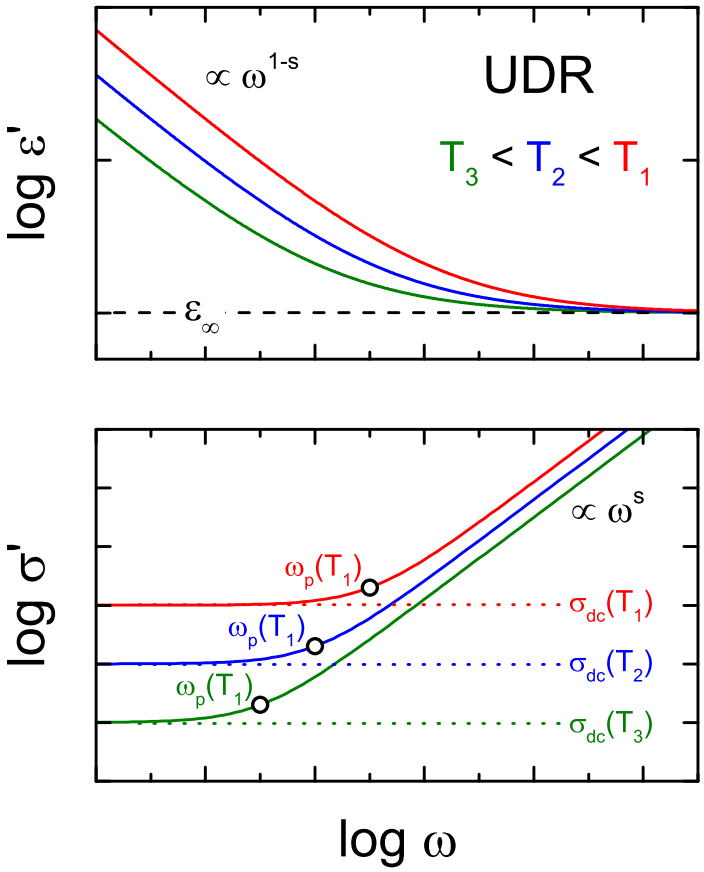

Figure 3.10: Schematic frequency dependence of ε' and σ' for three different temperatures following the UDR [143] (see text for details). Highlighted are σ_{dc} (dotted lines) and ω_p (circles) for each temperature. ε_∞ marks the contribution from displacement polarization for $\omega \to \infty$.

2, given in the temperature dependence) report a step wise decrease of ε' with increasing frequency, similar to a relaxation process. The qualitative prediction of such polarization effects emerging in ε' may be regarded as one advantage of the following model.

Random Barrier Model The Random Barrier Model (RBM) originally introduced by Dyre [112, 175] with solution

$$\sigma(\omega) = \sigma_{dc} \frac{i\omega\tau}{\ln(1+i\omega\tau)} \tag{3.34}$$

was derived for the frequency dependent conductivity of disordered solids and contains only two parameters σ_{dc} and the hopping rate τ. In the words of the author, it is the "simplest possible realistic model for ac conduction in disordered solids" [112].

Interestingly, the RBM also found considerable application to model the dielectric response of liquid ionic conductors [51, 170, 176, 177], hence, exceeding its original purpose. Those liquid ionic conductors, in most cases ILs, reveal the typical dc to ac pattern in σ' and a shallow relaxation-like step in ε'. Still, in many cases the RBM alone was not enough to describe the dielectric response sufficiently and the authors opted to introduce an additional relaxation term in their fitting routine [170, 177, 178].

In 2008 Schrøder and Dyre [164] derived a modified solution of the RBM

$$\ln\frac{\sigma(\omega)}{\sigma_{dc}} = \frac{i\omega\tau_{RBM}\sigma_{dc}}{\sigma(\omega)}\left[1+2.66\frac{i\omega\tau_{RBM}\sigma_{dc}}{\sigma(\omega)}\right]^{-1/3}, \tag{3.35}$$

which like the old solution only depends on two parameter, σ_{dc} and ion hopping rate τ_{RBM}. The authors considered equation 3.35 as the correct solution of the model and in the following the abbreviation RBM will be used for the modified solution from 2008.

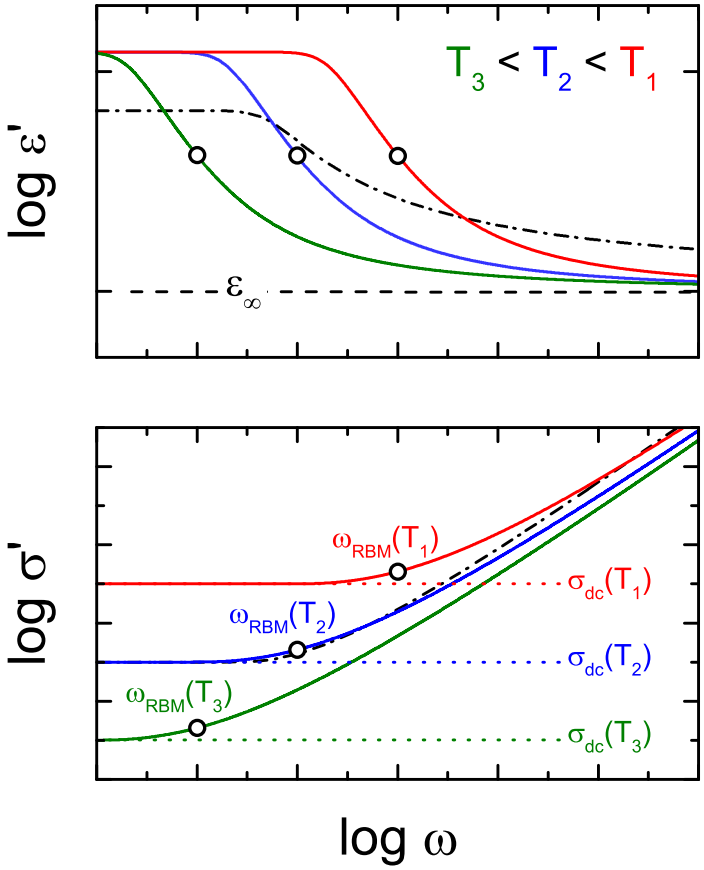

Figure 3.11: Numerical solutions of the RBM model from 2008 [164] for ε' and σ' and three different temperatures. Each temperature step accounts for a shift of σ_{dc} and τ_{RBM} of two orders of magnitude. Indications have the same meaning as in figure 3.10. The dash-dotted line shows the results of the old RBM solution for the same parameters as the intermediate temperature (blue line), thus highlighting the differences of the two models. Into both equations the contribution from displacement polarization ε_∞ was introduced.

Figure 3.11 presents a simulation of the new RBM solution. The model predicts the crossover from dc to ac conductivity in σ', qualitatively similar to the UDR. However, in ε' it produces a pronounced step-like decrease similar to a relaxation step. Additionally, figure 3.11 compares the old and the new solution. Obvious differences are a steeper ac-conductivity increase and the quantitative difference of the step in ε', which, for the new solution, is much higher and merges faster towards ε_∞.

To summarize, the contributions to the dielectric response from ionic conductivity are manifold. The straightforward dc conductivity arises from long-ranged translational diffusion of ions in the sample and yields a frequency independent plateau in σ'. The phenomena of dispersion at higher frequencies

due to ac conductivity is until today a controversial discussed topic. Many ion hopping models predict this dispersion phenomena and are more or less capable to describe experimental data. For the present work, the new solution of the RBM is chosen as an up-to-date model to be integrated in the fitting routine, whenever a spectral feature can be suspected to be of purely ionic nature.

3.2.5 The Dielectric Modulus

An alternative approach to analyze dispersion phenomena in ionic conductors is the dielectric modulus

$$M^*(\omega) = 1/\varepsilon^*(\omega) = M'(\omega) + M''(\omega) \tag{3.36}$$

representation. Proposed by Macedo *et. al.* [179] for ionic conductors without permanent dipoles, the modulus representation offers the advantage of an assumed direct access to the ionic dynamics. For an idealized sample with purely frequency independent dc conductivity σ_{dc} and a frequency independent relative permittivity ε_{s}, ε^* is given by:

$$\varepsilon^*(\omega) = \varepsilon_{\mathrm{s}} + i\frac{\sigma_{\mathrm{dc}}}{\omega\varepsilon_0}. \tag{3.37}$$

From the definition of the modulus $M^* = 1/\varepsilon^*$ follows further:

$$M^*(\omega) = M_{\mathrm{s}}\left(\frac{i\omega\tau_\sigma}{1+i\omega\tau_\sigma}\right) = M_{\mathrm{s}}\left(1 - \frac{1}{1+i\omega\tau_\sigma}\right) \tag{3.38}$$

with

$$M_{\mathrm{s}} = 1/\varepsilon_{\mathrm{s}} \tag{3.39}$$

and

$$\tau_\sigma = \frac{\varepsilon_0\varepsilon_{\mathrm{s}}}{\sigma_{\mathrm{dc}}}. \tag{3.40}$$

Thus, for an idealized conductor M' exhibits a step-like increase from 0 to M_{s} and M'' a symmetrical peak with peak position frequency $\nu_{\mathrm{peak}} = 1/(2\pi\tau_\sigma)$. The formalism calls τ_σ the conductivity relaxation time. In real systems, however, a broadened peak in M'' is found and is, analogously to the dielectric relaxation, interpreted as a distribution of conductivity relaxation times. Such broadening can be modeled by a CD expansion of equation 3.38 [180]:

$$M^*(\omega) = M_{\mathrm{s}}\left(1 - \frac{1}{(1+i\omega\tau_{\mathrm{CD}})^\beta}\right). \tag{3.41}$$

However, in ionic conductors without permanent dipoles, a frequency independent relative permittivity ε_{s} arises due to quasi-instantaneous displacement polarizations, hence $\varepsilon_{\mathrm{s}} = \varepsilon_\infty$. Consequently, the position and shape of the peak in M'' dependents on contributions from displacement polarizations, which physically are not directly related to the motion of mobile charge carriers. Therefore, the analysis and interpretation of the dielectric modulus as conductivity relaxation has received criticism [181–183].

It should be noted, that criticism of the modulus representation does only apply to its interpretations about the ionic dynamics. The modulus representation itself has the same validity as any other complex dielectric quantity (ε^*, σ^* and ρ^*) and by no means does the standart dielectric measurement routine relate to one of those representations more than to another [184].

In the present work, where in all cases mobile permanent dipoles are present, the interpretation of the M'' spectra is anyway questionable, as the M'' peak will be a superposition of ionic and dipolar contributions. However, the modulus representation is commonly applied in mechanical spectroscopy and an adequate comparison of dielectric and mechanical data includes the modulus representation.

3.2.6 Equivalent Circuit Approach

So far the contributions and the mathematical framework for dipolar relaxation, the ionic conductivity and the displacement polarization were introduced. Together with the extrinsic inferfacial polarizations they compose the dielectric response of an ionically conducting material with permanent dipoles. The overlap and interdependence of these processes in the dielectric spectrum make its evaluation non-trivial. Commonly, an equivalent-circuit approach is used to model the dielectric data and to extract the important parameters like dipolar relaxation time, relaxation strength, dc conductivity and so on.

From all kind of different inferfacial polarizations only the EP plays an important role for the evaluation of the dielectric data in the present work. In the following, a phenomenological model for the EP will be introduced [117]. Afterwards, the equivalent-circuit with the interconnection of the individual components and the fitting routine will be explained.

Distributed RC circuit In ionically conducting systems, solid and liquid, EP is an often observed phenomenon in the dielectric spectrum (see, e.g., ref. [117] and references within). It arises from the translational motion of the ions. At low frequencies, i.e., with long time periods of the external field pointing in one direction, ions diffusing through the sample will eventually reach the electrodes before the reversal of the field. This accumulation of ions at the metallic electrodes leads to the formation of a space-charge region, effectively acting as thin isolating layers between the electrodes and the sample. Macroscopically, this results in a significant increase of the measured capacity and an decrease of the conductivity of the sample inside the capacitor. Hence, in the dielectric spectrum ε' reaches extraordinary high values, not accountable for by intrinsic polarizations, and in σ' lower conductivities than σ_{dc} are obtained.

In highly conducting systems, EP effects often hamper the analysis of the intrinsic contributions in the dielectric spectrum. To overcome this problem, either the application of special measurement techniques to avoid EP (e.g., four point measurements or varying electrode distances [185–187]) or the modeling of the EP, e.g., by an equivalent circuit are possible. Special measurement techniques, however, require significant additional effort and sometimes entail disadvantages by itself, e.g., a larger electrode distance results in a smaller measurement resolution at very low losses. Numerous phenomenological and microscopic models were proposed to describe the EP (see ref. [188] for a review), still in many cases the EP effects are not in the focus of the investigation but have to be taken into account when analyzing the dielectric spectrum. In such cases, the modeling of the EP effects with an equivalent circuit offers an easy approach to the problem.

Most commonly, a constant phase element [189–195] or a parallel RC circuit [143, 196–198] are applied and deliver reasonable results as long as only the onset of EP effects arises at the low frequency boundary of the spectrum. In ref. [117], it was shown that a distributed RC equivalent circuit (DRC) is able to describe the EP in the dielectric spectrum of many different materials over the complete investigated frequency range. Hence, the DRC is the method of choice in the present work to model the EP effects.

The DRC is a straightforward extension of the standard RC equivalent circuit in manner of the empirical extension of the Debye relaxation formula, i.e., the HN function (equation 3.17) [117]. The DRC is connected in series to the bulk response of the sample and the overall impedance Z_{total} is a function of the impedance of the bulk Z_{bulk} and the capacitance C_{EP} and resistance R_{EP} of the thin blocking layers:

$$Z_{\mathrm{total}} = Z_{\mathrm{bulk}} + \frac{R_{\mathrm{EP}}}{\left[1 + (i\omega\tau_{\mathrm{EP}})^{1-\alpha}\right]^{\beta}}. \tag{3.42}$$

$0 \leq \alpha < 1$ and $0 < \beta \leq 1$ are the width parameters and $\tau_{EP} = C_{EP}R_{EP}$. For all the spectra measured in this work, the 'Cole-Cole' case ($\beta = 1$) was sufficient to achieve a reasonable description of the EP effects.

Equivalent Circuit Collectively, the EP, the orientational relaxation, secondary relaxations, displacement polarization and the ionic conductivity compose the dielectric response of the materials investigated in the present work. The equivalent circuit approach connects each of the individual components and from it the overall complex permittivity (or any dielectric measure) can be calculated.

Figure 3.12 shows the interconnection of the different components. The DRC circuit, accounting for extrinsic EP effects, is connected in series to intrinsic part. At high temperatures, some highly conducting systems reveal a second dispersion step in the EP region [20, 54, 117, 199]. Here, a second DRC connected in series can be employed to accurately describe the data [117]. Within the intrinsic part, all the contributions are connected in parallel. Those are in particular the dc conductivity, the displacement polarization ε_∞, the dipolar relaxation (α-relaxation) and further relaxations. The flexibility of the equivalent circuit approach offers an easy way to include other relaxations slower than the α-relaxation, e.g., the normal mode in polymers, or faster relaxations, such as the β_{JG}-relaxation. Also ionic conductivity models including ac contributions can be adopted by replacing the simple dc conductivity contribution.

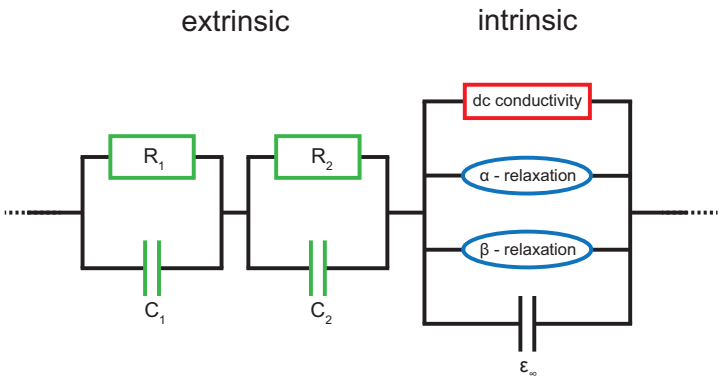

Figure 3.12: Equivalent circuit to model the dielectric response of ionically conducting systems. Extrinsic electrode polarization effects are accounted for by one (or optional two) DRC circuits connected in series to the intrinsic contribution. The intrinsic part consists of the dc conductivity, relaxation functions and the displacement polarization ε_∞. Color code corresponds to figure 2.13.

Figure 3.13 demonstrates the output of an equivalent circuit including one DRC, the dc conductivity and the α-relaxation for ε', ε'' and σ'. In ε', with increasing frequency a double-step-like decrease can be seen. The slower (at lower frequencies) process with the much higher step height is due to EP effects (in the picture abbreviated with BE for blocking electrode). The faster process comes from the α-relaxation. In ε'', two peak-like features occur, with the same origins as the steps in ε'. Additionally between EP and α-relaxation, the dc conductivity shows up as decreasing contribution ($\propto \nu^{-1}$). $\sigma' = \varepsilon''\varepsilon_0 2\pi\nu$ includes the same contributions, but this representation highlights the frequency dependent plateau arising from dc conductivity.

In ionically conducting systems, the spectral position of the dc contribution with respect to the α-relaxation is not constant, but depends on the material properties and the temperature. In some cases,

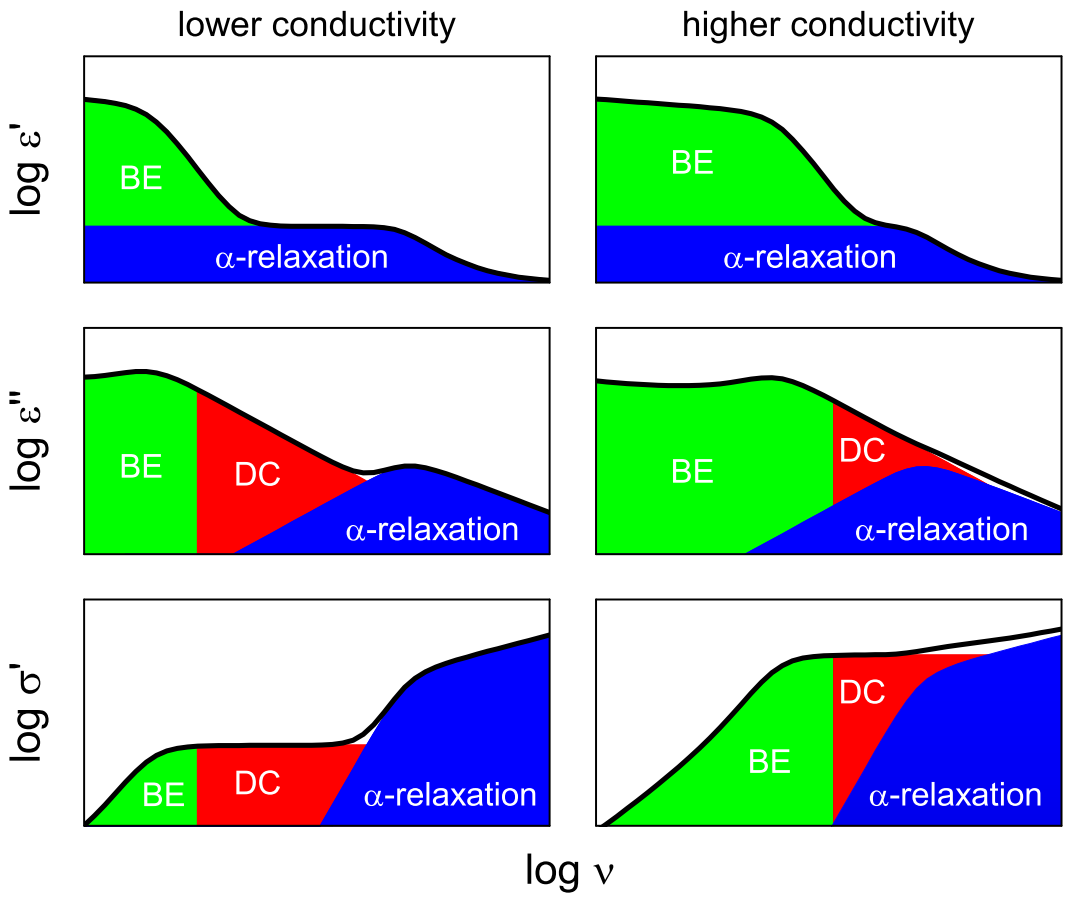

Figure 3.13: Dielectric spectra of ε', ε'' and σ' simulated with the equivalent-circuit approach utilizing one distributed RC circuit ($\alpha = 0.1$), the dc conductivity, one CD relaxation function ($\beta = 0.7$) and ε_∞. Left (lower conductivity) and right (higher conductivity) column represent results for two different conductivity values while all other parameters were held constant. The different contributions are highlighted by the colored areas: electrode polarization (green), dc conductivity (red) and relaxation (blue). The overall response is represented by the black solid line. For the lower dc conductivity (left column) the three processes are well separated while for the higher dc conductivity (right column) the onset of electrode polarization significantly shifts to higher frequencies, the dc conductivity plateau rises and the relaxation gets superimposed by the dc conductivity.

very high values of the dc conductivity lead to a merging of the two processes in the dielectric spectrum (figure 2.13 right column). The dc contribution shifts to higher frequencies in ε'' and the plateau in σ' rises, effectively overlapping with the peak position of the α-relaxation. Additionally, in ε' the onset of the EP shifts towards the relaxation step. The resulting dielectric response resembles that of the dc-ac conductivity sequence introduced in chapter 3.2.4. Hence, from the spectral shape alone it is rather difficult to distinguish between the two scenarios: combination of dc conductivity and α-relaxation or ac conductivity. Often, both models achieve a reasonable fit to the data [23, 200].

Altogether, the equivalent circuit approach enables a description of the dielectric response of ionically conducting systems over the whole dielectric frequency range. From the fitting routine the important parameters, such as dipolar relaxation time and dc conductivity, can be obtained with high

accuracy. Still, often the spectral shape does not unequivocally define the composition of the equivalent circuit but rather the individual components must be chosen with some consideration. For example, in highly conducting systems the high frequency part can sometimes be modeled with either a combination of dc conductivity and a relaxation function or an ac conductivity model. Here, consideration about the material composition or supporting measurements can help with the determination of the model.

3.3 Rheology of Liquids

In the present work, shear viscosity measurements were conducted to complement the results from dielectric spectroscopy. Unlike dielectric spectroscopy, which is only sensitive to certain aspects of the molecular and ionic dynamics in a liquid, mechanical spectroscopy measures the liquid's resistance to flow, which is a macroscopic measure built up from all different kinds of dynamics and interactions of the liquid's constituents. Thus mechanical spectroscopy measures the 'real' structural relaxation, where dielectric spectroscopy only detects dipolar reorientations and ionic translations. Therefore, the comparison of both offers valuable insights on the interdependencies of these processes.

The following chapters will introduce the basic mathematical framework for the interpretation of the viscoelastic response of liquids [201, 202]. The interpretation and analysis of the mechanical spectrum will be presented in straight analogy to the dielectric spectrum.

3.3.1 Basic Definitions

Rheology is the study of the flow and deformation properties of condensed matter. The following introduction will be reduced to the mechanical response of small-molecule liquids and the linear region, i.e., the ratio of mechanical stress and deformation is constant.

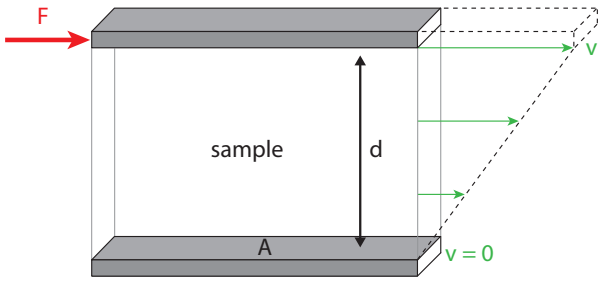

Figure 3.14: Parallel plates shear experiment [202].

The terminology of rheological measurements may well be introduced with the example of a parallel-plates shear experiment (figure 3.14) [201]. A force F is applied to the upper of two identical plates with plate area A and plate distance d. A viscous sample fills the space between the plates. The movement of the upper plated induces a flow velocity v in the sample depending on the distance from the lower static plate. The force F generates a mechanical shear stress σ_m in the sample:

$$\sigma_m = F/A. \tag{3.43}$$

The shear deformation γ of the sample is defined by the horizontal displacement Δs of the upper plate

$$\gamma = \Delta s/d \tag{3.44}$$

and the shear deformation rate $\dot{\gamma}$ by the velocity v of the upper plate

$$\dot{\gamma} = v/d. \tag{3.45}$$

For an ideal viscous fluid, Newton's law gives the steady-state flow viscosity η_0 (or simply called the viscosity) as the ratio of shear stress σ_m and shear rate $\dot{\gamma}$:

$$\eta_0 = \sigma_\mathrm{m}/\dot{\gamma}. \tag{3.46}$$

It describes the continuous deformation of a ideal liquid under applied mechanical stress. This deformation is irreversible and permanent even after the relief of the mechanical stress. In an equivalent circuit it is represented by a purely viscous damper.

On the other hand, for ideal elastic (reversible) deformation the elastic shear modulus G_∞ is introduced, known as Hooke's law:

$$\sigma_\mathrm{m} = G_\infty \gamma. \tag{3.47}$$

This law only holds as long as all energy supplied to the system is stored as deformation energy and is used to completely reverse the induced deformation after the relief of the mechanical stress. In an equivalent circuit it is represented by a purely elastic spring.

The Maxwell model combines these two idealistic models (figure 3.15). The so-called viscoelastic behavior of a material is modeled by a combination of Newton's and Hook's law. The overall shear rate $\dot{\gamma}$ is given by:

$$\dot{\gamma} = \dot{\gamma}_\mathrm{ela} + \dot{\gamma}_\mathrm{visco} = \frac{\sigma_\mathrm{m}}{\eta_0} + \frac{\dot{\sigma}_\mathrm{m}}{G_\infty}. \tag{3.48}$$

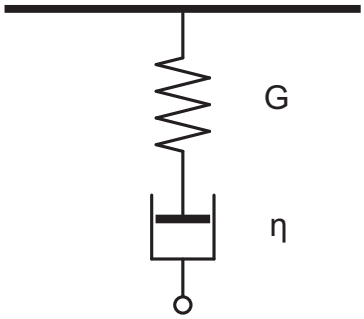

Figure 3.15: Equivalent circuit approach according to the Maxwell model. Viscoelasticity is described by a serial connection of a purely viscous η damper and a purely elastic spring G.

Much like in dielectric spectroscopy, dynamic mechanical measurements allow access to dynamic properties of the medium. The application of an harmonic oscillating shear deformation γ (in complex form)

$$\gamma^* = \gamma_0 \mathrm{e}^{i\omega t}, \tag{3.49}$$

produces an oscillating shear stress σ_m^* with certain phase retardation due to the inability of the material to instantaneously react to the deformation. In this case, the ratio of σ_m and γ becomes a complex quantity:

$$G^* = G' + iG'' = \sigma_\mathrm{m}^*/\gamma^*. \tag{3.50}$$

Hence the basic principal of measurement and analysis of dielectric and mechanical spectroscopy are very similar, which becomes especially obvious when looking at the interconnections of the different

complex mechanical quantities (see figure 3.16). As introduced, the complex mechanical modulus G^* can be obtained with the application of a harmonic oscillating deformation. The complex compliance J^* is the inverse of G^* and can be experimentally determined by applying a harmonic oscillating shear stress and measuring the deformation. The complex viscosity (resistance to flow) and the complex fluidity (ability to flow) are the analogous quantities to complex resistivity and complex conductivity, respectively. Each complex quantity includes the full information of the dynamic mechanical response of a system and from it each other quantity can be calculated.

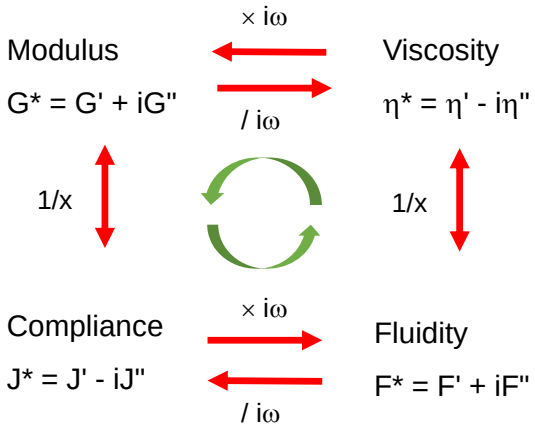

Figure 3.16: Correlation of the different mechanical quantities [203]. The relations between the different quantities are inscribed, e.g., $G^* = 1/J^*$ and $\eta^* \times i\omega = G^*$.

3.3.2 The Dynamic Mechanical Response

In analogy to the introduction of the dielectric relaxation in chapter 2.2.3, the frequency dependence of the mechanical response of a liquid will be explained based on the time dependent shear relaxation, followed by the transition into the frequency domain. Further similarities arise when comparing results and interpretation of the different complex mechanical quantities. Much like for the dielectric response, the complex mechanical modulus G^* and the complex compliance J^* are two fully valid representations of the mechanical response. From both a structural relaxation time can be obtained.

Modulus Representation The Maxwell model for viscoelastic materials may serve as starting point for the mechanical response of small-molecule liquids. After an sudden exposure to a constant deformation γ_0, a material will exhibit a decreasing shear stress $\sigma_\mathrm{m}(t)$ with time. In context of the Maxwell model, for $\dot{\gamma} = 0$ follows

$$\frac{\sigma_\mathrm{m}}{\eta_0} = -\frac{\dot{\sigma}_\mathrm{m}}{G_\infty} \tag{3.51}$$

with solution

$$\sigma_\mathrm{m}(t) = \sigma_0 \mathrm{e}^{-t/\tau_\mathrm{G}}. \tag{3.52}$$

τ_G is called the shear stress relaxation time (in context of the Maxwell model) and is often assumed to be the system's structural relaxation time. From equation 3.51 and 3.52 the Maxwell relation gives a simple expression for τ_G:

$$\tau_\mathrm{G} = \eta_0 / G_\infty. \tag{3.53}$$

In the frequency domain the application of a harmonic oscillating shear deformation γ^* with angular frequency $\omega = 2\pi\nu$ produces a shear stress with phase retardation. Inserting $\gamma^* = \gamma_0 \exp(i\omega t)$, into equation 3.48 one obtains the relaxation function of the Maxwell model:

$$G^* = G_\infty \frac{i\omega\tau_G}{1 + i\omega\tau_G}. \tag{3.54}$$

This equation can be rewritten in analogy to the Deybe relaxation function:

$$G^* = G_\infty \left(1 - \frac{1}{1 + i\omega\tau_G}\right). \tag{3.55}$$

For the real G' and the imaginary G'' part follows:

$$G' = G_\infty - \frac{G_\infty}{1 + \omega^2\tau_G^2} \tag{3.56}$$

and

$$G'' = \frac{G_\infty \omega\tau_G}{1 + \omega^2\tau_G^2}. \tag{3.57}$$

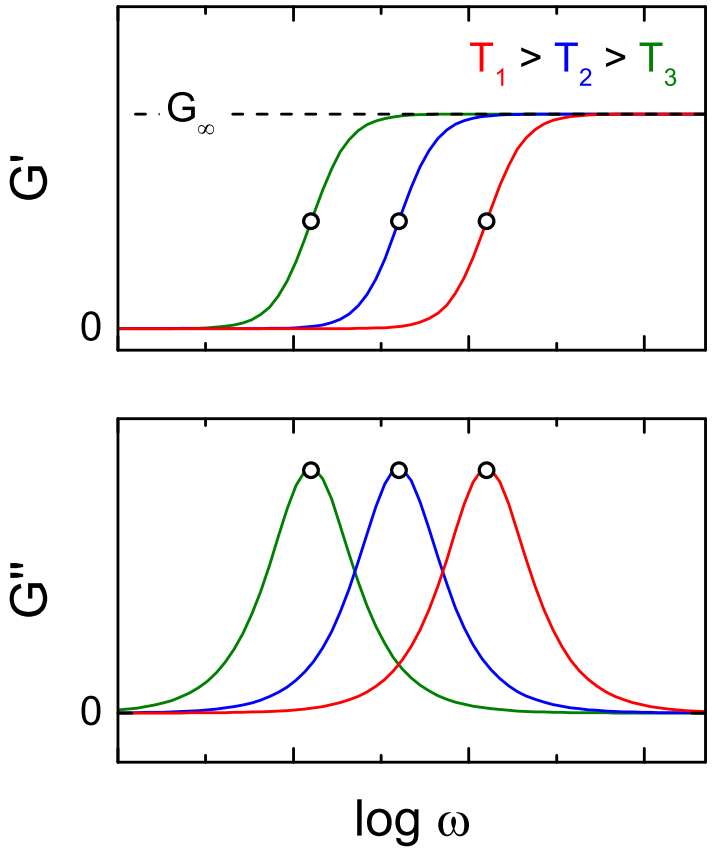

Figure 3.17: Simulation of the Maxwell model for the real and the imaginary part of the complex mechanical modulus G^* and for three different temperatures. For each temperature step, τ_G is assumed to change by one order of magnitude. Black circles mark $\omega_{max} = 1/\tau_G$. G_∞ is the elastic modulus in the high frequency limit.

Comparable to the dielectric Debye relaxation function, the Maxwell model for G^* displays a characteristic frequency dependence (see figure 3.17). G' monotonously increases from zero at low frequencies to G_∞ at high frequencies. Simultaneously, G'' exhibits a broad peak with peak position

$\nu_{max} = 1/(2\pi\tau_G)$ marking the structural relaxation time τ_G. Besides G_∞ and τ_G, the steady-state flow viscosity η_0 is often of interest when conducting rheological measurements. With

$$\eta' = G''/\omega = \frac{\tau_G G_\infty}{1+\omega^2\tau_G^2} \tag{3.58}$$

the frequency dependence of the real part η' of the viscosity is obtained and shown in figure 3.18.

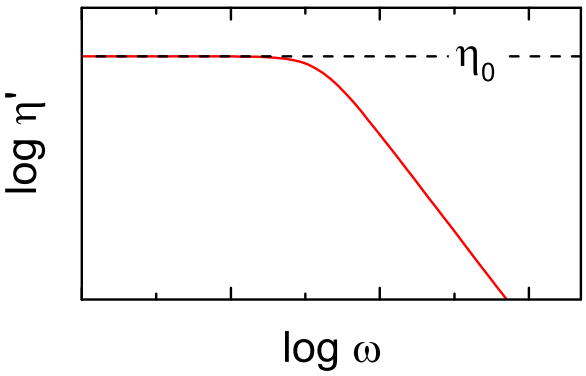

Figure 3.18: Frequency dispersion of η' calculated with equation 3.58 for the intermediate curve in figure 3.17. Indicated is the value of the steady-state flow viscosity η_0.

At low frequencies η' exhibits a plateau with

$$\lim_{\omega\to 0}\eta' = \tau_G G_\infty = \eta_0 \tag{3.59}$$

and going to higher frequencies the curve reveals a kink as dispersion sets in.

In real systems, often a significant broadening of the relaxation peak in G'' is found [204–207]. In analogy to the broadened dielectric relaxation peak, this can be ascribed to a non-exponential decrease of the shear stress after an initial permanent deformation and, hence, a distribution of relaxation times. Phenomenologically, the broadened peak can be accounted for by a Cole-Davidson modification (equation 3.19) of the Maxwell model

$$G^* = G_\infty\left(1 - \frac{1}{(1+i\omega\tau_{CD})^\beta}\right). \tag{3.60}$$

The structural relaxation time τ_G is often compared to the dielectric relaxation time τ_ε determined from the permittivity representation. Despite the common assumption of a coupling between both, Jakobsen *et al.* [208] studying seven different liquids found no general rule for the ratio τ_G/τ_ε besides $\tau_G < \tau_\varepsilon$. Similar results ($\tau_G < \tau_\varepsilon$) were found for the 'model' glass-former glycerol by Schröder and Donth [207]. Furthermore, Schröder and Donth [207] estimated a shear relaxation τ_J from the mechanical compliance representation, which came more closely to the dielectric relaxation time and, thus, prompting the comparison of τ_ε with both τ_G and τ_J.

Compliance Representation The mechanical counterparts of the dielectric permittivity and the conductivity are the mechanical compliance J^* and the fluidity F^*. Their utilization (e.g., [203, 207, 209, 210]) in literature has so far been small compared to the modulus representation. However, as shown by Bierwirth *et al.* [211], the mechanical response of viscous liquids presented in J^* and F^* shares many similarities with the dielectric response of ionic conductors presented in their corresponding counterparts.

In the standard Maxwell model derived for G^*, the real part of the compliance J' and the real part of the fluidity F' have no frequency dependence. However, in real systems, J' reveals a step-like decrease [200, 207, 209] and F' a frequency independent plateau crossing over in a strong increase with frequency [200, 203, 210, 211].

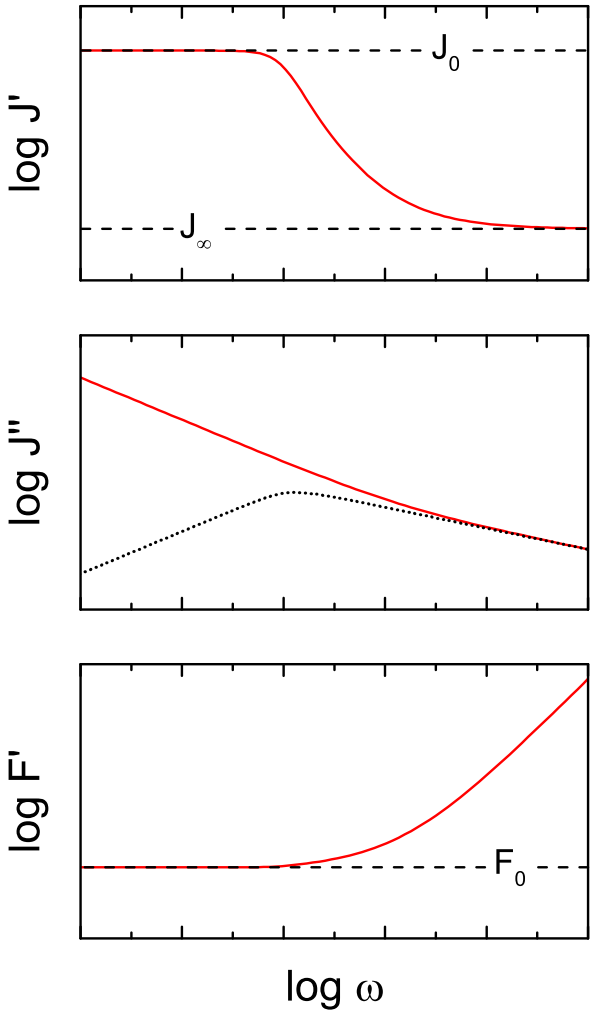

Figure 3.19: Mechanical response for the real J' and imaginary part J'' of the compliance as well as the real part of the fluidity F' according to equation 3.61 with $\beta = 0.5$. Indicated are J_∞, J_0 and F_0 with horizontal dashed lines. Dotted line in J'' represents the purely relaxational contribution.

One may describe the observed mechanical response on a purely phenomenological level with the adoption of the CD function (equation 3.19) for the compliance with the addition of the steady-state flow viscosity η_0:

$$J^* = J_\infty + \frac{\Delta J}{(1+i\omega\tau_{\mathrm{CD}})^\beta} + i\frac{1}{\omega\eta_0}. \tag{3.61}$$

Nomenclature follows the dielectric counterparts: J_∞ is the instantaneous shear compliance, J_0 the recoverable compliance, $\Delta J = J_0 - J_\infty$ the compliance relaxation strength, β is the with parameter and $F_0 = 1/\eta_0$ is called the steady-state fluidity [200, 211].

Figure 3.19 present the schematic frequency dependence of the compliance and the fluidity following equation 3.61. Here, J' exhibits a smeared out sigmoidal decrease with low frequency limit J_0 and high

frequency limit J_∞. For F' a frequency independent plateau with value F_0 is found at lower frequencies, while at higher frequencies F' increases strongly. $J'' = F'/\omega$ are the same data but the representation highlights the relaxational contribution in J''.

The obtained spectra look very similar to dielectric spectr of a ionic conductor with dipolar relaxation or an ionic conductor with strong ac conductivity contribution. It was pointed out in chapter 3.2.6 that the dielectric spectra of both are hardly distinguishable, which leaves room for interpretation. On this basis, Bierwirth *et al.* [211] successfully adopted the RBM (equation 3.35), originally derived for ionically conducting solids, to fit the mechanical response of liquids. In its fluidity representation, it reads:

$$\ln\frac{F^*}{F_0} = \frac{i\omega\tau_{\mathrm{RBM}}F_0}{F^*}\left[1+2.66\frac{i\omega\tau_{\mathrm{RBM}}F_0}{F^*}\right]^{-1/3}. \tag{3.62}$$

Both, equation 3.61 and 3.62 are able to well describe the typical mechanical response of a liquid in the J^* and F^* representation and naturally the obtained relaxation times from both models are very similar. While the CD approach is a purely phenomenological model, the application of the RBM on mechanical data requires the general assumption that translational molecular dynamics in liquids (which define the mechanical response) are physically similar to charge transport in ionically conducting systems [211]. Still the RBM uses two fitting parameters less than the CD approach and represents an interesting alternative.

Altogether, the mechanical response of liquids is commonly analyzed in the modulus representation. The Maxwell model gives a theoretical framework and the phenomenological expansions of the Maxwell model can well be used to describe real mechanical data. From the peak in G'' the structural relaxation τ_{G} can be obtained. Alternatively, the compliance representation can be used and a structural relaxation τ_{J} may be estimated via a CD approach or the application of the RBM. Independently, the important steady-state flow viscosity $\eta_0 = \lim_{\omega\to 0}\eta'$ may be obtained directly from the η' vs ω graph.

4 Experimental Techniques

The main experimental technique of the present work is the dielectric spectroscopy. It is used to investigate the molecular and ionic dynamics of the different ionic conductors. In case of the DES, mechanical spectroscopy was applied to complement the results from dielectric spectroscopy. Supporting information about the different transition temperatures were obtained with differential scanning calorimetry (DSC). This chapter introduces the basic principles of the experimental techniques and the used devices.

4.1 Broadband Dielectric Spectroscopy

The measurement of the frequency dependent dielectric response essentially comes down to the determination of the complex impedance $Z^*(\omega) = U^*(\omega)/I^*(\omega)$ of a sample for each frequency $\omega = 2\pi\nu$ of external electric field. For this purpose, the sample is typically filled into a parallel-plate capacitor with known empty capacity $C_0 = \varepsilon_0 A/d$, where A and d denote the plate surface and the distance between the plates, respectively. From the experimental observables current I and voltage U, the electric field E and the dielectric displacement D can be directly determined via $E = U/d$ and $D = \int I(t)dt/A$. In case of the application of an harmonic oscillating voltage input signal $U^*(\omega) = U_0 \exp(i\omega t)$ the current through the capacitor $I^*(\omega) = I_0 \exp(i\omega t + \varphi)$ is characterized by a phase retardation φ and from that the complex permittivity can be obtained [184]:

$$\varepsilon^*(\omega) = \frac{D^*(\omega)}{\varepsilon_0 E^*(\omega)} = \frac{I^*(\omega)}{U^*(\omega)} \frac{d}{i\omega\varepsilon_0 A} = \frac{1}{Z^*(\omega)} \frac{d}{i\omega\varepsilon_0 A}. \tag{4.1}$$

Thus, in the classical dielectric frequency range from 0 to 10^9 Hz, measurements come down to the detection of the input voltage signal and the output current signal including the phase retardation. In the laboratory, however, technical circumstances require the application of different measurement setups to cover the whole frequency range. Nowadays, with only two measurement devices the frequency range from 10^{-3} to 10^9 Hz can be continuously covered, namely with the "Alpha - A High Performance Frequency Analyzer" by Novocontrol Technologies and the "E4991B Impedance Analyzer" by Keysight Technologies.

Frequency Response Analyzer The "Alpha - A High Performance Frequency Analyzer" by Novocontrol Technologies ("Alpha Analyzer") covers a frequency range from 3×10^{-3} to 10^7 Hz. A detailed documentation of the measurement device is given in the user's manual provided by the company [212].

Together with the "4-Wire Impedance Interface ZG4" test interfaces, the "Alpha Analyzer" works on the principle of a frequency response analyzer. In figure 4.1 the basic electric circuit is shown.

In principle, a frequency generator applies an ac voltage to the sample. This voltage is measured in amplitude and phase as U_1^* in the analyzer channel I. The current I_s^* through the sample obtains an amplitude I_0 and phase retardation φ due to the samples complex impedance Z_s^*. The frequency

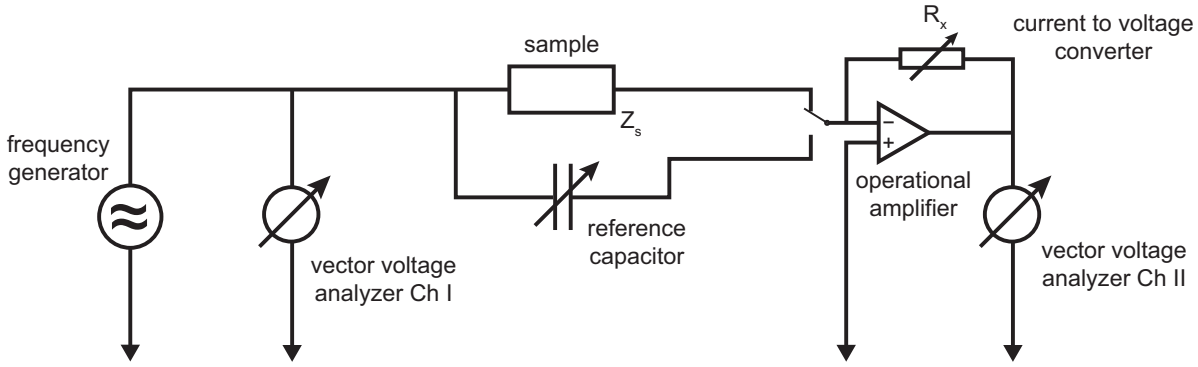

Figure 4.1: Basic electric circuit of the "Alpha Analyzer" [212].

response analyzer, however, works with voltages. Therefore, the current I_s^* is converted to the voltage U_2^* via a operational amplifier with an variable resistance R_x in its feedback loop. For U_2^* follows:

$$I_s^* = -\frac{U_2^*}{R_x} \tag{4.2}$$

The current through the variable resistance R_x effectively creates a virtual ground at the I_s^* input of the operational amplifier, which ensures that the voltage U_1^* corresponds to the voltage over the sample. Hence, the sample's impedance is given by:

$$Z_s^* = \frac{U_1^*}{I_s^*} = -\frac{U_1^*}{U_2^*} R_x. \tag{4.3}$$

If enabled, the "Alpha Analyzer" will perform a reference measurement after each sample measurement. The current to voltage converter is switched to the variable reference capacitor and the so-called "online calibration" is performed. This significantly improves the measurement accuracy.

From the complex sample impedance Z_s^* the dielectric quantities can be calculated with the sample's geometry (equation 4.1). For an accurate calculation, the sample's geometry must be well defined. For liquid samples, a so-called pot-in-pot capacitor design (see figure 4.2) has proven its worth.

The bottom side of the smaller pot serves as upper capacitor plate and is separated from the lower capacitor plate with glass fiber spacers. Typically, glass fibers with diameter of 100 µm were used for the present work. In this way, the sample's geometry is well defined by the glass fibers diameter and the area of the bottom side of the smaller pot. When contacted to the "Alpha Analyzer", the whole space between the two capacitor pots contributes to the dielectric response, including the plastic spacer ring. However, as long as the sample's thickness is much smaller than the ring thickness, the dielectric response will almost entirely come from the sample.

The sample's temperature is measured with a temperatures sensor attached inside a hole of the lower capacitor pot. To account for thermally induced volume changes of the liquid sample, the inside of the upper capacitor pot serves as a reservoir.

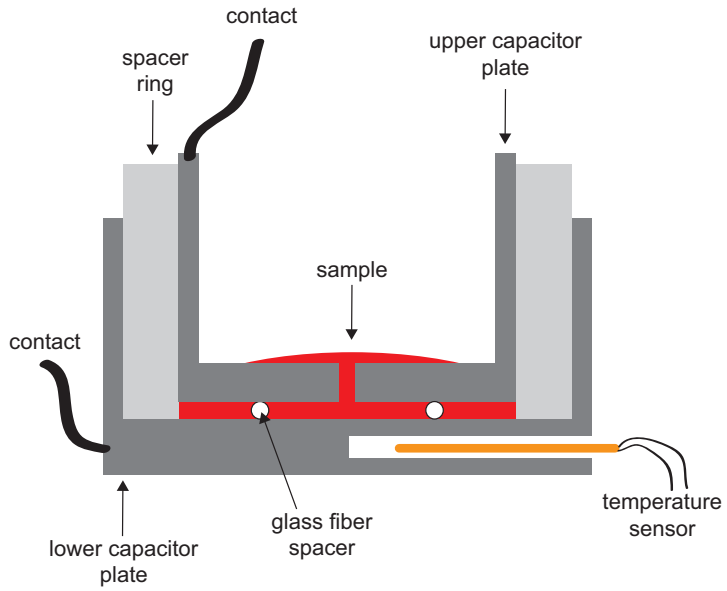

Figure 4.2: Schematic drawing of the pot-in-pot capacitor design.

Radio Frequency I-V method For frequencies between 1 MHz and 3 GHz an "E4991A/B Impedance Analyzer" from Agilent Technologies (now distributed by Keysight Technologies) was used. This device works with the radio frequency (RF) I-V method. A detailed documentation of the working principles can be found in the handbook provided by Keysight Technologies [213].

The basic I-V method is a straightforward estimation of an unknown impedance Z_s^* from a voltage and current measurement. A frequency generator applies an ac voltage to a low value resistor in series to the unknown impedance. The current can be calculated from the voltage across the known low value resistor and the overall voltage is measured across both elements. For the unknown impedance one obtains an equivalent to equation 4.3, thus the basic I-V method is essentially a simplified version of figure 4.1 without the virtual ground.

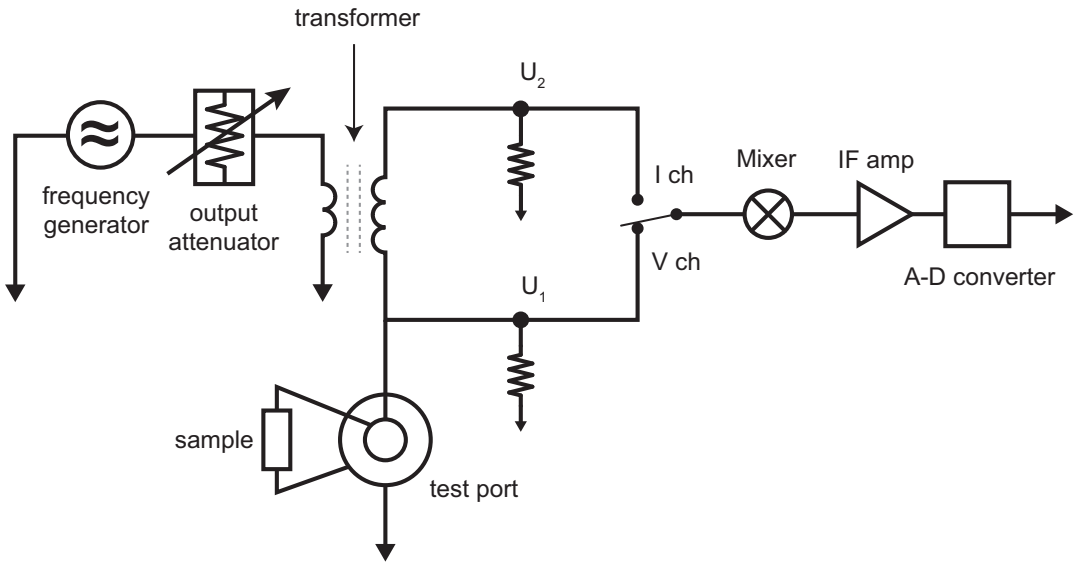

Figure 4.3: Basic electric circuit of the E4991B impedance analyzer [213].

The RF I-V method is based on the same principal with a few additions. The measurement circuit is fixed to 50 Ω and the sample is placed inside a precision coaxial test port designed for operations at higher frequencies. The basic electric circuit is shown in figure 4.3.

The ac signal provided by the frequency generator is adjusted to desired levels by the output attenuator and is then used via a transformer as input signal in the measurement circuit. The current in the measurement circuit is measured via the voltage U_2^* across the transformer's winding. Together with voltage U_1^* across the sample inside the test port the impedance of the sample Z_s^* can be calculated. Technically, the V/I multiplexer alternately selects the I and V channel, hence the outputs of the measurements of U_1^* and U_2^*, so that the two vector voltages can be measured by an identical vector ratio detector. The mixer circuit down converts the signal to a frequency matching the A-D converter's operation speed and the converter digitally separates the into 0° and 90° components, from which the dielectric quantities are obtained.

The capacitor in the case of an RF I-V method is built as an extension of the inner conductor of a 7 mm coaxial cable (see figure 4.4). The pin of the lower capacitor plate can be placed inside the inner conductor of an APC-7 connector. The upper capacitor plate is identical but with a hollow pin, which serves as reservoir. The two plates are spaced with a plastic ring, which defines the distance between the plates. The electrical contact to the inner conductor of the APC-7 connector is directly provided by the pins.

For temperature control the sample must be placed inside a cryostat. For this purpose, a special sample holder is used as extension of the test port of the "E4991A/B Impedance Analyzer". In the present work, measurements with the "E4991A/B Impedance Analyzer" were conducted inside a Novocontrol Quatro cryostat (see below for details) and the "RF Sample Cell Extension Line" sample holder was used as expansion between the test port an the cryostat.

Since with increasing frequencies parasitic inductance and impedance contributions from the sample holder and the cables become increasingly significant, a calibration of the sample holder is necessary.

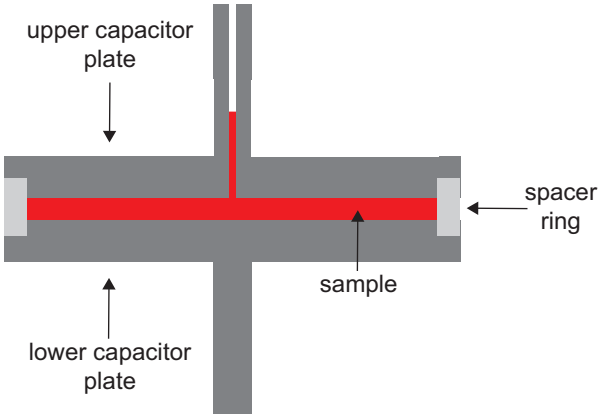

Figure 4.4: Schematic drawing of the high frequency capacitor design.

Temperature Control Dielectric measurements were conducted inside the sample chamber of a Novocontrol Technoglogies Quatro Cryosystem. The Quatro Cryosystem enables temperature control control between $113\,\mathrm{K} \leq T \leq 673\,\mathrm{K}$ and temperature ramps of 0.01 to $20\,\mathrm{K/min}$ [214]. A detailed description of the cryostat can be found in the manual provided by the company [215].

Figure 4.5 shows the basic working principle of the cryostat. A heating element evaporates liquid

nitrogen to create a controlled gas pressure inside a vacuum isolated dewar. The resulting nitrogen gas is directed through a gas-heater element to the sample chamber and the gas-heater power is controlled via a nearby temperature sensor to achieve a gas temperature appropriate to the desired sample temperature. The sample with temperature sensor is placed inside the sample chamber with a sample holder, which is specifically designed for the two utilized measurement devices.

The Quatro Cryosytem's design is especially suited for measurements of the investigated samples, because the N_2 atmosphere in the sample chamber is dry and ensures that there is no additional water uptake of the previously dried samples during the measurement. Additionally, the gas atmosphere works as heat exchanger between the sample and the temperature sensor, guaranteeing a precise determination of the sample temperature.

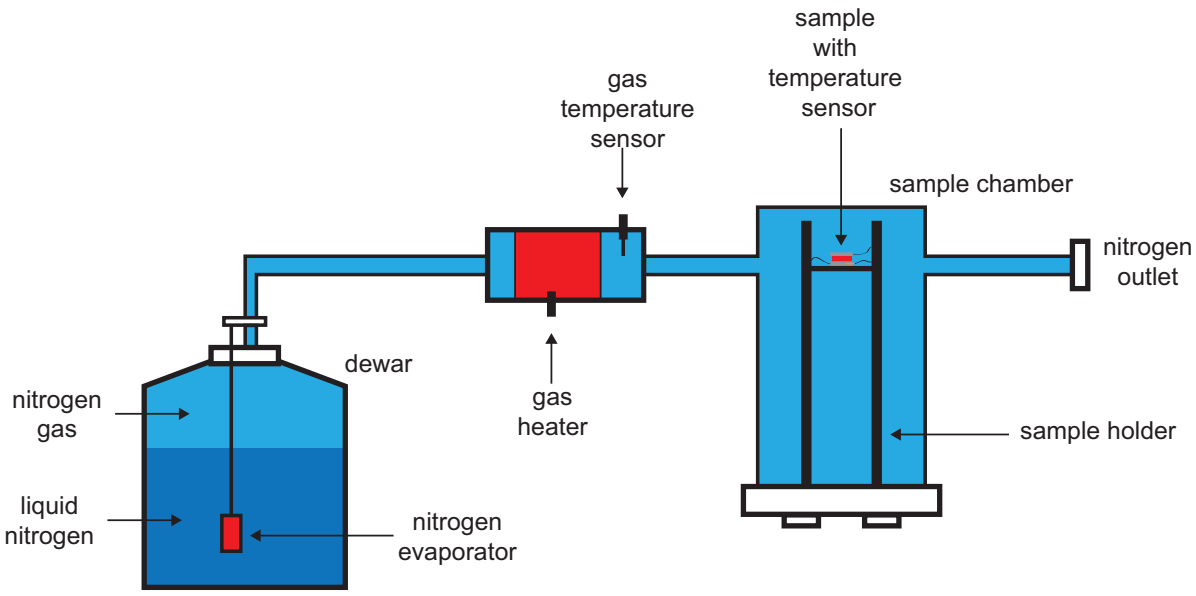

Figure 4.5: Simplified drawing of the Novocontrol Quatro cryosystem [214].

4.2 Mechanical Spectroscopy

The basic principle of parallel plate shear experiments, the experiment observables and the calculation of the complex mechanical quantities were introduced in chapter 3.3.1. Mechanical measurements for the present work were conducted with an MCR502 rheometer by Anton Paar. For the viscous liquids, the parallel plate set up was used. In this MCR502 set up, the σ_m and the sample's deformation γ are not measured by horizontally moving the upper plate but by rotating it (see figure 4.6). The rheometer has two principal operation modes: rotation and oscillation (see below). Temperature regulation is achieved with a N_2 gas-flow cryostat extension of the MCR502.

The measurement principle of the parallel plate shear measurements utilizing a horizontally moving or a rotating plate are very similar. In the case of a rotating upper plate, the device applies a defined torque M to the upper plate while the lower plates remains static. According to it's viscosity, the sample reacts with a opposing force to the applied torque and the resulting angle of rotation φ of the upper plate is measured. Via a geometry factor, from the applied torque M the shear stress σ_m and from the angle of rotation φ the sample's deformation γ can be calculated. Including the time, the speed of rotation and, further, the shear rate $\dot{\gamma}$ can be derived.

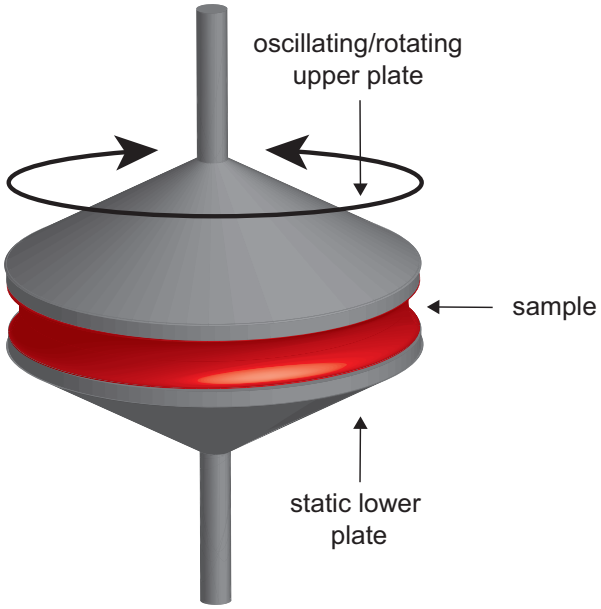

Figure 4.6: Schematic drawing of the rotating/oscillating parallel plate set up used for the rheological measurements. The liquid sample (red) fills the space between the upper and lower plate.

Rotation The rotational mode works with a full angular rotation of the upper plate. The MCR502 applies a constant torque to the upper plate and, after a short settling time, the upper plate rotates with a constant rotation speed. Hence, σ_m and $\dot{\gamma}$ are constant and for the steady-state flow viscosity η_0 follows:

$$\eta_0 = \sigma_m / \dot{\gamma} \tag{4.4}$$

In the present work, this method was used to determine η_0 in the low viscous region of the liquid samples.

Oscillation In the oscillating mode, the MCR502 applies a sinusoidal oscillating torque on the upper plate, effectively forcing it to perform small angle vibrations. The resulting angle of rotation and its phase retardation with respect to the torque are measured. Via the geometry factor, σ_m^* and γ^* can be calculated and for the complex mechanical modulus G^* follows:

$$G^* = \sigma_m^* / \gamma^* \tag{4.5}$$

The MCR502 is capable of applying oscillations with angular frequency $\omega = 2\pi\nu$ between $10^{-7}\,\text{Hz} \leq \omega \leq 628\,\text{Hz}$. Frequencies smaller 0.01 Hz, however, are usually not practical due to very long measurement duration.

4.3 Differential Scanning Calorimetry

A fast and convenient measurement technique to estimate phase-transition temperatures and the glass temperature is the differential scanning calorimetry (DSC). The technique is based on the principle of measuring the difference in the heat flow to a sample and a reference during a controlled measurement program. A detailed overview on this measurement method is given in ref. [216].

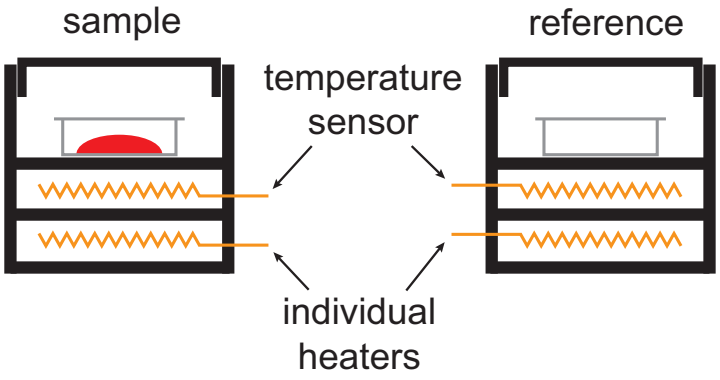

Figure 4.7: Schematic drawing of the sample and reference chamber in a power compensating DSC [216].

In the present work a DSC 8500 by Perkin Elmer was used. The device uses the power-compensating principle with a double-furnace design, i.e., two chambers (a sample and a reference chamber) are equipped with temperature sensors and individual heaters (see figure 4.7). For applications below room temperature, a N_2 gas-flow cryostat cools the dewar surrounding the furnaces to temperature $T \approx 90\,\mathrm{K}$ and helium gas enables heat transfer between the furnaces and the dewar. Equipped with the N_2 gas-flow croystat and helium as purge gas, the system covers an approximate temperature range from $100\,\mathrm{K} \leq T \leq 1000\,\mathrm{K}$ with controlled cooling and heating rates of up to $10\,\mathrm{K/min}$.

During a standard measurement in scanning mode, the system is programmed to follow a temperature ramp defined by the starting temperature T_{start}, the cooling/heating rate q and the time t. The individual heaters constantly work against the low temperature environment provided by the dewar and at any time during the measurement, the device aims to achieve equal sample temperature T_{sample} and reference temperature $T_{\mathrm{reference}}$:

$$T_{\mathrm{start}} + q \times t = T_{\mathrm{sample}} = T_{\mathrm{reference}} \tag{4.6}$$

If a sample is placed in one chamber and a reference in the other, during such a temperature program and due to the difference in specific heat, the chambers require different heating powers to remain at equal temperatures and the difference in heating power ΔP is the experiment observable. For ideal conditions and assuming a constant specific heat of the reference, ΔP is proportional to the heat flow rate Φ into the sample and further the heat flow Φ is proportional to the specific heat c_{p} (at constant pressure) of the sample:

$$\frac{\Phi}{mq} \propto c_{\mathrm{p}} \tag{4.7}$$

where m is the sample's mass and q is the cooling/heating rate.

The heat capacity C_{p} of a material is defined by the amount of heat needed to change its temperature by one kelvin at constant pressure. The specific heat c_{p} then is C_{p} divided by the mass of the material. The measurement of the temperature dependence of the specific heat of a sample is an ideal tool to observe phase transitions and the glass transition. During a first-order phase transition like, e.g., the melting of a crystal into a liquid, heat is absorbed by the sample which does not result in a further temperature increase but is used for the melting process itself, where molecules take up energy to detach from the crystal lattice. At this point, c_{p} of the sample theoretically diverges and in real DSC measurements, where the amount of the sample is limited and after a certain heat transfer the melting is completed, the heat flow Φ reveals a peak. On the other hand, the glass transition is no phase transition

but the liquid and the glass state possess different specific heats, due to the frozen molecular dynamics in the glass state, and, thus, the heat flow Φ exhibits a step-wise increase from the glass to the liquid state.

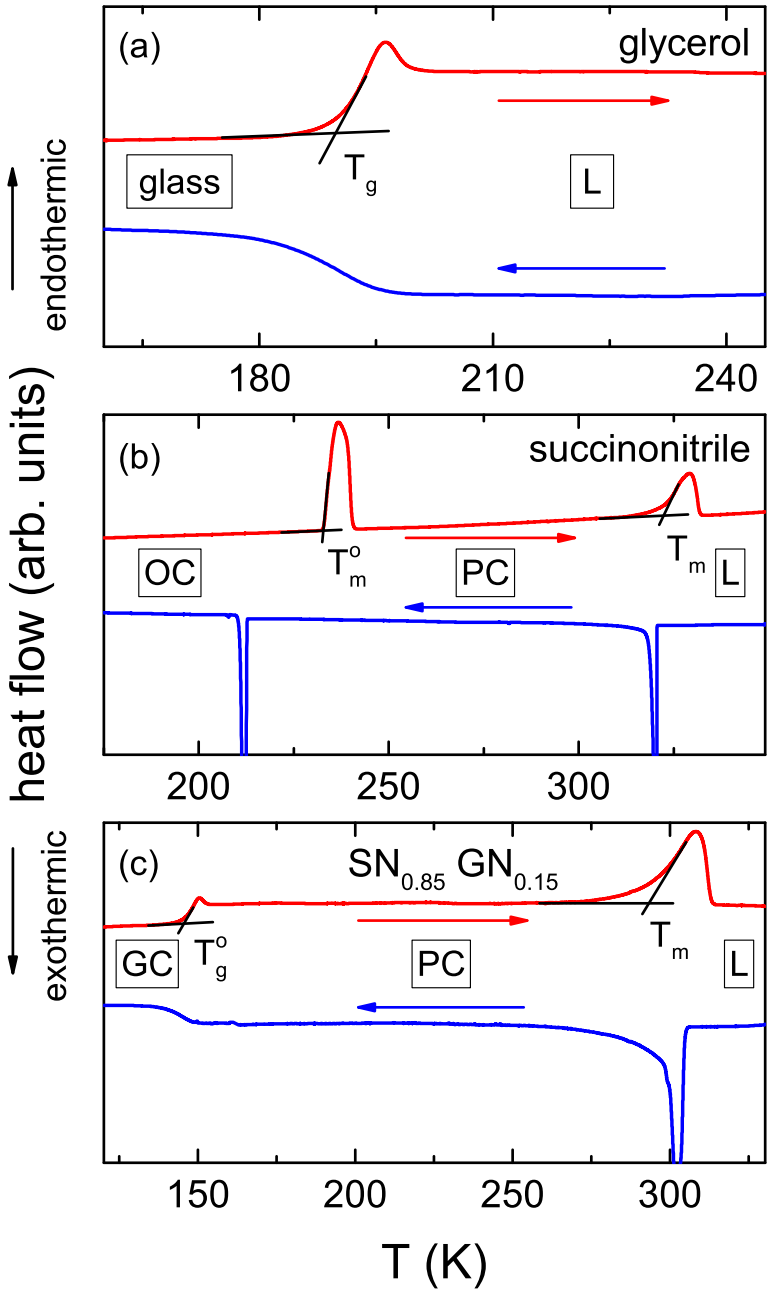

Figure 4.8: 10 K min^{-1} cooling (blue) and subsequent heating (red) DSC measurements of glycerol (a), succinonitrile (b) and a mixture of succinonitrile (SN) and glutaronitrile (GN) (c) [20]. Endothermic processes point in positive y-direction. The different phases are labeled: liquid (L), plastic crystal (PC), glass, ordered crystal (OC) and glassy crystal (GC). Transition temperatures are evaluated from the heating data with the onset method and abbreviations are noted.

Following the different possible transitions introduced with figure 2.4, here figure 4.8 presents three characteristic DSC measurements corresponding to these transitions. Frame (a) shows a DSC mea-

surement of glycerol. Glycerol is a prime example of a glass-forming liquid and, consequently, in the DSC measurement during cooling only a step-like anomaly at temperatures between 180 and 190 K can be found, without indications of a crystallization at higher temperatures. During reheating from the glass state, the glass melts in a corresponding step-like increase with a characteristic over-shooting of the DSC curve at the upper edge of the step. The glass temperature can be obtained from the heating data with the onset method visualized in figure 4.8 with $T_g = 189\,\mathrm{K}$. For this method, the intersection of the interpolation of the temperature dependence of the heat flow below the glass transition and the interpolation of the temperature dependence at the point of inflection of the step-wise increase is determined.

In contrast to glycerol, succinonitrile (SN) (b) reveals two first-order transitions. During cooling, first the liquid crystallizes and a plastic crystal is formed, which later crystallizes into a fully ordered crystal (OC). The corresponding melting processes also show up in the heating measurement, where the OC melts at $T_m^o = 233\,\mathrm{K}$ and the PC melts at $T_m = 322\,\mathrm{K}$. Both the formation of the PC and the OC during cooling are crystallization processes and, thus, reveal supercooling effects, i.e., the eventual formation of the OC and the PC appears at temperatures below the thermodynamic phase transition temperature determined by the melting during heating. In this example, especially for the formation of the OC, this hysteresis is well pronounced.

Lastly, figure 4.8 (c) presents the peculiar example of a glassy crystal. During cooling, the SN-GN mixture [20] forms a PC much like pure SN, though noticeably this transition is shifted to lower temperatures. Upon further cooling, however, no second first-order transition is detected but the system exhibits a step-like anomaly similar to glycerol. This marks the orientational glass transition which arises from the glassy freezing of the reorientational degrees of freedoms of the molecules in the PC phase. The corresponding orientational glass transition with $T_m^o = 146\,\mathrm{K}$ and melting with $T_m = 295\,\mathrm{K}$ of the PC phase consequently occur upon heating.

5 Results and Discussion

This chapter presents the experimental results of both investigated material classes. For the DESs, results from dielectric and mechanical spectroscopy will be given for each liquid (glyceline, ethaline and reline) separately and afterwards all data will be compared in the conclusion. In the case of the PC electrolytes, the materials split into three types of mixture systems: dinitrile, cyclic alcohol and adamantane based. Here, the conclusion summarizes the key findings obtained from each binary mixture system.

5.1 Deep Eutectic Solvents

The three studied DESs are mixtures of the commonly used ChCl with the HBDs glycerol, ethylene glycol (EG) and urea in the mole composition 1 ChCl : 2 HBD. In literature, these liquids already obtained the trivial names glyceline, ethaline and reline, respectively [7]. The investigated liquids have a 33 mol% content of ChCl in common.

ChCl $[(CH_3)_3NCH_2CH_2OHCl]$ (see figure 5.1) is a quaternary ammonium salt and an alcohol. Importantly, it is non-toxic, even classified as provitamin, and cheap, because it is mass-produced as an animal feed supplement [4]. In solution with the HBDs, the choline ion and the chloride anion are dissociated and can move independently [13]. Pure ChCl cannot be measured in its liquid phase at ambient conditions, because it decomposes before it forms a liquid during heating.

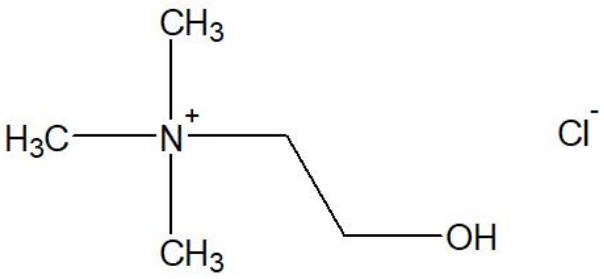

Figure 5.1: Chemical structure of ChCl.

The following results from dielectric spectroscopy on these systems were already published in the course of the present work (glyceline [53], ethaline and reline [54]).

5.1.1 Glyceline

Glycerol $[C_3H_5(OH)_3]$ is a colorless and non-toxic liquid with countless technical applications in, e.g., food and pharmaceutical industry. It is a hydrogen-bonded liquid with $T_m = 291\,K$ and $T_g \approx 189\,K$. Pure glycerol does not tend to crystallize easily and is widely regarded as a prime example of a glass-forming liquid, especially in the research field of dielectric spectroscopy [217]. Thus, comprehensive literature on the liquid dynamics of glycerol exist. Relevant for the present work are broadband dielectric data [218], temperature dependence of the the dipolar relaxation time [101] and viscosity data [207].

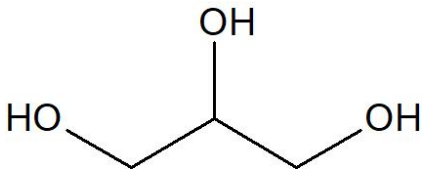

Figure 5.2: Chemical structure of glycerol.

In 2007 Abbott *et al.* [219] established the binary phase diagram of the glycerol with ChCl mixture. At the eutectic 1 ChCl : 2 glycerol mixture a melting point depression occurs from 291 K of pure glycerol to approximately 230 K. Simultaneously the viscosity decreases with increasing ChCl content (reported up until 33 mol%) [220]. Those changes are also reflected in a decreased glass temperature of $T_g = 175\,\mathrm{K}$, as clearly demonstrated in figure 5.3.

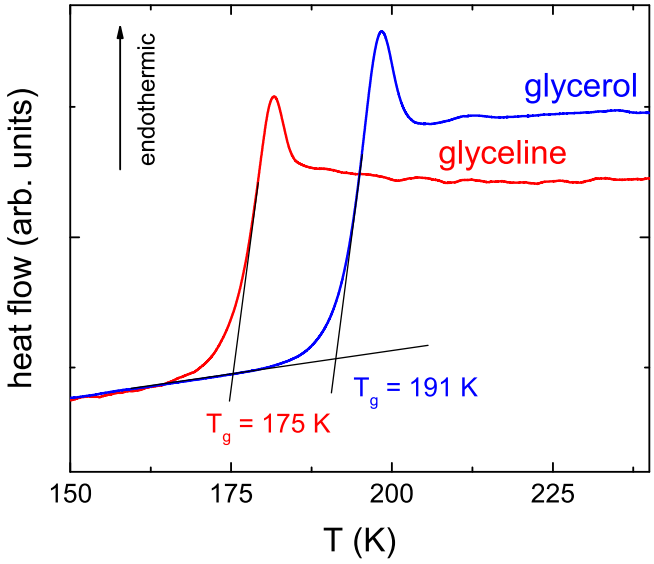

Figure 5.3: Calorimetric glass transition of glycerol (blue) and glyceline (red) as measured by DSC during heating with $10\,\mathrm{K\,min^{-1}}$ [54]. The onset evaluation method is visualized by the black solid lines and the obtained glass temperatures are noted.

Figure 5.4 presents the results from dielectric spectroscopy on glyceline [53]. Chosen representations are the dielectric constant ε', the dielectric loss ε'' and the conductivity σ'. The measurements were done in the frequency range from 1 to 10^9 Hz, thus combining the frequency response and the RF I-V method.

For temperatures $T \geq 209\,\mathrm{K}$, in ε' the spectrum is dominated by a huge step-like decrease, e.g., for $T = 245\,\mathrm{K}$ from approximately 10^6 to 30 in the range from 1 to 10^4 Hz. Such extremely large values in ε' clearly indicate a non-intrinsic origin and can undoubtedly be attributed to EP effects [117]. With increasing frequency, the EP steps are followed by another step-wise decrease from approximately 30 to 2, e.g., for $T = 209\,\mathrm{K}$ between 10^2 and 10^7 Hz (see inset). These steps continuously shift from higher to lower frequencies with decreasing temperature, thus mirroring the gradual slowing down of the structural relaxation of a liquid during the transition from the low-viscous to the glassy state. Hence, these steps can be identified as the α-relaxation of glyceline and arise from the collective reorientational dynamics of the dipolar glycerol molecules and the dipolar choline ions.

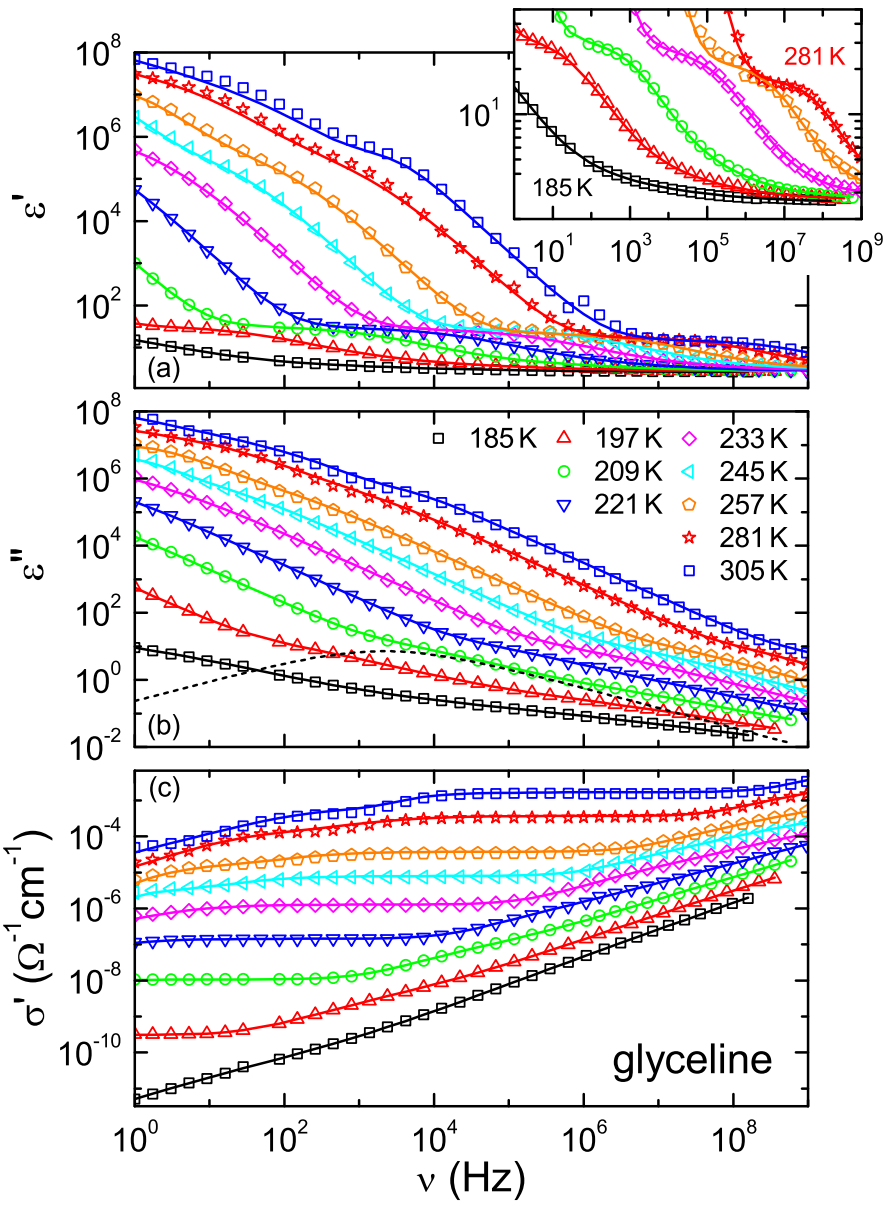

Figure 5.4: Dielectric spectra of ε' (a), ε'' (b) and σ' (c) of glyceline for various temperatures [53]. For selected temperatures, the inset in (a) magnifies the relaxation steps in ε'. The solid lines in (a) and (b) are fits with the equivalent circuit approach utilizing two distributed RC circuits, two CC relaxation functions and a dc-conductivity contribution (see text for details). For $T = 209\,\mathrm{K}$, the dashed line in (b) indicates the contribution of the α-relaxation. The lines in (c) are calculated via $\sigma' = \varepsilon'' \varepsilon_0 \omega$.

The α-relaxation, clearly visible in ε', should also lead to peaks in ε'', however, the high conductivity contribution largely superimposes these peaks. For temperatures $T \geq 209\,\mathrm{K}$, the ε'' spectrum shows a marked decrease with slope -1 in the double-logarithmic plot due to the dc conductivity, e.g., for $T = 221\,\mathrm{K}$ between 1 and $10^4\,\mathrm{Hz}$. Much like the α-relaxation in ε', the dc-conductivity contribution shifts continuously from higher to lower frequencies with decreasing temperature. Subsequently following the dc conductivity, at higher frequencies the data show a kink resulting in a flatter slope (e.g., for $T = 221\,\mathrm{K}$ at $10^4\,\mathrm{Hz}$). This change in slope is due to the right flank of the relaxation peak, which

emerges below the rapidly decreasing dc conductivity. In figure 5.4 (b) for $T = 209\,\mathrm{K}$, the contribution from the α-relaxation alone, as determined by the fitting routine, is visualized with a black dashed line. Near the high frequency limit, the black dashed line clearly drops below the data. This marks the presence of an additional faster relaxation or an excess-wing-like contribution, as known for pure glycerol [218], which becomes especially pronounced at the lowest temperatures $T = 197$ and $185\,\mathrm{K}$.

For the three highest temperatures at the low frequency side of the spectrum, the data deviate from the -1 slope of the dc conductivity. This deviation marks the onset of the EP region in ε''. σ' essentially presents the same data as ε'' due to $\sigma' = \varepsilon'' \varepsilon_0 \omega$, however, highlights more clearly the dc conductivity and the EP. In figure 5.4 (c) the data exhibit a large frequency-independent region (e.g., for $T = 245\,\mathrm{K}$ between 10^2 and $10^5\,\mathrm{Hz}$), called the dc-conductivity plateau. Right to the plateau the conductivity increases due to contributions from the relaxations and left to the plateau the conductivity decreases due to EP effects. The EP effects in this liquid lead to a double-step-like decrease (best visible for $T = 305\,\mathrm{K}$).

On this basis, ε' and ε'' were simultaneously fitted with the equivalent circuit approach. The EP region was described by two DRC circuits in series to the intrinsic contributions. For $T \leq 233\,\mathrm{K}$, the number of DRC circuits was reduced to one, because here the EP contributions have largely shifted out of the frequency window leaving only the onset of the effects visible. To account for the ionic conductivity of the sample, only a sole dc-conductivity contribution was implemented without complex ac-conductivity models. The α-relaxation was described by a CC function in contrast to the established usage of the CD function for pure glycerol [218]. This choice provided significantly better fits, which becomes especially visible in the inset of figure 5.4 (a), where the upper edge of the relaxations steps are significantly smeared out, a feature the CC function can better account for than the CD function. α-relaxation times as obtained from the fits of the permittivity data will be name τ_ε in the following to differentiate them from relaxation times determined in the modulus representation. Additional faster relaxations or a possible excess-wing contribution were modeled by an additional CC function. Altogether, the fitting routine provided a good description of the experimental data and from it precise values for the dc-conductivity and the α-relaxation time were obtained.

In this interpretation of the dielectric spectra the step in ε' and the intrinsic frequency dependence of σ' is generated by the reorientational dynamics of the glycerol molecules and the dipolar choline ions. As introduced in chapter 3.2.6, the spectral shape of highly ionically conducting liquids may be interpreted as either a dc conductivity plus relaxation combination or a dc to ac conductivity sequence. In the case of glyceline, where 66 mol% of the sample are dipolar molecules, a total absence of a dipolar relaxation contribution seems highly unlikely. Still figure 5.5 compares the fits obtained from the two different scenarios for glyceline at $T = 221\,\mathrm{K}$. As already shown in figure 5.4, the equivalent circuit approach with a CC function to describe the α-relaxation, a dc conductivity contribution and a DRC circuit to account for the EP effects is able to describe the data very well. For the ac conductivity scenario, now the dc conductivity and the CC function are replaced by the RBM model [164] in which an additional ε_∞ contribution is included. For both fits, the same parameters of the DRC circuit are used.

As rather expected, the RBM model, which exclusively considers translational ion motions, is not able to describe the step in ε' and the increasing conductivity in σ'. Thus, it further indicates that this spectral feature marks the reorientational α-relaxation of glyceline. A combination of ion hopping model and relaxation function, as applied by some authors for ionic liquids (e.g., [170]), also seems not justified due to the excellent fitting result of the sole CC function.

Since the modulus is the standard representation of mechanical relaxation data, here the dielectric

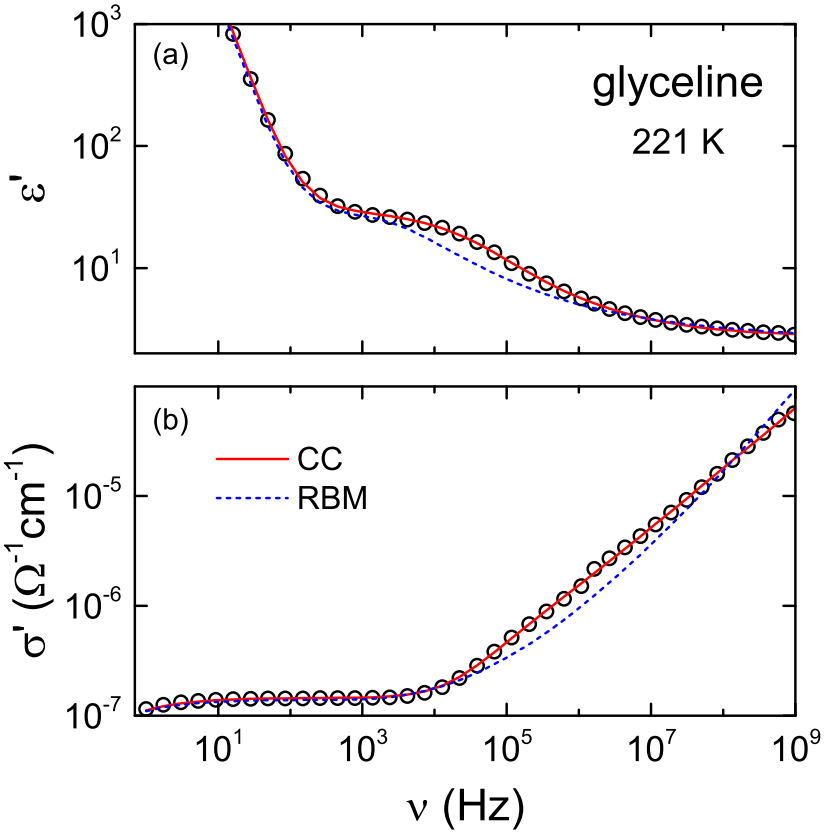

Figure 5.5: Frequency dependence of ε' (a) and σ' (b) of glyceline for $T = 221\,\mathrm{K}$. The solid red line is the same fit as shown in figure 5.4 for $T = 221\,\mathrm{K}$. For the blue dashed line, in the equivalent circuit, the CC function and the dc conductivity were replaced by the RBM from 2008 [164] with an additional ε_∞ contribution.

modulus of glyceline shall be investigated as well (see figure 5.6). In M' the data exhibit a continuous increase with increasing frequency. Here, a distinct region of constant slope (e.g., for $T = 233\,\mathrm{K}$ between 10^3 and $10^5\,\mathrm{Hz}$) separates the intrinsic and extrinsic contributions. For each temperature, the lower end of the region of constant slope approximately coincides with the onset of the huge EP step in ε', thus marking all data left of it as heavily influenced by EP effects. Above the region of constant slope, M' reveals a double-step-like behavior. These double-steps are accompanied by a broad peak in M'', which reveals asymmetric broadening and a shoulder on its left flank. Similar to the α-relaxation in the permittivity, this peak shifts continuously to lower frequencies with decreasing temperature. Additionally the peak maximum occurs at a roughly one decade higher frequency than the peak in ε'' (see $T = 209\,\mathrm{K}$). It was shown that a relaxation, marked by a step in ε' and a peak in ε'', also leads to a peak in M'', which is significantly shifted to higher frequencies [180, 221]. Thus, the maximum of the peak in M'' can be attributed to the reorientational α-relaxation of glyceline.

According to the picture of the conductivity relaxation proposed by Macedo *et. al.* [179] a peak arising from the translationally moving ions inside the liquid should emerge additionally in the spectrum. And indeed, the observed peaks in M'' clearly reveal a shoulder on their left flank, which may be interpreted as a second peak somewhat submerged below the main peak. Hence, the modulus spectrum is a composition of a conductivity relaxation with conductivity relaxation time τ_σ and the signature of a dipolar relaxation in the modulus representation with relaxation time τ_M, as indicated in figure 5.6

(b). This interpretation is well supported by findings by Köhler *et. al.* [180], who studied a series of lithium chloride (LiCl) with glycerol mixtures, ranging from 0.1 to 20 mol% amount of LiCl. For small amounts of ions the M'' spectrum revealed two well separated peaks due to conductivity and dipolar relaxation and with increasing amount of ions the peak positions continuously merged. According to this interpretation, the present modulus spectra were fitted with a combination of two CD functions adapted for the modulus (equation 3.41) and obtained were τ_σ and τ_M values.

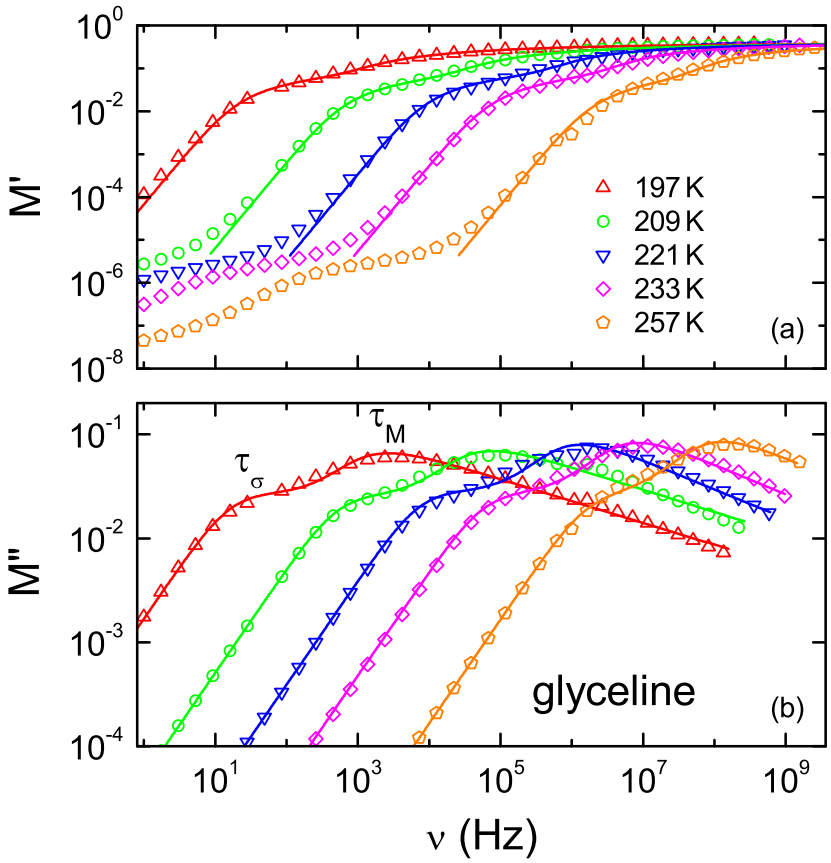

Figure 5.6: Frequency dependence of the real M' (a) and the imaginary M'' (b) dielectric modulus of glyceline for selected temperatures as calculated from the data shown in figure 5.4. Solid lines are fits using two CD relaxation functions adapted for the modulus representation (equation 3.41). For $T = 197\,\mathrm{K}$, the separate ionic and dipolar contributions are denoted as τ_σ and τ_M, respectively.

For mechanical spectroscopy, the modulus representation is the standard way of presenting the data. Figure 5.7 shows the G' and G'' spectrum of glyceline for selected temperatures between 174 and 190 K. The data reveal the commonly expected mechanical response of a liquid according to the Maxwell model as introduced in chapter 3.3.2. In log-log representation, with increasing frequency G' continuously increases until smoothly approaching the G_∞-plateau at the highest frequencies. Accordingly, G'' exhibits a broadened peak with the peak position coinciding with the transition from constant increase to G_∞-plateau in G'. This peak corresponds to the structural α-relaxation of glyceline and from the peak positions the relaxation time τ_G can be obtained. These findings highlight the fundamental difference of the dielectric and the mechanical spectroscopy. While dielectric spectroscopy is simultaneously sensitive to both ionic translational and dipolar reorientational motion, thus revealing two peaks in M'',

mechanical spectroscopy measures the collective translational diffusion of all constituents of the liquid, hence exhibiting only one broadened peak in G''.

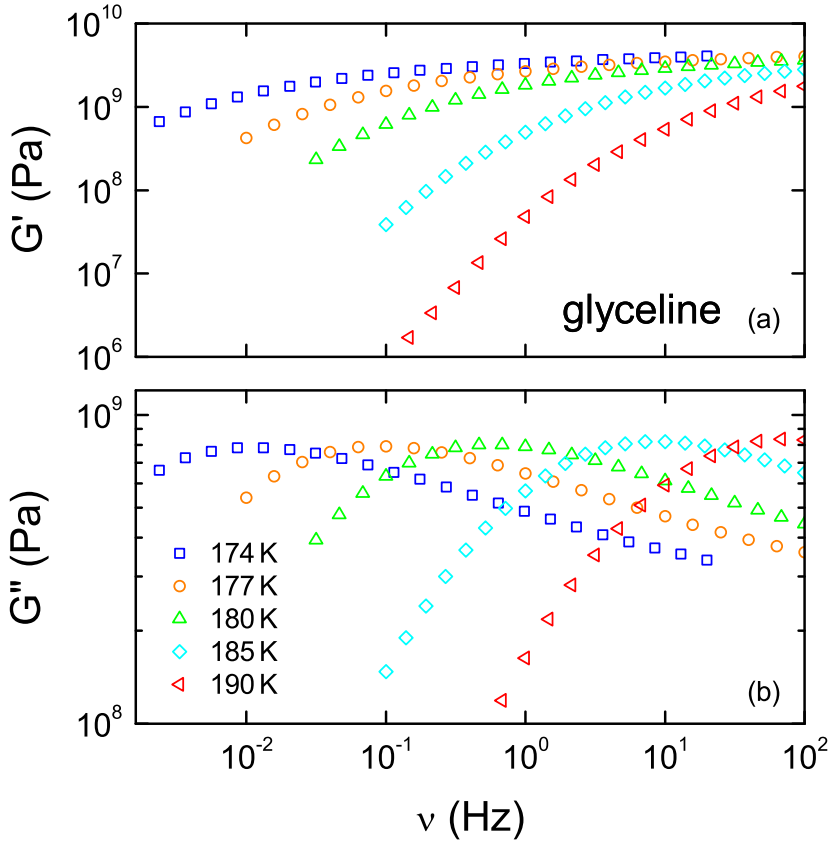

Figure 5.7: Spectra of the real G' and the imaginary G'' mechanical modulus of glyceline for selected temperatures as measured with plate size $r = 4\,\text{mm}$.

According to Schröter and Donth [207], in pure glycerol relaxation times τ_J obtained from the compliance representation better match the dielectric relaxation times τ_ε. To check for a similar systematic in glyceline, figure 5.8 presents the mechanical compliance of glyceline. The data reveal the general schematic introduced in chapter 3.3.2: a step like decrease in J' arising from the structural relaxation and a continuous decrease in J'' as superposition of steady-state flow viscosity η_0 and relaxation peak.

Unlike in dielectric spectroscopy, the rather limited frequency range of rheological measurements does not enable a continuous observation of the complete relaxation steps in J' over a broad temperature range. The lower temperatures $T \leq 183\,\text{K}$ only reveal the right hand side of the relaxation step eventually approaching J_∞, while at higher temperatures $T \geq 190\,\text{K}$ the left hand side and the upper plateau of the step become visible. Only at the intermediate temperature $T = 185\,\text{K}$ the whole evolution of the relaxation step in J' was measured. For all temperatures, J'' exhibits a continuous decrease with a hardly visible kink in the slope coinciding with the point of inflection of the steps in J'. Much like the peaks in G'', the relaxation steps in J' shift continuously to lower frequencies with decreasing temperature, thus, mirroring the slowing down of the liquid's structural relaxation during cooling. Consequently, these steps can be identified as the appearance of the structural α-relaxation in the compliance representation and the corresponding relaxation time may be denoted τ_J.

Due to the rather limited frequency range and,hence, the incomplete measurement of the relaxation step in J' at most temperatures, for simultaneous fits of J' and J'' according to equation 3.61, constant

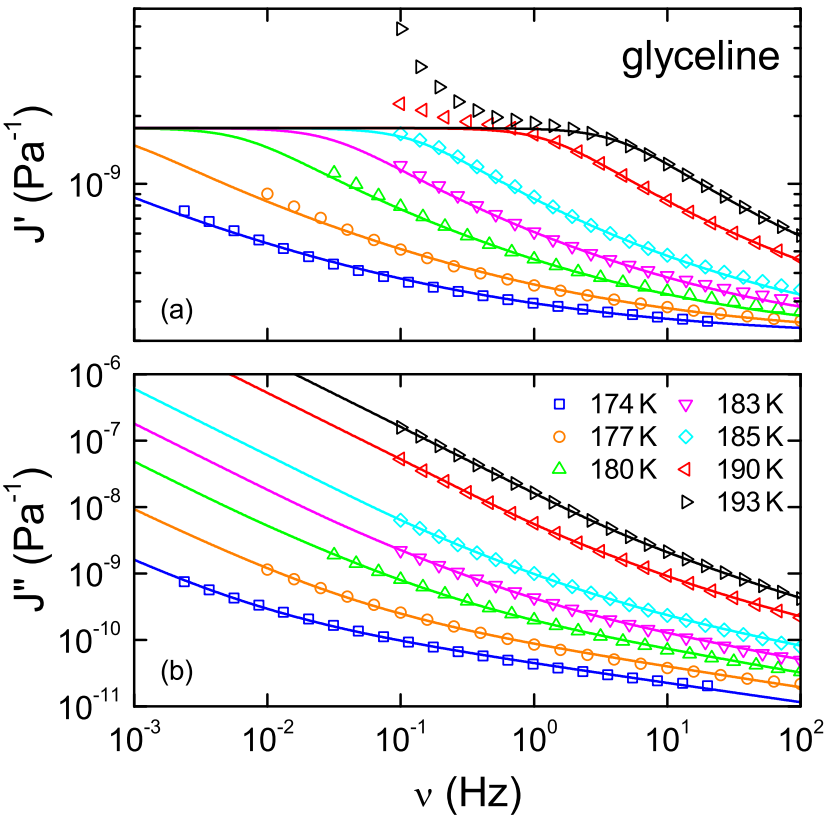

Figure 5.8: Real J' (a) and imaginary J'' (b) mechanical compliance of glyceline for all temperatures measured with plate size $r = 4\,\text{mm}$. Solid lines are fits using equation 3.61 (see text for details).

values of J_∞ and ΔJ for all temperatures had to be assumed. Thus, the fits (solid lines in figure 5.8) converge at the upper plateau of the relaxation step in J'. For the other three parameters the fitting routine revealed: a monotonously decreasing β from 0.4 to 0.29 from the highest to the lowest temperature, continuously increasing relaxation time τ_J and steady-state flow viscosity η_0 with decreasing temperature mirroring glassy freezing.

Alternatively, the construction of a so-called master curve on basis of the time-temperature superposition principle is a common procedure in the evaluation of mechanical spectroscopy data [200, 211, 222]. For the α-process of many glass-forming liquids the time-temperature superposition holds, which implies that the shape of the response function of the α-process does not change during cooling but only its characteristic time and amplitude [222]. As long as this principle holds, frequency-dependent measurement data from different temperatures can be horizontally shifted to largely overlap with the data of a specified reference temperature T_{ref} and to compose a master curve, which mimics the course of the α-process of T_{ref} over a significantly expanded frequency range.

Such master curve was constructed for glyceline in the compliance representation for $T_{\text{ref}} = 190\,\text{K}$ (see figure 5.9). The master curve, composed from all data presented in figure 5.8, reveals a continuous evolution of the α-process over the expanded frequency range. In principle the master curve for $T_{\text{ref}} = 190\,\text{K}$ should be equal to a measurement over the same expanded frequency range at $T = 190\,\text{K}$ as long as the time-temperature superposition holds. Hence, also the fit for $T = 190\,\text{K}$ from figure 5.8 should describe the master curve in good approximation, which figure 5.9 clearly demonstrates. The fit according to equation 3.61 does well account for the upper edge of the relaxation step in J' and the

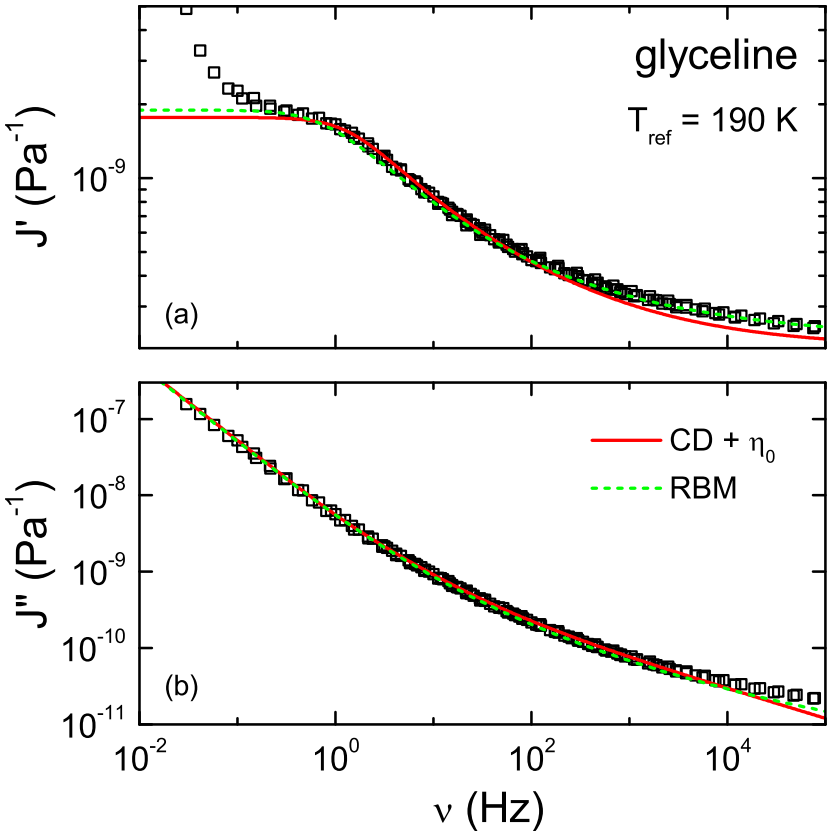

Figure 5.9: Constructed master curve of the mechanical data of glyceline as measured with plate size $r = 4\,\mathrm{mm}$ shown for the real J' (a) and imaginary J'' (b) mechanical compliance. $T = 190\,\mathrm{K}$ was used as reference temperature. Solid red line is the same fit as shown in figure 5.8 for $T = 190\,\mathrm{K}$, dashed green line is a fit using the adapted RBM model (equation 3.62).

steady-state shear viscosity region in J''. Only approaching J_∞ in J' and at the highest frequencies in J'', the fit drops below the data. This reflects the decreased broadening parameter β used for the fits in figure 5.8 at the lowest temperatures and, hence, is an indication of a non-perfect time-temperature superposition in glyceline or the presence of an additional faster relaxation process.

Alternatively, the master curve can be fitted with the modified RBM model (see equation 3.62) and the fit describes the data in good approximation, confirming the schematic identified by Bierwirth *et al.* [211]. The relaxation times obtained from either the CD function for $T = 190\,\mathrm{K}$ or the RBM fit of the master curve are approximately equal ($\tau_{\mathrm{RBM}} = 0.05\,\mathrm{s}$ and $\tau_{\mathrm{CD}}\beta_{\mathrm{CD}} = 0.04\,\mathrm{s}$). With this relaxation time and the applied shifting factor of each temperature in the master curve, the temperature dependence of the relaxation time can be calculated. In the end, the calculated relaxation times are effectively equal to the relaxation times obtained from the individual fits in figure 5.8.

Both methods demonstrated here aim to overcome the problem of the restricted frequency range and to derive relaxation times in a larger frequency range. On the one hand, fitting of the normal compliance spectra (figure 5.8) requires to fix J_∞ and ΔJ in the fitting routine. On the other hand, the master curve assumes time-temperature superposition and calculates relaxation times via a shifting factor.

With the many different relaxation times evaluated in the analysis of the dielectric and mechanical data of glyceline, figure 5.10 gives a comprehensive comparison. The dielectric permittivity relaxation time τ_ε [53] arises from the reorientational dynamics of the dipolar glycerol molecules and choline

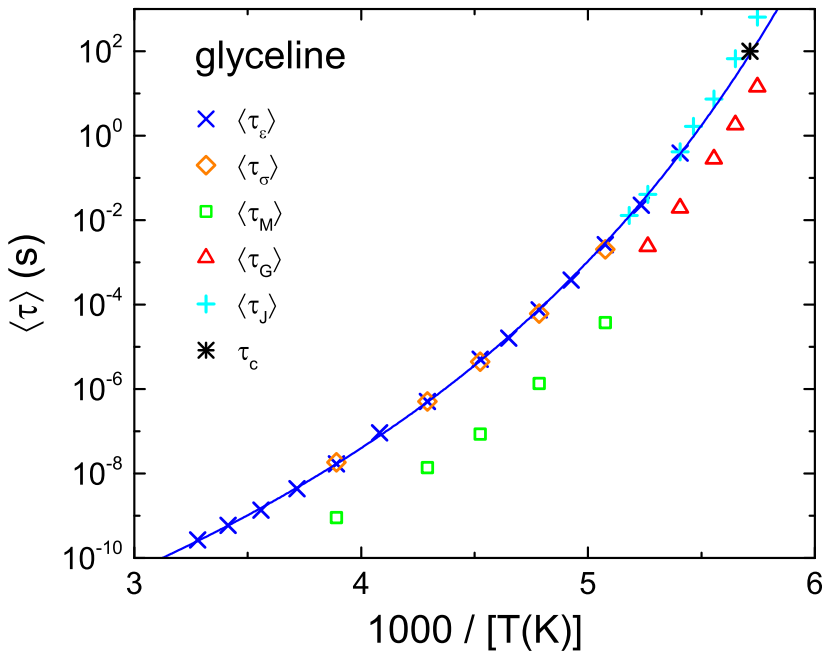

Figure 5.10: Arrhenius representation of the different average relaxation times of glyceline: dielectric permittivity τ_ε (blue crosses) [53], dielectric modulus conductivity τ_σ (orange diamonds), dielectric modulus dipolar τ_M (green squares), mechanical compliance τ_J (cyan pluses) and mechanical modulus τ_G (red triangles). Solid blue line is a fit of τ_ε with the VFT formula (see [54] for fit parameters). Black star is derived from the T_g of the DSC measurement via $\tau(T_g) = 100\,s$.

ions and exhibits non-Arrhenius behavior. A VFT fit of the data delivers a strength parameter $D = 21.3$ [54], making glyceline more fragile than pure glycerol ($D = 15.8$ [101]). At $\tau = 100\,s$ the fit, as interpolation of τ_ε, coincides with the relaxation time τ_c determined from the calorimetric DSC measurement (estimated via $\tau(T_g) = 100\,s$).

The corresponding modulus dipolar relaxation time τ_M is shifted to smaller relaxation times by roughly two orders of magnitude, in accordance to ref. [180, 221]. Interestingly, the conductivity relaxation time τ_σ closely matches τ_ε. However, Köhler *et. al.* [180] demonstrated in a series of LiCl with glycerol mixtures, that τ_σ and τ_ε progressively merge with increasing LiCl content, mainly because of the increasing ion density and the resulting increase of dc conductivity. Thus, the conductivity relaxation time depends on the density of charge carriers while the dipolar relaxation time τ_ε does not depend on the dipole density, which marks another problematic in the straightforwards analysis of the peaks in the modulus representation. Hence, the close match of τ_σ and τ_ε in glyceline probably only reflects the high ion density in the liquid.

Finally, from the peak positions in figure 5.7 τ_G could be estimated and, compared to the other relaxation times, τ_G clearly drops below τ_ε and τ_c, but rather continues the trend of τ_M towards lower temperatures. At the same time, τ_J obtained from the fits of the compliance spectra (figure 5.8) well agrees with τ_ε. Even near T_g, τ_J closely matches the VFT fit of τ_ε. This separation of τ_G and τ_J mimics the separation of the two dielectric dipolar relaxation times, which can be explained with very similar spectral shape of ε^* and J^*. In both cases the real part reveals a step and the imaginary part a peak that is strongly superimposed by a contribution proportional to ν^{-1}.

Altogether, τ_ε, τ_J and τ_c reveal a consistent temperature dependence, which might indicate that they

provide the best estimate of the true structural relaxation time of glyceline. Compared to τ_ε and τ_J, τ_M and τ_G are shifted to shorter times by approximately a constant factor over the whole temperature range.

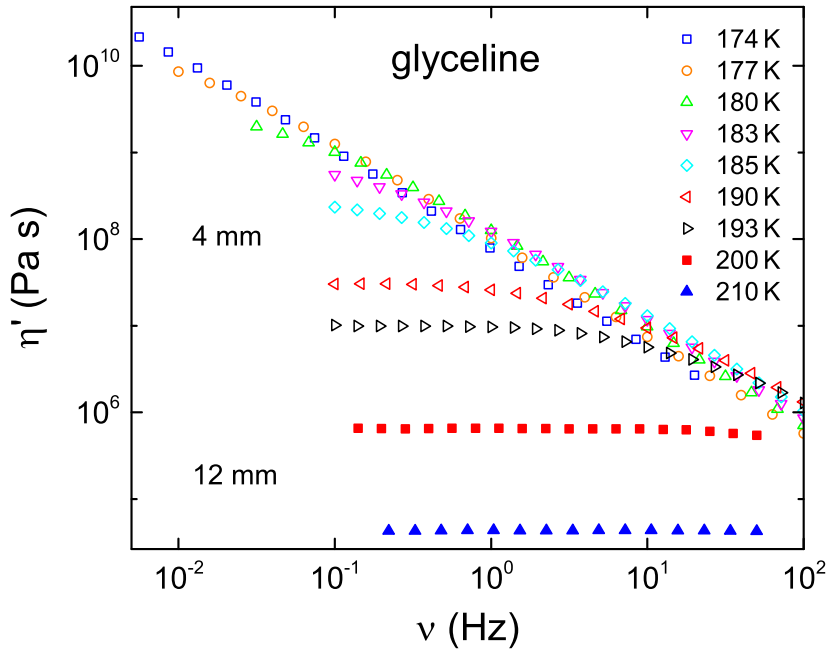

Figure 5.11: Real part of the viscosity of glyceline measured for $T \leq 193\,\mathrm{K}$ with a plate diameter of 4 mm (open symbols) and for $T \geq 200\,\mathrm{K}$ with a plate diameter of 12 mm (closed symbols).

So far the important steady-state flow viscosity η_0 has only shown up in the mechanical spectra as a contribution in J''. However, in contrast to the measurements of the dynamic response, η_0 can be measured over a larger temperature range by applying either a larger plate diameter or the rotation technique. Figure 5.11 presents the real part of the viscosity, where η_0 characteristically emerges as a plateau at lower frequencies. For the plate distance 4 mm, however, this plateau can only be undoubtedly identified for $T = 190$ and 193 K. The estimation of η_0 for the lower temperatures again relies on the time-temperature superposition and can be calculated via the shifting factors used to produce the master curve in figure 5.9. For the higher temperatures $T = 200$ and 210 K, on the other hand, with a plate diameter of 12 mm pronounced plateaus in η' could be measured. And further, for temperatures between 220 and 290 K, η_0 was determined with the rotation technique. The temperature dependence of η_0 will be presented a discussed in comparison with the results from the other liquids in chapter 5.1.4.

5.1.2 Ethaline

Figure 5.12: Chemical structure of ethylene glycol.

In comparison to glycerol, ethylene glycol (EG) $[(CH_2OH)_2]$ (or often named 1,2-ethanediol) is one

CH_2OH-group shorter. Unlike glycerol, EG can not easily be supercooled below it melting temperature of $T_m \approx 260\,K$. Still dielectric relaxation times for pure EG are available around T_m [223, 224] and near T_g [54, 225]. The latter were obtained by rapidly quenching the sample to temperatures well below its T_g, reheating the sample and measuring relaxation times until cold crystallization sets in. From the relaxation times of the quenched sample, the glass temperature of pure EG can be estimated to be $T_g \approx 154\,K$ [54].

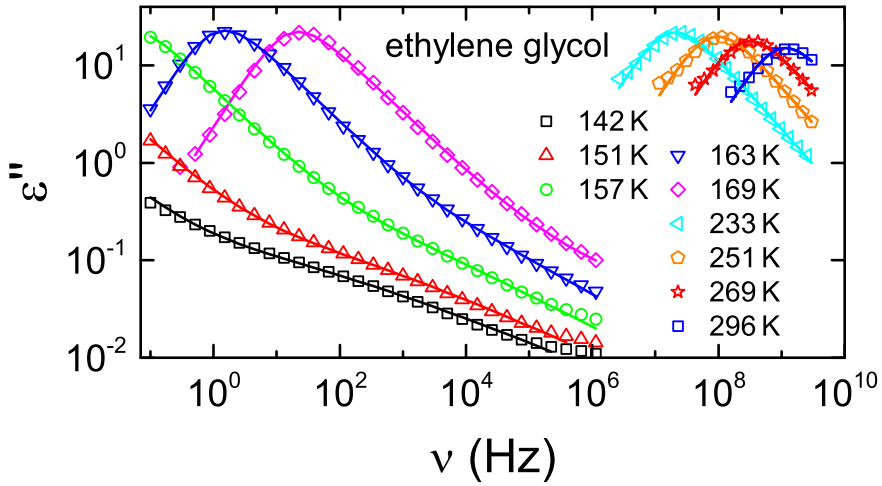

Figure 5.13: Dielectric loss spectrum of EG for various temperatures. Solid lines are fits with a single CD function for temperature $T \geq 233\,K$ and a combination of CD and CC function for $T \leq 169\,K$.

As both publications [54, 225] with relaxation times of pure EG near T_g do not have a dielectric spectrum included, figure 5.13 presents the dielectric loss spectrum of EG. ε'' of pure EG is dominated by a large loss peak at all temperatures above $T_g \approx 154\,K$. These loss peak shift from higher to lower frequencies with decreasing temperature and thus can be ascribed to the α-relaxation of EG. Characteristically the left flanks of these peaks are not broadened and all peaks could be described with a CD function. Due to the crystallization tendency of EG no dielectric data of liquid EG could be obtained in the temperature range between $T = 169$ and $233\,K$. For temperatures below this gap, on the right flank of the α-relaxation peaks an additional contribution arises, similar to the excess wing in glycerol [218]. However, below T_g this excess-wing-like contribution transforms into a rather distinct peak-like contribution and, for all temperatures below the gap, this faster relaxation process was modeled with an additional CC function.

The interpretation of the faster relaxation in EG, especially below T_g, is problematic because it was shown that rapidly quenched samples can display pronounced β-relaxations below T_g, which disappear irreversibly when heating above T_g [226], EG can only be prepared in its liquid state near T_g when rapidly quenched below T_g and subsequently reheated.

Ethaline is the eutectic mixure of EG and ChCl in composition $2:1$ [227], in straight analogy to glyceline. The DSC measurement (figure 5.14) reveals a glass temperature of $T_g = 155\,K$ for ethaline, which agrees well with the T_g of pure EG as estimated from the dielectric relaxation times. This equivalence of the glass temperatures of pure EG and ethaline stands in contrast to the findings for glycerol and glyceline and this difference will be further discussed in the comparison of all investigated DESs in chapter 5.1.4.

Figure 5.15 presents the results from dielectric spectroscopy on ethaline. The spectra reveal, in most

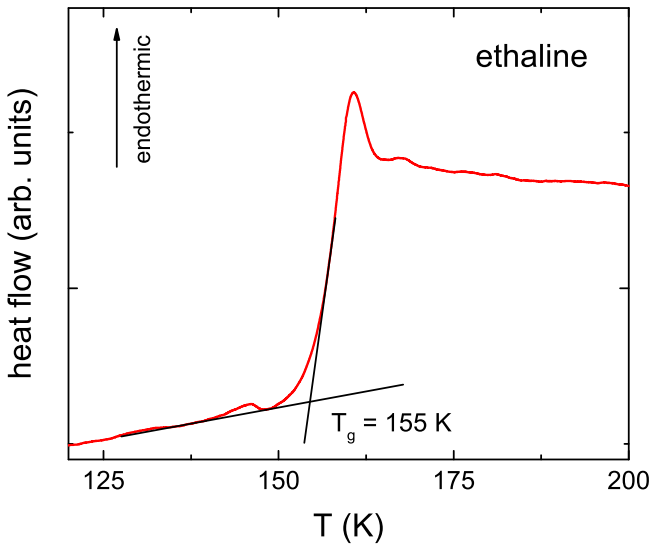

Figure 5.14: Calorimetric glass transition of ethaline as measured by DSC during heating with $10\,\mathrm{K\,min^{-1}}$ [54]. The onset evaluation method is visualized by the black solid lines and the obtained glass temperature is noted.

respects, qualitatively the same features as the glyceline dielectric spectra. EP effects arise as large step-wise decrease in ε' and as reduced conductivity in σ' compared to the σ_{dc}-plateau. In contrast to glyceline, however, the EP region of ethaline for $T \leq 284\,\mathrm{K}$ can be well described by only one DRC circuit in the fitting routine and only for $T = 350\,\mathrm{K}$, which is only shown in ε'' and σ', a second DRC circuit was necessary. The α-relaxation of ethaline likewise shows up as a second, smaller step in ε' at higher frequencies than the EP effects (see figure 5.15 (a) inset). For the description of the α-relaxation a CD function was used in accordance with ref. [54]. Much like for glyceline, the corresponding relaxation peak in ε'' is strongly superimposed by the dc-conductivity contribution and the isolated α-relaxation contribution ε'' for $T = 187\,\mathrm{K}$ is visualized in figure 5.15 (b) by a black dashed line. Interestingly, ethaline does not reveal indications of faster relaxation processes, as the whole spectrum in ε'' up to the highest frequencies and for the lowest temperatures can be described by the strongly broadened α-relaxation peak.

Thus, ethaline, similar to glyceline, exhibits a high conductivity contribution and an α-relaxation arising from reorientational dynamics of the dipolar EG molecules and the dipolar choline ions. The fitting routine was once again able to produce robust and reliable fit results, from which precise values of τ_ε and σ_{dc} were obtained.

In ethaline, like in any highly ionically conducting liquid, the dc conductivity strongly superimposes the relaxation peak in ε'' and, thus, the spectral shape also resembles the dc-to-ac conductivity pattern, discussed above. Figure 5.16 compares the CD fit from figure 5.15 with a RBM fit for ethaline at $T = 199\,\mathrm{K}$. Once again, the RBM fit is not able to describe the relaxation step in ε' and conductivity increase in σ', thus, further providing evidence for the correct interpretation of the step-wise decrease in ε' as reorientational α-relaxation.

The thorough analysis and comparison of the permittivity and modulus representation, as well as the obtained relaxation times for glyceline, have demonstrated that τ_ε provides a good estimate of the structural relaxation time in accordance with τ_{J} and the glass temperature determined with DSC. Due to simple mathematical relation $M^* = 1/\varepsilon^*$, the qualitatively very similar permittivity spectra of ethaline

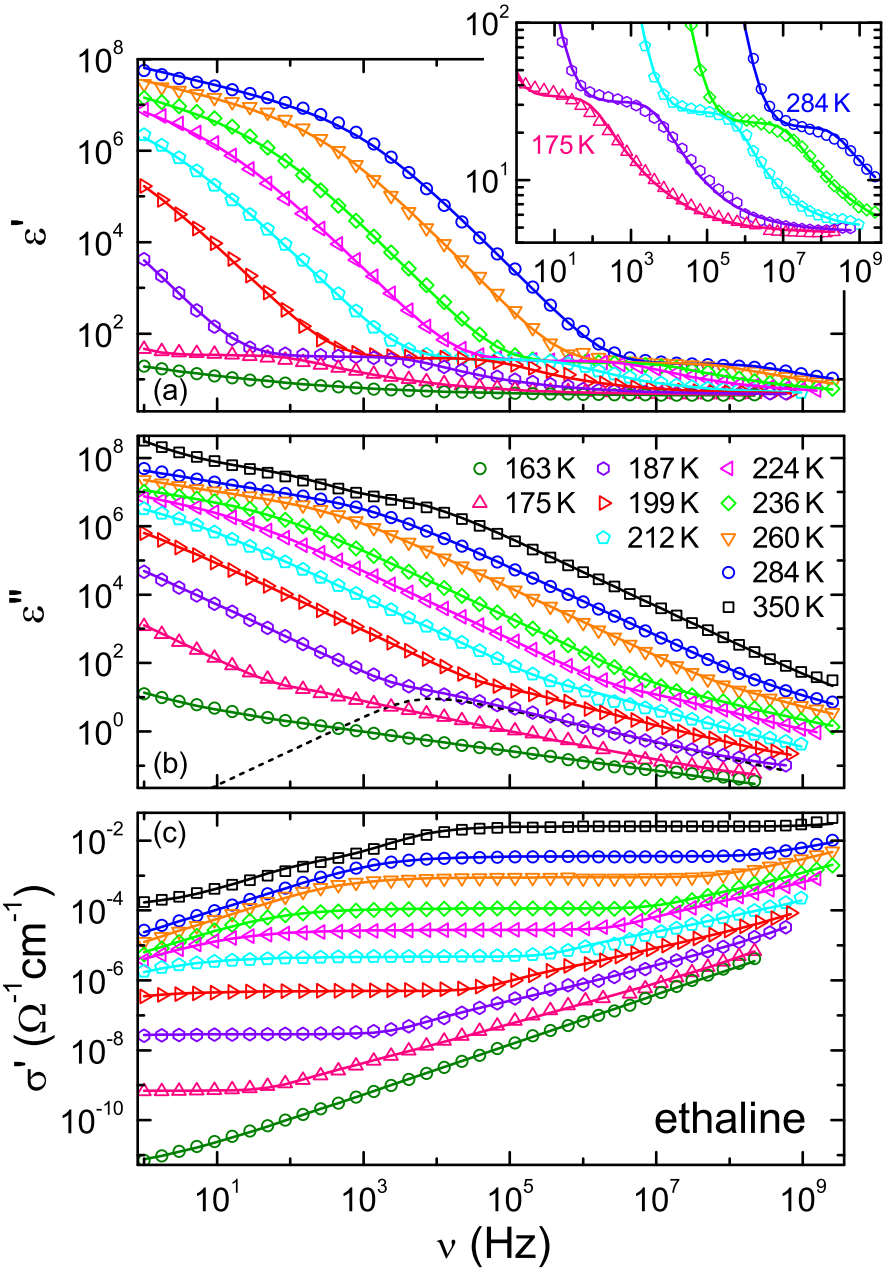

Figure 5.15: Dielectric spectra of ε' (a), ε'' (b) and σ' (c) of ethaline for various temperatures [54]. The inset in (a) magnifies the relaxation steps in ε' for some selected temperatures. The solid lines in (a) and (b) are fits with the equivalent circuit approach utilizing two distributed RC circuits, one CD relaxation function and a dc-conductivity contribution (see text for details). For $T = 187\,\mathrm{K}$, the dashed line in (b) indicates the contribution of the α-relaxation. The lines in (c) are calculated via $\sigma' = \varepsilon'' \varepsilon_0 \omega$.

(compared to glyceline) produce modulus spectra similar to the ones found for glyceline. Thus, the conclusions for glyceline may well be also applied to ethaline and τ_ε of ethaline will be used in the following comparison in chapter 5.1.4.

Ethaline itself unfortunately tends to crystallize much easier than glyceline and dielectric measurements had to be done with increased cooling rates to avoid crystallization during cooling. Such ten-

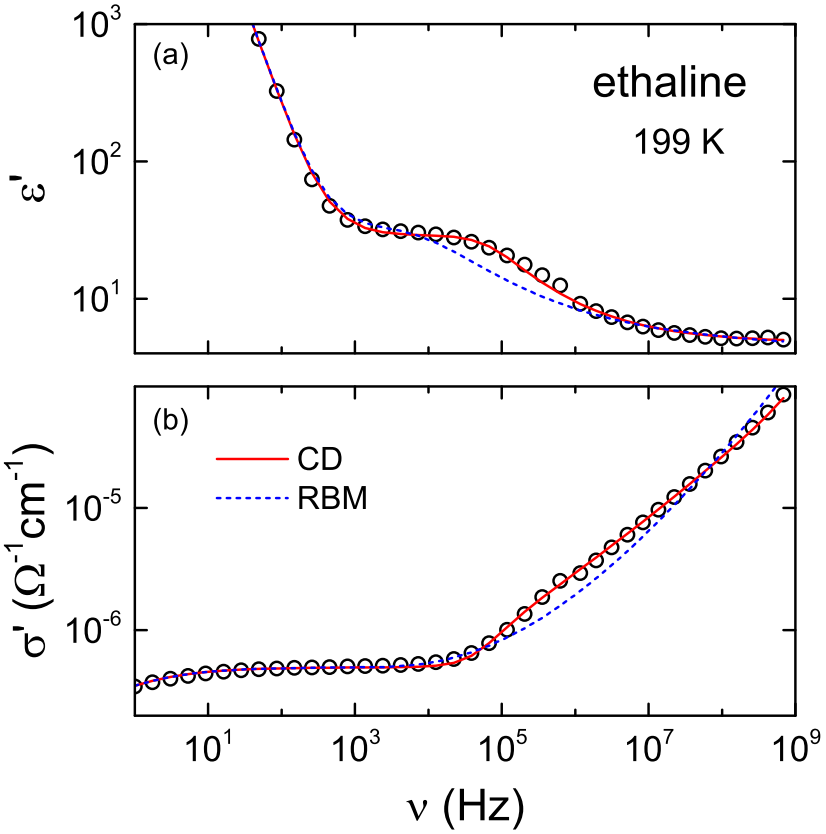

Figure 5.16: Frequency dependence of ε' (a) and σ' (b) of ethaline for $T = 199\,\mathrm{K}$ [54]. The solid red line is the same fit as shown in figure 5.15 for $T = 199\,\mathrm{K}$. For the blue dashed line, in the equivalent circuit the CD function and the dc conductivity were replaced by the RBM from 2008 [164] with an additional ε_∞ contribution.

dency to crystallize, however, produces greater experimental problems in dynamic rheology measurements, because the longer sweeping times and the constant mechanical deformation makes a crystallization of the liquid during the measurement more likely. Hence, for ethaline it was not possible to produce mechanical spectra in the temperature range approaching T_g, from which τ_J and τ_G could have been estimated. Only at some temperature with the rotation and the oscillation technique η_0 data were obtained, which will be discussed in the comparison in chapter 5.1.4.

5.1.3 Reline

Urea $[CO(NH_2)_2]$ is well known to be the main nitrogen-containing compound in the urine of mammals. In its pure form, it is a white crystalline solid at RT with a melting point of $T_m = 405\,\mathrm{K}$. Nowadays urea is mass-produced and commercially used especially in fertilizers for agriculture, as raw material for chemical industry and in pharmaceutics. Thus, it truly classifies as environmentally friendly and cheap material.

In one of the earliest works on eutectic mixtures with ChCl as ionic liquid analogue, Abbott *et al.* [13] reported the binary phase diagram of ChCl and urea. The eutectic point of this mixture lies at around 66 mol% urea (2 urea : 1 ChCl) with a melting temperature of $T_m = 285\,\mathrm{K}$ and this liquid was later named reline.

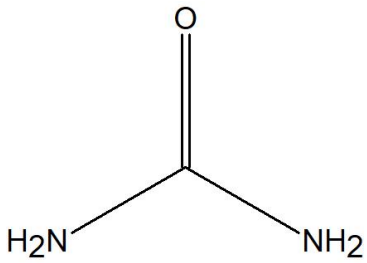

Figure 5.17: Chemical structure of urea.

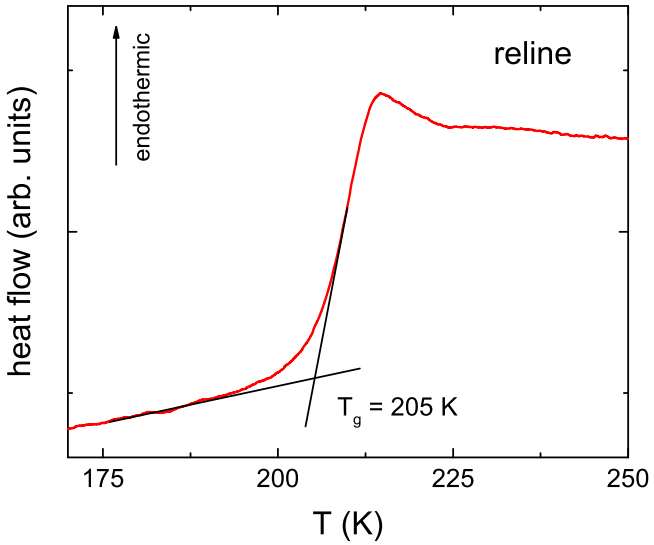

Figure 5.18: Calorimetric glass transition of reline as measured by DSC during heating with $10\,\mathrm{K\,min^{-1}}$. The onset evaluation method is visualized by the black solid lines and the obtained glass temperature is noted.

Unlike ethaline, reline does not tend to crystallize easily upon cooling below its T_m and a DSC measurement reveals a glass temperature of $T_\mathrm{g} = 205\,\mathrm{K}$. This is the highest T_g of the three DESs investigated in this work. In fact, the glass temperatures of the three DESs increase with increasing T_m of the pure HBDs:

- pure EG: $T_\mathrm{m} = 260\,\mathrm{K} \rightarrow$ ethaline: $T_\mathrm{g} = 155\,\mathrm{K}$,
- pure glycerol: $T_\mathrm{m} = 291\,\mathrm{K} \rightarrow$ glyceline: $T_\mathrm{g} = 175\,\mathrm{K}$,
- pure urea: $T_\mathrm{m} = 405\,\mathrm{K} \rightarrow$ reline: $T_\mathrm{g} = 205\,\mathrm{K}$.

The dielectric spectra of reline (figure 5.19) strongly resemble the previously presented spectra of glyceline and ethaline. ε' is largely dominated by the EP effects and, similar to ethaline, for temperatures between 236 and 302 K one DRC circuit was enough to describe the EP contributions in the fitting routine, while for the two highest temperatures an additional DRC circuit was used. Consequently, the EP effects lead to a pronounced decrease of the conductivity in σ' compared to the σ_dc-plateaus.

Once again, the step-wise decrease of $\varepsilon'(\nu)$ due to EP effects is followed by a small step at higher frequencies. Inset in Figure 5.19 (a) presents a zoomed in view on these steps. These steps can be attributed to the α-relaxation of reline arising from reorientational dynamics of the dipolar urea

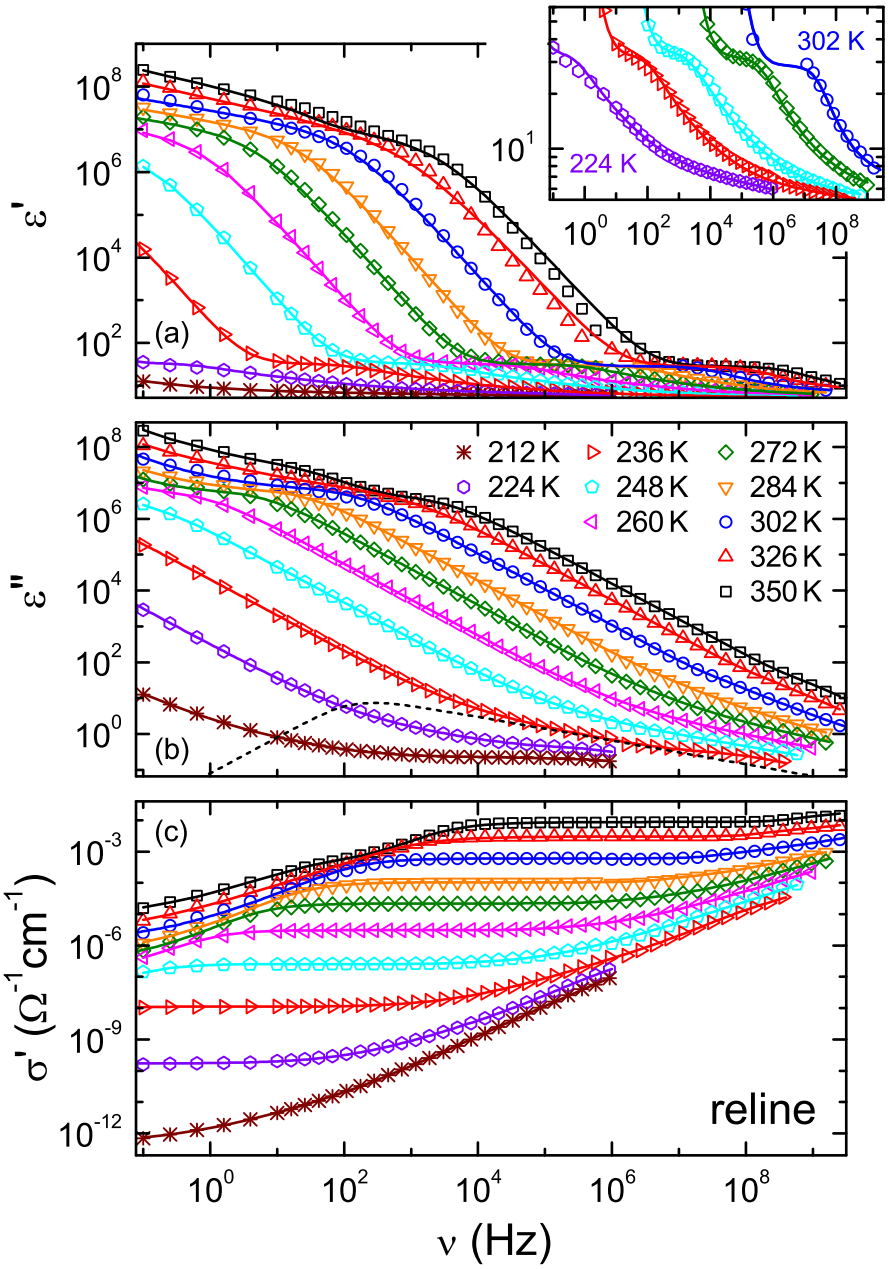

Figure 5.19: Dielectric spectra of ε' (a), ε'' (b) and σ' (c) of reline for various temperatures [54]. The inset in (a) magnifies the relaxation steps in ε' for some selected temperatures. The solid lines in (a) and (b) are fits with the equivalent circuit approach utilizing two distributed RC circuits, one CD relaxation function, one CC relaxation function and a dc-conductivity contribution (see text for details). For $T = 236\,\mathrm{K}$, the dashed line in (b) indicates the contribution of the α-relaxation. The lines in (c) are calculated via $\sigma' = \varepsilon'' \varepsilon_0 \omega$.

molecule and the dipolar choline ion, in accord with the interpretation of similar steps in glyceline and ethaline. In contrast to the previous examples, however, in reline the onset of EP effects and the α-relaxation steps ε' seem to be more closely merged. This merging becomes especially visible for $T = 236\,\mathrm{K}$, where, with decreasing frequency, hardly any distinct upper plateau of the α-relaxation step shows up before the steep increase due to EP sets in. Since the EP effects are dependent on the

geometry of the capacitor, in which the liquids were measured, it has to be noted, that ethaline and reline were measured with the same capacitor with same plate distance.

This peculiarity of reline is also reflected in the relaxation-peak position in ε''. While for glyceline and ethaline the peak maximum in ε'' roughly coincides with the change of slope of the data, which occurs at the transition from the dc conductivity to the relaxation dominated region, in the case of reline [see figure 5.19 (b) dashed line] the peak maximum is comparatively shifted to lower frequencies and lies well inside the dc conductivity dominated region. From the ε'' data alone, the height and position of the peak cannot be objectively estimated, though the relaxation step in ε' precisely determines the height and position of the peak.

Both, the almost submerged steps in ε' and the relative shift of the relaxation peak below the dc-conductivity contribution occur due to the same reason: For a given α-relaxation time, the dc conductivity is noticeably enhanced in reline compared glyceline and ethaline. This difference between the three liquids will be further investigated in chapter 5.1.4.

The dashed line in figure 5.19 (b) visualizes the contribution of the α-relaxation in ε''. At the very right flank of the peak, the dashed line clearly drops below the data, which indicates the presence of an additional faster relaxation process. This faster relaxation is especially visible for $T = 212\,\mathrm{K}$ between 10^3 and $10^6\,\mathrm{Hz}$ and is modeled by an additional CC function in the fitting routine. Mukherjee *et al.* [56] reported a dielectric measurement of pure urea in its liquid state at $T = 406\,\mathrm{K}$ and used a multi-Debye approach to fit the data. Such a multi-Debye fit may either account for the standard non-exponentiality of the dielectric relaxation of molecular liquids or may indicate the presence of a faster relaxation in pure urea, which then consequently is also, to some extent, present in reline.

As stated already, the occurrence of faster, so-called β-relaxations in the dielectric spectra of glass-forming liquids is a controversial and ongoing research topic. Tripathy *et al.* [16] observed two secondary relaxation processes in their study on acetamide based DESs. They interpreted those faster relaxations as a dipolar and an ionic Johari-Goldstein β-relaxation. The findings of the present work concerning β-relaxations in DESs are rather puzzling. Glyceline displays a β-relaxation, which is even stronger pronounced than the excess wing in pure glycerol. Ethaline reveals no faster relaxation although the α-relaxation of pure EG near T_g clearly possess an excess wing, which transforms into a pronounced β-relaxation below T_g (see figure 5.13). Reline, from all three systems, exhibits the most pronounced β-relaxation. However, here a comparison with pure liquid urea is hardly meaningful, because liquid urea can only be measured above 400 K, where the α-relaxation time is in the region of pico seconds, and glass-forming liquids usually only reveal distinguishable β-relaxations in the dielectric spectra when approaching T_g.

Additionally, in all three liquids, the α-relaxation does not solely arise due to reorientational motions of the HBD molecules but also the reorientational motions of the dipolar choline ions. It was shown that liquids consisting of two dipolar components often display an α-relaxation, which can be interpreted as a single (but broadened) relaxation process [228, 229]. Hence similar behavior may be concluded for the present DESs. Further, it seems reasonable that also possible faster relaxation processes are influenced by the presence of the dipolar choline ion and the purely ionic Cl^-. A more in-depth analysis of the faster relaxation processes in DESs is out of the scope of the present work, because they are presumably not inherently related to the ionic conductivity of the liquids. Thus, here only a phenomenological description of the observed phenomena shall be given.

As mentioned above, for a given α-relaxation time the corresponding dc conductivity is distinctly higher in reline than in glyceline and ethaline. This fact also becomes visible in the dielectric modulus representation (see figure 5.20). In general, the modulus spectra of reline resemble the modulus spectra

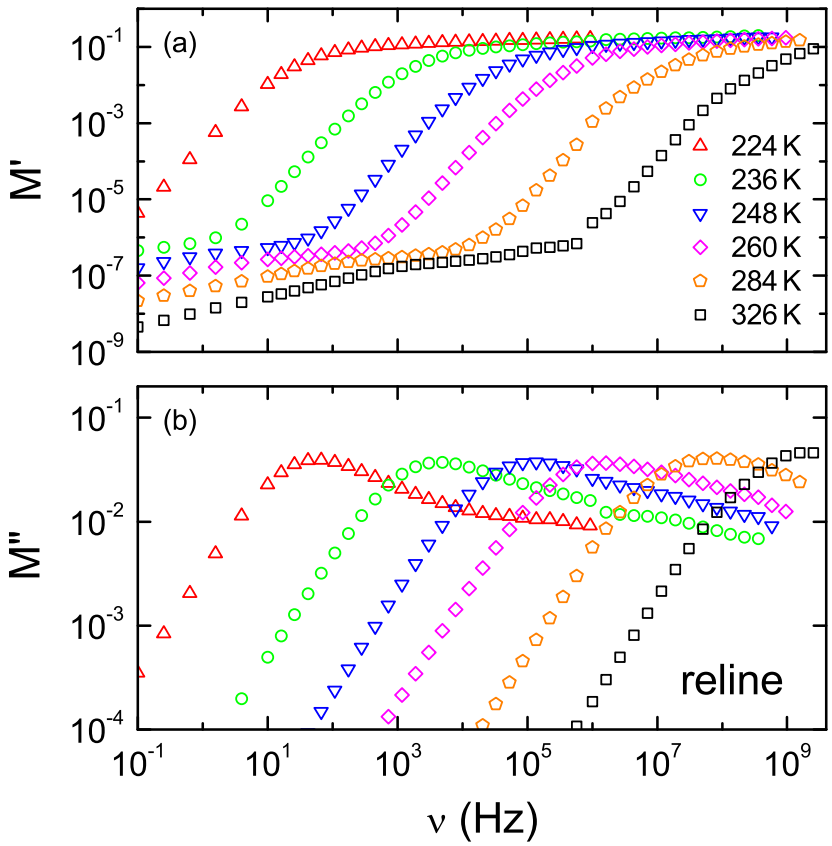

Figure 5.20: Frequency dependence of the real M' (a) and the imaginary M'' (b) dielectric modulus of reline for selected temperatures as calculated from the data shown in figure 5.19.

of glyceline (figure 5.6). In M' again a distinct region of constant slope arises (e.g., for $T = 260\,\mathrm{K}$ between 10^3 and $10^6\,\mathrm{Hz}$). Below this region the data are heavily influenced by EP effects and above this region M' smoothly approaches a plateau for all temperatures. Interestingly and in contrast to glyceline, no pronounced double-step like behavior when approaching the plateau in M' is visible. Correspondingly the M'' spectrum is dominated by a large broadened peak, however, without indications of a second peak submerged below the main peak.

In glyceline, the two peaks found in M'' were identified as the conductivity relaxation, arising due to translationally moving ions, and the emergence of the dipolar reorientational relaxation in the modulus representation. Obviously, both spectral features are to be expected to also occur in the modulus spectrum of reline, because reline also possesses translationally moving ions and dipolar molecules. However, figure 5.20 (b) only reveals one broadened peak. Thus, for reline it has to be assumed that the conductivity-relaxation peak has fully merged below the main dipolar relaxation peak and the resulting superposition of both peaks can not be distinguished from a single broadened peak. In the discussion of figure 5.24, a comparison of all different relaxation times estimated for reline, further evidence will be provided, that the peak position of the single peak found in M'' of reline is mainly determined by the dipolar relaxation and the conductivity relaxation is presumably indistinguishably submerged below it.

Figure 5.21 presents the comparison of the CD-function plus dc conductivity approach with the RBM as already provided for the other DESs. Interestingly and in contrast to the previous examples, in reline the RBM is able to describe the data equally well as the CD plus dc conductivity approach. In the RBM, the step height in ε' is determined by both the dc conductivity and the ionic relaxation time

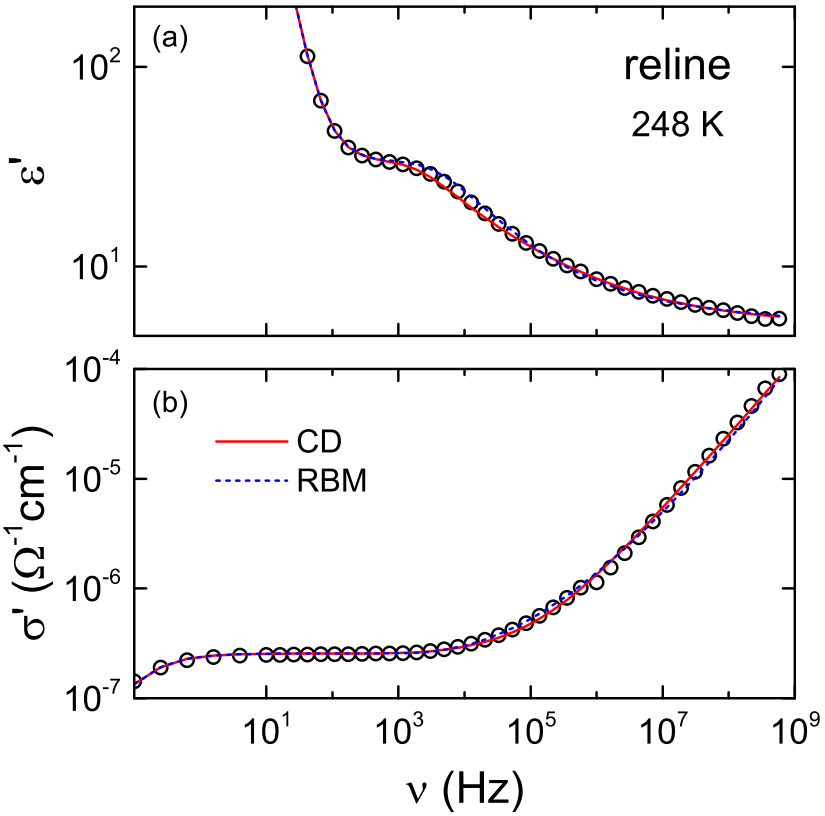

Figure 5.21: Frequency dependence of ε' (a) and σ' (b) of reline for $T = 248\,\mathrm{K}$ [54]. The solid red line is the same fit as shown in figure 5.19 for $T = 248\,\mathrm{K}$. For the blue dashed line, in the equivalent circuit, the CD function and the dc conductivity were replaced by the RBM from 2008 [164] with an additional ε_∞ contribution. The RBM fit was simultaneously performed for ε' and σ'.

τ_{RBM}. Obviously, this does not prove that the relaxation feature detected in reline purely stems from translational ionic dynamics, which is highly unlikely with 66 mol% dipolar urea molecules within the sample. It rather shows that the unusually high dc conductivity with respect to the relaxation time determined by the step in ε' creates a spectral form which can also be described by the RBM. From the dielectric data alone, one cannot differentiate whether the relaxation feature in reline is of fundamentally different physical origin than those in glyceline and ethaline and, here, supporting experimental results from, e.g., light scattering or nuclear magnetic resonance would be necessary.

The mechanical spectroscopy data of reline reveal similar results as those for glyceline. The thorough analysis of mechanical modulus and mechanical compliance for glyceline showed that the relaxation times τ_{J} obtained from the compliance representation better relate to the dielectric relaxation times τ_ε. Thus, here only the compliance spectra of reline and the compliance master curve will be discussed. Structural relaxation times τ_{G} from the mechanical modulus representation of reline were determined from the peak positions in the G''-spectrum and the temperature dependence of τ_{G} is shown in figure 5.24.

Figure 5.22 presents the real and imaginary part of the compliance of reline. Qualitatively, the mechanical response of reline is very similar to glyceline and fitting with equation 3.61 delivers a reasonable description of the data. Much like in glyceline, the restricted frequency range of mechanical spectroscopy requires to fix J_∞ and ΔJ during the fitting routine.

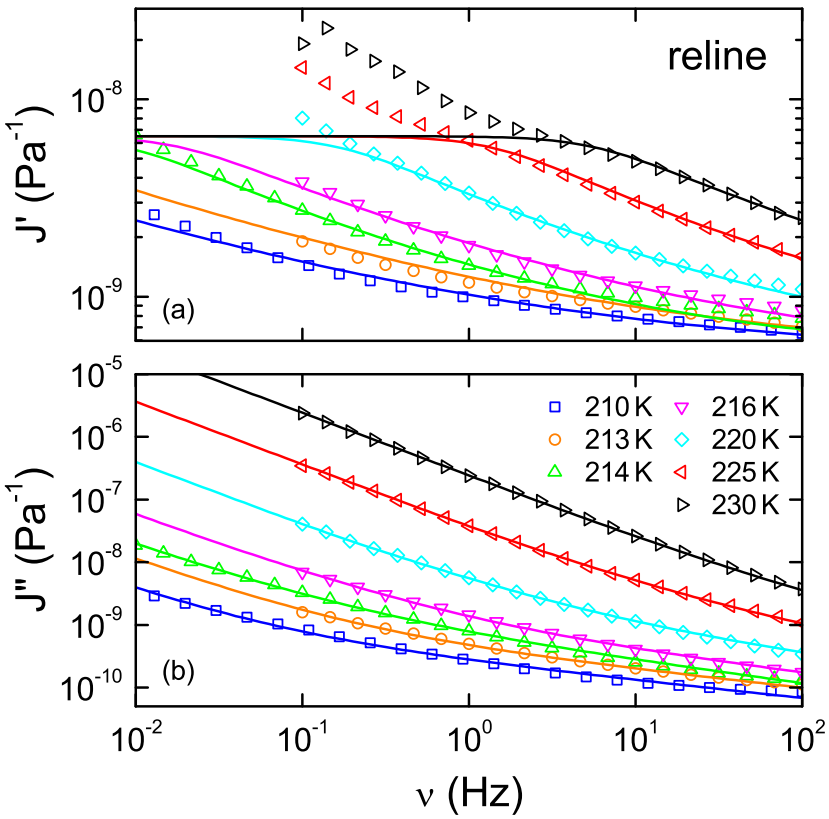

Figure 5.22: Real J' (a) and imaginary J'' (b) mechanical compliance of reline for all temperatures measured with plate size $r = 4\,\text{mm}$. Solid lines are fits using equation 3.61 (see text for details).

The master curve for $T_{\text{ref}} = 225\,\text{K}$ of reline (figure 5.23) displays a nearly prefect match of the data in J'' but rather noticeable deviations of the data at the upper edge of the relaxation step in J'. Still, the imported fit from figure 5.22 for $T = 225\,\text{K}$ is able to describe the master curve reasonably well. Only at the highest frequencies in J'' and at the lower edge of the relaxation step in J', the fit clearly deviates from the data, which might indicate the presence of an additional faster relaxation process for $T = 225\,\text{K}$ at around $10^5\,\text{Hz}$. This finding nicely agrees with the dielectric data, which display an faster relaxation process in the same frequency range at this temperature.

The RBM fit (equation 3.62) of the master curve reveals very similar results as the CD plus η_0 function with nearly equal relaxation times ($\tau_{\text{RBM}} = 0.03\,\text{s}$ and $\tau_{\text{CD}}\beta_{\text{CD}} = 0.04\,\text{s}$). Thus, for the following comparison in chapter 5.1.4, from the fits in figure 5.22 relaxation times τ_{J} and a calculated temperature dependence of η_0 via the shifting factors applied in figure 5.23 will be used.

With relaxation times determined from the dielectric and mechanical spectra of reline, figure 5.24 presents the same comparison of all different relaxation times as previously given for glyceline (see figure 5.10). The reorientational relaxation time τ_ε reveals a pronounced non-Arrhenius behavior and can be described reasonably well by a VFT fit (see ref. [54] for fit parameters). Like in glyceline, the structural relaxation times τ_{J} as obtained from the compliance representation closely coincide with τ_ε. A surprisingly large deviation of more than one order of magnitude is found for the calorimetric relaxation time τ_{c} estimated via the relation $\tau(T_{\text{g}}) = 100\,\text{s}$ from the glass-transition step measured in the DSC. For glyceline, this relation worked quite well and the calorimetric relaxation time coincided with the VFT fit of τ_ε.

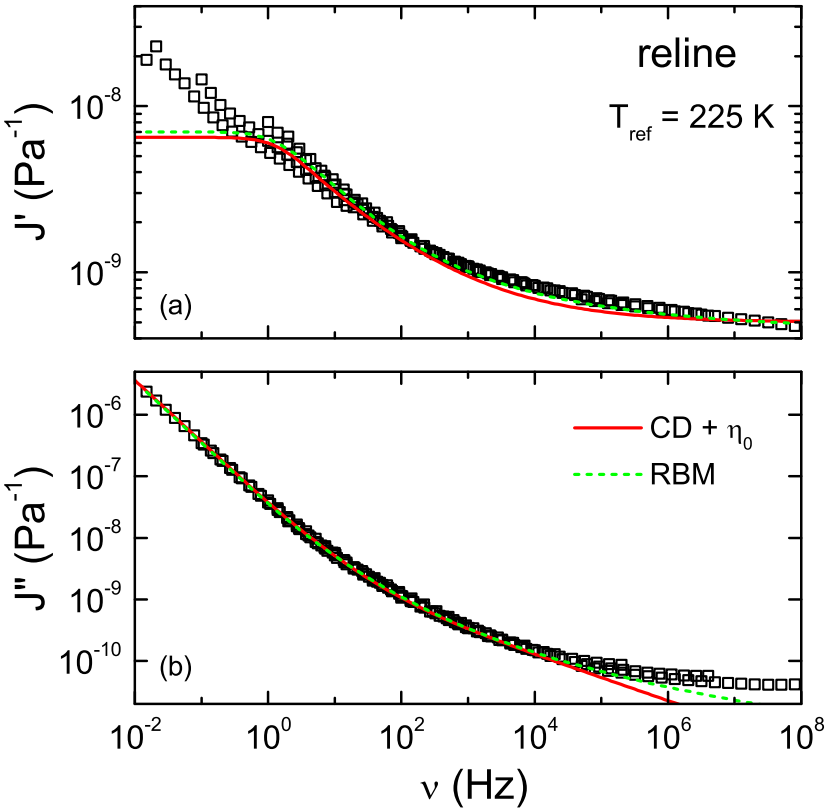

Figure 5.23: Constructed master curve of the mechanical data of reline as measured with plate size $r = 4\,\mathrm{mm}$ shown for the real J' (a) and imaginary J'' (b) mechanical compliance. $T = 225\,\mathrm{K}$ was used as reference temperature. The solid red line is the same fit as shown in figure 5.22 for $T = 225\,\mathrm{K}$ and the dashed green line is a fit using the adapted RBM model (equation 3.62).

Again, the structural relaxation time τ_G from the modulus representation is distinctly shifted to faster relaxation times when compared with τ_J. Importantly, the relaxation times as obtained from the single peak in the dielectric modulus representation (here denoted τ_M) are also shifted to faster relaxation times compared to τ_ε by a similar factor as τ_G when compared with τ_J. Therefore, τ_G roughly continuous the trend of τ_M down to lower temperatures.

Very similar behavior was found for glyceline, where the faster relaxation peak in the dielectric modulus representation could unequivocally be attributed to the dipolar reorientation. This strongly suggests that for reline the single relaxation peak in the modulus representation is mainly dominated by the dipolar relaxation contribution and the conductivity relaxation peak is submerged under this peak without significant influence on the peak position. Thus, both the case of glyceline and reline support the notion that relaxation times from mechanical and dielectric spectroscopy are best comparable when both analyzed in the modulus representation or in the permittivity/compliance representation.

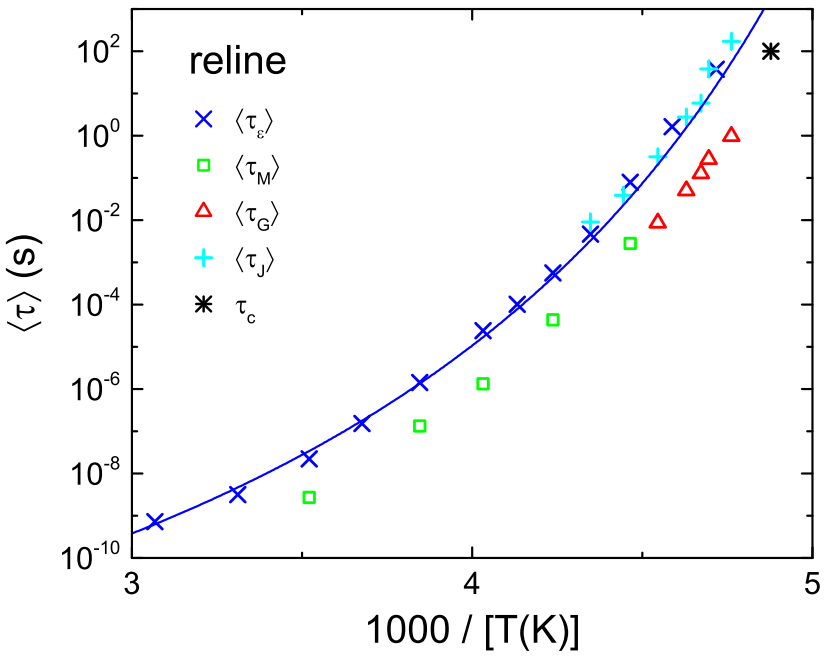

Figure 5.24: Arrhenius representation of the different average relaxation times of reline. The symbols and the line have the same meaning as in figure 5.10.

5.1.4 Conclusion

After a thorough investigation of the dielectric and mechanical spectra of the three DESs, in this chapter the absolute values of conductivity, relaxation times and viscosity of the different systems will be compared and the coupling of ionic and translational dynamics will be analyzed.

Figure 5.25 (a) presents the dc conductivity of glyceline, ethaline and reline in Arrhenius representation. The temperature dependence of the conductivity of all three liquids reveals strong deviations from Arrhenius behavior and can be described by a VFT fit. Previous studies [13, 220, 227] on the conductivity of these three liquids did not conclude a deviations from Arrhenius behavior due to rather restricted investigated temperature ranges, however, VFT behavior of σ_{dc} of other DESs has already been reported [8, 9, 16]. From the three systems, ethaline is the best conductor with a RT conductivity of $\approx 6\,\mathrm{mS\,cm^{-1}}$.

Similar to the dc conductivity, average reorientational α-relaxations times τ_ε of all three DESs [5.25 (b)] reveal strong deviations from Arrhenius behavior and the data can be well described by the VFT law. From the VFT fits of the relaxation times the strength parameter D characterizing the fragility of the liquids can be obtained and further from the strength parameter D the fragility index m via equation 3.5 can be calculated. The investigated DESs reveal: $m = 44$ for glyceline, $m = 61$ for ethaline and $m = 57$ for reline. This characterizes the three liquids as intermediate within the strong-fragile classification of liquids.

Further interesting insights can be obtained when comparing the relaxation times of the DESs with those of the pure HBDs. Relaxation times of molten ChCl are not available, since it has no stable liquid phase. Unfortunately in the case of urea, to the best of the authors knowledge, there is no successful investigation of the relaxation time of urea well below its melting temperature and, here, only a single relaxation time at $T = 406\,\mathrm{K}$ [56] can be given. Still, this relaxation time agrees well with the interpolation of the VFT fit of the relaxation times of reline.

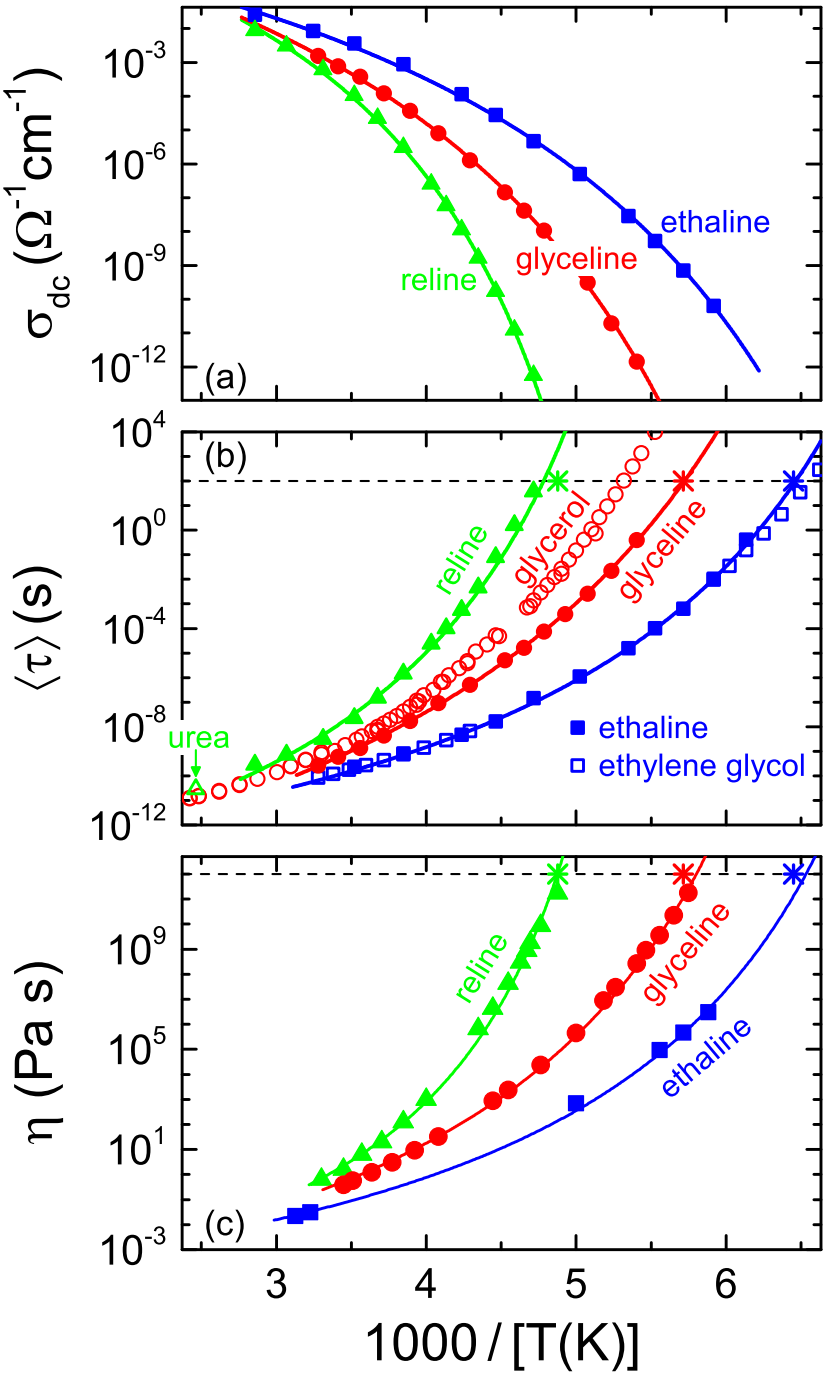

Figure 5.25: Dc conductivity σ_{dc} (a), reorientational relaxation times τ_ε (b) and steady-state flow viscosity η_0 (c) of the three investigated DESs in Arrhenius representation as obtained from the fits of the dielectric spectra and the J^* master curve [54]. The solid lines are fits with the VFT formula (equation 3.2) and its modification for the conductivity (equation 3.30) (fit parameters for (a) and (b) are given in ref. [54]). Open symbols in (b) are relaxation times of the corresponding pure HBDs: glycerol [101], ethylene glycol [54] and urea [56]. The horizontal dashed line indicates $\tau(T_g) = 100\,s$ in (b) and $\eta_0(T_g) = 10^{12}\,Pa\,s$ in (c). Stars are derived from T_g of the DSC measurements.

In the case of ethylene glycol and glycerol, on the other hand, an interesting phenomenon occurs. Glycerol exhibits as significantly increased relaxation time compared to glyceline and the difference gets further enhanced when approaching low temperatures, reaching a difference of several orders of magnitude at T_g of pure glycerol. In contrast, the addition of LiCl to glycerol was shown to slow down the reorientational dynamics of the mixture, thus, leading to the opposite behavior [180]. However, this present finding is supported by viscosity measurements of glyceline, which detected a decreasing viscosity with increasing ChCl amount in glycerol [220, 230], and the presented DSC measurements for pure glycerol and glyceline (chapter 5.1.1).

It is well known fact that the addition of a solute to a solvent can, depending on the type of solute, increase or decrease the viscosity of the solution compared to the viscosity of the original solvent. This phenomenon was summarized in the Jones-Dole equation, [231] in which the *B*-coefficient, representing solute-solvent interaction, can be positive or negative, i.e. the solute acts as a structure maker or structure breaker, respectively. For example, the *B*-coefficient of glycerol-salt mixtures is found negative or positive for different types of salts [232] and assuming a strong correlation of viscosity and relaxation time, this can rationalize the findings for glyceline.

However, a look at the ethaline to EG ratio further complicates the situation. In figure 5.25 the relaxation times of pure EG well agree with those of ethaline at high temperatures and fall slightly below those near T_g, an effect even more pronounced for relaxation times of pure EG estimated by Kremer *et al.* [225]. Still, Abbott *et al.* [230] measured a slight viscosity increase with increasing amount of ChCl in EG at RT. Hence, in the case of EG plus ChCl mixtures, the reorientation relaxation time may not change perfect proportionally with the viscosity. However, more important, the addition of ChCl to the two chemically very similar compounds EG and glycerol has opposite effects on the viscosity of the mixture. The different effect of the admixture of ChCl on the viscosity may be explained by the network structure of the two HBDs [54, 230]. EG with the two OH-groups forms rather linear aggregates of hydrogen-bonded molecules, while glycerol with three OH-groups builds a three dimensional hydrogen-bounded network, which is more susceptible to be broken up by the addition of ions.

Additionally, figure 5.25 (c) presents the steady-state flow viscosity η_0 of all three DESs. The data are collected from both the rotation, which directly delivers η_0 values, and the oscillation technique, where η_0 was determined for a reference temperature from the η' vs ν plot and the temperature dependence of η_0 was further calculated with the shifting factors used in the master curves. With this, for both reline and glyceline, η_0 vales were from the low viscous, high temperature region until near the glass transition. For ethaline, due to the crystallization tendency of the liquid, only some values were obtained. Still and as expected, η_0 mimics the temperature dependence of the reorientational relaxation times for all three DESs and can be fitted with a VFT law. The extrapolations of these fits reasonably agree with the glass temperatures estimated by DSC, here added to figure 5.25 (c) via the correlation $\eta(T_g) = 10^{12}\,\mathrm{Pa\,s}$.

Thus, all the measured dynamic processes, ionic translation (as represented by σ_{dc}), dipolar reorientation (τ_ε) and translational motion of all constituents (η_0), reveal non-Arrhenius behavior, which raises the question to what extent they are correlated or coupled. The natural way to check whether two processes are coupled or somewhat connected is to check whether they reveal the same activation energy. In the case of pronounced non-Arrhenius behavior, however, the activation energy seems to change with temperature. Hence, the temperature evolution of the activation energy has to be compared by plotting both quantities in the same Arrhenius plot.

Figure 5.26 presents such a comparison of the different dynamic process. τ_ε, τ_J, τ_c, ρ_{dc} and η_0 are plotted in Arrhenius representation in a common frame. $\rho_{dc} = 1/\sigma_{dc}$ is chosen over σ_{dc}, because it has

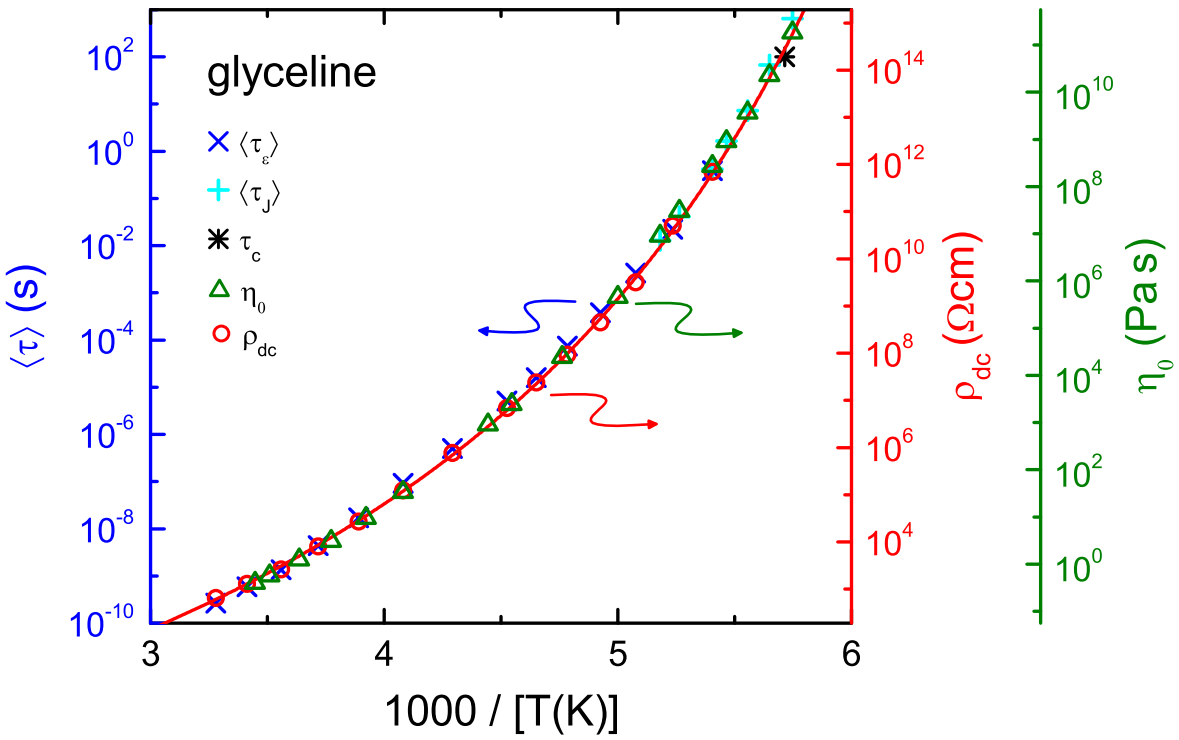

Figure 5.26: Comparison of the temperature dependence of translational and reorientational dynamics in glyceline [54]. The average reorientational α-relaxation times τ_ε from dielectric spectroscopy (blue crosses; left scale), the average structrual relaxation τ_J from the mechanical compliance (cyan pluses; left scale), the calorimetric relaxation from DSC (black star, left scale), the dc resistivity ρ_{dc} (red circles; first right scale) and steady-state flow viscosity η_0 (olive triangles; second right scale) are combined in one Arrhenius representation. The different ordinates cover the same number of decades (in log scale) and the starting values were chosen to achieve the best match of the data. Red solid line is a VFT fit of ρ_{dc} (see ref. [54] for fit parameters).

a negative temperature gradient just like the relaxation time and, therefore, enables a direct comparison with the relaxation time. For this plot, at first the y-axes for all quantities were adjusted to cover the same number of decades (in log scale) and then the starting values of the y-axes were chosen to achieve the best match. In the case of glyceline, all quantities reveal a non-Arrhenius behavior and a nearly perfect match of all different quantities was achieved. This indicates that the activation energy of all these processes changes in a similar manner when approaching T_g from the low viscous liquid and, thus, they are directly or indirectly coupled.

In ref. [54], which only included the dielectric data of glyceline and viscosity data from literature [46] in a small temperature range, the question was proposed whether the coupling of dipolar reorientational and ionic translational motion is of direct nature, via a revolving-door mechanism considered for plastic crystals [17, 20, 66, 69] and ILs [23], or indirectly mediated by the viscosity. The updated data set with the included τ_J and η_0 from mechanical spectroscopy favors the explanation that all dynamics in the liquid are determined by viscosity.

Similar to glyceline, all measured dynamic processes in ethaline exhibit the same temperature dependence and, thus, can be perfectly scaled onto each other in the Arrhenius representation (figure 5.27). For ethaline, however, the very restricted low-temperature viscosity data set does not allow for

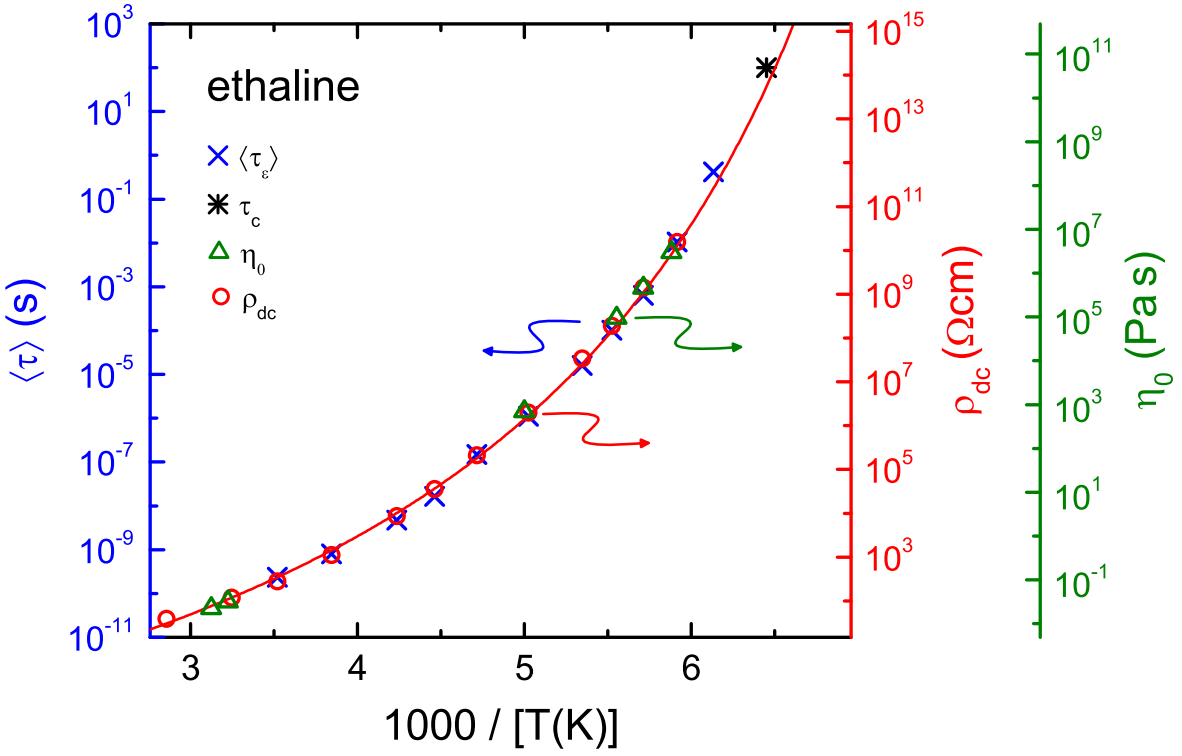

Figure 5.27: Comparison of the temperature dependence of translational and reorientational dynamics in ethaline [54]. Plot constructed in straight analogy to figure 5.26.

a similar accurate tracking of all three quantities down to the glass temperature, as demonstrated for glyceline. Furthermore, no structural relaxation time τ_J could be estimated from the oscillation data. Still, absolute η_0 values from both rotation (higher temperatures) and oscillation (lower temperatures) technique precisely follow the trend of the VFT fit calculated for ρ_{dc}, which strongly indicates the plausibility of the data and the conclusion of a coupling of all quantities.

Interesting deviations from the perfect coupling observed in ethaline and glyceline demonstrates reline (figure 5.28). Here, the structural relaxation time τ_J nicely complements the dielectric reorientational relaxation times τ_ε and continuous the trend down to lower temperatures. Additionally, as already visible in figure 5.25 (b), the relaxation time τ_c estimated from the glass temperature of the DSC scan via the relation $\tau(T_g) = 100\,\mathrm{s}$ does not align very well with τ_ε, but rather displays a decoupling of two orders of magnitude. On the other hand, the the data point estimated via $\eta_0(T_g) = 10^{12}\,\mathrm{Pa\,s}$ from the DSC measurement agrees much better with the η_0 data from mechanical spectroscopy, as can be seen in figure 5.25 (c).

Also the temperature dependence of the different dynamic processes does not scale perfectly. In figure 5.28, τ_ε, ρ_{dc} and η_0 are scaled to match at the highest temperatures, when following the trend to lower temperatures, however, ρ_{dc} clearly lags behind the other two quantities and displays as much as two orders of magnitude decoupling near T_g. It seems like, during cooling, the ionic translational motion more slowly decelerates than the structural and the dipolar reorientational dynamics.

In other words, while the dipolar reorientation is dictated by the overall viscous flow of the liquid, some amounts of ions can travel distinctively faster than the viscous flow of all particles. One may speculate about physical explanations for this phenomenon. Stillinger and Hodgdon [154] explained the decoupling of translational and rotational diffusion coefficients in normal fragile glass-forming

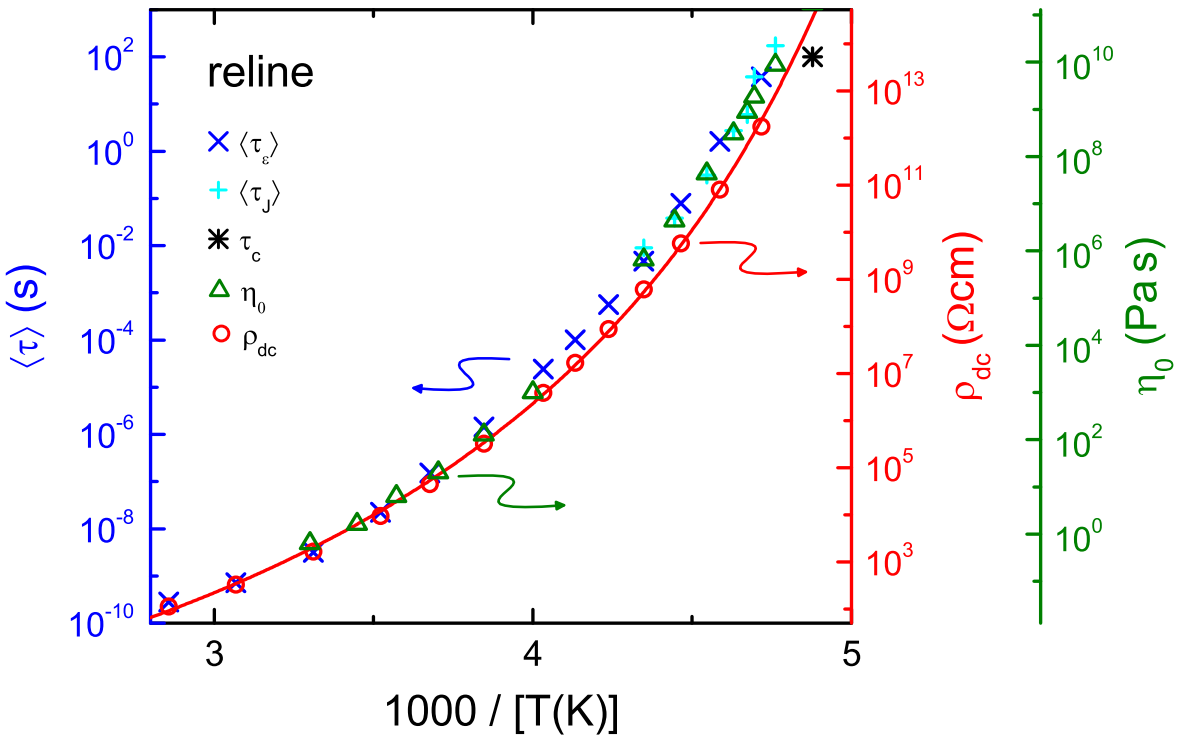

Figure 5.28: Comparison of the temperature dependence of translational and reorientational dynamics in reline [54]. Plot constructed in straight analogy to figure 5.26.

liquids with a "fluidized domain" model. In this model, a liquid, when approaching T_g, displays a multitude of different regions with varying viscosity, similarly to the explanation of broadened dielectric relaxations, where a distribution of relaxation times is due to varying surroundings of the dipoles. The idea then is that the reorientational coefficient measures an average of all different regions while the translational coefficient measures disproportionately fast particles moving preferably only through low viscous regions. Thus, in the current example, ions would travel through low viscous regions and ρ_{dc} would only artificially decouple from the viscosity, because η_0 measures an average viscosity over the whole sample and ρ_{dc} is distorted towards lower values to the disproportional contribution from low viscous regions. However, even though reline is the most fragile of the studied DESs and the decoupling might be most pronounced in fragile liquids, this model does not explain why no such decoupling is found in glyceline and ethaline.

One might also consider a revolving door like scenario [17, 20, 23, 66, 69]. Here the reorientation motion of the dipolar molecules opens additional vacant volume for the smaller ions to travel through, thus, disproportionally increasing the mobility of the smaller ionic species. The reorientation motion of the molecules is still coupled to the overall viscosity and, thus, this scenario would predict the schematic found in figure 5.28. Once again, this explanation cannot account for the absence of similar effects in glyceline and ethaline.

The obvious difference between reline and glyceline as well as ethaline is the different H-bond network of the HBD molecules. In the case of glycerol and EG, this is a strong H-O-bond network. For urea, however, the N-H-bonds presumably build a much weaker network. Additionally, the chemical structure of urea might result in weaker correlation to the ionic species due to the smaller electronegativity of the nitrogen compared to the oxygen. Thus, the chemical structure of reline might somehow explain the observed phenomenon.

To further explore the relation of ionic translational motion, dipolar reorientational motion and overall viscous flow, figure 5.29 presents the interdependence of the three representative measurement quantities σ_{dc}, τ_ε and η_0. In comparison to figures 5.26 to 5.28, directly plotting the quantities vs one another allows to visualize both the difference in temperature dependence and the vertical shifting factor used in figures 5.26 to 5.28. As long as two quantities display a matching temperature dependence in a common Arrhenius representation, in figure 5.29 they will display a straight line with slope 1 in the double-logarithmic plot. Additionally, vertical and horizontal variations between the different DESs in figure 5.29 account for different vertical shifting factors used in figures 5.26 to 5.28.

Figure 5.29 (a) is a modified version of the original Walden plot, here, σ_{dc} vs η_0^{-1}. The original Walden plot utilizes the limiting molar conductivity $\Lambda_m^0 = \sigma_{dc}/n$, where n is the ion concentration in units mol per volume. Since no temperature dependent density data are available for the investigated DESs, here, a simpler molar conductivity Λ_m shall be defined as $\Lambda_m = \sigma_{dc}/c$, where c is the ion concentration in units mol%, i.e., the ratio of mole of ion pairs to mole of all constituents. For all three investigated DESs c is equal to 33 mol% and, thus, Λ_m are σ_{dc} equivalent representations of the Walden rule.

The modified Walden plot [figure 5.29 (a)] nicely demonstrates the Walden rule, i.e., the linear dependence of the conductivity with the inverse steady-state flow viscosity. All three DESs display roughly the same dc-conductivity vales for the same value of viscosity. Thus, the charge transport in these DESs is controlled by the overall viscous flow of the liquids. Interestingly, no significant indications of a decoupling of ionic translational motion and viscsoity in reline can be found here, as otherwise indicated by figure 5.28. However, the estimated viscosity data for figure 5.29 rely on the VFT fits in figure 5.25 and, thus, introduce the possibility of a significant error margin.

In figure 5.29 (b) the dependence of τ_ε on η_0 is investigated. Both glyceline and ethaline display a linear dependence with slope 1 and roughly the same τ_ε values for a given viscosity. Only reline clearly reveals an increased τ_ε for the same viscosity over the whole temperature range and a possible deviation from the slope 1 at lower temperatures. This trend, however, is even more clearly pronounced in the ρ_{dc} vs τ_ε dependence [figure 5.29 (c)]. Reline shows the highest conductivity for a given τ_ε throughout the whole temperature range and, additionally, a dependence with slope 0.93.

To summarize, glyceline and ethaline reveal a behavior altogether as expected. All dynamics in the liquid are coupled and for a given viscosity value, both liquids display the same τ_ε and σ_{dc} values. Reline, however, displays puzzling deviations. Even though the temperature dependence in the common Arrhenius plot indicates a decoupling of the ionic translational dynamics, figure 5.29 demonstrates that it is rather the reorientational relaxation time, which effectively decouples from the viscosity and the conductivity. This relaxation in the dielectric spectrum is more merged below the dc-conductivity contribution than in the cases of glyceline and ethaline, and also this relaxation step can be well fitted with the RBM, a model based purely on ionic translational dynamics. Thus, one might speculate, that this relaxation step in the dielectric spectrum is indeed a superposition of both dipolar reorientational relaxation and an ionic contribution. However, the present data set does not allow for further conclusions about the physical origin of these deviations in reline and here further experimental results are needed.

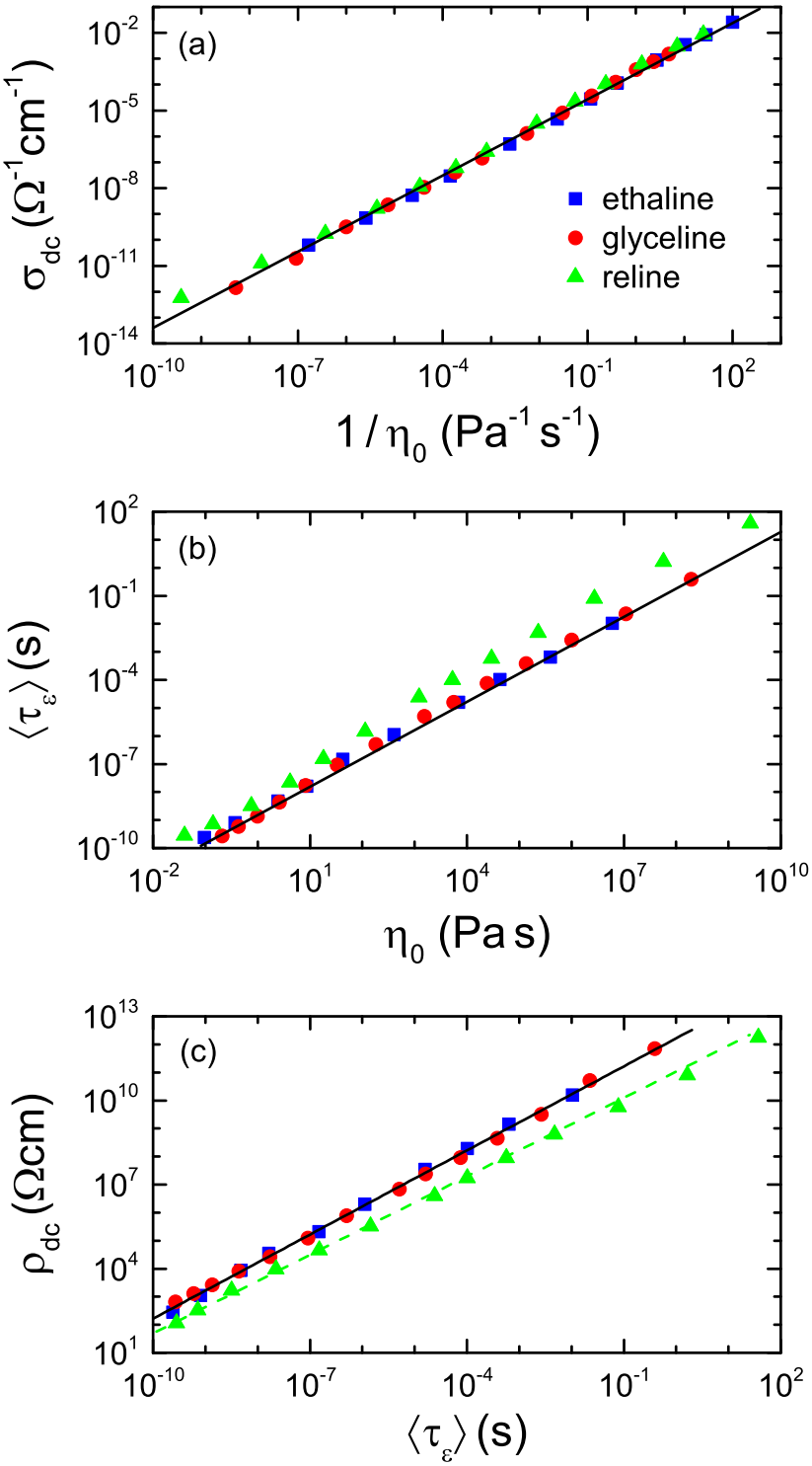

Figure 5.29: Interdependence of the three dynamics quantities determined from the dielectric and mechanical spectra of all three DESs [54] in double-logarithmic representation. (a) shows the dependence of ionic dc conductivity on the inverse viscosity (thus, a Walden plot), (b) the dependence of the reorientational α-relaxation time on the viscosity and (c) the dependence of the ionic dc resistivity on the reorientational α-relaxation time. For each temperature, from dielectric spectroscopy σ_{dc} and τ_ε are obtained in a single frequency sweep. The corresponding viscosity η_0 for each temperature was determined from the VFT fit in figure 5.25 (c). Solid black lines indicate linear behavior (slope 1 in the double-logarithmic plot) and green dashed line in (c) is a fit of the reline data obtaining slope 0.93 (thus, $\rho_{dc} \propto \tau_\varepsilon^{0.93}$).

The present work is the first experimental characterization of the dielectric and mechanical properties of the commonly investigated DESs glyceline, ethaline and reline in a broad frequency and temperature range. The intrinsic contributions in the dielectric spectrum arise from ionic translational motion and dipolar reorientational motion, while an interpretation of the spectra, purely based on ionic translational motion, cannot describe the data in the case of glyceline and ethaline. The steady-state flow viscosity data as obtained from the mechanical spectra reveals the same temperature dependence as the ionic and dipolar dynamics and, thus, demonstrates a coupling of all dynamics in glyceline and ethaline, while some peculiar decoupling of the dipolar dynamics seems to be present in reline. Furthermore, for both reline and glyceline it was shown that the structural relaxation times τ_J estimated from the compliance representation better matches the dielectric relaxation times τ_ε than those obtained from the modulus representation.

5.2 Plastic Crystalline Electrolytes

The investigation of the DESs showed that by means of dielectric spectroscopy the ionic translational and the dipolar reorientational motion in these liquids can be analyzed separately, however, both processes seem to be more or less coupled via the viscosity. Meanwhile, PC electrolytes offer the interesting opportunity to further study the correlation of ionic translational and the dipolar reorientational motion in a system without viscous flow. Thus, PCs are model systems to study the direct interaction of the two dynamics and the present work aims to answer a number of fundamental questions concerning the ionic conductivity of molecular PC electrolytes.

Generally, for all PC electrolytes it is often assumed that the reorientational motion of the constituents (both ionic or molecular), which form the PC lattice, is beneficial for the ionic conductivity of these materials. However, so far no quantitative correlation between both dynamics has been established. This raises the question, whether the ionic mobility directly scales with the on-site reorientational motion of the molecules (or ions in case of ionic PCs).

In the picture of the "revolving door" mechanism in PC electrolytes (see chapter 2.2.2), the reorientational motions of the dipolar molecules opens additional transient vacant volume for the translationally moving ions and, thus, enhances the dc conductivity of the material. To profoundly test this hypothesis, three different PC materials were selected for the present work, each consisting of a differently shaped molecule:

- The dinitrile-based mixtures use succinonitrile as starting materials, which resembles a rather one dimensionally stretched bar.
- The cyclic-alcohol-based mixtures consist of cyclohexanol and cyclooctanol. Both are essentially two dimensional, disc-shaped molecules.
- All compounds in the adamantane-based mixtures possess the adamantane molecule as basic element, which is a three dimensional, globular cage.

Theoretically, the "revolving door" mechanism should be more pronounced in systems with the one and two dimensionally stretched molecules, because here reorientational motion opens effective paths for the ions. In systems with globular, three dimensionally shaped molecules, reorientational motion does not significantly alter the experienced energy barrier for ions to pass through and, thus, such systems should display no pronounced indications of a "revolving door" mechanism.

Also ionic translational motion is believed to exhibit distinct dispersion phenomena in the dielectric spectrum, e.g., an intrinsic increase of the conductivity in σ' (see chapters 3.2.4). While it is difficult to distinguish such contributions from relaxation contributions in the dielectric spectrum of liquids, PC electrolytes offer an alternative material class to study this phenomenon.

5.2.1 Dinitrile Based Mixtures

As already mentioned in the introduction of ionic conductivity of PCs (chapter 2.2.2), succinonitrile [SN; $C_2H_4(CN)_2$] (see figure 5.30) is presumably the molecular PC which has been studied the most concerning its ionic conductivity, especially after Alarco *et al.* [11] identified the PC phase of SN as "universal matrix for solid-state ionic conductors". It is a rather bar shaped molecule, which is on both ends of its short carbon chain completed with a strong N-C triple bond. Pure SN reveals a PC phase between 233 and 322 K and a reorientational relaxation time of roughly $\tau_\varepsilon = 0.1$ ns at RT, as determined with dielectric spectroscopy [20].

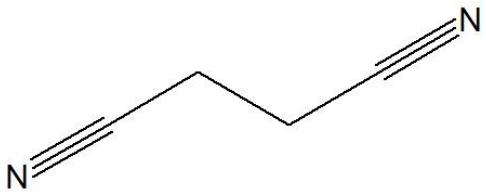

Figure 5.30: Chemical structure of succinonitrile.

Interestingly, the PC phase of SN can be significantly expanded to lower temperatures by admixing the related compound glutaronitrile [GN; $C_3H_6(CN)_2$] [233, 234], where mixtures of 15 mol% or more GN display an orientational glass transition at around $T_g^o \approx 150\,K$. Consequently, the question arose whether such admixture and the resulting modification of the PC lattice also has an influence on the ionic conductivity of these materials. Thus, Geirhos *et al.* [20] and Zachariah *et al.* [21, 22] simultaneously studied various concentrations of SN-GN mixtures and the addition of a number of different salts.

For a $SN_{0.85}GN_{0.15}$ mixture without added ions, Zachariah *et al.* [22] found a perfect coupling of dc conductivity and molecular reorientational dynamics in its PC phase. While findings like that are to be expected in a liquid, for a PC and, therefore, a solid material without viscous flow, this is an exception. It shows that in this peculiar compound the long-ranged ion drift and the collective reorientational dynamics of the molecules located in fixed positions in the PC lattice are perfectly correlated, which might indicate an effective "revolving door" mechanism. However, it remained unclear whether the measured dc conductivity of the mixture stems from a small proportion of ionized dinitrile molecules [22] or simply a very low concentration of impurities, because theoretically a purely molecular compound should display a dc conductivity of zero.

In partly unpublished dielectric measurements on pure SN without added ions, a similar correlation of ionic and molecular dynamics can be seen (see figure 5.31). Due to the limited temperature range of the PC phase of pure SN, the data set for SN is rather limited, still the temperature dependence of the molecular reorientational relaxation time and the dc resistivity are more or less the same. However, like in ref. [22] the ionic conductivity of pure SN is probably caused by small amounts of impurities in the material. Thus, it is clear that for very small amounts of ionic species in pure SN and the $SN_{0.85}GN_{0.15}$ mixture an effective "revolving door" mechanism seems to be present, which means the ionic translational drift is to a significant degree controlled and/or promoted by the rotational motion of the molecules on the lattice sites.

Interestingly, this correlation breaks down when enough ions are added to the system. Zachariah *et al.* [22] reported non-perfect scaling after the addition of 1 mol% of $LiBF_4$ to the $SN_{0.85}GN_{0.15}$ mixture and Geirhos *et al.* [20] showed the same deviations for the SN and a $SN_{0.85}GN_{0.15}$ mixture each mixed with 1 mol% $LiPF_6$. Thus, for a certain surplus or saturation with ions in the system, the presumably weak "revolving door" effect in SN or mixtures with small amount of GN is not able to provide enough path ways for all ions and in the temperature dependence the dc resistivity rises faster than the reorientational relaxation time upon cooling. However, in SN-GN mixtures with higher amounts of GN, the coupling of ionic and molecular dynamics becomes progressively better until it reaches nearly perfect correlation for the $SN_{0.20}GN_{0.80}$ mixture with 1 mol% $LiPF_6$ [20]. This indicates that replacing SN with the larger, more stretched GN molecules promotes a "revolving door" mechanism, because they can provide more transient vacant volume for the ions.

To further test this phenomenon, in the present work, not only GN but three closely related molecular

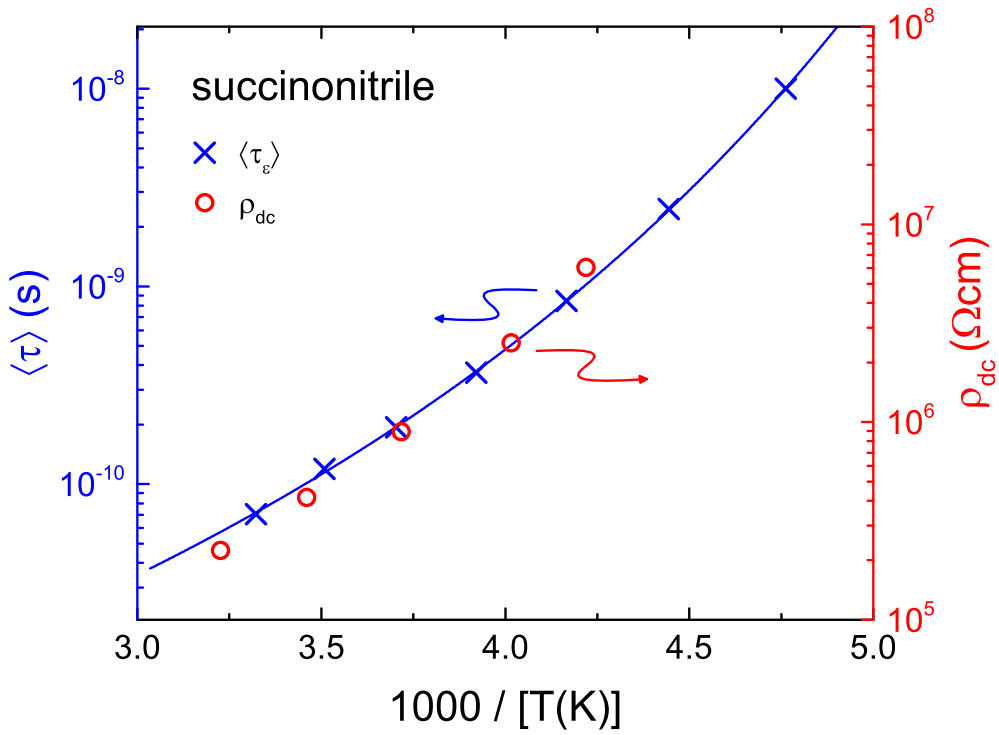

Figure 5.31: Comparison of the temperature dependence of translational and reorientational dynamics in SN. Plot constructed in straight analogy to figure 5.26 without a third frame for the viscosity. Data were measured by Thomas Bauer at Experimental Physics V, University of Augsburg and relaxation time data were used in ref. [20].

compounds with varying carbon-chain lengths are admixed to SN:

- Malononitrile [MN; $CH_2(CN)_2$], which is one CH_2-group shorter than SN.
- Adiponitrile [AN; $C_4H_8(CN)_2$], which is one CH_2-group longer than GN and, thus, two CH_2-group longer than SN.
- Pimelonitrile [PN; $C_5H_{10}(CN)_2$], which is even one CH_2-group longer than AN.

To enable a comparison with results from ref. [20], the mixtures $SN_{0.85}X_{0.15}$ (with X = MN, AN or PN) were admixed with 1 mol% $LiPF_6$ and the final nomenclature is $(SN_{0.85}X_{0.15})_{0.99}(LiPF_6)_{0.01}$. The results of these measurements were published in ref. [76].

DSC Results The addition of GN to SN has significant influence on the transition temperatures [233, 234], hence DSC measurement were performed on all three mixtures of the present work to identify PC phases and transition temperatures (see figure 5.32).

The DSC results of the X = MN mixture [figure 5.32 (a)] strongly resemble the DSC curve of the $SN_{0.85}GN_{0.15}$ mixture shown in the introduction of the DSC measurement technique (chapter 4.3). It is a clear example of a PC, formed at around $T = 305\,\mathrm{K}$ during cooling, which exhibits an orientational glass transition at $T_g^o \approx 150\,\mathrm{K}$. Thus, for X = MN the system reveals a stable PC phase over a broad temperature range, much like the $SN_{0.85}GN_{0.15}$ mixture and with very similar transition temperatures. Therefore, at least concerning the thermodynamic phase behavior, the addition of 15 mol% MN has very similar effects on the SN PC as the addition of 15 mol% GN.

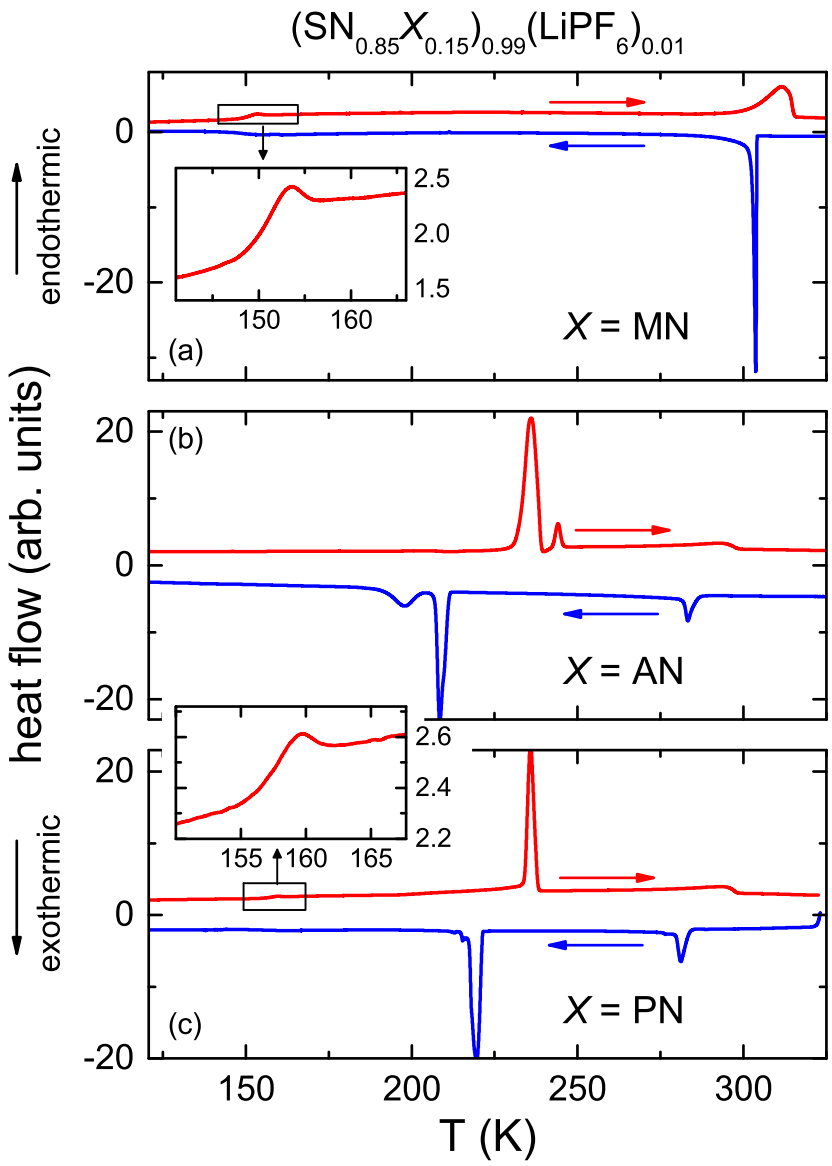

Figure 5.32: DSC measurements under cooling (lower blue line) and heating (upper red line) with $10\,\mathrm{K\,min^{-1}}$ for the three mixtures with $X =$ MN (a), AN (b) and PN (c) [76]. Endothermic processes are pointing in positive y-direction. The insets in (a) and (c) are zoomed in on the orientational glass transition as revealed by the MN and PN mixture during heating.

In contrast to $X =$ MN, the $X =$ AN mixture [figure 5.32 (b)] exhibits a phase behavior more like pure SN, where a PC at around $T = 280\,\mathrm{K}$ and a fully ordered crystal at around $T = 210\,\mathrm{K}$ are formed during cooling. The corresponding melting of these phases occurs at $T_\mathrm{m}^\mathrm{o} \approx 236\,\mathrm{K}$ and $T_\mathrm{m}^\mathrm{t} \approx 290\,\mathrm{K}$. The low-temperature crystallization process can most likely be identified as the transition into the fully ordered crystal and not a PC phase with restricted reorientational degrees of freedom, as there are no indications of a glass transition at lower temperatures.

Interestingly, the $X =$ PN [figure 5.32 (c)] mixture displays the aforementioned case of restricted reorientational degrees of freedom below a second first-order phase transition. Generally, the curve for $X =$ PN resembles the one for $X =$ AN with crystallization processes occurring at around $T = 280$ and $220\,\mathrm{K}$ during cooling and corresponding melting at $T_\mathrm{m}^\mathrm{o} \approx 236\,\mathrm{K}$ and $T_\mathrm{m}^\mathrm{t} \approx 290\,\mathrm{K}$. However, this

sample reveals the signature of a glass transition at temperatures far below the second first-order phase transition [see inset figure 5.32 (c)]. Thus, this second first-order phase transition does not mark a crystallization into a fully ordered crystal, but the formation of a PC phase with restricted orientational degrees of freedom, which eventually undergo glassy freezing at $T_g^o \approx 156\,\mathrm{K}$.

SN-MN As seen above, all three mixtures reveal PC phases in more or less extended temperature ranges and, thus, with dielectric spectroscopy the influence of the molecular size of the added molecule X on the ionic conductivity can be studied. Starting with $X = \mathrm{MN}$, figure 5.33 shows the results from dielectric spectroscopy on the mixture $(\mathrm{SN}_{0.85}\mathrm{MN}_{0.15})_{0.99}(\mathrm{LiPF}_6)_{0.01}$. In contrast to the above discussed dielectric spectra of DESs, the present example of the SN-MN mixture presents the case of a clear separation of dc-conductivity contribution and α-relaxation peak in ε''.

In ε' the SN-MN mixture [figure 5.33 (a)] reveals a large step-like decrease with increasing frequency, e.g., for $T = 218\,\mathrm{K}$ from 2×10^4 to 30 between 0.1 and $10^3\,\mathrm{Hz}$. This marks the known EP effects, here occurring due to the high ionic conductivity in the solid SN-MN PC. Well separated from the EP effects, at higher frequencies for the same temperature follows a second step-like decrease from around 30 to 2 between 10^7 and $10^9\,\mathrm{Hz}$. This step progressively shifts to lower frequencies with decreasing temperature, mirroring the continuous slowing down of the molecular dynamics under cooling, typical for glassy freezing. Thus, this step marks the α relaxation of the material arising from reorientational motions of the dipolar molecules sitting on the PC lattice sites.

The relaxation steps in ε' are accompanied by clearly visible, well-pronounced relaxation peaks in ε''. Left of the peaks, the dc-conductivity contribution arises as contribution with steepness -1 in the double-logarithmic representation, e.g., for $T = 218\,\mathrm{K}$ from 10^4 to $10^6\,\mathrm{Hz}$. In the present case this contribution does not strongly superimpose the relaxation peaks, which means, for a giving reorientational relaxation time, the dc conductivity is much lower than in the case of the DESs. This seems plausible since the PC mixture only has 1 mol% of ions and the conditions for ionic translational motion are inherently different than in the viscous DESs.

Notably, for $T = 157\,\mathrm{K}$ and lower temperatures, the amplitude of the steps in ε' and the peak height in ε'' are significantly reduced. Additionally, the α-relaxation peak changes its shape from a one sided broadening for $T \geq 163\,\mathrm{K}$ to a symmetric broadening for $T \leq 157\,\mathrm{K}$. This presumably reflects the transition into a partially ordered PC state with restricted reorientational degrees of freedom, as not detected by the DSC measurement, because it was performed with a much faster cooling rate of $10\,\mathrm{K\,min^{-1}}$ compared to the $0.4\,\mathrm{K\,min^{-1}}$ used for the dielectric spectroscopy measurements. Unfortunately, at these low temperatures no dc-conductivity plateau arises within the frequency window, so no statement on the influence of this transition on the ionic mobility can be made here.

The four lowest temperatures $T \leq 157\,\mathrm{K}$ also reveal indications of a β-relaxation process at the right flank of the α-relaxation peak, especially pronounced for $T = 140\,\mathrm{K}$ between 10^4 and $10^6\,\mathrm{Hz}$, where the broadened peak-like shape of the β-relaxation becomes partly visible. As for the DESs a detailed treatment of β relaxations is out of the scope of the present work. Also the σ' representation [figure 5.33 (c)], once again, shows the same data as ε'' but with more emphasis on the dc-conductivity plateau and the reduction of the conductivity due to EP effects at low frequencies for the three highest temperatures, which is not shown in figure 5.33 (b) in favor for a zoomed in view on the relaxation process.

For the fitting routine, two DRC circuits were used for $T = 236$ and $215\,\mathrm{K}$ and one for $T = 190\,\mathrm{K}$, where most of the EP effects have shifted out of the frequency window. The α relaxation was described by a CD function for $T \geq 163\,\mathrm{K}$ and a CC function for $T \leq 157\,\mathrm{K}$, while for the β-relaxation a CC

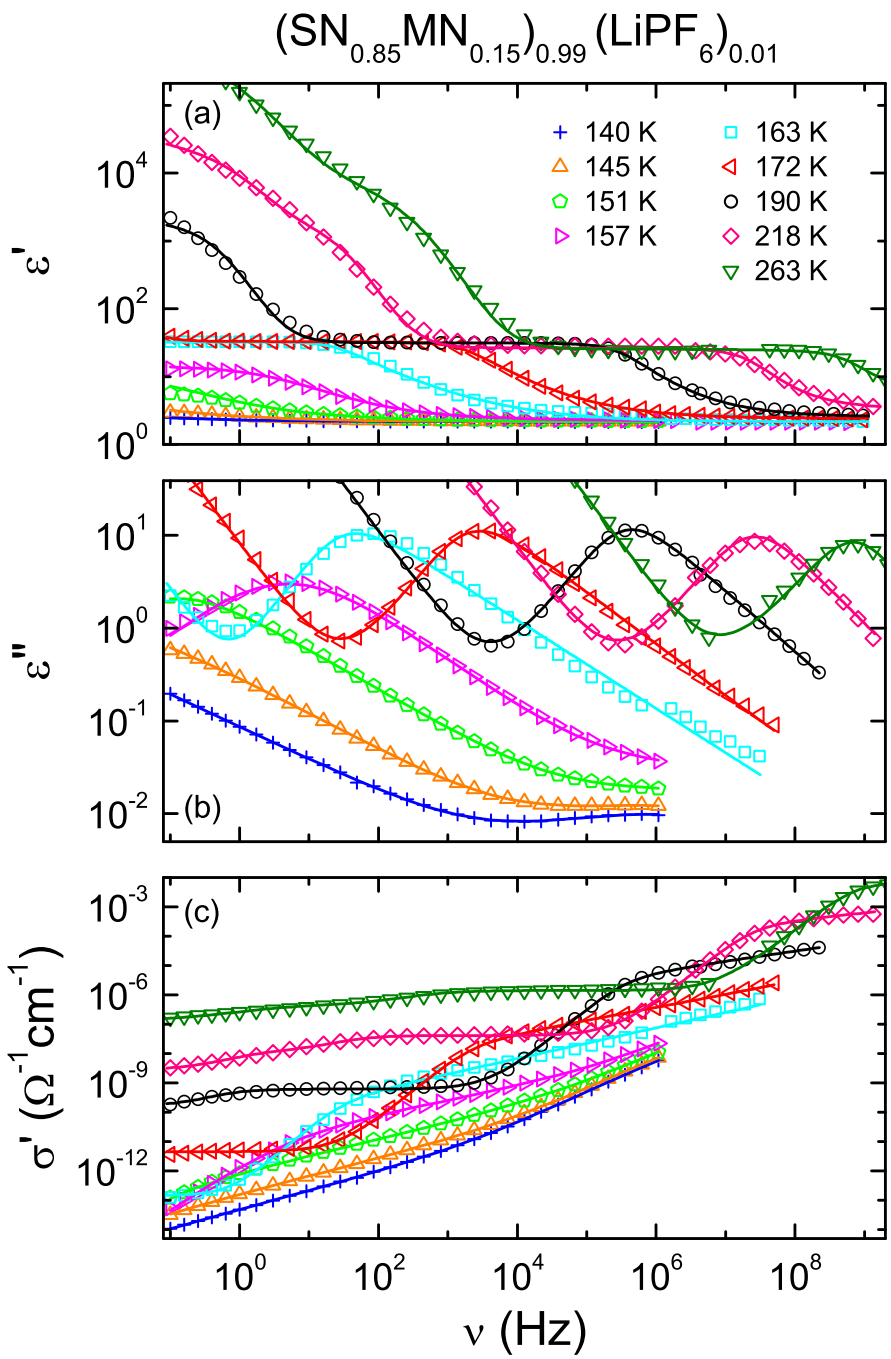

Figure 5.33: Dielectric spectra of ε' (a), ε'' (b) and σ' (c) of $(SN_{0.85}MN_{0.15})_{0.99}(LiPF_6)_{0.01}$ for various temperatures [76]. The solid lines in (a) and (b) are fits with the equivalent circuit approach utilizing two distributed RC circuits, two relaxation functions and a dc-conductivity contribution (see text for details). The lines in (c) are calculated via $\sigma' = \varepsilon'' \varepsilon_0 \omega$.

function was used. Altogether the fits obtained this way describe the data in reasonable agreement and deliver accurate values for the dc conductivity and the α-relaxation time.

SN-AN As demonstrated by the DSC measurement [figure 5.32 (b)], the temperature range of the PC phase of the SN-AN is very limited and below the second first-order transition no indication of a glass transition can be found, hence no significant relaxation contribution is expected to arise in the dielectric spectrum below this transition. Additionally, the very narrow temperature range does not allow for a meaningful investigation of the α relaxation in the PC phase, because at this high temperature the α relaxation is mostly shifted out of the frequency window, towards higher frequencies. In ref. [76] the dielectric spectrum of the SN-AN mixture is given and reveals the aforementioned problems for a meaningful evaluation of the relaxation processes in this mixture. Thus, from this spectrum only the temperature dependence of the dc conductivity in the PC phase can be extracted and is shown in figure 5.35 in Arrhenius representation.

SN-PN The dielectric spectra of the SN-PN mixture (figure 5.34) reveals qualitatively the same contributions as the SN-MN mixture. Here, the ε' [figure 5.34 (a)] and the ε'' [figure 5.34 (b)] spectra are zoomed in on the relaxations steps and peaks, respectively, so most of the EP effects are cut off in these representations, however, in σ' [figure 5.34(c)] the reduction of the conductivity due to EP effects left of the dc-conductivity plateaus is clearly visible.

In contrast to the SN-MN mixture, here the second first-order transition, identified in the DSC measurement as a transition into a partially ordered state, occurs in the expected temperature range at around $T = 225\,\mathrm{K}$ and results in a significant decrease of the relaxation strength but no clearly visible change in the peak shape. Thus, above and below the α relaxation was fitted with a CD function and for the β-process at the lowest temperatures a CC function was used. Notably, at the transition from the presumably isotropic reorientation to the somewhat restricted reorientational motion no clear discontinuity in the temperature dependence of the relaxation time or the dc conductivity is detected as well.

Small deviations between the fits and the data occur at the transition from the relaxation steps to the EP region in ε' and at the transition from the relaxation peaks to the dc-conductivity contribution in ε''. Such contributions were also found in the SN-GN mixtures and discussed in refs. [233] and [21] as another extrinsic or intrinsic relaxation process or an ac conductivity contribution. In the current example, however, firstly those deviations are small and any additional element in the equivalent circuit could effectively improve the fits to better describe the data, and secondly this unknown contribution most likely does not have significant influence on the dc conductivity or the α-relaxation time, which are the two important parameters the following discussion of the results will rely on.

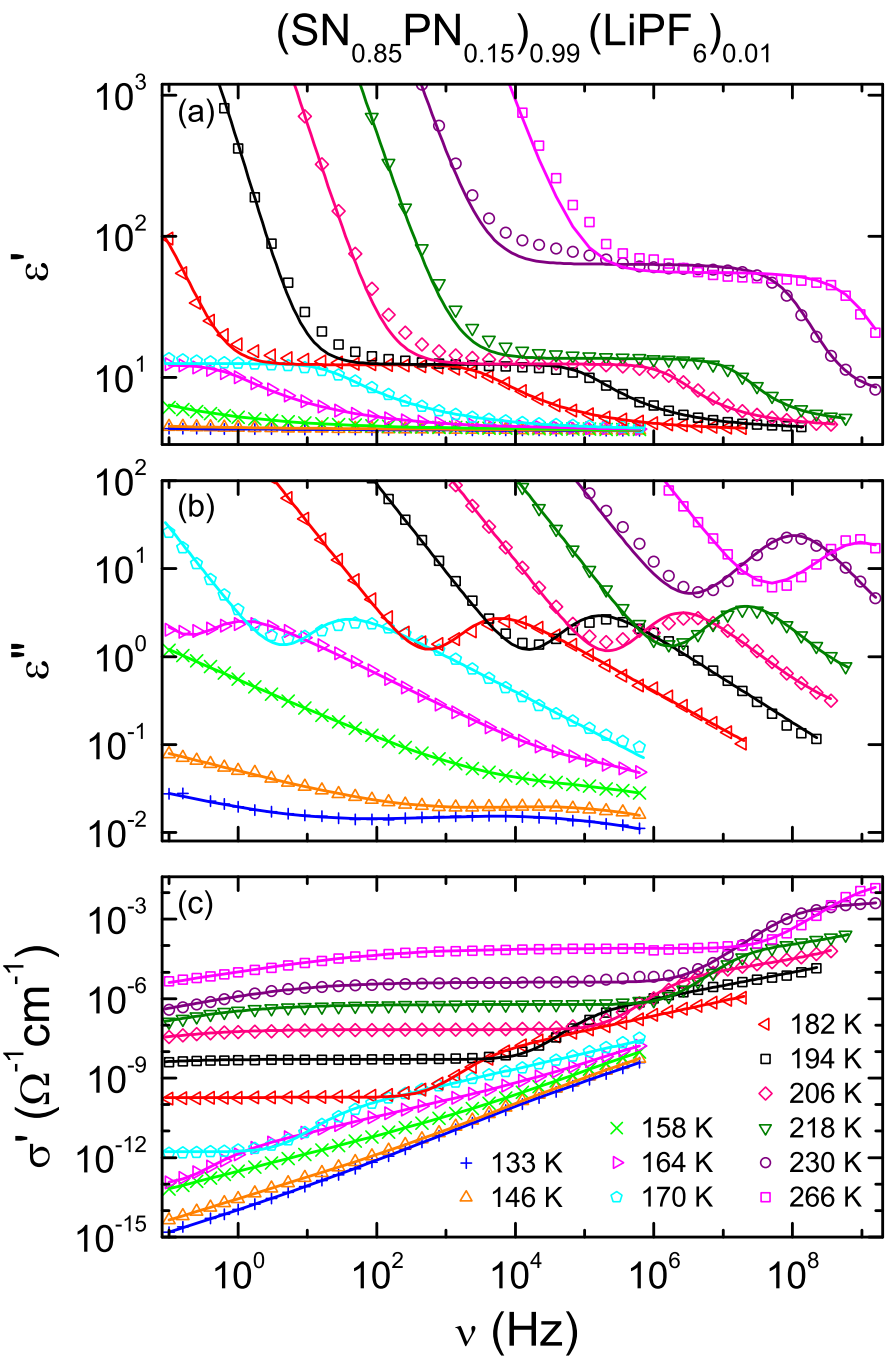

Figure 5.34: Dielectric spectra of ε' (a), ε'' (b) and σ' (c) of $(SN_{0.85}PN_{0.15})_{0.99}(LiPF_6)_{0.01}$ for various temperatures [76]. The solid lines in (a) and (b) are fits with the equivalent circuit approach utilizing one distributed RC circuits, two relaxation functions and a dc-conductivity contribution (see text for details). The lines in (c) are calculated via $\sigma' = \varepsilon'' \varepsilon_0 \omega$.

Ionic and Dipolar Dynamics To now estimate the influence of the geometrical shape of the added molecules X on the ionic conductivity, figure 5.35 present the temperature dependence of the dc conductivity of all three mixtures plus data for the corresponding SN-GN mixture and pure SN with each 1 mol% $LiPF_6$. It shows that all mixtures reveal a significantly higher conductivity than pure SN with

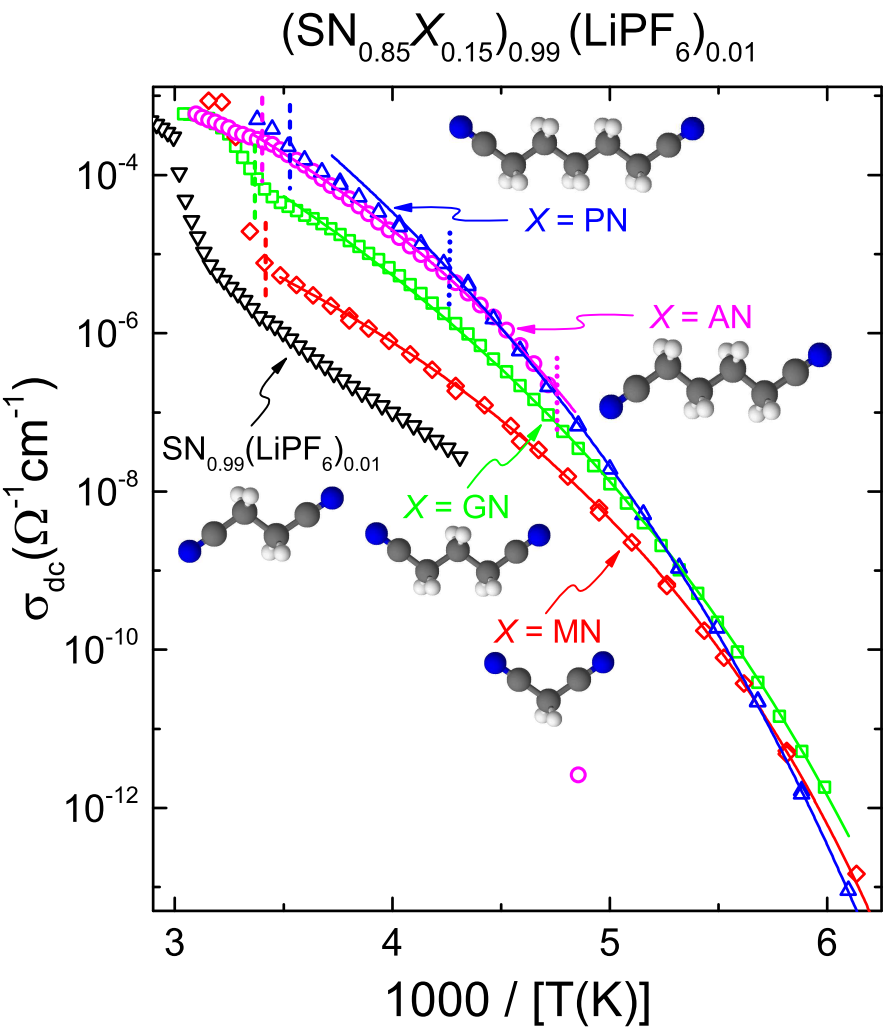

Figure 5.35: Temperature dependence of the dc conductivity of the investigated $(SN_{0.85}X_{0.15})_{0.99}(LiPF_6)_{0.01}$ mixtures in Arrhenius representation [76]. Additionally, results from the corresponding SN-GN mixture [20] and pure SN (remeasured for the present work) with each 1 mol% $LiPF_6$ are added. The molecules are schematically indicated. The solid lines are fits according to the VFT law adapted for the conductivity (equation 3.30). The vertical dashed and dotted lines are transition temperatures estimated from the DSC measurements during cooling for the transition into the PC or the more ordered phase, respectively.

1 mol% $LiPF_6$. Especially, at higher temperatures when approaching the individual melting temperatures of the systems, the dc conductivity considerably increases with increasing molecular size of added molecule X. In particular, at $T = 250\,\mathrm{K}$, from pure SN with 1 mol% $LiPF_6$ to the SN-MN mixture σ_{dc} gets enhanced by roughly one order of magnitude and form there to the SN-GN mixture by another order of magnitude. The further rise to the SN-AN mixture is slightly less than half an order of magnitude and, finally, the addition of PN does not significantly increase the dc conductivity any further.

Thus, the initial idea that the integration of bulkier, more stretched molecules into the SN PC lattice enhances the effectiveness of the "revolving door" mechanism and with this increases the conductivity,

seems to be validated by the found schematic, at least for $X =$ GN, AN and PN. Here, $X =$ MN presents a peculiar case of rather unexpected conductivity enhancement when a smaller, more globular molecule is added. Still, this finding can be rationalized by not focusing on the absolute molecule size but rather the ratio of the two molecules in the mixture. The integrated small MN molecules might take lattice sites, which were originally populated by SN molecules, and, due to their significant smaller size, now offer more vacant volume for the ions in their immediate surrounding.

Another interesting aspect here is the difference between dc conductivity in the liquid and PC phases of each mixture. For pure SN with 1 mol% $LiPF_6$ this difference is roughly three orders of magnitude, but the difference becomes progressively smaller with increasing molecule size of added molecules X, until the transition from liquid to PC phase cannot be identified from the dc conductivity data alone for $X =$ AN and PN. Here, the supporting information from the DSC measurements are necessary. This demonstrates that for reaching the highest conductivity values in such PC electrolytes the conservation of a liquid-like conductivity is important.

Also in figure 5.35 the different impact of the second first-order transition on the conductivity in the mixtures SN-AN and SN-PN can be seen. SN-AN, which undergoes a crystallization to a fully ordered crystal at around $T = 210\,\mathrm{K}$, as concluded from the DSC and dielectric measurement, exhibits a drastic conductivity drop at the orientational-ordering transition. Hence, from the dielectric spectrum only one dc conductivity value with $3 \times 10^{-12}\,\Omega^{-1}\,\mathrm{cm}^{-1}$ below the transition can be estimated (see figure 5.35). SN-PN, which reveals a transition in a partially ordered PC phase, where the molecules still reorientate even though somewhat restricted, does not display any distinct reduction of σ_{dc} at this transition. This highlights the importance of molecular reorientational motions for the ionic mobility in these systems and further supports the idea of the "revolving door" mechanism.

Besides pure SN with 1 mol% $LiPF_6$, all mixtures in figure 5.35 exhibit clear deviations from Arrhenius behavior and can be fitted with equation 3.30. Similar deviations were found for the dc conductivity and the reorientational relaxation time for various SN-GN mixtures [20–22, 233, 234]. Such deviation from Arrhenius behavior are well known from glass forming liquids, but also similar behavior was found for the reorientational α-relaxation times of some PCs [10], which highlights the collective, liquid-like character of the reorientational dynamics of the molecules in PCs. Interestingly, if the dc conductivity of PCs, like in the present example, reveals similar deviations from Arrhenius behavior, a connection to the reorientational dynamics seems probable.

To further examine this phenomenon, figure 5.36 compares the dc resistivity as representative for the ionic translational motion with the reorientational α-relaxation time as representative for the molecular dynamics. The same procedure was already applied for the DESs in chapter 5.1.4 and in ref. [20] for the whole SN-GN mixture series. In ref. [20] the scaling of the two quantities becomes progressively better with increasing GN amount and, as can be seen in figure 5.36 (c), is not perfect for 15 mol% GN. For the present mixtures, however, near perfect scaling was found for the SN-MN mixture over the whole temperature range and for the SN-PN mixture in the partially ordered low temperature phase. It should be once again noted here, that a good scaling of ionic translational and dipolar reorientational dynamics is a rather expected outcome in liquids, where everything is controlled by the liquid's viscous flow, but for a solid materials, like the PC electrolytes, this is a rather surprising finding and strongly indicates an inherent connection of the two dynamics like suggested by the "revolving door" mechanism.

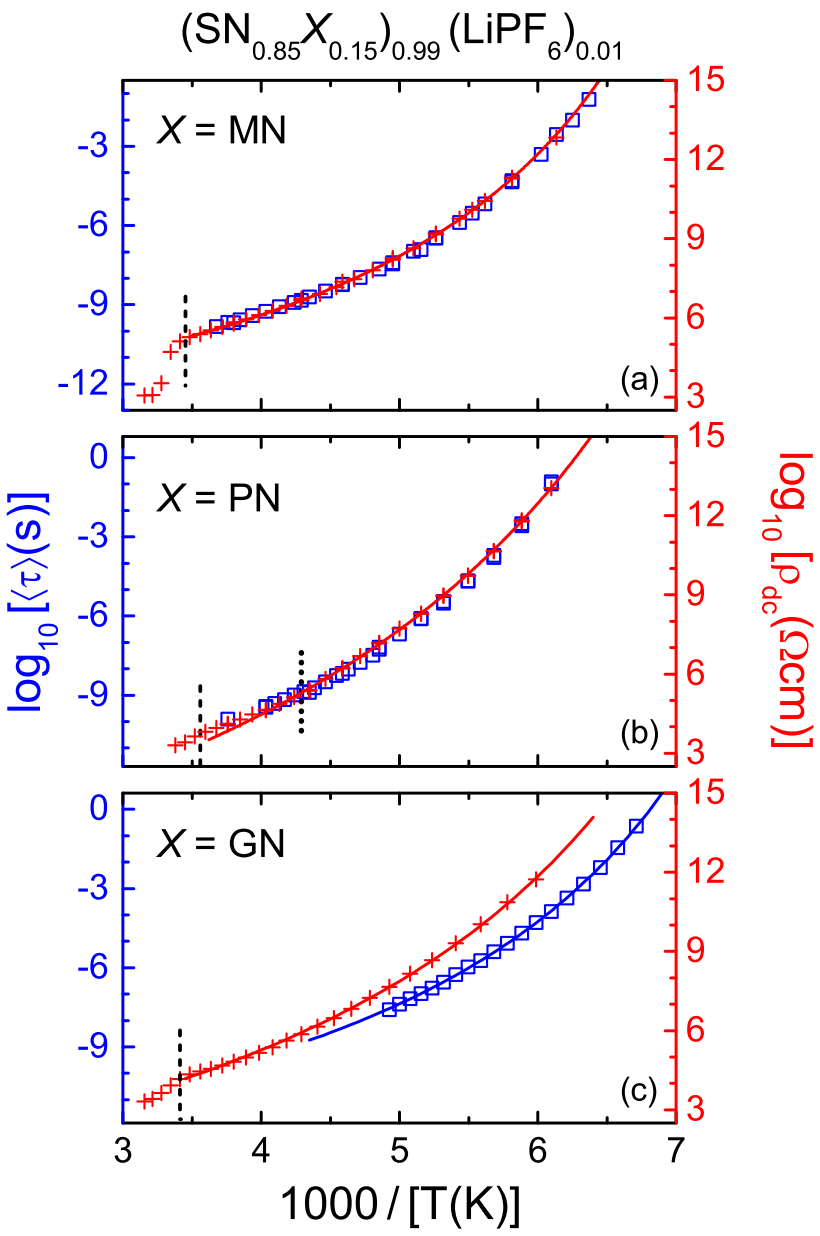

Figure 5.36: Comparison of the temperature dependence of translational and reorientational dynamics for X = MN, PN and GN [20] in the mixtures $(SN_{0.85}X_{0.15})_{0.99}(LiPF_6)_{0.01}$ [76]. Plots constructed in straight analogy to figure 5.26 without the third frame for the viscosity. For X = GN no good match of the data could be achieved and both quantities were shifted to match at the highest temperatures (here the extrapolation of the VFT of $\langle\tau\rangle$). Vertical dashed lines indicate liquid-PC transitions and for X = PN additionally the second first-ordered transition into the partially ordered PC phase. Solid red lines are VFT curves calculated from the fits in figure 5.35 and solid blue line in (c) is a separate VFT fit of the relaxation times $\langle\tau\rangle$.

In particular, the SN-MN and the SN-PN mixtures reveal close coupling of ionic and dipolar dynamics and, thus, resemble the behavior of the $(SN_{0.20}GN_{0.80})_{0.99}(LiPF_6)_{0.01}$ investigated in ref. [20]. This indicates that the integration of a rather small amount of *smaller* molecules in the PC lattice, like

in the cases of 15 mol% MN in the $SN_{0.85}MN_{0.15}$ mixture or 20 mol% SN in the $SN_{0.20}GN_{0.80}$ mixture [20], effectively promotes ionic translational motion and generates a good coupling of ionic and dipolar dynamics. On the other hand, the addition of small amounts of very large molecules, like the 15 mol% of PN molecules in the $SN_{0.85}PN_{0.15}$, is able to produce the same effect and, here, even in case of somewhat restricted molecular reorientation the "revolving door" mechanism seems to be effective.

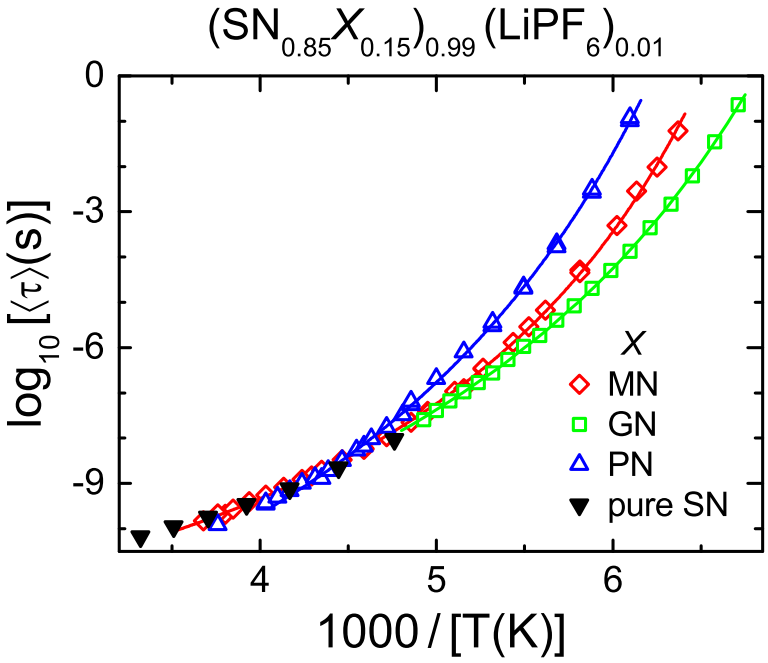

Figure 5.37: Comparison of the absolute values of the average α-relaxation times of the three mixtures shown in figure 5.36 and of pure SN (taken from figure 5.31) [76]. The solid lines are fits with the VFT law.

Thus, so far the conductivity enhancement in the $(SN_{0.85}X_{0.15})_{0.99}(LiPF_6)_{0.01}$ mixtures was solely explained by the geometrical shape of the added molecules X, but theoretically vastly different α-relaxation times could also account for the observed conductivity enhancement. To disprove this idea figure 5.37 shows the temperature dependence of the average α-relaxation times of the different mixtures. Especially in the temperature range of $T \approx 220$ to 280 K ($x = 4.5$ to 3.5 in the Arrhenius plot), where the greatest difference in conductivity between the different systems occurs (see figure 5.35), the average α-relaxation time are the same for all mixtures and for pure SN (see figure 5.37).

To summarize the findings of this mixing series, the presented results of the SN-MN and SN-PN mixtures nicely complement and further consolidate the findings of Geirhos *et al.* [20]. The ionic conductivity of SN-based PC electrolytes can be significantly enhanced by integrating chemically related (larger or smaller) molecules into the PC lattice. The enhancement cannot be explained by a simple variation of the reorientational relaxation time of the dipolar molecules, but rather a complex interplay of rotation-translation coupling, ion concentration and size of integrated molecules determines the conductivity enhancement.

5.2.2 Cyclic Alcohol Based Mixtures

As mentioned above, the second group of PCs, that will be investigated in the present work, are cyclic-alcohol-based mixtures, in particular a mixing series of cyclohexanol (HEX) and cyclooctanol (OCT). They represent the case of rather two-dimensional, disc-shaped molecules, where at least some coupling of rotation-translation coupling should emerge due to the "revolving door" mechanism, as known from the one-dimensionally stretched dinitrile-based PCs. Additionally, at the same temperature HEX displays a significantly faster dipolar reorientation in the PC phase as compared to OCT, which might allow to investigate the influence of the reorientational relaxation on the ionic conductivity. Furthermore, OCT is by two CH_2-groups larger than HEX, which might also influence the ionic conductivity, as known from the dinitrile-based mixtures (see previous chapter).

For this measurement series, six different concentrations ($x = 0, 0.2, 0.4, 0.6, 0.8, 1$) were prepared and to every mixture 1 mol% $LiPF_6$ was added. The used nomenclature is: $(HEX_{1-x}OCT_x)_{0.99}(LiPF_6)_{0.01}$. The findings of these measurements were published in ref. [75].

Cyclohexanol (HEX) The alcohol HEX [$C_6H_{11}OH$] consists of one hydroxyl (OH-) group bound to a hydrocarbon ring with six carbon atoms. While HEX itself is a rather simple molecule, its solid state displays a surprisingly rich polymorphism, which is said to be due to its "conformational flexibility and ability to form hydrogen bonds" [235]. So already Timmermans [63] identified HEX as a PC and, later, Adachi *et al.* [236] in 1968 firstly applied the term glassy crystal to the glassy state of the HEX PC phase. Until now, HEX is one of the best studied PCs.

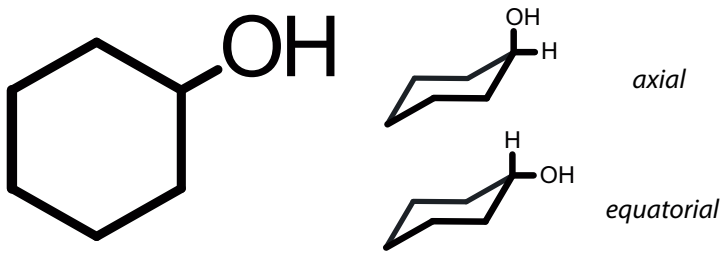

Figure 5.38: Molecular structure of cyclohexanol (left) and depiction of the axial and the equatorial chair conformation (right) [237].

The complex phase diagram of HEX was studied thoroughly over the past century [236, 238–244]. Below its melting point $T_m \approx 298\,K$, HEX forms a PC phase. This phase is named PC I and displays isotropic orientational disorder of the cyclohexyl ring and, additionally, configurational disorder of the OH-group (axial and equatorial conformation) in equal distribution [235]. The PC I phase is only stable between $T = 298$ and $265\,K$, however, when cooled sufficiently fast (e.g., $10\,K\,min^{-1}$) the PC I undergoes glassy freezing and forms a glassy crystal at around $T_g^o \approx 147\,K$ [236, 238, 245].

The crystal structure of PC I of HEX is face-centred cubic (fcc) with space group $Fm\bar{3}m$ ($Z = 4$, atoms per unit cell) and a lattice parameter of $8.809\,Å$ at $275\,K$ [235, 243, 246–248]. Alternatively a simple cubic (sc) structure was proposed [249]. Several further solid phases at lower temperatures with higher degree of orientational order are well documented in literature [235, 239, 240, 244, 250]. They are consequently numbered PC II, etc., however, in the context of this work only the PC I phase of HEX is of interest.

Due to the OH−group, the molecule obtains a dipolar moment of $1.7\,D$ [248] and many dielectric studies have been performed [239–241, 251–255]. Broadband dielectric measurements [10] revealed:

In the PC I phase, HEX exhibits a broadened, main loss peak, identified as α-relaxation, which can be best described by a CD function in the high temperature ($T \geq 200\,\mathrm{K}$) and a HN function in the low temperature region ($T \leq 160\,\mathrm{K}$). In between those two regions lies a hardly accessible temperature range, due to rapid formation of orientational order. At low temperatures, approaching T_g^o, two additional, faster relaxation processes (β and γ-relaxation) are necessary to fit the whole frequency range. The temperature dependence of the α-relaxation times shows an Arrhenius behavior at high temperatures and a divergence approaching T_g^o, best described by a VFT-law. The results from dielectric measurements, which strongly resemble the schematic known from canonical glass forming liquids, and results from NMR [256, 257] support the idea of isotropic reorientational motions of the molecules in the PC I.

Cyclooctanol (OCT) By enlarging the hydrocarbon ring of HEX with two additional CH_2-groups, one obtains OCT [$C_8H_{15}OH$]. Similar to HEX, OCT crystallizes in a PC I phase at $T_\mathrm{m} \approx 298\,\mathrm{K}$ and the PC I can easily be supercooled into a glassy crystal with $T_\mathrm{g}^\mathrm{o} \approx 155\,\mathrm{K}$ [240, 258, 259]. When cooled sufficiently slow or when heated from the quenched glassy crystal, OCT forms its PC II phase in the temperature range of $T = 190$ to $165\,\mathrm{K}$, [240, 260–263], which also reveals some disorder and a glass transition at $T_\mathrm{g,II}^\mathrm{o} \approx 140\,\mathrm{K}$ [259, 264]. Just like for HEX, the focus of this work lies on the PC I phase.

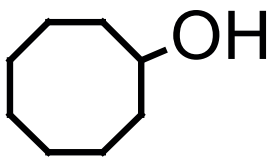

Figure 5.39: Molecular structure of cyclooctanol

The PC I of OCT was found to have sc structure ($Z = 8$, atoms per unit cell) with a lattice parameter of 11.96 Å at 273 K [259, 263]. The compound is well investigated dielectrically [240, 253, 254, 259, 262, 265–269] and, in its PC I, OCT exhibits a similar dielectric loss as HEX [267]. The α-relaxation peak is best described by a CD function and at low temperatures two additional relaxations occur. The temperature dependence of the α-relaxation processes reveals VFT-behavior [267] and $\tau = 100\,\mathrm{s}$ is reached at $T_\mathrm{g}^\mathrm{o} \approx 168\,\mathrm{K}$. The close similarity to HEX and results from NMR [257] suggest that in the PC I of OCT also isotropic molecular reorientational motion is present.

HEX-OCT mixture Both, HEX [270–272] and OCT [263, 273, 274] were studied in mixtures with other compounds. Especially, the mixture cyclopentanol with OCT was found to form a stable PC I phase down to T_g^o [263], which suggests that a similar behavior can be expected for the HEX-OCT mixture and, thus, inaccessible temperature ranges, like previous studies [10, 267] have struggled with, can be avoided.

In contrast to the dinitrile compounds, where only SN displays a PC phase, pure HEX and pure OCT both possess PC phases. Even though the compounds are chemically very similar, HEX and OCT reveal significantly different reorientational relaxation times in their PC phases, as estimated by dielectric spectroscopy (see figure 5.40). For example, this difference reaches nearly one order of magnitude at $T = 250\,\mathrm{K}$, where the relaxation times are $\tau_\mathrm{HEX}(250\,\mathrm{K}) = 1.4 \times 10^{-7}\,\mathrm{s}$ and $\tau_\mathrm{OCT}(250\,\mathrm{K}) = 8.3 \times 10^{-7}\,\mathrm{s}$. Thus, by mixing OCT with HEX, the reorientational relaxation might be expected to gradually evolve from that of pure HEX to that of pure OCT with increasing OCT amount, which would offer the

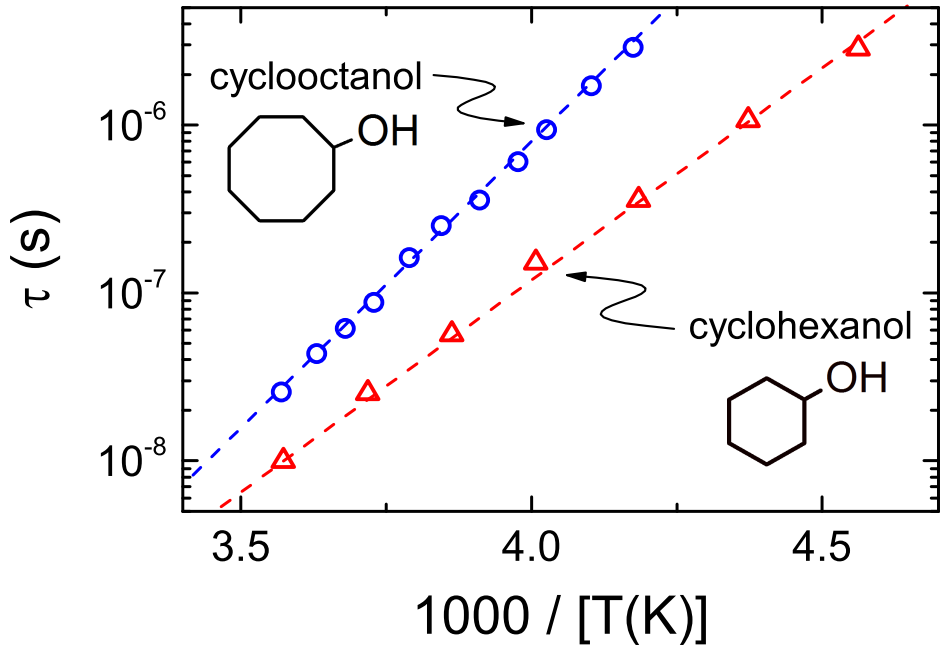

Figure 5.40: Relaxation times measured with dielectric spectroscopy for pure OCT [267] (blue circles) and HEX [10] (red triangles). Dashed lines are guides for the eye.

interesting opportunity to study the influence of the varying timescale of local molecular motion on the ionic conductivity.

To check for the formation of PC phases in the mixture of HEX and OCT, DSC measurements on all $(HEX_{1-x}OCT_x)_{0.99}(LiPF_6)_{0.01}$ samples were conducted (see figure 5.41). All mixtures but $x = 0$ reveal the desired case of a stable PC phase that exhibits glassy freezing at low temperatures via an orientational glass transition, as demonstrated for the $SN_{0.85}GN_{0.15}$ system in chapter 4.3. Exactly like the other samples, pure HEX with 1 mol% $LiPF_6$ ($x = 0$) forms a PC and, subsequently, a glassy crystal upon cooling without indications of further transitions (not shown in figure 5.41). On heating, however, after the transition into the liquid at $T_g^o \approx 152\,K$, this sample exhibits a cold crystallization with subsequent melting, as can be seen by the large swing in first exothermic and then endothermic direction between $T = 180$ and $250\,K$ in figure 5.41 for $x = 0$. This marks the formation and subsequent melting of a phase of increased orientational order.

Usually, eutectic behavior is expected for the melting temperatures in a binary mixture. In the $(HEX_{1-x}OCT_x)_{0.99}(LiPF_6)_{0.01}$ series, at first, going from $x = 0$ to 0.2, a $20\,K$ drop of T_m is found (see noted melting temperatures in figure 5.41). The melting temperature then increases and peaks for $x = 0.8$. Such unusual evolution of the melting temperature might be explained by looking into the crystal structures. As introduced in the upper paragraphs, in their PC I, HEX is present in a fcc and OCT in a sc crystal structure. In a continuous mixing series, a transition from fcc to sc has to emerge in the T-x-diagram. Thus, such transition occurs in the range between $x = 0.8$ and 1 and explains the slightly lower T_m of pure OCT with $LiPF_6$.

In summary, all mixtures display a PC phase with presumably isotropic reorientation of the molecules and this reorientational motion exhibits glassy freezing, as known from the dinitrile compounds. Additionally, the HEX-OCT mixing series reveals an eutectic point around $x = 0.2$ and a transition from dominantly fcc to sc lattice symmetry between $x = 0.8$ and 1, which causes the $x = 1$ sample to deviate from the typical evolution of the melting temperature in a binary phase diagram.

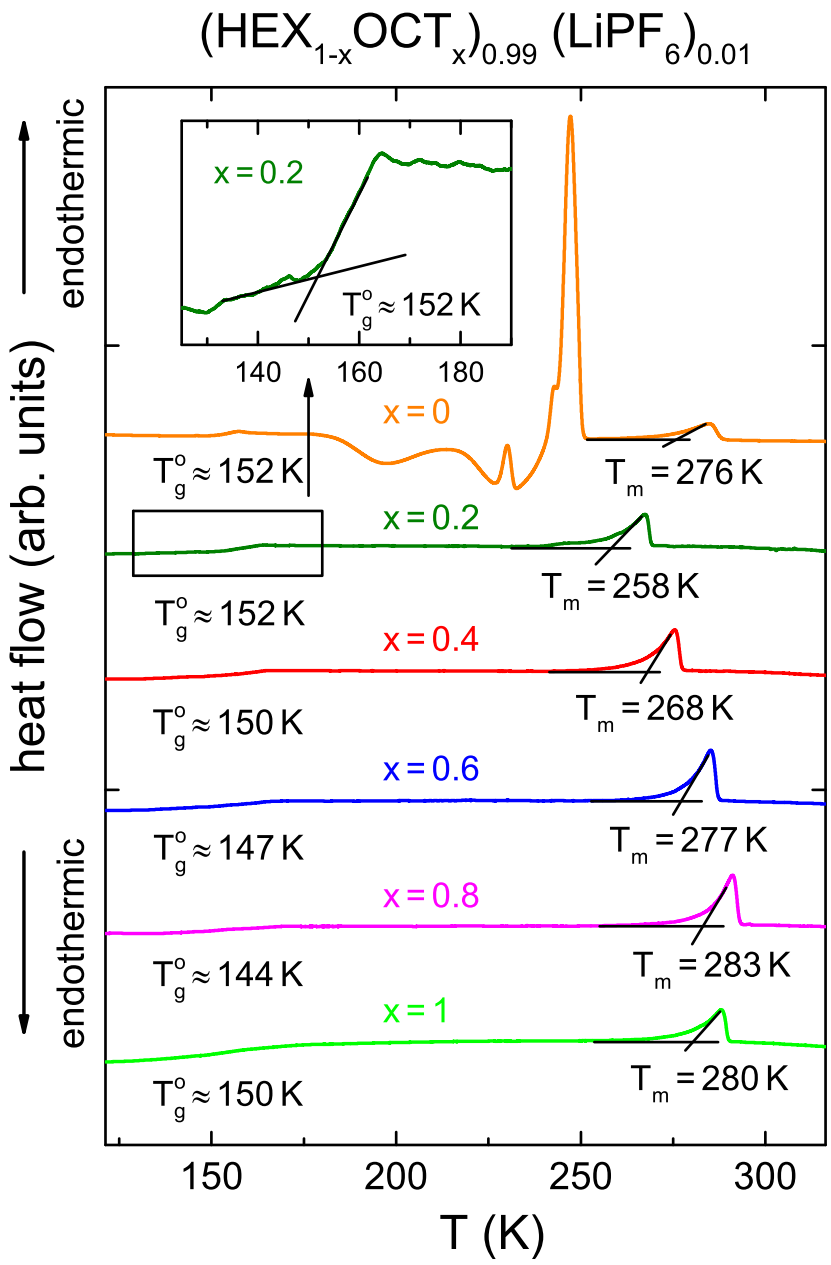

Figure 5.41: DSC measurements under heating with $10\,\mathrm{K\,min^{-1}}$ for all $(\mathrm{HEX}_{1-x}\mathrm{OCT}_x)_{0.99}(\mathrm{LiPF_6})_{0.01}$ mixtures [75]. Data are freely shifted above one another in y-direction, starting with $x = 0$ at the top and going in 0.2 steps to $x = 1$ at the bottom. The scans were taken after cooling the samples from $T = 320\,\mathrm{K}$ to $T = 110\,\mathrm{K}$ with $10\,\mathrm{K\,min^{-1}}$. Endothermic processes are pointing in positive y-direction. The inset is a zoomed in view of the glass-tranistion step of the $x = 0.2$ sample. Orientational glass temperatures T_g^o and melting temperatures T_m of the PC phases are noted.

Dielectric spectrum of HEX-OCT To gain insights into the ionic and dipolar dynamics in the HEX-OCT system, dielectric spectroscopy was performed on all samples. As the dielectric spectra of all mixtures reveal qualitatively the same results, figure 5.42 presents the dielectric spectrum of the $(\mathrm{HEX}_{0.4}\mathrm{OCT}_{0.6})_{0.99}(\mathrm{LiPF_6})_{0.01}$ mixture as representative for all other mixtures.

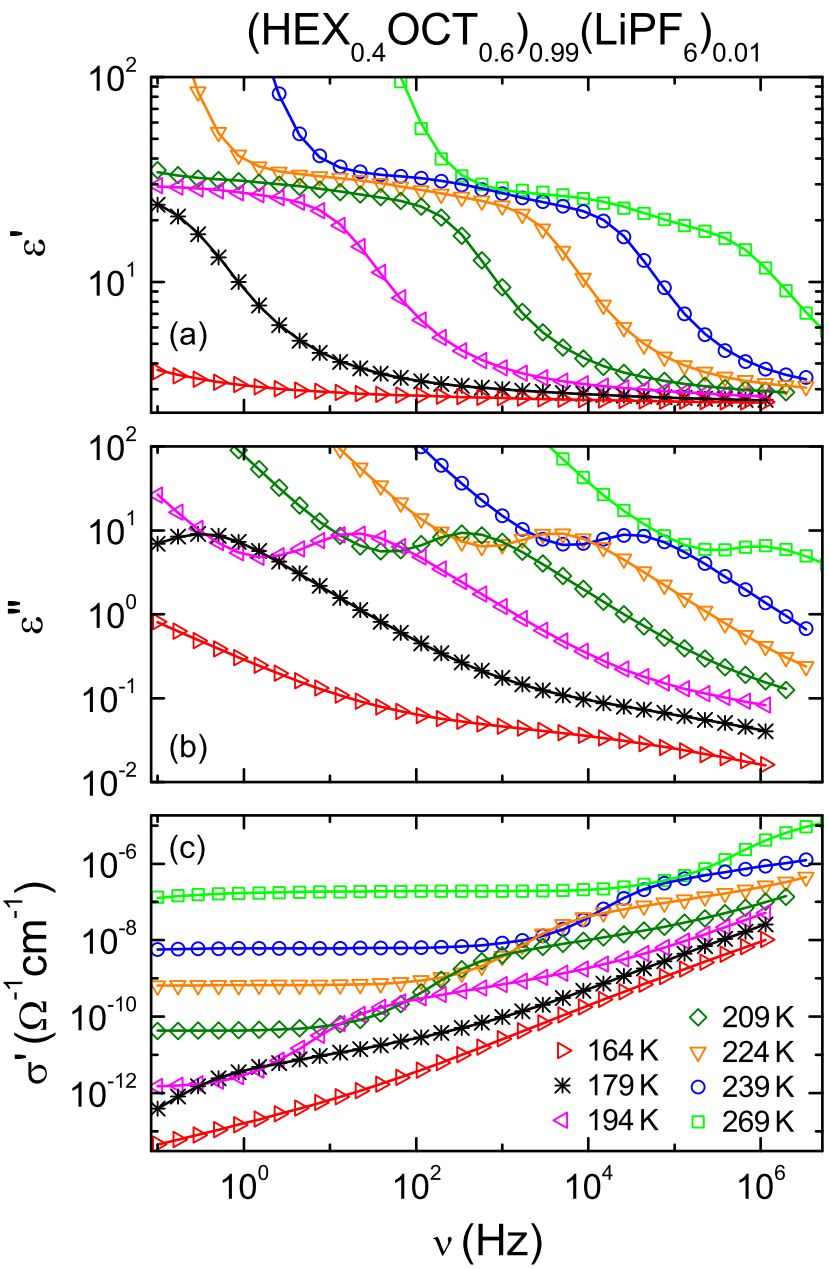

Figure 5.42: Dielectric spectra of ε' (a), ε'' (b) and σ' (c) of the PC phase of $(HEX_{0.4}OCT_{0.6})_{0.99}(LiPF_6)_{0.01}$ for various temperatures [75]. The solid lines in (a) and (b) are fits with the equivalent circuit approach utilizing one distributed RC circuits, three relaxation functions and a dc-conductivity contribution (see text for details). The lines in (c) are calculated via $\sigma' = \varepsilon'' \varepsilon_0 \omega$.

Unsurprisingly, the dielectric spectrum of the HEX-OCT mixture qualitatively resembles the results of the dinitrile compounds. For the three highest temperatures, ε' [figure 5.42 (a)] is dominated by EP effects, which again are cut off in favor of a zoomed in view on the relaxation steps. The relaxation steps in ε' exhibit a decrease from roughly 30 to 3, are shifting continuously from higher to lower frequencies with decreasing temperatures and are accompanied by distinct peaks in ε''. Thus, this feature can undoubtedly be identified as the α-relaxation of the PC arising from collective reorientational motions

of the dipolar molecules sitting on the lattice sites.

As pointed out in the SN-PN spectrum (see figure 5.34), in the HEX-OCT mixture for temperatures $T \geq 209\,\mathrm{K}$ a small second step seems to be superimposed on top of the main relaxation step in ε'. This steps reveals a relaxation strength of $\Delta \approx 6$ and is clearly visible, e.g., for $T = 269\,\mathrm{K}$ at around $10^5\,\mathrm{Hz}$. Once again this contribution could arise from ac conductivity or an extrinsic or instrinic relaxation, as discussed for the SN-PN sample. Either way, this contribution seemingly does not significantly influence the main α-relaxation or the dc conductivity and, thus, a detailed analysis is out of the scope of the present work.

In ε'' [figure 5.42 (b)], on the left side of the α-relaxation peaks the dc conductivity arises, e.g., for $T = 239\,\mathrm{K}$ between 10^2 and $10^4\,\mathrm{Hz}$. Additionally, for the lower temperatures on the right flank of the α-relaxation peaks a β-relaxation emerges, best seen for $T = 164\,\mathrm{K}$ between 10^2 and $10^6\,\mathrm{Hz}$. The dc conductivity is again better emphasized in the σ' representation [figure 5.42 (c)] and, here, also a comparatively small reduction in conductivity due to EP becomes visible ($T = 269\,\mathrm{K}$ between 0.1 and $1\,\mathrm{Hz}$).

For the fitting routine one DRC circuit for the EP effects, a CD for the α-relaxation, a CC for the β-relaxation and a dc-conductivity contribution were used. Additionally in this case a second CC function was utilized to account for the small relaxation step on top of the α-relaxation. Overall the fits provide a good estimate of the experimental data. The values for τ and σ_{dc} deduced from the fits perfectly agree with values directly read off from the spectrum and, therefore, for the following discussion of all samples the values were directly determined from the spectra.

Ionic and Dipolar Dynamics Figure 5.43 compares the temperature-dependent dc conductivity and reorientational α-relaxation time of all mixtures in Arrhenius representation. The lowest conductivity in figure 5.43 (a) displays the $\mathrm{HEX}_{0.2}\mathrm{OCT}_{0.8}$ mixing ratio, which represents the peculiar case of a small amount of *smaller* molecules added to the a larger molecules. Interestingly, exactly this configuration produced in the dinitrile based mixtures the best rotation-translation coupling and in the SN-GN series the best overall conductivity. Starting from this mixture, the conductivity gets enhanced with increasing amount of *smaller* HEX molecules and pure HEX with $\mathrm{LiPF_6}$ reveals the highest dc conductivity of all samples. Again the $x = 1$ mixture disobeys the trend and exhibits a slightly higher conductivity than the $\mathrm{HEX}_{0.2}\mathrm{OCT}_{0.8}$ sample, presumably again due to the transition of dominantly fcc to sc lattice symmetry.

The reorientational α-relaxation time in the PC phase of all mixtures [figure 5.43 (b)] somewhat mirrors the behavior of the dc conductivity. Pure HEX with $\mathrm{LiPF_6}$ has the fastest relaxation time over the whole temperature range. The relaxation times of the other mixtures nearly match at high temperatures, but systematically separate going to lower temperatures. Here, the relaxation times get progressively slower with increasing amount of OCT and pure OCT with 1 mol% $\mathrm{LiPF_6}$ notably does not reveal an anomaly here, but has the slowest relaxation time of all samples.

When explaining the conductivity enhancement in the dinitirle PC electrolytes, the coupling of ionic translational and dipolar reorientational motion played an important role. Thus, using the known procedure, figure 5.44 compares the temperature dependence of ρ_{dc} and of the α-relaxation time in a common Arrhenius plot for all samples.

The α-relaxation times of pure HEX with 1 mol% $\mathrm{LiPF_6}$ in the fully orientationally disordered PC I phase can be described by a simple Arrhenius law (equation 3.1), in agreement with ref. [10]. Upon cooling, in the dielectric measurement the formation of a second PC phase (PC II) with increased orientational ordered, however, could not be avoided, in contrast to the fast DSC cooling measurement.

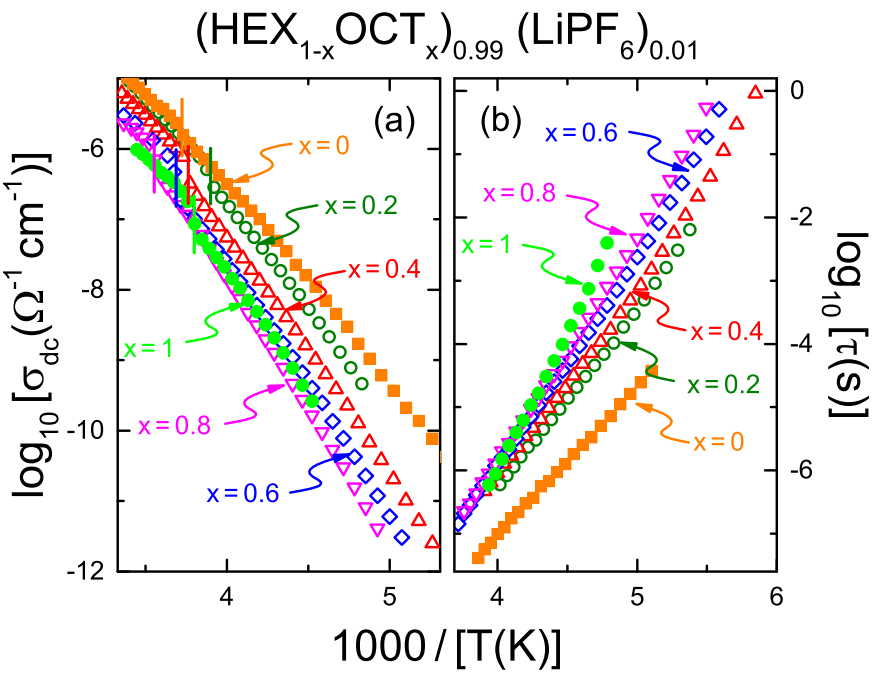

Figure 5.43: Temperature dependence of the dc conductivity (a) and the reorientational α-relaxation time (b) of all $(HEX_{1-x}OCT_x)_{0.99}(LiPF_6)_{0.01}$ mixtures in Arrhenius representation [75]. Vertical lines in (a) indicate the melting temperatures as determined from the dielectric spectra, slight deviations from those determined by DSC occur due to supercooling effects.

At this transition the relaxation time displays a discontinuity and changes its temperatures dependence.

For all other mixtures the simple Arrhenius law was not sufficient to describe the temperature dependence of the relaxation times and, thus, the VFT equation was used to describe them. Still, the deviations from Arrhenius behavior are only weakly pronounced in the HEX-OCT mixtures and strength parameter D values between 32 and 79 were obtained from the fits. This finding agrees with the general tendency of PCs to rather fall on the strong side of the fragile-strong classification of glass-forming systems [10].

Much like the relaxation times, the dc resistivity of pure HEX with 1 mol% $LiPF_6$ can also be described by a simple Arrhenius law, while for all other mixtures a VFT fit was used. Again, non-Arrhenius behavior of the ionic resistivity in a solid material is rather unexpected and indicates glassy freezing as known from the dipolar reorientational dynamics in PCs. And indeed, for all samples a good but not perfect scaling of ρ_{dc} and τ could be achieved. Thus, as expected for the two dimensionally stretched molecules, there is some indication of a "revolving door" mechanism, however, the pronounced changes between the different mixtures and perfect coupling for some systems, as known from the dinitrile compounds, is not present for the HEX-OCT series. Therefore, changes in the effectiveness of the rotation-translation coupling cannot explain the observed significant variation of the dc conductivity throughout the mixing series.

Also the influence of the geometrical shape can hardly explain the observed variation of ionic conductivity, because the trend rather points in the opposite direction, where the addition of the *smaller* molecules enhances the conductivity. Eventually, the effect of the timescale of local reorientation of the dipolar molecules is the only candidate left to explain the conductivity variation throughout the

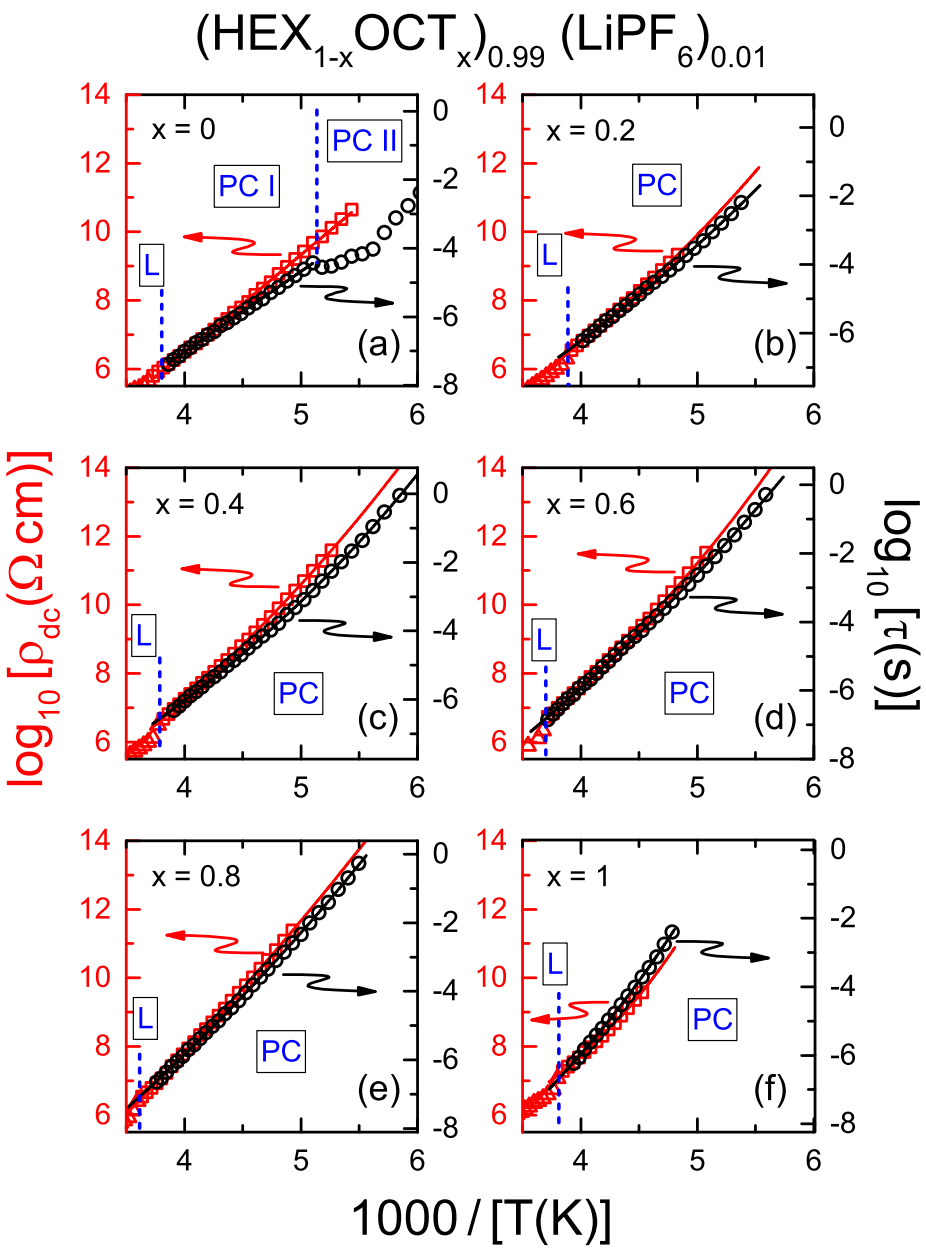

Figure 5.44: Comparison of the temperature dependence of translational and reorientational dynamics for all $(HEX_{1-x}OCT_x)_{0.99}(LiPF_6)_{0.01}$ mixtures [75]. The plots are constructed in straight analogy to figure 5.26 without the third frame for the viscosity. The vertical dashed lines indicate liquid-PC transitions and for $x = 0$ an additionally first-order transition into a partially ordered PC phase, here named PC II. The solid red lines and black lines are VFT fits of the ρ_{dc} and relaxation time τ data for $x = 0.2$ to 1 and Arrhenius fits for $x = 0$.

mixing series.

Therefore, figure 5.45 (a) and (b) show the dependence of the dc conductivity and the relaxation time on the mixing ratio at a representative temperature $T = 220\,\mathrm{K}$. This plot visualizes the trends already identified in the discussion of figure 5.43. Further, figure 5.45 (c) highlights the direct interdependence of the two quantities and reveals a roughly linear dependence of the ionic conductivity on the dipolar reorientational motion. Obviously, the data do not follow the linear trend very well and the interdepen-

dence might be disturbed by factors like variations in the rotation-translation coupling and the fcc to sc transition between $x = 0.8$ and 1. Nevertheless, this finding shows that, as long as there is to some extend a "revolving door" mechanism present in the PC electrolyte (as shown in figure 5.44), the ionic mobility scales with the on-site reorientational motion of the lattice molecules. And furthermore that the geometrical shape of added molecules and its influence on the ionic conductivity might only be relevent for rather one dimensionally stretched molecules like in the dinitrile compounds.

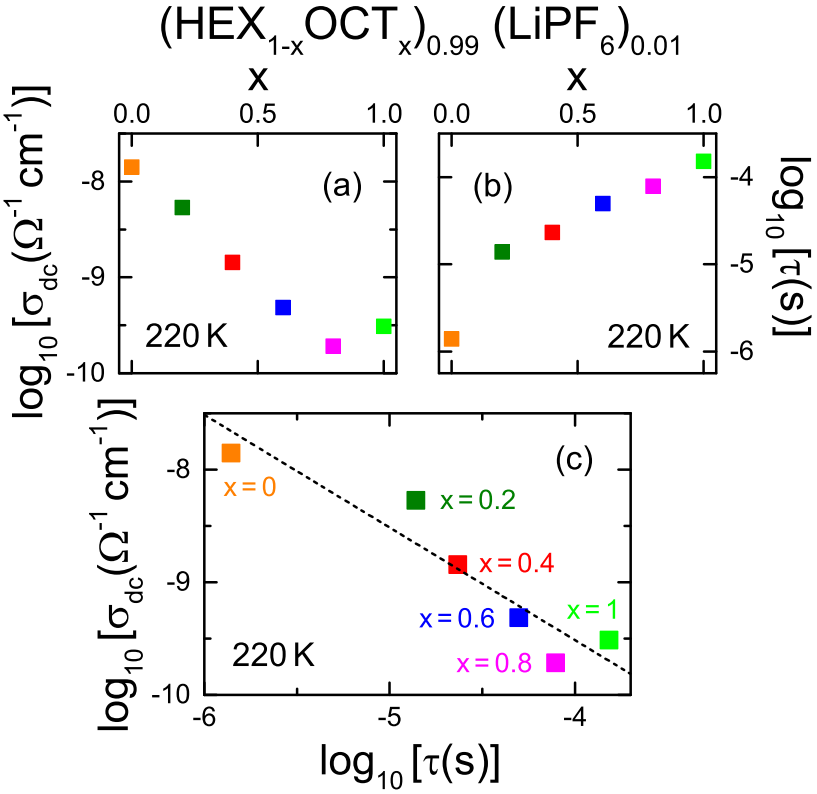

Figure 5.45: Dependence of the dc conductivity (a) and the relaxation time (b) on the mixing ration and direct interdependence of the two quantities (c), all for $T = 220\,\mathrm{K}$. The dashed line in (c) is a linear fit with fixed slope of -1 in the double logarithmic plot, thus, corresponding to $\sigma_{\mathrm{dc}} \propto 1/\tau$.

In summary, while in the dinitrile-based mixtures the addition of *larger* molecules causes an up to three-decade enhancement of the conductivity, in the cyclic-alcohol-based mixtures the conductivity increases with the addition of the *smaller* HEX molecules. This difference can be explained assuming that in the HEX-OCT mixtures the translation-rotation coupling via the "revolving door" mechanism is given for all mixtures and the conductivity only scales with the timescale of the on-site reorientational motions of the molecules. In contrast, in the dinitrile-based mixtures the coupling of ionic and dipolar dynamics strongly varies with the mixing ration and the size of the admixed molecule, which effectively dominates the conductivity enhancement in these mixtures. The reason for this qualitatively different behavior is presumably the different geometrical shape of the molecules [75].

5.2.3 Adamantane Based Mixtures

Lastly, to complete the measurement series on PC electrolytes, a PC build from three dimensional, globular molecules was needed. After some testing in the laboratory, the material of choice was cyano-adamantane (CNA) (see figure 5.46). CNA belongs to the group of adamantane-based compounds, a highly symmetrical non-dipolar carbon cage. Compared to the many other adamantane-based compounds, CNA has a rather low melting temperature, displays a stable liquid phase, which not immediately starts to evaporate, and possesses a dipolar moment.

Thus, with CNA as a starting material, pure CNA as well as mixtures with each 20 mol% adamantane (ADA) and 2-adamantanon (AON) were prepared with each 1 mol% lithium bis(trifluoromethane)-sulfonimide (LiTFSI) to study the influence of integrating other molecules into the PC lattice and to introduced mobile ions into the system. This yields the following mixtures: $CNA_{0.99}LiTFSI_{0.01}$, $(CNA_{0.8}ADA_{0.2})_{0.99}LiTFSI_{0.01}$ and $(CNA_{0.8}AON_{0.2})_{0.99}LiTFSI_{0.01}$. Results on these adamantane-based mixtures were prepared for publication during the making of this thesis [275].

Because of the adamantane cage, all three molecules used here display a rather globular shape, where only the side groups in case of CNA and AON distort the molecule and give it a dipolar moment. Hence, the effectiveness of the "revolving door" mechanism should theoretically be significantly reduced compared to the previously presented dinitrile and cyclic alcohol based PC electrolytes. This fact should emerge in the dielectric characterization of the samples as strongly reduced ionic conductivity and/or decoupling of ionic diffusion from the rotational motions of the molecules.

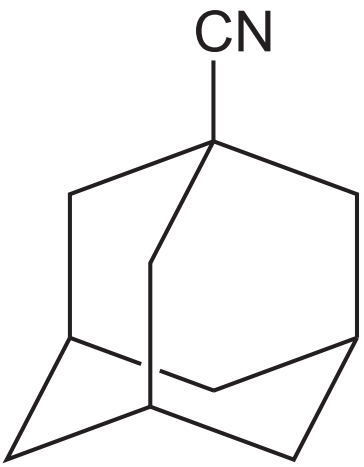

Figure 5.46: Chemical structure of cyano-adamantane.

The materials are best introduced starting with ADA ($C_{10}H_{16}$) (compare figure 5.46 without the CN side group). As mentioned, ADA is a highly symmetrical non-dipolar carbon cage built up from ten carbon atoms and, due to its nearly perfect globular shape, it is a prototypical molecular PC. ADA forms a PC below its melting temperature of $T_m \approx 543\,K$ with fcc symmetry and undergoes a order-disorder transition at around 208 K [276, 277]. Since it has no dipolar moment, its PC molecular dynamics cannot be studied by dielectric spectroscopy. Additionally, ADA starts to rapidly evaporate when heated above its melting temperature. Thus, it is not suitable as basic material for the mixing series.

CNA ($C_{10}H_{15}CN$) is the same molecule as ADA with the addition of a CN side group (figure 5.46). Interestingly, due to this side group, CNA displays a drastically reduced melting temperature of $T_m \approx 460\,K$, below which it forms a PC phase with fcc symmetry [278]. There are reports of at least two

further low temperature PC phases with higher degrees of orientational order [262, 279], still the high temperature PC phase can easily be supercooled, however, various values between 163 and 178 K for the orientational glass transition T_g^o of this phase are reported in literature [10, 262, 279–281]. Importantly, in the high temperature PC phase of CNA, in contrast to the previously studied PCs, the molecules do not exhibit isotropic dynamic reorientation, but somewhat restricted motion [262, 281]. As shown for the SN-PN mixture in chapter 5.2.1, in some cases such restricted reorientational motions may not significantly reduced the ionic mobility compared to full isotropic reorientations of the molecules, however, this may vary from material to material.

In AON, as compared to CNA, the CN group is replaced by an oxygen atom connected with a double bond to the carbon cage. Like the other two compounds, AON forms a PC phase with fcc symmetry below its melting temperature of $T_m \approx 529$ K [282, 283] and at least one low temperature PC phase below 180 K with restricted orientational degrees of freedome [10, 283] is known. Similar to ADA, in laboratory tests the liquid phase rapidly evaporates after heating above T_m.

Since both AON and ADA did not display a stable liquid phase above their melting temperatures, no simple liquid-liquid mixtures of the materials could be produced. Thus utilizing that CNA possesses a significantly lower T_m than the other two compounds, larger amounts of CNA were melted and held closely above T_m. Then weighted amounts (estimated for the desired concentration) of AON, ADA and LiTFSI were added in powder form to the melt. The mixture was held at high temperatures until CNA had dissolved the added powders and a homogeneous liquids was obtained.

DSC Results As for the HEX-OCT mixing series, DSC measurement were conducted on the adamantane-based mixtures to obtain information on the phase- and glass-transition temperatures (see figure 5.47). Prior to the heating scans shown in figure 5.47 the samples were cooled from $T = 490$ K to 110 K, from the liquid state deep into the glassy crystal state. During those runs all mixtures revealed an exothermic first-order transition into the PC and a glass transition into the glassy crystal. Hence, for pure CNA the applied cooling rate and the addition of 1 mol% LiFSI was sufficient to suppress the formation of any low temperature PC or fully ordered phases. Also for the two mixed systems no such transitions were recorded, which like for the SN-GN mixture demonstrates, that in a binary mixture PCs are less likely to form additional low temperature phases with higher degree of orientational order.

During reheating, the melting of the glassy crystal via the orientational glass transition occurs for $CNA_{0.99}LiTFSI_{0.01}$ in the temperature range from $T = 165$ to 190 K. An onset evaluation of the step-like anomaly corresponding to this orientational glass transition gives $T_g^o \approx 167$ K, which falls into the broad range of different values reported in literature (see above). This orientational glass transition is followed by a cold-crystallization, marked by a slight swing in exothermic direction at around $T \approx 220$ K, and a subsequent melting, marked by a peak in endothermic direction at around $T \approx 270$ K. This shows the formation and subsequent melting of a partially ordered phase and before and after this sequence the mixture is in its PC phase, which finally melts into the liquid at around $T \approx 460$ K.

The mixtures with 20 mol% ADA and AON, as to be expected, display a very similar behavior. They reveal orientational glass transitions with $T_g^o \approx 157$ K and 156 K, respectively. Further, no indication for a cold-crystallization into partially or fully orientationally ordered phases can be found in the heating scans and both mixtures melt into the liquid at around the same temperature as $CNA_{0.99}LiTFSI_{0.01}$.

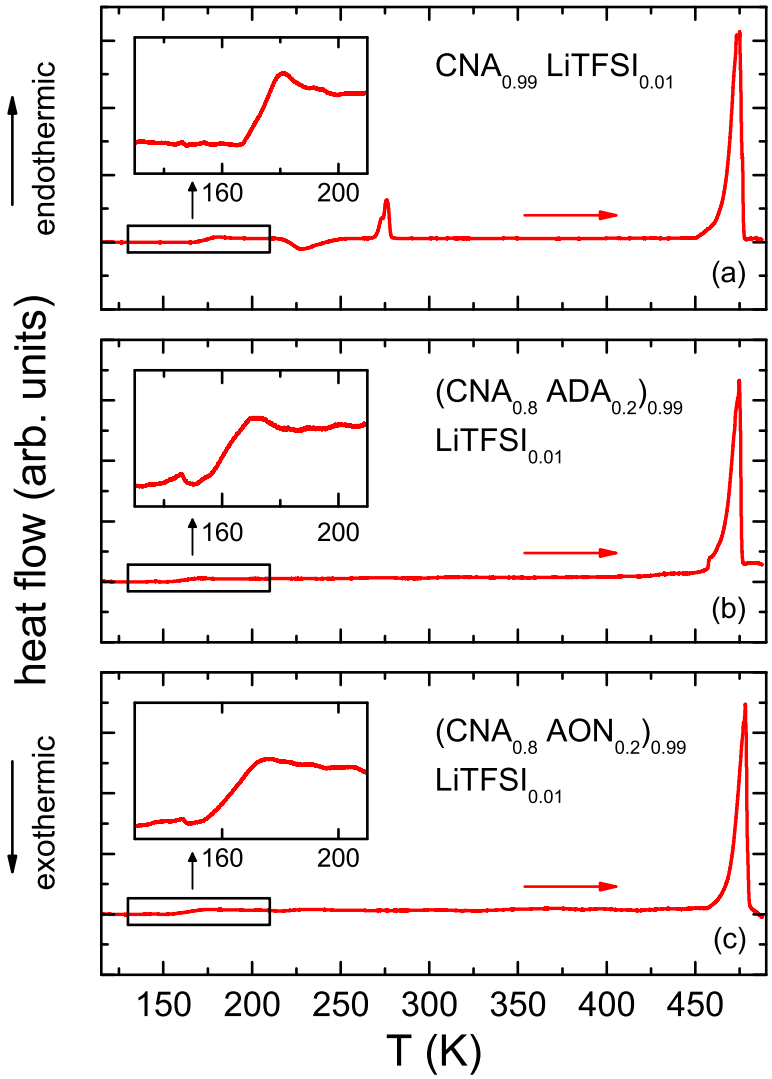

Figure 5.47: DSC measurements under heating with $10\,\mathrm{K\,min^{-1}}$ for $CNA_{0.99}LiTFSI_{0.01}$ (a), $(CNA_{0.8}ADA_{0.2})_{0.99}LiTFSI_{0.01}$ (b) and $(CNA_{0.8}AON_{0.2})_{0.99}LiTFSI_{0.01}$ (c) [275]. The scans were taken after cooling the samples from $T = 490\,\mathrm{K}$ to $110\,\mathrm{K}$ with $10\,\mathrm{K\,min^{-1}}$. Endothermic processes are pointing in positive y-direction. Insets in each frame magnify the temperature range of the orientational glass transitions.

Dielectric Spectroscopy Consequently, dielectric spectroscopy was employed to characterize the ionic and dipolar dynamics of the adamantane-based PC electrolytes. The obtained spectra are qualitatively very similar to the previously discussed ones of the dinitrile and cyclic alcohol based PCs. Figure 5.48 shows the dielectric spectra of $CNA_{0.99}LiTFSI_{0.01}$ as representative for all three mixtures. What immediately stands out about this spectrum is the well pronounced double-step like decrease in ε' from around 10 to 2. These steps do not stem from the typical EPs, observed in the other PC electrolytes, but the EP sets in at lower frequencies than the double-step, e.g., for $T = 334\,\mathrm{K}$ below $10^2\,\mathrm{Hz}$. Both in ε' and ε'', the contribution of the EP was cut off from the spectra in favor of a zoomed in view on the intrinsic relaxation steps.

Corresponding to the double-step in ε' a distinct relaxation peak in ε'' emerges with, e.g., peak frequency at around $10^3\,\mathrm{Hz}$ for $T = 229\,\mathrm{K}$. By comparing the two features, the relaxation peak can

undoubtedly be assigned to the lower and faster relaxation step in ε' and, further, when comparing with literature data [10, 262, 284, 285], this relaxation can be identified with the α relaxation of CNA arising from the on-site reorientational motion of the molecules.

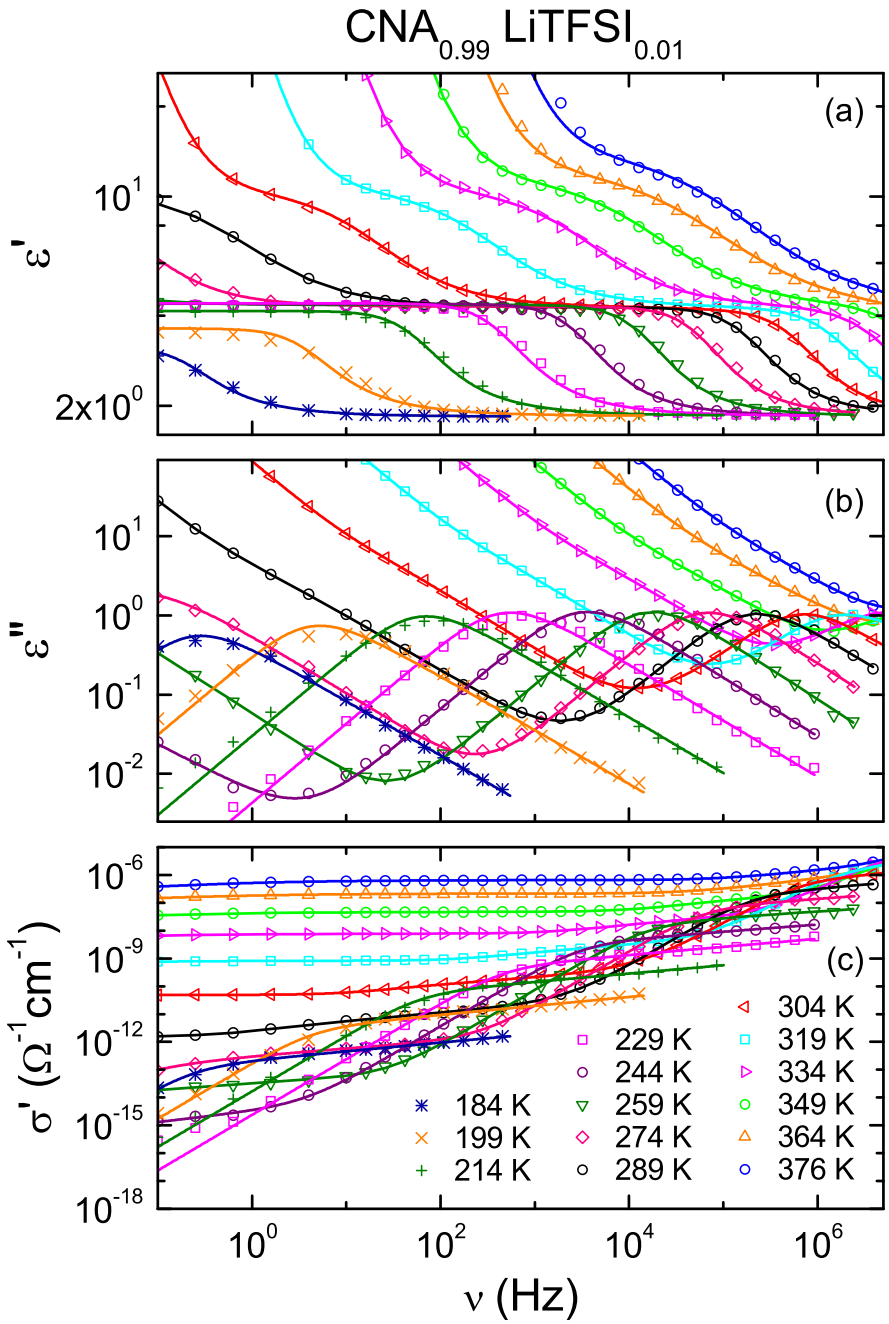

Figure 5.48: Dielectric spectra of ε' (a), ε'' (b) and σ' (c) of $CNA_{0.99}LiTFSI_{0.01}$ for various temperatures [275]. The solid lines in (a) and (b) are fits with the equivalent circuit approach utilizing one distributed RC circuits, two relaxation functions and a dc-conductivity contribution (see text for details).

This raises the question about the physical origin of the second step in ε'. In ε'' no second relaxation peak is visible and left to the α-relaxation peaks the seemingly typical dc-conductivity contribution shows up. When inspected closely, however, the slope of the decreasing contribution left of the α-

relaxation peaks is not -1 but rather changes. For example, for $T = 304\,\mathrm{K}$ between 10 and $10^4\,\mathrm{Hz}$ the curve is notably flatter than below 10 Hz. Here, the relaxation peak corresponding to the upper, slower step in ε' is somewhat hidden below the dc conductivity, as already known from the α relaxation of the DESs. Correspondingly, in the σ' spectrum, following the σ_{dc} plateau the data first reveal a slight increase before the onset of the α-relaxation contribution. Further evidence about the origin of this second relaxation feature will be given in the discussion of figure 5.49.

Once again the data were fitted with the equivalent-circuit approach. To describe the EP effects, here, one DRC was sufficient. In accordance with ref. [10] the α-relaxation was fitted with a CD function and the second slower relaxation process with a CC function. Altogether a good agreement of the fits with the experimental data was achieved and accurate values for the two relaxation times and σ_{dc} were obtained. The two other mixtures $(\mathrm{CNA}_{0.8}\mathrm{ADA}_{0.2})_{0.99}\mathrm{LiTFSI}_{0.01}$ and $(\mathrm{CNA}_{0.8}\mathrm{AON}_{0.2})_{0.99}\mathrm{LiTFSI}_{0.01}$ reveal very similar dielectric spectra as presented in figure 5.48, with the same double-step like decrease in ε' and similar conductivity values. From the fitting routine also two relaxation times and σ_{dc} were obtained for each mixture. The spectra and fits can be found in ref. [275].

To clarify the physical origin of the slower relaxation-like contribution, a dielectric measurement of pure CNA without LiTFSI was conducted under the very same conditions as for $\mathrm{CNA}_{0.99}\mathrm{LiTFSI}_{0.01}$. In figure 5.49 the results from this measurement are compared with the data of $\mathrm{CNA}_{0.99}\mathrm{LiTFSI}_{0.01}$ for $T = 319\,\mathrm{K}$. Interestingly, in ε', pure CNA without ions does not reveal a second, slower relaxation step, but the static permittivity plateau expands down to the lowest measured frequencies. At higher frequencies, i.e., in the region of the α-relaxation, however, both measurements show good agreement. Similar deviation occur in in ε''. Here, the data match in the region of the α-relaxation peak, however, the pure CNA sample reveals a largely unobstructed left flank of the α-relaxation peak stretching from around 10^3 to $10^6\,\mathrm{Hz}$, because of the drastically reduced dc-conductivity. Additionally, no contribution arises between the dc-conductivity contribution with slope -1 (0.1 to $10^3\,\mathrm{Hz}$) and the left flank of the α-relaxation peak. The reduced dc conductivity is even better visible in the σ' representation, where the pure CNA sample without ions shows an around 4 orders of magnitude drop in σ_{dc}.

This finding allows for two conclusions. Firstly, the dc conductivity of CNA can be enhanced by around four orders of magnitude with the addition of 1 mol% of LiTFSI, while it should be noted that pure CNA should theoretically posses zero dc conductivity but in real measurements always small concentrations of ionic impurities lead to a non-zero dc conductivity of purely molecular samples. Secondly, the emergence of the slower relaxation-like process is undoubtedly connected to the addition of the ions in the system.

Several scenarios might explain this ion-related relaxation-like contribution. Obviously by introducing 1 mol% LiTFSI, also 1 mol% of dipolar TFSI anions are brought into the system, which might exhibit a rather independent reorientational relaxation accounting for the slow relaxation. However, as only every one hundredth dipole in this system is a TFSI anion and the slow relaxation is of similar relaxation strength as the α relaxation, this explanation seems unlikely. Alternatively, ions could attach to the CNA molecules. Such formations would display an enhanced dipolar moment and experience increased steric hindrance for reorientational motion, thus explaining the observed properties of the slow relaxation. Also non-intrinsic Maxwell-Wagner type relaxation (see chapter 3.2.2) could be imagined arising from the different ionic mobility along the grain boundaries and in the bulk of the polycrystalline sample.

However, most likely seems a relaxation-like contribution due the ionic diffusion inside the sample, as discussed in chapters 3.2.4 and 3.2.5. To test this hypothesis, in figure 5.49 the slow relaxation was fitted with the RBM (blue dashed line). For this purpose, both the CC function and the independent dc-

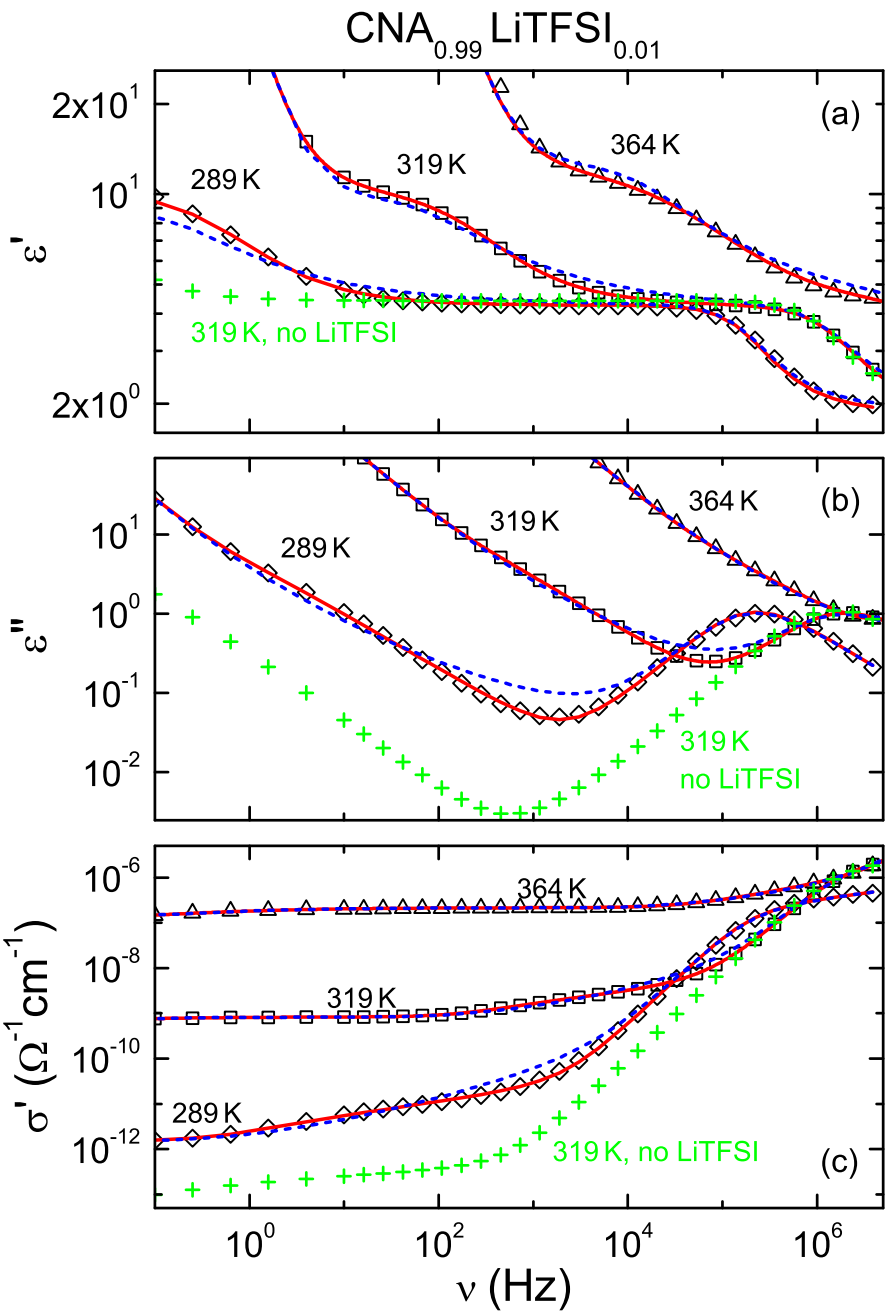

Figure 5.49: Comparison of two different fit functions to describe the slower relaxation in $CNA_{0.99}LiTFSI_{0.01}$ for selected temperatures [275]. The solid red lines are the same fits as presented in figure 5.48, which use a CC function for this relaxation-like contribution. The blue dashed lines are fits using the RBM (equation 3.35) integrated into the equivalent circuit approach (see text for details). The green cross are data of pure CNA without LiTFSI at $T = 319\,\mathrm{K}$, revealing the absence of the slower relaxation process. The data of pure CNA were vertically shifted to match the $CNA_{0.99}LiTFSI_{0.01}$ data.

conductivity contribution of the above described equivalent circuit used for $CNA_{0.99}LiTFSI_{0.01}$ were replaced by the RBM, which only contains two parameters, the ion relaxation time τ_{RBM} and dc conductivity σ_{dc}. So in the case of the slow relaxation in $CNA_{0.99}LiTFSI_{0.01}$, the RBM can qualitatively

describe the step-wise decrease in ε' and the dc-conductivity plateau, which is connected to the step height in ε' within the model. At the lowest presented temperature, however, deviations between the fits and the experimental data occur, especially visible in ε'' at the transition from the slow relaxation process to the α-relaxation peak. Keeping in mind that the CC plus dc conductivity approach utilizes two parameters more than the RBM, such deviation could be expected. Hence, the ability of the RBM to describe the observed slow relaxation-like contribution in reasonable agreement supports the notion that this process arises due to ionic translational motion.

With this, $CNA_{0.99}LiTFSI_{0.01}$ is an interesting system to study the simultaneous emergence of a dipolar and a presumably ionic relaxation process in a solid material, where both processes reveal classical relaxation features (step in ε') and both are distinctly separated in the dielectric spectrum. A constellation which, to the best of the author's knowledge, has not been reported like this in literature so far.

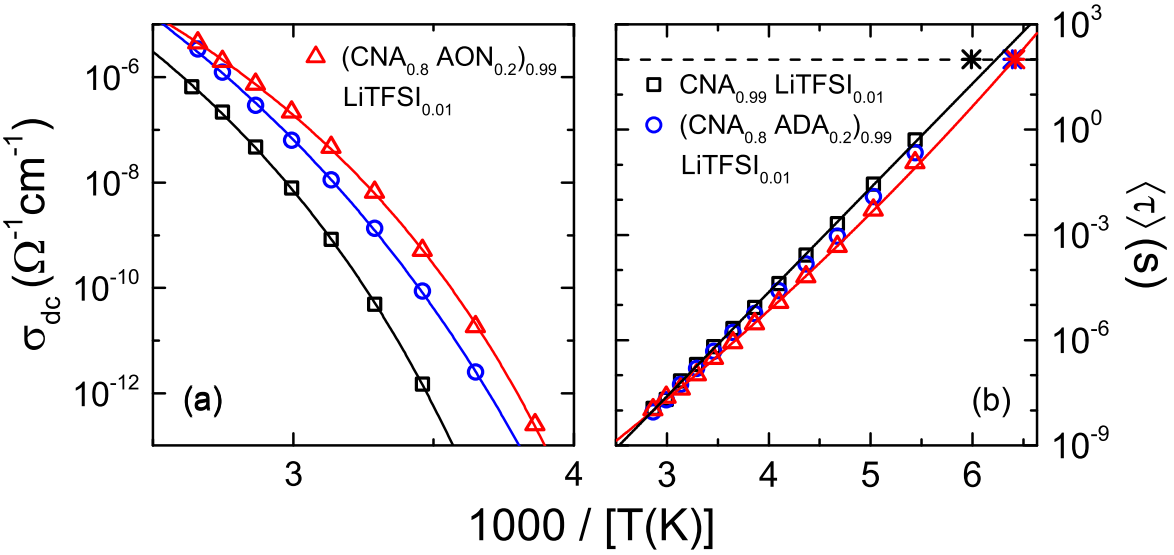

Figure 5.50: Temperature dependence of the dc conductivity (a) and the α-relaxation time (b) of all three adamantane based mixtures in Arrhenius representation [275]. (a) The solid lines are fits with the VFT equation adapted for the conductivity (equation 3.30). (b) The solid black line through the black squares is a fit with the Arrhenius law (equation 3.1) and the solid red line through the red triangles is a fit with the VFT law (equation 3.2). The horizontal dashed line highlights $\tau = 100\,\mathrm{s}$ and the stars are relaxation times estimated from the DSC measurements via $\tau(T_g) = 100\,\mathrm{s}$.

Ionic and Dipolar Dynamics Figure 5.49 nicely demonstrated the massive conductivity enhancement in CNA with the addition of only 1 mol% ions. With the results from the dinitrile and cyclic alcohol based mixtures a further increase of the dc conductivity can be expected with the addition of 20 mol% ADA and AON. Thus, figure 5.50 presents the temperature dependence of the dc conductivity and the α-relaxation times of all three mixtures as obtained from the fitting routine [275]. Indeed, in the adamantane-based mixtures $CNA_{0.99}LiTFSI_{0.01}$ possesses the smallest dc conductivity over the whole temperatures range [see 5.50 (a)], while at around RT the addition of ADA enhances the ionic conductivity by roughly one order of magnitude and the addition of AON by another half an order of magnitude. The difference in dc conductivity between the systems increases with decreasing tempera-

ture, which is the opposite behavior as found for the dinitrile mixtures (see figure 5.35), thus, indicating a different enhancement mechanism compared to those samples.

With the results of the cyclic alcohol PCs in mind, the dc-conductivity enhancement in the adamantane-based mixtures might arise from increasingly faster reorientational motions of the molecules. Surprisingly, however, the α-relaxation times of the adamantane based mixtures reveal a significantly different temperature dependence than the dc conductivity for all mixtures [see 5.50 (b)]. The α-relaxation times of $CNA_{0.99}LiTFSI_{0.01}$ can even sufficiently be described by an Arrhenius fit and the other two mixtures only exhibit slight deviations from linear behavior in the τ vs. $1000/T$ plot, demonstrated by a VFT fit of the $(CNA_{0.8}AON_{0.2})_{0.99}LiTFSI_{0.01}$ mixture. Furthermore, the α-relaxation times of all there mixtures are almost equal and only reach about an order of magnitude difference at the lowest temperature, far below temperatures at which the dc-conductivity could effectively be measured. Thus, faster reorientational dynamics cannot explain the conductivity enhancement in the adamantane-based mixtures.

An alternative explanation of the conductivity enhancement might be an improved coupling of rotational and translational dynamics in the PC, as present for the dinitrile mixtures. Already the fundamentally different temperature dependencies in figure 5.50 indicate no such coupling, still figure 5.51 provides the established comparison of the temperature dependence of the α-relaxation times and the dc resistivity in a common Arrhenius plot for all mixtures, however, with the interesting addition of the relaxations times of the slower relaxation found in the dielectric spectrum.

As expected, figure 5.51 demonstrates a complete decoupling of the translational ionic motion, represented by the dc resistivity, from the on-site reorientational dynamics of the dipolar molecules, represented by the α-relaxation time, here denoted as τ_{dipolar}, for all three mixtures. However, interestingly the relaxation times determined from the slower relaxation process with the CC function, here denoted τ_{ion}, perfectly couple to the dc resistivity. Additionally, for $CNA_{0.99}LiTFSI_{0.01}$ the relaxation times obtained from the alternative RBM fits of the slower relaxation closely coincide with the relaxation times estimated by the CC function. This finding clearly demonstrates the inherent connection of the slower relaxation process to the ionic translational motion.

Altogether, there is no rotation-translation coupling and there is no conductivity enhancement effect from faster reorientational dynamics in the adamantane based mixtures. Hence, no indications of an effective "revolving door" mechanism are present here. This supports the notion that for an effective "revolving door" mechanism the reorientation of the molecules must provide some transient vacant volume, which is not the case for three dimensional, globular molecules like the adamantane based compounds.

As introduced in chapter 2.2.2, a large amount of literature on ionic PC electrolytes discusses the peculiar properties of the PC lattice and its influence on the ionic conductivity (e.g., [18, 19, 71, 79, 80]). Thus, in the adamantane-based mixtures also rather vacancies and grain boundaries within the PC lattice might promote the ionic migration than the on-site reorientational motions of the molecules. Further, the introduction of 20 mol% ADA or AON might increase the density of vacancies and grain boundaries and, thus, lead to an enhancement of the dc-conductivity.

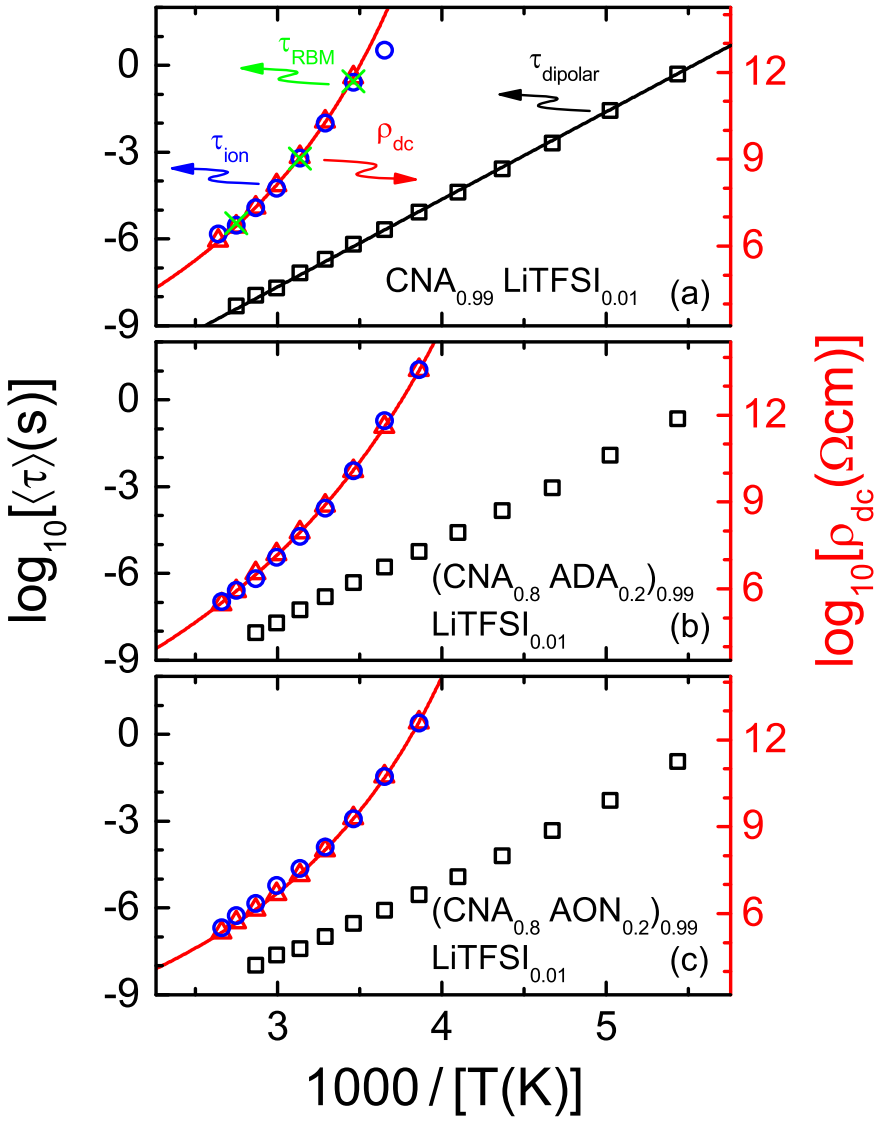

Figure 5.51: Comparison of the temperature dependence of translational and reorientational dynamics for all three adamantane based mixtures [275]. The plots were constructed in straight analogy to figure 5.26 without the third frame for the viscosity. Here, black squares (left scale) present α-relaxation times corresponding to the faster, dipolar relaxation process (τ_{dipolar}) in the dielectric spectrum. Blue circles and green crosses (left scale) are relaxation times corresponding to the slower relaxation process determined by either the CC (τ_{ion}) or the RBM (τ_{RBM}) function, respectively. The red triangles (right scale) are the dc resistivity (ρ_{dc}). The red solid lines are the VFT fits from 5.50 (a) calculated for the resistivity and the black solid line is the Arrhenius fit from 5.50 (b).

5.2.4 Conclusion

Altogether, the presented measurement series is a systematic investigation of molecular PC electrolytes with special focus on the influence of reorientational motion and geometrical shape of the molecules on the ionic conductivity. With the findings from the three different PC systems, the proposed questions in the introduction of this chapter 5.2 can be answered.

The established notion that the reorientational motions in the molecular PC electrolytes is beneficial to the ionic mobility could be validated for systems with good rotation-translation coupling. In particular with the HEX-OCT mixture, an example where the rotation-translation coupling does not significantly change throughout the mixing series, the direct proportionality of the reorientational motions and the ionic mobility could be demonstrated: the faster the reorientational motion the higher the ionic conductivity. This findings hints to the relevance of a "revolving door" mechanism in molecular PC electrolytes.

For the rotation-translation coupling in PC electrolytes the geometrical shape of the molecules is especially relevant. One or two dimensional molecules like the dinitrile and the cyclic alcohol based PCs revealed the best examples of this coupling and a complete decoupling was found for the adamanatane based mixtures. Additionally, the integration of rather large and asymmetrical molecules into the SN PC lattice shown extraordinary enhancement effects for the ionic conductivity. This finding clearly indicates the presence of a "revolving door" mechanism in molecular PC electrolytes, at least in the roughly one-dimensional dinitrile compounds.

Finally, the adamantane-base mixtures served rather as a prove of concept by demonstrating a rotation-translation *de*coupling for three dimensional globular compounds. Interestingly, however, this complete decoupling allowed for the dipolar and ionic relaxation in the dielectric spectrum to clearly separate and enables an unobstructed investigation of ionic conductivity relaxation processes in molecular PCs.

With these findings, the present work paves the way for the further enhancement of the ionic conductivity of molecular PC electrolytes. The clear objective for such efforts should be to improve the rotation-translation coupling by introducing large, asymmetric molecules in PC systems with already very fast reorientational dynamics at around RT and to simultaneously achieve melting-points of these systems well above $T = 350\,\mathrm{K}$.

Theoretically, in any binary mixture, e.g., SN-GN or even SN with 1 mol% $LiPF_6$, according to the binary phase diagram introduced in chapter 2.1.1, for every mixing ratio besides the eutectic, below its initial melting a suspension is formed. The composition of this suspension is then a liquid in eutectic composition and a solid material of one component. All here presented PC electrolytes could, therefore, be reinterpreted as suspensions, where the main conductive path for the ions goes along the liquid proportions. Since, no discontinuities in the conductivity or the α-relaxations can be found at the temperature of eventual crystallization of the liquid proportions, which occurs at T_m of the eutectic mixture, one could assume that this transition is supercooled and the liquid proportions undergo normal glassy freezing. To clarify this criticism, further experimental work is necessary.

6 Summary

This work presents a comprehensive dielectric characterization of two classes of ionic conductors with potential for wide-spread technical application in the future. Furthermore, the two material classes enabled a thorough investigation of the interdependence and interaction of dipolar reorientational and ionic translational dynamics in highly ionically conducting amorphous systems.

The present work is the first investigation of DESs combining dielectric and mechanical spectroscopy in a broad temperature and frequency range. In particular for the DESs, the findings can be summed up by the following points:

- The here investigated DESs possess large amounts of dipolar molecules, the so-called HBDs, and, consequently, in their dielectric spectra a reorientational relaxation arises. This relaxation may be strongly superimposed by the dc-conductivity contribution in ε'' but is clearly visible and analyzable in ε'.

- The comparison with dielectric data of the pure HBDs supports this notion and gives further insights into the influence of the salt on the dynamics of the HBDs. Interestingly, even in the chemically very similar compounds glycerol and ethylene glycol, the addition of ChCl has opposing effects on the reorientational relaxation times, due to the spatially different formation of the H-bond network in these two systems.

- It could be shown that the dielectric spectra of DESs are best analyzed in the permittivity representation and then compared with the compliance representation of the mechanical data. Relaxation times τ_ε and τ_J obtained in this way complement each other. The dielectric modulus representation is rather unsuited, because the contributions from the dipolar relaxation and the ionic conductivity are partly merged and hardly distinguishable. Still, when comparing with the mechanical modulus, the main peak in the dielectric modulus fits best.

- For glyceline and ethaline, the comparison of dielectric and mechanical data clearly demonstrates that both, dipolar reorientational and ionic translational dynamics, are coupled to the viscosity. The peculiar case of reline, however, which displays a partial decoupling of the two processes and a distinctly increased ionic conductivity for a given τ_ε compared to the other two DESs, needs further experimental data for a conclusive explanation. Still such decoupling could point towards possible optimization strategies for DESs.

For the molecular PC electrolytes, the present work provides a systematic investigation of the effect of the molecular reorientational motions and the shape and size of the molecules on the ionic conductivity. The findings can be summed up by the following points:

- The rotation-translation coupling in molecular PC electrolytes strongly depends on the geometrical shape and size of the molecules forming the PC lattice. The small and only little one-dimensionally stretched succinonitrile reveals only a weak "revolving door" mechanism,

but the integration of larger or smaller molecules into the PC lattice increases the rotation-translation coupling. The larger two-dimenisonal, disc-shaped cyclic-alcohol molecules HEX and OCT display good coupling throughout the mixing series and the three-dimensional, globular adamantane-based systems demonstrate a complete decoupling.

- An increasing rotation-translation coupling seems beneficial for the ionic mobility, which is especially evident in the SN-GN series and by the low conductivity values found for the adamantane-based mixtures with decoupled ionic dynamics.
- If there is rotation-translation coupling, as present in the HEX-OCT mixing series, the ion mobility scales proportionally to the timescale of on-site molecular reorientational motions.
- Systems like the adamantane-based mixtures exhibit complete rotation-translation decoupling and, thus, offer the opportunity to study a presumably ionic relaxation separately.

The fact, that both material classes possess reorienting dipolar molecules and translational moving ions and are now thoroughly characterized by dielectric spectroscopy, offers the unique opportunity to compare all investigated systems in an adapted Walden plot (see figure 6.1). This plot uses the molar conductivity $\Lambda_m = \sigma_{dc}/c$ for the y-axis, where c is the ion concentration in units mol%. Λ_m is effectively the conductivity contribution per ion pair in the sample and is, thus, proportional to the ion mobility, which makes it possible to directly compare the DESs with the PC electrolytes. Comparing absolute dc-conductivity values would distort the data towards the DESs, which have vastly higher ion concentrations. For the x-axis, figure 6.1 uses the inverse of the reorientational relaxation time τ_ε, since especially the PCs do not display a liquid-like viscosity.

So figure 6.1 presents the dependence of the effective ion mobility on the reorientational dynamics of the dipolar molecules in both DESs and PC electrolytes. It enables basically a similar classification of ionic conductors as after Angell and coworkers [152, 159, 162] (chapter 3.2.4), where systems with high ion mobility for a given τ_ε lie towards the upper left corner in figure 6.1 and systems with low ion mobility in the lower right corner.

Starting with the DESs, figure 6.1 is a mirrored representation of figure 5.29 (c). Glyceline and ethaline fall on a line with slope 1 in the double logarithmic plot, meaning both systems display the same ion mobility for a given τ_ε and the two processes are coupled. Reline is the exception. It displays a higher ion mobility for a given τ_ε than the other two DESs and a non-linear trend indicating decoupling of the two dynamics. Reline is the system most shifted towards to the upper left corner in this plot and is, thus, in this specific criterion the best of all investigated systems, because it shows the highest ion mobility for a given τ_ε of all systems. Still looking at absolute values, reline of all investigated DESs has the lowest ionic conductivity for a given temperature.

Surprisingly, the HEX-OCT mixtures fall in line with glyceline and ethaline. Even though these mixtures are no candidates for application, because their melting temperatures lie well below RT and even there the mixtures are poorly conducting, when solely focusing on conductivity contribution per ion pair for a given τ_ε, the HEX-OCT mixtures reveal a liquid-like conductivity. That means, in the HEX-OCT mixtures, for a certain reorientation velocity of the surrounding molecules the ion mobility is enormously high and comparable to the DESs, where the surrounding molecules not only reorient with the same velocity but additionally move translationally.

Close but distinctly shifted towards the bottom right corner are the dinitrile mixtures. Especially the SNPN mixture, which from all PCs revealed the best dc conductivity when approaching RT, displays only an by an order of magnitude reduced Λ_m compared to glyceline, ethaline and the HEX-OCT

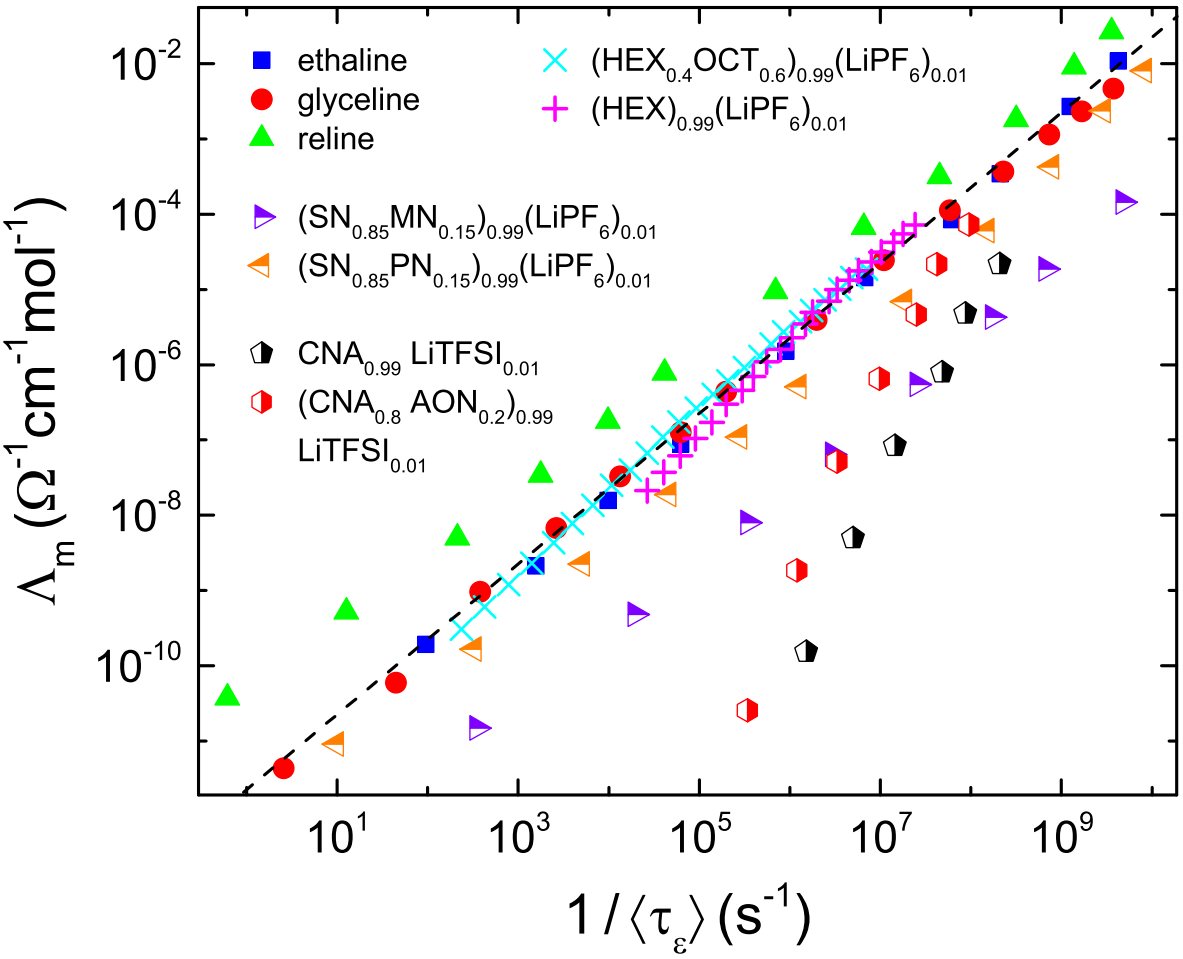

Figure 6.1: Molar conductivity Λ_m vs inverse reorientational relaxation time τ_ε plot for selected mixtures including all different systems investigated in the present work. The full symbols are the DESs, horizontally half-filled symbols are selected dinitrile based mixtures, vertically half-filled symbols are selected adamantane based mixtures and crosses as well as pluses are selected cyclic alcohol based mixtures. The dashed black line visualizes a slope of 1 in the double logarithmic plot.

mixtures. The SNMN mixture is further shifted to the bottom right corner and Λ_m is reduced by roughly two orders of magnitude for a given τ_ε compared to SNPN. Both mixtures still follow a linear trend with slope 1, as expected since both dynamic processes were already identified as being coupled.

Finally, for the adamantane-based mixtures the meaningfulness of this plot is questionable, since the complete decoupling of dc conductivity and reorientational dynamics was unequivocally demonstrated in figure 5.51. Due to this decoupling, these systems reveal a much steeper slope than 1. They start at low temperatures (i.e. low Λ_m) shifted far to the right compared to the other systems and rapidly approach good ion mobility comparable to the DESs with increasing temperature.

Figure 6.1 demonstrates the relevance of reorientational dynamics for the ionic conductivity in most systems, where both dynamics are present. On the basis of these data possible routes for the optimization of DESs and the PC electrolytes can be concluded. DESs, due to being liquids, naturally display a coupling of the ionic and dipolar dynamics to the overall viscosity. Only for cases like reline some sort of decoupling can be found and here for a given τ_ε higher ion mobility can be obtained. Still,

in terms of absolute conductivity values those are minor effects compared to the overall conductivity enhancement with decreasing T_g, as seen when comparing reline with ethaline (see RT conductivitiy in figure 5.25). For the PCs, however, the dinitrile and cyclic-alcohol-based PC electrolytes reveal an astonishing high ion mobility for solid materials. Ironically, the HEX-OCT mixtures show the best ion mobility but are the least suitable system for technical application. Thus, the future goal to optimize PC electrolytes may be to generate an ionic conductivity mechanism as present in the HEX-OCT or SNPN mixtures in PCs with high melting points like CNA.

Bibliography

[1] Etacheri, V., Marom, R., Elazari, R., Salitra, G. & Aurbach, D. Challenges in the development of advanced Li-ion batteries: a review. *Energy Environ. Sci.* **4**, 3243 (2011).

[2] Goodenough, J. B. & Kim, Y. Challenges for rechargeable Li batteries. *Chem. Mat.* **22**, 587 (2010).

[3] Paiva, A. *et al.* Natural deep eutectic solvents - Solvents for the 21st century. *ACS Sustain. Chem. Eng.* **2**, 1063 (2014).

[4] Smith, E. L., Abbott, A. P. & Ryder, K. S. Deep eutectic solvents (DESs) and their applications. *Chem. Rev.* **114**, 11060 (2014).

[5] Rogers, R. D. & Seddon, K. R. Ionic liquids - Solvents of the future? *Science* **302**, 792 (2003).

[6] Zhang, Q. H., Vigier, K. D., Royer, S. & Jerome, F. Deep eutectic solvents: Syntheses, properties and applications. *Chem. Soc. Rev.* **41**, 7108 (2012).

[7] Wagle, D. V., Zhao, H. & Baker, G. A. Deep eutectic solvents: Sustainable media for nanoscale and functional materials. *Accounts Chem. Res.* **47**, 2299 (2014).

[8] Geiculescu, O. E. *et al.* Novel binary deep eutectic electrolytes for rechargeable Li-ion batteries based on mixtures of alkyl sulfonamides and lithium perfluoroalkylsulfonimide salts. *J. Power Sources* **307**, 519 (2016).

[9] Millia, L. *et al.* Bio-inspired choline chloride-based deep eutectic solvents as electrolytes for lithium-ion batteries. *Solid State Ion.* **323**, 44 (2018).

[10] Brand, R., Lunkenheimer, P. & Loidl, A. Relaxation dynamics in plastic crystals. *J. Chem. Phys.* **116**, 10386 (2002).

[11] Alarco, P. J., Abu-Lebdeh, Y., Abouimrane, A. & Armand, M. The plastic-crystalline phase of succinonitrile as a universal matrix for solid-state ionic conductors. *Nat. Mater.* **3**, 476 (2004).

[12] Motavalli, J. A solid future. *Nature* **526**, S96 (2015).

[13] Abbott, A. P., Capper, G., Davies, D. L., Rasheed, R. K. & Tambyrajah, V. Novel solvent properties of choline chloride/urea mixtures. *Chem. Commun.* 70 (2003).

[14] Abbott, A. P., Boothby, D., Capper, G., Davies, D. L. & Rasheed, R. K. Deep eutectic solvents formed between choline chloride and carboxylic acids: Versatile alternatives to ionic liquids. *J. Am. Chem. Soc.* **126**, 9142 (2004).

[15] Abbott, A. R., Capper, G. & Gray, S. Design of improved deep eutectic solvents using hole theory. *ChemPhysChem* **7**, 803 (2006).

[16] Tripathy, S. N. *et al.* Glass transition dynamics and conductivity scaling in ionic deep eutectic solvents: The case of (acetamide + lithium nitrate/sodium thiocyanate) melts. *J. Chem. Phys.* **142**, 184504 (2015).

[17] MacFarlane, D. R. & Forsyth, M. Plastic crystal electrolyte materials: New perspectives on solid state ionics. *Adv. Mater.* **13**, 957 (2001).

[18] Pringle, J. M., Howlett, P. C., MacFarlane, D. R. & Forsyth, M. Organic ionic plastic crystals: Recent advances. *J. Mater. Chem.* **20**, 2056 (2010).

[19] Pringle, J. M. Recent progress in the development and use of organic ionic plastic crystal electrolytes. *Phys. Chem. Chem. Phys.* **15**, 1339 (2013).

[20] Geirhos, K., Lunkenheimer, P., Michl, M., Reuter, D. & Loidl, A. Communication: Conductivity enhancement in plastic-crystalline solid-state electrolytes. *J. Chem. Phys.* **143**, 081101 (2015).

[21] Zachariah, M. *et al.* Self-diffusion, phase behavior, and Li^+ ion conduction in succinonitrile-based plastic cocrystals. *J. Phys. Chem. C* **119**, 27298 (2015).

[22] Zachariah, M., Romanini, M., Tripathi, P., Tamarit, J. L. & Macovez, R. Molecular diffusion and dc conductivity perfectly correlated with molecular rotational dynamics in a plastic crystalline electrolyte. *Phys. Chem. Chem. Phys.* **17**, 16053 (2015).

[23] Sippel, P., Krohns, S., Reuter, D., Lunkenheimer, P. & Loidl, A. Importance of reorientational dynamics for the charge transport in ionic liquids. *Phys. Rev. E* **98**, 052605 (2018).

[24] Wilkes, J. S. & Zaworotko, M. J. Air and water stable 1-ethyl-3-methylimidazolium based ionic liquids. *J. Chem. Soc.-Chem. Commun.* 965 (1992).

[25] Angell, C. A., Ansari, Y. & Zhao, Z. F. Ionic liquids: Past, present and future. *Faraday Discuss.* **154**, 9 (2012).

[26] Seddon, K. R. Ionic liquids for clean technology. *J. Chem. Technol. Biotechnol.* **68**, 351 (1997).

[27] Welton, T. Room-temperature ionic liquids. Solvents for synthesis and catalysis. *Chem. Rev.* **99**, 2071 (1999).

[28] Armand, M., Endres, F., MacFarlane, D. R., Ohno, H. & Scrosati, B. Ionic-liquid materials for the electrochemical challenges of the future. *Nat. Mater.* **8**, 621 (2009).

[29] MacFarlane, D. R. *et al.* Energy applications of ionic liquids. *Energy Environ. Sci.* **7**, 232 (2014).

[30] Romero, A., Santos, A., Tojo, J. & Rodriguez, A. Toxicity and biodegradability of imidazolium ionic liquids. *J. Hazard. Mater.* **151**, 268 (2008).

[31] Deetlefs, M. & Seddon, K. R. Assessing the greenness of some typical laboratory ionic liquid preparations. *Green Chem.* **12**, 17 (2010).

[32] Petkovic, M., Seddon, K. R., Rebelo, L. P. N. & Pereira, C. S. Ionic liquids: A pathway to environmental acceptability. *Chem. Soc. Rev.* **40**, 1383 (2011).

[33] Abbott, A. P. *et al.* Preparation of novel, moisture-stable, lewis-acidic ionic liquids containing quaternary ammonium salts with functional side chains. *Chem. Commun.* 2010 (2001).

[34] Marcus, Y. *Deep Eutectic Solvents* (Springer Nature Switzerland AG, 2019).

[35] Alonso, D. A. *et al.* Deep eutectic solvents: The organic reaction medium of the century. *Eur. J. Org. Chem.* 612 (2016).

[36] Parnham, E. R. & Morris, R. E. Ionothermal synthesis of zeolites, metal-organic frameworks, and inorganic-organic hybrids. *Accounts Chem. Res.* **40**, 1005 (2007).

[37] Morris, R. E. Ionothermal synthesis-ionic liquids as functional solvents in the preparation of crystalline materials. *Chem. Commun.* 2990 (2009).

[38] Zhang, J., Wu, T., Chen, S. M., Feng, P. Y. & Bu, X. H. Versatile structure-directing roles of deep-eutectic solvents and their implication in the generation of porosity and open metal sites for gas storage. *Angew. Chem.-Int. Edit.* **48**, 3486 (2009).

[39] Carriazo, D., Serrano, M. C., Gutierrez, M. C., Ferrer, M. L. & del Monte, F. Deep-eutectic solvents playing multiple roles in the synthesis of polymers and related materials. *Chem. Soc. Rev.* **41**, 4996 (2012).

[40] del Monte, F., Carriazo, D., Serrano, M. C., Gutierrez, M. C. & Ferrer, M. L. Deep eutectic solvents in polymerizations: A greener alternative to conventional syntheses. *ChemSusChem* **7**, 999–1009 (2014).

[41] Gutierrez, M. C., Rubio, F. & del Monte, F. Resorcinol-formaldehyde polycondensation in deep eutectic solvents for the preparation of carbons and carbon-carbon nanotube composites. *Chem. Mat.* **22**, 2711 (2010).

[42] Abbott, A. P., Capper, G., Davies, D. L. & Rasheed, R. K. Ionic liquid analogues formed from hydrated metal salts. *Chem.-Eur. J.* **10**, 3769 (2004).

[43] Abbott, A. P., El Ttaib, K., Ryder, K. S. & Smith, E. L. Electrodeposition of nickel using eutectic based ionic liquids. *Trans. Inst. Metal Finish.* **86**, 234 (2008).

[44] Haerens, K., Matthijs, E., Chmielarz, A. & Van der Bruggen, B. The use of ionic liquids based on choline chloride for metal deposition: A green alternative? *J. Environ. Manage.* **90**, 3245 (2009).

[45] Ferreira, E. S. C., Pereira, C. M. & Silva, A. F. Electrochemical studies of metallic chromium electrodeposition from a Cr(III) bath. *J. Electroanal. Chem.* **707**, 52 (2013).

[46] Lapena, D., Lomba, L., Artal, M., Lafuente, C. & Giner, B. The NADES glyceline as a potential green solvent: A comprehensive study of its thermophysical properties and effect of water inclusion. *J. Chem. Thermodyn.* **128**, 164 (2019).

[47] Nkuku, C. A. & LeSuer, R. J. Electrochemistry in deep eutectic solvents. *J. Phys. Chem. B* **111**, 13271–13277 (2007).

[48] Simon, P. & Gogotsi, Y. Materials for electrochemical capacitors. *Nat. Mater.* **7**, 845 (2008).

[49] Beguin, F., Presser, V., Balducci, A. & Frackowiak, E. Carbons and electrolytes for advanced supercapacitors. *Adv. Mater.* **26**, 2219 (2014).

[50] Rivera, A., Brodin, A., Pugachev, A. & Rossler, E. A. Orientational and translational dynamics in room temperature ionic liquids. *J. Chem. Phys.* **126**, 114503 (2007).

[51] Sangoro, J. R. *et al.* Charge transport and mass transport in imidazolium-based ionic liquids. *Phys. Rev. E* **77**, 051202 (2008).

[52] Sippel, P., Lunkenheimer, P., Krohns, S., Thoms, E. & Loidl, A. Importance of liquid fragility for energy applications of ionic liquids. *Sci. Rep.* **5**, 13922 (2015).

[53] Faraone, A. *et al.* Glycerol hydrogen-bonding network dominates structure and collective dynamics in a deep eutectic solvent. *J. Phys. Chem. B* **122**, 1261 (2018).

[54] Reuter, D., Binder, C., Lunkenheimer, P. & Loidl, A. Ionic conductivity of deep eutectic solvents: the role of orientational dynamics and glassy freezing. *Phys. Chem. Chem. Phys.* **21**, 6801 (2019).

[55] Mukherjee, K., Das, A., Choudhury, S., Barman, A. & Biswas, R. Dielectric relaxations of (acetamide + electrolyte) deep eutectic solvents in the frequency window, $0.2 \leq \nu/\mathrm{GHz} \leq 50$: Anion and cation dependence. *J. Phys. Chem. B* **119**, 8063 (2015).

[56] Mukherjee, K., Das, S., Tarif, E., Barman, A. & Biswas, R. Dielectric relaxation in acetamide plus urea deep eutectics and neat molten urea: Origin of time scales via temperature dependent measurements and computer simulations. *J. Chem. Phys.* **149**, 124501 (2018).

[57] Mukherjee, K., Tarif, E., Barman, A. & Biswas, R. Dynamics of a peg based non-ionic deep eutectic solvent: Temperature dependence. *Fluid Phase Equilib.* **448**, 22–29 (2017).

[58] Das, S., Biswas, R. & Mukherjee, B. Collective dynamic dipole moment and orientation fluctuations, cooperative hydrogen bond relaxations, and their connections to dielectric relaxation in ionic acetamide deep eutectics: Microscopic insight from simulations. *J. Chem. Phys.* **145**, 084504 (2016).

[59] Griffin, P. J., Cosby, T., Holt, A. P., Benson, R. S. & Sangoro, J. R. Charge transport and structural dynamics in carboxylic-acid-based deep eutectic mixtures. *J. Phys. Chem. B* **118**, 9378 (2014).

[60] Harifi-Mood, A. R. & Buchner, R. Density, viscosity, and conductivity of choline chloride plus ethylene glycol as a deep eutectic solvent and its binary mixtures with dimethyl sulfoxide. *J. Mol. Liq.* **225**, 689 (2017).

[61] Shekaari, H., Zafarani-Moattar, M. T. & Mohammadi, B. Thermophysical characterization of aqueous deep eutectic solvent (choline chloride / urea) solutions in full ranges of concentration at T = (293.15 - 323.15) K. *J. Mol. Liq.* **243**, 451 (2017).

[62] Timmermans, J. Un nouvel état mésomorphe les cristaux organiques plastiques. *J. Chim. Phys.* **35**, 331 (1938).

[63] Timmermans, J. Plastic crystals - A historical review. *J. Phys. Chem. Solids* **18**, 1 (1961).

[64] Sherwood, J. N. *The Plastically Crystalline State - Orientationally-Disordered Crystals*, chap. 1.1, 1–2 (John Wiley & Sons, New York, 1979).

[65] Tombari, E. & Johari, G. P. Structural fluctuations and orientational glass of levoglucosan - High stability against ordering and absence of structural glass. *J. Chem. Phys.* **142**, 104501 (2015).

[66] Aronsson, R. *et al.* Fast ion conductors with rotating sulphate ions. *J. Phys. Colloq.* **41**, 35 (1980).

[67] Nilsson, L., Thomas, J. O. & Tofield, B. C. The structure of the high-temperature solid electrolyte lithium sulfate at 908 K. *J. Phys. C: Solid State Phys.* **13**, 6441 (1980).

[68] Börjesson, L. & Torell, L. M. Reorientational motion in superionic sulfates - A raman linewidth study. *Phys. Rev. B* **32**, 2471 (1985).

[69] Cooper, E. I. & Angell, C. A. Ambient-temperature plastic crystal fast ion conductors (PLICFICS). *Solid State Ion.* **18-19**, 570 (1986).

[70] MacFarlane, D. R., Huang, J. H. & Forsyth, M. Lithium-doped plastic crystal electrolytes exhibiting fast ion conduction for secondary batteries. *Nature* **402**, 792 (1999).

[71] Abu-Lebdeh, Y., Alarco, P. J. & Armand, M. Conductive organic plastic crystals based on pyrazolium imides. *Angew. Chem.-Int. Edit.* **42**, 4499 (2003).

[72] Udovic, T. J. *et al.* Exceptional superionic conductivity in disordered sodium decahydro-closo-decaborate. *Adv. Mater.* **26**, 7622 (2014).

[73] Mauger, A., Armand, M., Julien, C. M. & Zaghib, K. Challenges and issues facing lithium metal for solid-state rechargeable batteries. *J. Power Sources* **353**, 333 (2017).

[74] Long, S., MacFarlane, D. R. & Forsyth, M. Fast ion conduction in molecular plastic crystals. *Solid State Ion.* **161**, 105 (2003).

[75] Reuter, D., Geiss, C., Lunkenheimer, P. & Loidl, A. Variation of ionic conductivity in a plastic-crystalline mixture. *J. Chem. Phys.* **147**, 104502 (2017).

[76] Reuter, D., Lunkenheimer, P. & Loidl, A. Plastic-crystalline solid-state electrolytes: Ionic conductivity and orientational dynamics in nitrile mixtures. *J. Chem. Phys.* **150**, 244507 (2019).

[77] Sherwood, J. N. *The Plastically Crystalline State - Orientationally-Disordered Crystals*, chap. 1.1, 39–41 (John Wiley & Sons, New York, 1979).

[78] Li, B. *et al.* Colossal barocaloric effects in plastic crystals. *Nature* **567**, 506 (2019).

[79] Pas, S. J., Huang, J., Forsyth, M., MacFarlane, D. R. & Hill, A. J. Defect-assisted conductivity in organic ionic plastic crystals. *J. Chem. Phys.* **122**, 064704 (2005).

[80] Huang, J. H., Hill, A., Forsyth, M., MacFarlane, D. & Hollenkamp, A. Conduction in ionic organic plastic crystals: The role of defects. *Solid State Ion.* **177**, 2569 (2006).

[81] Abouimrane, A., Whitfield, P. S., Niketic, S. & Davidson, I. J. Investigation of Li salt doped succinonitrile as potential solid electrolytes for lithium batteries. *J. Power Sources* **174**, 883 (2007).

[82] Fan, L. Z., Hu, Y. S., Bhattacharyya, A. J. & Maier, J. Succinonitrile as a versatile additive for polymer electrolytes. *Adv. Funct. Mater.* **17**, 2800 (2007).

[83] Patel, M., Chandrappa, K. G. & Bhattacharyya, A. J. Increasing ionic conductivity and mechanical strength of a plastic electrolyte by inclusion of a polymer. *Electrochim. Acta* **54**, 209 (2008).

[84] Klein, I. S., Zhao, Z. F., Davidowski, S. K., Yarger, J. L. & Angell, C. A. A new version of the lithium ion conducting plastic crystal solid electrolyte. *Adv. Energy Mater.* **8**, 1801324 (2018).

[85] Lunkenheimer, P., Schneider, U., Brand, R. & Loidl, A. Glassy dynamics. *Contemp. Phys.* **41**, 15 (2000).

[86] Scherer, G. W. *Glass Formation and Relaxation*. In Zarzycki, J. (ed.) *Materials Science and Technology: A Comprehensive Treatment, Volume 9, Glasses and Amorphous Materials*, chap. 3 (VCH Verlagsgemeinschaft mbH, Weinheim, 1991).

[87] Kremer, F. & Schönhals, A. *The Scaling of the Dynamics of Glasses and Supercooled Liquids*. In Kremer, F. & Schönhals, A. (eds.) *Broadband Dielectric Spectroscopy*, chap. 4 (Springer Verlag, Berlin, 2003).

[88] Jones, J. E. On the determination of molecular fields II. From the equation of state of a gas. *Proc. R. Soc. Lond. A.* **106**, 463 (1924).

[89] Debenedetti, P. G. & Stillinger, F. H. Supercooled liquids and the glass transition. *Nature* **410**, 259 (2001).

[90] Ediger, M. D., Angell, C. A. & Nagel, S. R. Supercooled liquids and glasses. *J. Phys. Chem.* **100**, 13200 (1996).

[91] Lunkenheimer, P. & Loidl, A. Dielectric spectroscopy of glass-forming materials: α-relaxation and excess wing. *Chem. Phys.* **284**, 205 (2002).

[92] Arrhenius, S. Über die Dissociationswärme und den Einfluss der Temperatur auf den Dissociationsgrad der Elektrolyte. *Z. Phys. Chem.* **4**, 226 (1889).

[93] Vogel, H. Das Temperaturabhängigkeitsgesetz der Viskosität von Flüssigkeiten. *Phys. Z.* **22**, 645 (1921).

[94] Fulcher, G. S. Analysis of recent measurements of the viscosity of glasses. *J. Am. Ceram. Soc.* **8**, 339 (1925).

[95] Tammann, G. & Hesse, W. Die Abhängigkeit der Viskosität von der Temperatur bei unterkühlten Flüssigkeiten. *Z. Anorg. Allg. Chem.* **156**, 245 (1926).

[96] Adam, G. & Gibbs, J. H. On temperature dependence of cooperative relaxation properties in glass-forming liquids. *J. Chem. Phys.* **43**, 139 (1965).

[97] Hecksher, T., Nielsen, A. I., Olsen, N. B. & Dyre, J. C. Little evidence for dynamic divergences in ultraviscous molecular liquids. *Nat. Phys.* **4**, 737 (2008).

[98] Schönhals, A., Kremer, F., Hofmann, A., Fischer, E. W. & Schlosser, E. Anomalies in the scaling of the dielectric α-relaxation. *Phys. Rev. Lett.* **70**, 3459 (1993).

[99] Stickel, F., Fischer, E. W. & Richert, R. Dynamics of glass-forming liquids. I. Temperature-derivative analysis of dielectric-relaxation data. *J. Chem. Phys.* **102**, 6251 (1995).

[100] Stickel, F., Fischer, E. W. & Richert, R. Dynamics of glass-forming liquids. II. Detailed comparison of dielectric relaxation, dc-conductivity, and viscosity data. *J. Chem. Phys.* **104**, 2043 (1996).

[101] Lunkenheimer, P., Kastner, S., Kohler, M. & Loidl, A. Temperature development of glassy α-relaxation dynamics determined by broadband dielectric spectroscopy. *Phys. Rev. E* **81**, 051504 (2010).

[102] Angell, C. A., Poole, P. H. & Shao, J. Glass-forming liquids, anomalous liquids, and polyamorphism in liquids and biopolymers. *Nuovo Cimento D* **16**, 993 (1994).

[103] Mauro, J. C., Yue, Y. Z., Ellison, A. J., Gupta, P. K. & Allan, D. C. Viscosity of glass-forming liquids. *Proc. Natl. Acad. Sci. U. S. A.* **106**, 19780 (2009).

[104] Angell, C. A. *Strong and fragile liquids*. In Ngai, K. L. & Wright, G. B. (eds.) *Relaxations in Complex Systems* (NRL, Washington DC, 1985).

[105] Angell, C. A. Perspective on the glass-transition. *J. Phys. Chem. Solids* **49**, 863 (1988).

[106] Plazek, D. J. & Ngai, K. L. Correlation of polymer segmental chain dynamics with temperature-dependent time-scale shifts. *Macromolecules* **24**, 1222 (1991).

[107] Böhmer, R. & Angell, C. A. Correlations of the nonexponentiality and state dependence of mechanical relaxations with bond connectivity in Ge-As-Se supercooled liquids. *Phys. Rev. B* **45**, 10091 (1992).

[108] Böhmer, R., Ngai, K. L., Angell, C. A. & Plazek, D. J. Nonexponential relaxations in strong and fragile glass formers. *J. Chem. Phys.* **99**, 4201 (1993).

[109] Raistrick, I. D. *2.1 The Electrical Analogs of Physical and Chemical Processes*. In Macdonald, J. R. (ed.) *Impedance Spectroscopy - Emphasizing Solid Materials and Systems*, chap. 2.1.2 (John Wiley & Sons, Inc., 1987).

[110] Feldman, Y., Ben Ishai, B., Puzenko, A. & Raicu, V. *Theoretical Background - Elementary Theory of the Interaction of Electromagnetic Fields with Dielectric Materials*. In Raicu, A. & Feldman, Y. (eds.) *Dielectric relaxation in biological systems - physical principles, methodes, and application*, chap. 1.1 (Oxford University Press, 2015).

[111] Schönhals, A. & Kremer, F. *Theory of Dielectric Relaxation*. In Kremer, F. & Schönhals, A. (eds.) *Broadband Dielectric Spectroscopy*, chap. 1 (Springer Verlag, Berlin, 2003).

[112] Dyre, J. C. The random free-energy barrier model for ac conduction in disordered solids. *J. Appl. Phys.* **64**, 2456 (1988).

[113] Hodge, I. M., Ngai, K. L. & Moynihan, C. T. Comments on the electric modulus function. *J. Non-Cryst. Solids* **351**, 104 (2005).

[114] Wagner, K. W. Zur Theorie der unvollkommenen Dielektrika. *Ann. Phys.* **40**, 817 (1913).

[115] Wagner, K. W. Erklärung der dielektrischen Nachwirkung auf Grund Maxwellscher Vorstellungen. *Arch. Elektrotech.* **2**, 371 (1914).

[116] Sillars, R. W. The properties of a dielectric containing semi-conducting particles of various shapes. *J. Inst. Elec. Eng.* **80**, 378 (1937).

[117] Emmert, S. *et al.* Electrode polarization effects in broadband dielectric spectroscopy. *Eur. Phys. J. B* **83**, 157 (2011).

[118] Kittel, C. *Einführung in die Festkörperphysik*, chap. 13, p. 428 (Oldenbourg Verlag GmbH, München, 1996).

[119] Böttcher, C. J. F. & Bordewijk, P. *Theory of electrical polarization*, chap. 8 (Elsevier Scientific Publishing Company, Amsterdam, 1978).

[120] Debye, P. *Polar molecules* (Dover Publications, New York, 1929).

[121] Richert, R. Homogeneous dispersion of dielectric responses in a simple glass. *J. Non-Cryst. Solids* **172**, 209 (1994).

[122] Schiener, B., Böhmer, R., Loidl, A. & Chamberlin, R. V. Nonresonant spectral hole burning in the slow dielectric response of supercooled liquids. *Science* **274**, 752 (1996).

[123] Richert, R. & Weinstein, S. Nonlinear dielectric response and thermodynamic heterogeneity in liquids. *Phys. Rev. Lett.* **97**, 095703 (2006).

[124] Schmidt-Rohr, K. & Spiess, H. W. Nature of nonexponential loss of correlation above the glass-transition investigated by multidimensional NMR. *Phys. Rev. Lett.* **66**, 3020 (1991).

[125] Williams, G. & Watts, D. C. Non-symmetrical dielectric relaxation behaviour arising from a simple empirical decay function. *Trans. Faraday Soc.* **66**, 80 (1970).

[126] Havriliak, S. & Negami, S. A complex plane representation of dielectric and mechanical relaxation processes in some polymers. *Polymer* **8**, 161 (1967).

[127] Cole, K. S. & Cole, R. H. Dispersion and absorption in dielectrics I. Alternating current characteristics. *J. Chem. Phys.* **9**, 341 (1941).

[128] Davidson, D. W. & Cole, R. H. Dielectric relaxation in glycerol, propylene glycol, and n-propanol. *J. Chem. Phys.* **19**, 1484 (1951).

[129] Böttcher, C. J. F. & Bordewijk, P. *Theory of electrical polarization*, chap. 9 (Elsevier Scientific Publishing Company, Amsterdam, 1978).

[130] Lindsey, C. P. & Patterson, G. D. Detailed comparison of the Williams-Watts and Cole-Davidson functions. *J. Chem. Phys.* **73**, 3348 (1980).

[131] Boersma, A., van Turnhout, J. & Wubbenhorst, M. Dielectric characterization of a thermotropic liquid crystalline copolyesteramide: I. Relaxation peak assignment. *Macromolecules* **31**, 7453 (1998).

[132] Diaz-Calleja, R. Comment on the maximum in the loss permittivity for the Havriliak-Negami equation. *Macromolecules* **33**, 8924 (2000).

[133] Johari, G. P. & Goldstein, M. Viscous liquids and glass transition. II. Secondary relaxations in glasses of rigid molecules. *J. Chem. Phys.* **53**, 2372 (1970).

[134] Johari, G. P. Source of JG-relaxation in the entropy of glass. *J. Phys. Chem. B* **123**, 3010 (2019).

[135] Stillinger, F. H. A topographic view of supercooled liquids and glass-formation. *Science* **267**, 1935 (1995).

[136] Harmon, J. S., Demetriou, M. D., Johnson, W. L. & Samwer, K. Anelastic to plastic transition in metallic glass-forming liquids. *Phys. Rev. Lett.* **99**, 135502 (2007).

[137] Ngai, K. L. & Paluch, M. Classification of secondary relaxation in glass-formers based on dynamic properties. *J. Chem. Phys.* **120**, 857 (2004).

[138] Schneider, U., Brand, R., Lunkenheimer, P. & Loidl, A. Excess wing in the dielectric loss of glass formers: A johari-goldstein β relaxation? *Phys. Rev. Lett.* **84**, 5560 (2000).

[139] Ngai, K. L. *et al.* Nature and properties of the Johari-Goldstein β-relaxation in the equilibrium liquid state of a class of glass-formers. *J. Chem. Phys.* **115**, 1405 (2001).

[140] Döß, A., Paluch, M., Sillescu, H. & Hinze, G. From strong to fragile glass formers: Secondary relaxation in polyalcohols. *Phys. Rev. Lett.* **88**, 095701 (2002).

[141] Kudlik, A., Benkhof, S., Blochowicz, T., Tschirwitz, C. & Rossler, E. The dielectric response of simple organic glass formers. *J. Mol. Struct.* **479**, 201 (1999).

[142] Hensel-Bielowka, S. & Paluch, M. Origin of the high-frequency contributions to the dielectric loss in supercooled liquids. *Phys. Rev. Lett.* **89**, 025704 (2002).

[143] Dyre, J. C., Maass, P., Roling, B. & Sidebottom, D. L. Fundamental questions relating to ion conduction in disordered solids. *Rep. Prog. Phys.* **72**, 046501 (2009).

[144] Demtröder, W. *Experimentalphysik 2 - Elektrizität und Optik*, chap. 2.6, 57–58 (Springer-Verlag Berlin Heidelberg, 1995).

[145] Johari, G. P. & Andersson, O. On the nonlinear variation of dc conductivity with dielectric relaxation time. *J. Chem. Phys.* **125**, 124501 (2006).

[146] Stokes, G. G. On the effect of the internal friction of fluids on the motion of pendulums. *Trans. Cambridge Philos. Soc.* **9**, 8 (1851).

[147] Einstein, A. Über die von der molekularkinetischen Theorie der Wärme geforderte Bewegung von in ruhenden Flüssigkeiten suspendierten Teilchen. *Ann. Phys. (Leipzig)* **322**, 549 (1905).

[148] Sutherland, W. LXXV. A dynamical theory of diffusion for non-electrolytes and the molecular mass of albumin. *Philos. Mag.* **9**, 781 (1905).

[149] Rössler, E. Indications for a change of diffusion mechanism in supercooled liquids. *Phys. Rev. Lett.* **65**, 1595 (1990).

[150] Fujara, F., Geil, B., Sillescu, H. & Fleischer, G. Translational and rotational diffusion in supercooled orthoterphenyl close to the glass-transition. *Z. Phys. B-Condens. Mat.* **88**, 195 (1992).

[151] Sillescu, H. Heterogeneity at the glass transition: A review. *J. Non-Cryst. Solids* **243**, 81 (1999).

[152] Xu, W., Cooper, E. I. & Angell, C. A. Ionic liquids: Ion mobilities, glass temperatures, and fragilities. *J. Phys. Chem. B* **107**, 6170 (2003).

[153] Habasaki, J., Leon, C. & Ngai, K. *Dynamics of Glassy, Crystalline and Liquid Ionic Conductors - Experiment, Theories, Simulation*, chap. 2.3.2 Conductivity Formalism, 23–24 (Springer International Publishing Switzerland, 2019).

[154] Stillinger, F. H. & Hodgdon, J. A. Translation-rotation paradox for diffusion in fragile glass-forming liquids. *Phys. Rev. E* **50**, 2064 (1994).

[155] Tarjus, G. & Kivelson, D. Breakdown of the Stokes-Einstein relation in supercooled liquids. *J. Chem. Phys.* **103**, 3071 (1995).

[156] Cicerone, M. T. & Ediger, M. D. Enhanced translation of probe molecules in supercooled *o*-terphenyl: Signature of spatially heterogeneous dynamics? *J. Chem. Phys.* **104**, 7210 (1996).

[157] Chang, I. & Sillescu, H. Heterogeneity at the glass transition: Translational and rotational self-diffusion. *J. Phys. Chem. B* **101**, 8794 (1997).

[158] Walden, P. Über organische Lösungs- und Ionisierungsmittel - III. Teil: Innere Reibung und deren Zusammenhang mit dem Leitvermögen. *Z. Phys. Chem.* **55**, 207 (1906).

[159] Angell, C. A., Imrie, C. T. & Ingram, M. D. From simple electrolyte solutions through polymer electrolytes to superionic rubbers: Some fundamental considerations. *Polym. Int.* **47**, 9 (1998).

[160] Schreiner, C., Zugmann, S., Hartl, R. & Gores, H. J. Fractional walden rule for ionic liquids: Examples from recent measurements and a critique of the so-called ideal KCl line for the walden plot. *J. Chem. Eng. Data* **55**, 1784 (2010).

[161] Wojnarowska, Z., Wang, Y. Y., Paluch, K. J., Sokolov, A. P. & Paluch, M. Observation of highly decoupled conductivity in protic ionic conductors. *Phys. Chem. Chem. Phys.* **16**, 9123 (2014).

[162] Xu, W. & Angell, C. A. Solvent-free electrolytes with aqueous solution-like conductivities. *Science* **302**, 422 (2003).

[163] Angell, C. A., Byrne, N. & Belieres, J. P. Parallel developments in aprotic and protic ionic liquids: Physical chemistry and applications. *Accounts Chem. Res.* **40**, 1228 (2007).

[164] Schroder, T. B. & Dyre, J. C. Ac hopping conduction at extreme disorder takes place on the percolating cluster. *Phys. Rev. Lett.* **101**, 025901 (2008).

[165] Habasaki, J., Leon, C. & Ngai, K. *Dynamics of Glassy, Crystalline and Liquid Ionic Conductors - Experiment, Theories, Simulation*, chap. 4.1 Electrical Conductivity Relaxation in Glassy, Crystalline and Molten Ionic Conductors, 89–92 (Springer International Publishing Switzerland, 2019).

[166] Jonscher, A. K. The 'universal' dielectric response. *Nature* **267**, 673 (1977).

[167] Dyre, J. C. & Schroder, T. B. Universality of ac conduction in disordered solids. *Rev. Mod. Phys.* **72**, 873 (2000).

[168] Elliott, S. R. & Owens, A. P. The diffusion-controlled relaxation model for ionic transport in glasses. *Philos. Mag. B* **60**, 777 (1989).

[169] Funke, K. Ion dynamics and correlations - Translational and localized ionic hopping motion in solid electrolytes. *Philos. Mag. A* **68**, 711 (1993).

[170] Griffin, P. *et al.* Decoupling charge transport from the structural dynamics in room temperature ionic liquids. *J. Chem. Phys.* **135**, 114509 (2011).

[171] Pimenov, A. *et al.* Ion transport in the fragile glass former $3KNO_3 - 2Ca(NO_3)_2$. *Phys. Rev. E* **54**, 676 (1996).

[172] Almond, D. P., Duncan, G. K. & West, A. R. The determination of hopping rates and carrier concentrations in ionic conductors by a new analysis of ac conductivity. *Solid State Ion.* **8**, 159 (1983).

[173] Almond, D. P., West, A. R. & Grant, R. J. Temperature-dependence of the A.C. conductivity of Na β-alumina. *Solid State Commun.* **44**, 1277 (1982).

[174] Howell, F. S., Bose, R. A., Macedo, P. B. & Moynihan, C. T. Electrical relaxation in a glass-forming molten-salt. *J. Phys. Chem.* **78**, 639 (1974).

[175] Dyre, J. C. On the mechanism of glass ionic-conductivity. *J. Non-Cryst. Solids* **88**, 271 (1986).

[176] Sangoro, J. *et al.* Electrical conductivity and translational diffusion in the 1-butyl-3-methylimidazolium tetrafluoroborate ionic liquid. *J. Chem. Phys.* **128**, 214509 (2008).

[177] Cosby, T., Vicars, Z., Mapesa, E. U., Tsunashima, K. & Sangoro, J. Charge transport and dipolar relaxations in phosphonium-based ionic liquids. *J. Chem. Phys.* **147**, 234504 (2017).

[178] Fan, F. *et al.* Ion conduction in polymerized ionic liquids with different pendant groups. *Macromolecules* **48**, 4461 (2015).

[179] Macedo, P. B., Moynihan, C. T. & Bose, R. Role of ionic diffusion in polarization in vitreous ionic conductors. *Phys. Chem. Glasses* **13**, 171 (1972).

[180] Köhler, M., Lunkenheimer, P. & Loidl, A. Dielectric and conductivity relaxation in mixtures of glycerol with LiCl. *Eur. Phys. J. E* **27**, 115 (2008).

[181] Almond, D. P. & West, A. R. Impedance and modulus spectroscopy of real dispersive conductors. *Solid State Ion.* **11**, 57 (1983).

[182] Dyre, J. C. Some remarks on ac conduction in disordered solids. *J. Non-Cryst. Solids* **135**, 219 (1991).

[183] Roling, B. What do electrical conductivity and electrical modulus spectra tell us about the mechanisms of ion transport processes in melts, glasses, and crystals? *J. Non-Cryst. Solids* **244**, 34 (1999).

[184] Richert, R. & Wagner, H. The dielectric modulus: Relaxation versus retardation. *Solid State Ion.* **105**, 167 (1998).

[185] Schwan, H. P. Electrode polarization impedance and measurements in biological materials. *Ann. N.Y. Acad. Sci.* **148**, 191 (1968).

[186] Springer, M. M., Korteweg, A. & Lyklema, J. The relaxation of the double-layer around colloid particles and the low-frequency dielectric-dispersion - Part II. Experiments. *J. Electroanal. Chem.* **153**, 55 (1983).

[187] Mazzeo, B. A. & Flewitt, A. J. Two- and four-electrode, wide-bandwidth, dielectric spectrometer for conductive liquids: Theory, limitations, and experiment. *J. Appl. Phys.* **102**, 104106 (2007).

[188] Ben Ishai, P., Talary, M. S., Caduff, A., Levy, E. & Feldman, Y. Electrode polarization in dielectric measurements: A review. *Meas. Sci. Technol.* **24**, 102001 (2013).

[189] Fricke, H. XXXIII. The theory of electrolytic polarization. *Philos. Mag.* **14**, 310 (1932).

[190] Bottelberghs, P. H. & Broers, G. H. J. Interfacial impedance behavior of polished and paint platinum-electrodes at $Na_2WO_4 - Na_2MoO_4$ solid electrolytes. *J. Electroanal. Chem.* **67**, 155 (1976).

[191] Liu, S. H. Fractal model for the ac response of a rough interface. *Phys. Rev. Lett.* **55**, 529 (1985).

[192] Macdonald, J. R. Impedance spectroscopy and its use in analyzing the steady-state ac response of solid and liquid electrolytes. *J. Electroanal. Chem.* **223**, 25 (1987).

[193] Bates, J. B., Chu, Y. T. & Stribling, W. T. Surface-topography and impedance of metal-electrolyte interfaces. *Phys. Rev. Lett.* **60**, 627 (1988).

[194] Feldman, Y., Nigmatullin, R., Polygalov, E. & Texter, J. Fractal-polarization correction in time domain dielectric spectroscopy. *Phys. Rev. E* **58**, 7561 (1998).

[195] Bordi, F., Cametti, C. & Gili, T. Reduction of the contribution of electrode polarization effects in the radiowave dielectric measurements of highly conductive biological cell suspensions. *Bioelectrochemistry* **54**, 53 (2001).

[196] Seeger, A. *et al.* Charge carrier localization in $La_{1-x}Sr_xMnO_3$ investigated by ac conductivity measurements. *J. Phys.-Condes. Matter* **11**, 3273 (1999).

[197] Lunkenheimer, P., Resch, M., Loidl, A. & Hidaka, Y. Ac conductivity in La_2CuO_4. *Phys. Rev. Lett.* **69**, 498 (1992).

[198] Umino, M., Oda, N. & Yasuhara, Y. Experimental and theoretical studies of the effect of electrode polarisation on capacitances of blood and potassium chloride solution. *Med. Biol. Eng. Comput.* **40**, 533 (2002).

[199] Thoms, E. *et al.* Dielectric study on mixtures of ionic liquids. *Sci Rep* **7**, 7463 (2017).

[200] Munzner, P., Hoffmann, L., Bohmer, R. & Gainaru, C. Deeply supercooled aqueous LiCl solution studied by frequency-resolved shear rheology. *J. Chem. Phys.* **150**, 234505 (2019).

[201] Whorlow, R. W. *Rheological techniques* (Ellis Horwood Limited, 1992).

[202] Mezger, T. G. *Das Rheoogie Handbuch: Für Anwender von Rotations- und Oszillations-Rheometern* (Viincentz Network GmbH & Co. KG, Hamburg, 2010).

[203] Verney, V. & Michel, A. Representation of the rheological properties of polymer melts in terms of complex fluidity. *Rheol. Acta* **28**, 54 (1989).

[204] Menon, N., Nagel, S. R. & Venerus, D. C. Dynamic viscosity of a simple glass-forming liquid. *Phys. Rev. Lett.* **73**, 963 (1994).

[205] Deegan, R. D., Leheny, R. L., Menon, N., Nagel, S. R. & Venerus, D. C. Dynamic shear modulus of tricresyl phosphate and squalane. *J. Phys. Chem. B* **103**, 4066 (1999).

[206] Mandanici, A. *et al.* Mechanical response of a simple molecular glass former in the glass transition region. *Mater. Sci. Eng. A-Struct. Mater. Prop. Microstruct. Process.* **432**, 299 (2006).

[207] Schröter, K. & Donth, E. Viscosity and shear response at the dynamic glass transition of glycerol. *J. Chem. Phys.* **113**, 9101 (2000).

[208] Jakobsen, B., Niss, K. & Olsen, N. B. Dielectric and shear mechanical alpha and beta relaxations in seven glass-forming liquids. *J. Chem. Phys.* **123**, 234511 (2005).

[209] Schröter, K. & Donth, E. Comparison of shear response with other properties at the dynamic glass transition of different glassformers. *J. Non-Cryst. Solids* **307-310**, 270 (2002).

[210] Santic, A., Wrobel, W., Mutke, M., Banhatti, R. D. & Funke, K. Frequency-dependent fluidity and conductivity of an ionic liquid. *Phys. Chem. Chem. Phys.* **11**, 5930 (2009).

[211] Bierwirth, S. P., Bohmer, R. & Gainaru, C. Generic primary mechanical response of viscous liquids. *Phys. Rev. Lett.* **119**, 248001 (2017).

[212] Novocontrol Technologies. *Alpha - A high resolution dielectric, conductivity, impedance, and gain phase modular measurement system - user's manual*.

[213] Keysight Technologies. *Impedance measurement handbook - A guide to measurement technology and techniques*.

[214] Novocontrol Technologies. *Quatro cryosystem - Brochure*.

[215] Novocontrol Technologies. *Quatro cryosystem - Owner's manual*.

[216] Höhne, G. W. H., Hemminger, W. F. & Flammersheim, H.-J. *Differential Scanning Calorimetry* (Springer-Verlag Berlin, 2003), 2nd edn.

[217] Lunkenheimer, P., Pimenov, A., Schiener, B., Bohmer, R. & Loidl, A. High-frequency dielectric spectroscopy on glycerol. *Europhys. Lett.* **33**, 611 (1996).

[218] Schneider, U., Lunkenheimer, P., Brand, R. & Loidl, A. Dielectric and far-infrared spectroscopy of glycerol. *J. Non-Cryst. Solids* **235**, 173 (1998).

[219] Abbott, A. P., Cullis, P. M., Gibson, M. J., Harris, R. C. & Raven, E. Extraction of glycerol from biodiesel into a eutectic based ionic liquid. *Green Chem.* **9**, 868 (2007).

[220] Abbott, A. P. *et al.* Glycerol eutectics as sustainable solvent systems. *Green Chem.* **13**, 82 (2011).

[221] Howell, F. S., Moynihan, C. T. & Macedo, P. B. Electrical relaxations in mixtures of lithium chloride and glycerol. *Bull. Chem. Soc. Jpn.* **57**, 652 (1984).

[222] Maggi, C., Jakobsen, B., Christensen, T., Olsen, N. B. & Dyre, J. C. Supercooled liquid dynamics studied via shear-mechanical spectroscopy. *J. Phys. Chem. B* **112**, 16320 (2008).

[223] Jordan, B. P., Sheppard, R. J. & Szwarnowski, S. Dielectric properties of formamide, ethanediol and methanol. *J. Phys. D-Appl. Phys.* **11**, 695 (1978).

[224] Lifanova, N. V., Usacheva, T. M. & Zhuravlev, M. V. Equilibrium and relaxation dielectric properties of 1,2-ethanediol. *Russ. J. Phys. Chem. A* **81**, 820 (2007).

[225] Kremer, F., Huwe, A., Arndt, M., Behrens, P. & Schwieger, W. How many molecules form a liquid? *J. Phys.-Condes. Matter* **11**, A175 (1999).

[226] Wagner, H. & Richert, R. Dielectric beta relaxations in the glassy state of salol? *J. Chem. Phys.* **110**, 11660 (1999).

[227] Abbott, A. P., Capper, G., Swain, B. G. & Wheeler, D. A. Electropolishing of stainless steel in an ionic liquid. *Trans. Inst. Metal Finish.* **83**, 51 (2005).

[228] Duvvuri, K. & Richert, R. Binary glass-forming materials: Mixtures of sorbitol and glycerol. *J. Phys. Chem. B* **108**, 10451 (2004).

[229] Wang, L. M., Tian, Y. J., Liu, R. P. & Richert, R. Structural relaxation dynamics in binary glass-forming molecular liquids with ideal and complex mixing behavior. *J. Phys. Chem. B* **114**, 3618 (2010).

[230] Abbott, A. P., Harris, R. C. & Ryder, K. S. Application of hole theory to define ionic liquids by their transport properties. *J. Phys. Chem. B* **111**, 4910 (2007).

[231] Jones, G. & Dole, M. The viscosity of aqueous solutions of strong electrolytes with special reference to barium chloride. *J. Am. Chem. Soc.* **51**, 2950 (1929).

[232] Hammadi, A. & Champeney, D. C. Ion-solvent interactions of some alkali halides in glycerol from density and viscosity data. *J. Chem. Eng. Data* **43**, 1004 (1998).

[233] Bauer, T., Kohler, M., Lunkenheimer, P., Loidl, A. & Angell, C. A. Relaxation dynamics and ionic conductivity in a fragile plastic crystal. *J. Chem. Phys.* **133**, 144509 (2010).

[234] Gotz, M., Bauer, T., Lunkenheimer, P. & Loidl, A. Supercooled-liquid and plastic-crystalline state in succinonitrile-glutaronitrile mixtures. *J. Chem. Phys.* **140**, 094504 (2014).

[235] Ibberson, R. M., Parsons, S., Allan, D. R. & Bell, A. M. T. Polymorphism in cyclohexanol. *Acta Crystallogr. Sect. B-Struct. Sci.* **64**, 573 (2008).

[236] Adachi, K., Suga, H. & Seki, S. Phase changes in crystalline and glassy-crystalline cyclohexanol. *Bull. Chem. Soc. Jpn.* **41**, 1073 (1968).

[237] Kabo, G. J. *et al.* Thermodynamic properties of cyclohexanol and cyclohexanone. *J. Chem. Thermodyn.* **20**, 429 (1988).

[238] Kelley, K. K. Cyclohexanol and the third law of thermodynamics. *J. Am. Chem. Soc.* **51**, 1400 (1929).

[239] Adachi, K. *et al.* Dielectric relaxations in various crystal modifications of cyclohexanol and 2,3-dimethylbutane. *Mol. Cryst. Liq. Cryst.* **18**, 345 (1972).

[240] Shablakh, M., Dissado, L. A. & Hill, R. M. Structure and dipole relaxation mechanisms in the cyclic alcohols cyclopentanol to cyclo-octanol. *J. Chem. Soc., Faraday Trans. 2* **79**, 369 (1983).

[241] Pingel, N., Poser, U. & Würflinger, A. Dielectric measurements at high-pressures and low-temperatures - Part 6. dielectric and thermodynamic properties of cyclohexanol. *J. Chem. Soc., Faraday Trans. I* **80**, 3221 (1984).

[242] Mayer, J., Rachwalska, M., Sciesinska, E. & Sciesinski, J. On the polymorphism of solid cyclohexanol by adiabatic calorimetry and far infrared methods. *J. Phys. France* **51**, 857 (1990).

[243] Hartmann, M., Jenau, M., Würflinger, A., Godlewska, M. & Urban, S. High pressure DTA study on the phase behaviors in some selected plastic and liquid crystals. *Z. Phys. Chem.* **177**, 195 (1992).

[244] Suzuki, H., Hoshina, H. & Otani, C. Kinetics of polymorphic transitions of cyclohexanol investigated by terahertz absorption spectroscopy. *Cryst. Growth Des.* **14**, 4087 (2014).

[245] Mizukami, M., Fujimori, H. & Oguni, M. Possible emergence of plural sets of α- and β-glass transitions in orientationally disordered crystal, cyclohexanol. *Solid State Commun.* **100**, 83 (1996).

[246] Green, J. R. & Wheeler, D. R. X-ray investigation of some plastic crystals - II. Density of vacancies in cyclohexane, cyclohexanol and dl-camphene. *Mol. Cryst. Liq. Cryst.* **6**, 13 (1969).

[247] Andre, D., Ceccaldi, D. & Szwarc, H. Glassy crystals III: X-ray determination of the structures of the plastic and glassy crystalline phases of cyclohexanol. *J. Phys. (Paris)* **45**, 73 (1984).

[248] Ceccaldi, D. X-ray diffuse-scattering by cyclohexanol in the plastic phase - A theoretical-model including orientational and translational molecular correlations. *Phys. Rev. B* **31**, 8221 (1985).

[249] Sciesinska, E., Mayer, J., Natkaniec, I. & Sciensinski, J. Neutron-scattering study of polymorphism of cyclohexanol. *Acta Phys. Pol. A* **76**, 617 (1989).

[250] James, D. W., Shurvell, H. F. & Parry, R. M. Polymorphism in cyclohexanol: A raman spectroscopic study. *J. Raman Spectrosc.* **5**, 201 (1976).

[251] Green, J. R. & Griffith, W. T. Phase transformations in solid cyclohexanol. *J. Phys. Chem. Solids* **26**, 631 (1965).

[252] Garg, S. K. & Smyth, C. P. Microwave absorption and molecular structure in liquids - LXVIII. Dielectric behavior at 2.2mm wavelength and intramolecular motion in five substituted benzenes and cyclohexanes. *J. Chem. Phys.* **46**, 373 (1967).

[253] Shinomiya, T. Dielectric-relaxation and intermolecular association of alicyclic alcohols in liquid and solid states. *Bull. Chem. Soc. Jpn.* **63**, 1087 (1990).

[254] Stockhausen, M. & von Hornhardt, S. Dielectric-relaxation of liquid alicyclic alcohols. *Z. Naturfors. Sect. A-J. Phys. Sci.* **47**, 1135 (1992).

[255] Gangasharan & Murthy, S. S. N. Study of α-, β-, and γ-relaxation processes in some supercooled liquids and supercooled plastic crystals. *J. Chem. Phys.* **99**, 9865 (1993).

[256] Kuhns, P. L. & Conradi, M. S. NMR study of molecular motions in cyclohexanol, a glass-forming rotor crystal. *J. Chem. Phys.* **80**, 5851 (1984).

[257] Fuchs, A. H., Virlet, J., Andre, D. & Szwarc, H. Glassy crystals. V: Structural and dynamic studies of large-amplitude molecular motions. *J. Chim. Phys.* **82**, 293 (1985).

[258] Yamamuro, O., Yamasaki, H., Madokoro, Y., Tsukushi, I. & Matsuo, T. Calorimetric and neutron scattering studies of plastically crystalline cyclooctanol. *J. Phys.-Condes. Matter* **15**, 5439 (2003).

[259] Puertas, R. *et al.* Thermodynamic, crystallographic, and dielectric study of the nature of glass transitions in cyclo-octanol. *Phys. Rev. B* **69**, 224202 (2004).

[260] Edelmann, R. & Würflinger, A. Phase-behavior of cyclo-octanol up to pressures of 300 MPa and temperatures between 100 and 370 K. *Mol. Cryst. Liq. Cryst.* **148**, 249 (1987).

[261] Andersson, O. & Ross, R. G. Thermal-conductivity, heat-capacity and phase-diagram of cyclooctanol in liquid, solid and glassy crystal-states under high-pressure. *Mol. Phys.* **71**, 523 (1990).

[262] Tyagi, M. & Murthy, S. S. N. Study of the nature of glass transitions in the plastic crystalline phases of cyclo-octanol, cycloheptanol, cyanoadamantane and cis-1,2-dimethylcyclohexane. *J. Chem. Phys.* **114**, 3640 (2001).

[263] Rute, M. A. *et al.* Two-component system cycloheptanol (C7) + cyclooctanol (C8): An extraordinary system. *J. Phys. Chem. B* **107**, 5914 (2003).

[264] Sciesinski, J., Mayer, J., Wasiutynski, T., Sciesinska, E. & Wojtowicz, J. Calorimetric study of cyclooctanol. *Phase Transit.* **54**, 15 (1995).

[265] Leslie-Pelecky, D. L. & Birge, N. O. Dielectric measurement of the model glass-transition in orientationally disordered cyclo-octanol. *Phys. Rev. B* **50**, 13250 (1994).

[266] Leslie-Pelecky, D. L. & Birge, N. O. Universal scaling of the relaxation near a model glass-transition. *Phys. Rev. Lett.* **72**, 1232 (1994).

[267] Brand, R., Lunkenheimer, P. & Loidl, A. Relaxations and fast dynamics of the plastic crystal cyclo-octanol investigated by broadband dielectric spectroscopy. *Phys. Rev. B* **56**, R5713 (1997).

[268] Lunkenheimer, P., Brand, R., Schneider, U. & Loidl, A. Excess wing and high frequency dynamics in plastic crystals. *Philos. Mag. B* **79**, 1945 (1999).

[269] Michl, M., Bauer, T., Lunkenheimer, P. & Loidl, A. Cooperativity and heterogeneity in plastic crystals studied by nonlinear dielectric spectroscopy. *Phys. Rev. Lett.* **114**, 067601 (2015).

[270] Corfield, G. & Davies, M. Dielectric relaxation studies of rotator phase solids - Part 3. Cyclohexane derivatives. *Trans. Farad. Soc.* **60**, 10 (1964).

[271] Singh, L. P. & Murthy, S. S. N. Dielectric and calorimetric investigation of an unusual two-component plastic crystal: cyclohexanol-neopentylglycol. *Phys. Chem. Chem. Phys.* **11**, 5110 (2009).

[272] Singh, L. P., Murthy, S. S. N. & Singh, G. Study of supercooled orientationally disordered binary solid solutions II: cyclohexyl derivatives, neopentanol and neopentylglycol. *Phys. Chem. Chem. Phys.* **11**, 9278 (2009).

[273] Singh, L. P. & Murthy, S. S. N. Dielectric and calorimetric study of orientationally disordered phases in two unusual two-component systems. *J. Phys. Chem. B* **112**, 2606 (2008).

[274] Martinez-Garcia, J. C. *et al.* Disentangling the secondary relaxations in the orientationally disordered mixed crystals: Cycloheptanol + cyclooctanol two-component system. *J. Phys. Chem. B* **114**, 6099 (2010).

[275] Reuter, D., Seitz, K., Lunkenheimer, P. & Loidl, A. unpublished .

[276] Nordman, C. E. & Schmitkons, D. L. Phase transition and crystal structures of adamantane. *Acta Cryst.* **18**, 764 (1965).

[277] Amoureux, J. P., Bee, M. & Damien, J. C. Structure of adamantane, $C_{10}H_{16}$, in the disordered phase. *Acta Crystallogr., Sect. B: Struct. Commun.* **36**, 2633 (1980).

[278] Amoureux, J. P. & Bee, M. Crystal-structure of 1-cyanoadamantane, $C_{10}H_{15}CN$, in its plastic phase. *Acta Crystallogr., Sect. B: Struct. Commun.* **35**, 2957 (1979).

[279] Foulon, M., Amoureux, J. P., Sauvajol, J. L., Cavrot, J. P. & Muller, M. Different aspects of an interesting glassy crystal - 1-cyanoadamantane. *J. Phys. C: Solid State Phys.* **17**, 4213 (1984).

[280] Yamamuro, O., Ishikawa, M., Kishimoto, I., Pinvidic, J. J. & Matsuo, T. Thermodynamic approach to glass transitions of plastically crystalline cyanoadamantane and isocyanocyclohexane. *J. Phys. Soc. Jpn.* **68**, 2969 (1999).

[281] Carpentier, L., Decressain, R. & Descamps, M. Influence of phase transformation on the low temperature dielectric measurements in 1-cyanoadamantane. *J. Chem. Phys.* **128**, 024702 (2008).

[282] Amoureux, J. P. & Bee, M. Crystal-structure of 2-adamantanone $C_{10}H_{14}O$ in its plastic phase. *J. Phys. C: Solid St. Phys.* **13**, 3577 (1980).

[283] Romanini, M. *et al.* Emergence of glassy-like dynamics in an orientationally ordered phase. *Phys. Rev. B* **85**, 134201 (2012).

[284] Amoureux, J. P., Castelain, M., Benadda, M. D., Bee, M. & Sauvajol, J. L. Dielectric-properties of 1-cyanoadamantane $C_{10}H_{15}CN$, in its plastic phase. *J. Phys.* **44**, 513 (1983).

[285] Pathmanathan, K. & Johari, G. P. Molecular relaxations in a rigid molecular glassy crystal. *J. Phys. C: Solid State Phys.* **18**, 6535 (1985).

Danksagung

Natürlich wäre diese Arbeit nicht ohne die Hilfe vieler netter Menschen möglich gewesen und deswegen möchte ich die letzte Seite dieser Arbeit nutzen, um einige beim Namen zu nennen.

Zuallererst möchte ich mich bei meinem Doktorvater Prof. Dr. Alois Loidl bedanken, dessen Betreuungsarbeit und Vorbildsfunktion weit über den Fachbereich der Physik hinausging. Gleichfalls möchte ich mich bei Prof. Dr. Dirk Volkmer für das Zweitgutachten dieser Arbeit und bei Prof. Dr. Ulrich Eckern für die Teilnahme an der mündlichen Prüfung bedanken.

Besonderer Dank gebührt Priv.-Doz. Dr. Peter Lunkenheimer für die Teilnahme an der mündlichen Prüfung und vor allem für die engagierte, geduldige und kompetente Betreuungsarbeit im Labor, bei der Datenauswertung und beim wissenschaftlichen Schreiben.

Große Bereicherung für diese Arbeit stellen die Viskositätsmessungen dar, die ich bei EP 3 der TU Dortmund durchführen konnte. Für die Ermöglichung dieser und die ausgesprochene Gastfreundschaft möchte ich mich bei Prof. Dr. Roland Böhmer, Priv.-Doz. Dr. Catalin Gainaru, Peter und Phillipp bedanken.

Außerdem möchte mich auch bei allen Kollegen des EP5-Lehrstuhls bedanken, insbesondere bei meinem langjährigen EP5-Weggefährten Korbinian. Ebenso geht ein fettes Dankeschön an die etwas entfernteren Kollegen Markus und Marc für die unzähligen Calisthenics-Sessions in Begleitung von Herrn Krause und Co.

Schließlich gilt mein größter Dank meinen Eltern Claudia und Stefan für die bedingungslose Unterstützung während meines ganzen Studiums.